

**Compact Objects in the Disk
and Globular Clusters**

Thesis by

Helen Margaret Johnston

In Partial Fulfillment of the Requirements
for the Degree of
Doctor of Philosophy

California Institute of Technology

Pasadena, California

1992

(Defended May 4, 1992)

Astronomye is an harde thynge and yvel for to knowe.

— *William Langland (1330? – 1400?), Piers the Plowman*

To my parents

Acknowledgements

It seems a very long time ago that I arrived in Pasadena, only to find that the entire Astronomy department was out hosting the Pasadena AAS conference. I was told to “just go on over — it’ll be interesting”, so I wandered around looking lost until I was rescued by Chris, Rich and Steve, who took me out for a pizza. That team spirit was what made Caltech enjoyable, despite the smog and the earthquakes.

Many people have contributed in many ways to this thesis, in more ways than I can remember. If I have forgotten anyone, accept my heartfelt apologies.

Most importantly, I wish to give special thanks to Shri. I started working with Shri almost by accident, and am extremely grateful he agreed to work with me on a thesis project. Though it was at times infuriating (always *just one* more proposal to write...), not to mention exhausting, I have nothing but admiration for Shri’s enthusiasm and abundance of ideas, and would not have traded advisors for anything. I look forward to Shri getting old so we can finally keep up with him[†]. Not many advisors give their students opportunities to observe at seven (I think that’s all!) different observatories during their thesis work; I promise one of these days I’ll even get all of the data reduced! Shri was also very accommodating about my continually shifting timetable for completion of the thesis, for which my thanks; also to Frank Verbunt for similar forbearance over my eventual arrival!

I’d like to thank the denizens of these various observatories; without their help, I’d still be struggling. Juan Carrasco as the night assistant for nearly all my Palomar runs, and Dave Tennant, John Hennings and Mike Doyle as engineers deserve a large round of applause for the work they do to keep Palomar Observatory running. I’d like to thank Miller Goss and Dale Frail for putting up with (yet another) AIPS neophyte and teaching me the fine art of VLA data reduction. Richard Strom similarly taught me the voodoo of DWARF, and helped make two trips to Dwingeloo very enjoyable experiences.

But it was the residents of Robinson who did the most to make my stay here fun. I’d especially like to thank those students who welcomed me into the department, especially by means of PJ Fund trips to Death Valley, the Colorado River, *etc.*: Chris W., Rich, Steve, Karl, Debbie, Irwin, Chris T. and Josh, and the young whippersnappers who came afterwards: Nick, Tom, Todd and Angela. It’s all because of people like you that I convinced youngsters like Angela to come to Caltech! I’d also like to thank all the faculty members who were so ready to answer questions or suggest ideas: Judy Cohen, Jesse Greenstein, Jeremy Mould, Sterl Phinney, Tony Readhead, and Wal Sargent. Thanks also to Helen Knudsen, for her sterling job as librarian, and all the others who keep life in Robinson

[†] This, however, doesn’t seem to have worked with Jesse!

running.

I'd also like to thank Don Campbell for convincing me to come to Caltech. Well, he was hoping I'd go to Cornell, but he failed there! Anyway, for all help received, as well as encouragement along the way — thanks, Don.

Many organisations have supported this research financially (via Shri): my thanks go to the Dudley Observatory, the National Science Foundation, the Packard Foundation, the Perkin Fund, and the Sloan Foundation.

Special thanks go to the *Cantores Atri Mortis* members, past and present (Jen, Bryan, Howard, Donnie, Molly, Cathy, Neill, Jamie, Joel, Rachel, Barb, Chris W., Chris T., Beth, Roger): it was our weekly practices that kept me sane in the middle there. Monteverdi will never be the same! And thanks to Will and Molly for hosting me during my return trip to defend my thesis.

I thank Dr. William Caton for doing such a successful brain reconstruction job — even if he *was* from MIT.

Shri's Army — Will, José, Gautam, Steve, Jagmit (and honorary member Tony) — will continue to hold a special place in my heart. The camaraderie developed down in the lab was really wonderful, and I'm sure I'll miss it. Particular thanks are due to Will and José for keeping the Suns running so well, for being willing to answer stupid Unix question, for dissolving my computer screen while I was trying to write...

In a long overdue acknowledgement, I would like to thank Chris Kochanek for not only providing me with a numerical integrator, but for being willing to debug it for me (he didn't *actually* debug it, you understand, he was just willing!) But I would like to thank Chris and Barb for their friendship over the years.

Most especially, I want to thank my whole family for their love and support, particularly during crisis situations. My heartfelt thanks go to my mother and Emma (and Johns Bunyan and Mandeville) for their lifeline of correspondence: I can only apologise for not being as diligent in my own writing! And I cannot thank both my parents enough for the encouragement they have always given me, not the least for not laughing when I decided to become an astronomer at the age of seven.

And last of all, my thanks to my husband Alain, for always being there. His love, support, help and encouragement have kept me going and shown me what is important. I am privileged to have him as companion and colleague.

Abstract

This thesis presents a multi-wavelength study of compact objects in globular clusters and in the disk. It is divided into two sections, and contains seven independent chapters, linked by the general theme of the study of the evolution and distribution of recycled pulsars and low mass X-ray binaries.

Part I deals with pulsars in globular clusters. Clusters appear to contain large numbers of pulsars, and this section is devoted to analyzing the pulsar content of the globular cluster system. The smearing of a pulsar signal in a binary orbit is analyzed numerically, and empirical relations between the observing time and the parameters of detectable binaries are presented. It appears that current searches should already have found a large fraction of cluster pulsars.

In Chapter 3, sensitive VLA images of four clusters are presented. No emission is detected from the dense cluster Liller 1, which suggests that the pulsar population of a cluster is not dependent only on its density. Seven unidentified sources are detected in or near the cores of three clusters. There appears to be no large population of pulsars in tight binaries.

In Chapter 4, the ultra-short period binary 4U 1820–30 in NGC 6624 is detected at 1.4 GHz. The source is confirmed to be several arc seconds away from the cluster core, implying its negative period derivative cannot be due to gravitational acceleration by the cluster. It is suggested that identification of cluster X-ray sources via their radio emission is a potentially powerful tool.

In Chapter 5, a statistical analysis of all previous pulsar surveys, as well as new VLA and Westerbork observations, is used to derive the cluster pulsar luminosity function and the cluster density weighting function. The derived luminosity function is very similar to that of disk pulsars, and the density weighting function scales significantly less steeply than predicted by the tidal capture model. It is suggested that this may be due to the importance of single star-binary interactions.

Part II presents optical spectroscopy of a variety of compact binaries in the disk. Chapter 6 presents observations of the X-ray nova A0620–00. The mass of the compact object is confirmed to be above the maximum allowed mass for a neutron star, and therefore must be a black hole. More stringent limits are placed on the black hole mass by analysis of the emission lines from the disk.

Chapter 7 presents spectroscopy of the recurrent nova U Scorpii, which has been argued to be a very massive white dwarf, $M \sim 1.4 M_{\odot}$. As a candidate for a white dwarf which may collapse to form a neutron star, this object is highly interesting for understanding

the evolution of millisecond pulsars and LMXBs. From analysis of the absorption lines, an upper limit is placed on the mass of the white dwarf: $M \lesssim 0.9 M_{\odot}$ (3σ). Hydrogen is also detected in absorption, suggesting that the observed high helium abundance in the emission lines is not due to the nature of the companion. Thus it appears there is no viable model for this interesting source.

In Chapter 8, radial velocities of nine disk LMXBs are presented. These are considered in the light of the direct formation model for LMXBs, where the neutron star is formed by the supernova explosion of a massive star in a binary system. With the inclusion of a random kick given to the neutron star at birth, the observations are found to be consistent with this model.

Table of Contents

| | |
|--|-----------|
| Acknowledgments | iv |
| Abstract | vi |
| 1 Introduction | 1 |
| 1.1 Historical overview | 1 |
| 1.2 Aims of this thesis | 2 |
| 1.3 Structure of this thesis | 3 |
| References | 5 |
| | |
| I Pulsars in Globular Clusters | 7 |
| | |
| 2 On the detectability of pulsars in close binary systems | 8 |
| 2.1 Introduction | 9 |
| 2.2 The detectability of pulsars in binary systems | 13 |
| 2.2.1 Standard pulse searches | 14 |
| 2.2.2 Searches using an acceleration code | 18 |
| 2.3 Improving the odds: Repeated observations | 20 |
| 2.4 The optimum integration time | 21 |
| 2.5 Discussion | 23 |
| Table 2.1: P_o and T_{best} for tidal capture theory | 26 |
| Table 2.2: Disk and cluster pulsars in binary systems | 27 |
| References | 28 |
| Figure captions | 30 |
| | |
| 3 Deep VLA images of globular clusters | 38 |
| 3.1 Introduction | 39 |
| 3.2 Observations | 40 |
| 3.3 Cluster pulsars | 42 |
| 3.3.1 Pulsars in binaries | 42 |
| 3.3.2 The density scaling of cluster pulsars: A third parameter? | 42 |
| 3.3.3 The spectral index of cluster pulsars | 43 |
| 3.4 Other sources | 44 |
| 3.4.1 Planetary nebulae | 44 |

| | |
|---|-----------|
| 3.4.2 Low mass X-ray binaries: A new diagnostic? | 44 |
| Table 3.1: Globular cluster sources detected at 20 cm | 46 |
| References | 47 |
| Figure caption | 49 |
| | |
| 4 Deep VLA images of globular clusters: NGC 6624 | 51 |
| 4.1 Introduction | 52 |
| 4.2 Observations and Discussion | 54 |
| 4.3 Radio studies of cluster LMXBs: A powerful probe | 55 |
| Table 4.1: Previous detections of 4U 1820–30 | 57 |
| References | 58 |
| Figure captions | 60 |
| | |
| 5 The statistics of pulsars in globular clusters | 63 |
| 5.1 Introduction | 64 |
| 5.2 Predictions of the standard model | 66 |
| 5.3 New observations and description of previous surveys | 68 |
| 5.3.1 VLA data | 68 |
| 5.3.2 Westerbork data | 68 |
| 5.3.3 Previous pulsar surveys | 68 |
| 5.4 The luminosity function of recycled pulsars | 70 |
| 5.4.1 Ages and birthrates of cluster pulsars | 70 |
| 5.4.2 The luminosities of cluster pulsars | 70 |
| 5.5 Density dependence of the cluster pulsar birthrate | 73 |
| 5.6 A self-consistent estimate of the cluster pulsar population | 74 |
| 5.6.1 Choice of luminosity function | 74 |
| 5.6.2 Choice of weighting function | 77 |
| 5.7 The total number of cluster pulsars | 80 |
| Table 5.1: New observations | 85 |
| Table 5.2: Globular cluster parameters and search limits | 86 |
| Table 5.3: Pulsar fluxes | 90 |
| Table 5.4: Luminosity function simulations | 91 |
| References | 92 |
| Figure captions | 95 |

| | |
|---|------------|
| 6 The black hole A0620–00 and its accretion disk | 102 |
| 6.1 Introduction | 103 |
| 6.2 Observations | 104 |
| 6.3 Radial velocity measurements | 105 |
| 6.4 Emission line analysis | 106 |
| 6.5 The mass of the black hole | 109 |
| 6.6 Discussion | 111 |
| Table 6.1: Journal of observations | 113 |
| Table 6.2: Parameters for the largest stable orbit for a range of μ | 114 |
| References | 115 |
| Figure captions | 116 |
| Appendix: Further observations of A0620–00 | 121 |
| Table A1: Parameters derived from fit | 122 |
| Figure captions | 123 |
| | |
| 7 Spectroscopy of the recurrent nova U Scorpii..... | 125 |
| 7.1 Introduction | 126 |
| 7.2 Observations | 128 |
| 7.3 Results | 129 |
| 7.3.1 Emission features | 129 |
| 7.3.2 Absorption features | 129 |
| 7.3.3 Emission line velocities | 130 |
| 7.3.4 Absorption line velocities | 131 |
| 7.4 Discussion | 133 |
| Table 7.1: Journal of observations | 135 |
| Table 7.2: Line widths and intensities | 136 |
| Table 7.3: Orbital parameters for U Sco | 137 |
| References | 138 |
| Figure captions | 139 |

| | |
|---|------------|
| 8 The kinematics of low mass X-ray binaries..... | 145 |
| 8.1 Introduction | 146 |
| 8.2 Observations | 149 |
| 8.2.1 Reliability of the velocities | 149 |
| 8.2.1 Individual objects | 150 |
| 8.3 A definitive list of LMXB velocities | 152 |
| 8.4 The direct formation model for LMXB formation | 155 |
| 8.4.1 Common envelope evolution | 155 |
| 8.4.2 The numerical experiment | 157 |
| 8.4.3 Solar motion solutions | 159 |
| 8.5 Discussion | 161 |
| Table 8.1: New velocity measurements | 163 |
| Table 8.2: Radial velocities of disk LMXBs..... | 164 |
| References..... | 165 |
| Figure captions..... | 168 |

Chapter 1

Introduction

1.1 Historical overview

1992 represents the twenty-fifth anniversary of the discovery of pulsars (Hewish *et al.* 1968), the tenth anniversary of the discovery of the first millisecond pulsar (Backer *et al.* 1982), and the fifth anniversary of the discovery of the first cluster pulsar (Lyne *et al.* 1987).

The first extra-solar system X-ray source, Sco X-1, was discovered in 1962 (Giacconi *et al.* 1962), and several more compact sources were discovered in the next few years. The binary nature of the galactic X-ray sources was suggested very early, when Sandage *et al.* (1966) pointed out the similarity between the spectrum of the optical counterpart to Sco X-1 and that of old novae. Several authors quickly realized that binary systems containing accreting compact objects provided an efficient mechanism for converting gravitational potential energy into radiation (“*We have such a large amount of gravitational energy in such a binary system; we must use it! of course!*” — Ginzburg, quoted in Gursky & Ruffini 1974). The discovery of pulsars (Hewish *et al.* 1968) provided the first observational detection of a neutron star.

As no binary motion could be detected in the optical spectra of the Galactic X-ray binaries, the binary model languished until the discovery of the eclipsing binary system Cen X-3 (Schreier *et al.* 1972). Subsequently, most Galactic compact X-ray sources were identified as binary systems where matter is being transferred from one star to a compact star (a white dwarf, neutron star or black hole).

With the completion of the *Uhuru* all-sky X-ray survey, two classes of bright X-ray binaries were identified: the low mass X-ray binaries (LMXBs), where the mass-transferring star is a low mass star, typically with mass less than $1 M_{\odot}$, and massive X-ray binaries, where the companion mass is typically more than $10 M_{\odot}$.

The first pulsar in a binary system, PSR 1913+16, was discovered in 1975 (Hulse & Taylor 1975), and the first millisecond pulsar, PSR1937+21, in 1982 (Backer *et al.* 1982). Subsequently, it was realized that the millisecond and binary pulsars form a distinct class of objects known as “recycled” pulsars, so-called because the neutron star was spun-up by the accretion of matter from a binary companion. This led to the suggestion that these systems could be the descendants of the X-ray binaries, after mass transfer onto the neutron star has ceased. It is now widely believed that the high-mass binary pulsars like PSR1913+16

are the descendants of the massive X-ray binaries, while PSR1937+21 and the low-mass binary pulsars descend from the low mass X-ray binaries.

The next important step came with the discovery of the first cluster pulsar, PSR 1821-24 in M28 (Lyne *et al.* 1987). The high incidence of X-ray binaries in globular clusters had long been noticed: though they contain only 10^{-3} of the stars in the galaxy, clusters contain 10^{-1} of the LMXBs. This and the proposed evolutionary link between the two classes of objects led to the discovery of a point radio source in M28 (Hamilton *et al.* 1985), and the subsequent discovery of the pulsar. Since then several intensive searches towards clusters have been made, and so far 27 cluster pulsars are known.

The prevalence of pulsars and X-ray binaries in clusters has been attributed to the efficiency of stellar captures in the high densities found in clusters. In the simplest model, primeval neutron stars, born in the first wave of star formation, tidally capture field stars, and later mass transfer spins up the neutron star. However, several lines of reasoning have led some authors to propose that the neutron stars are not formed in supernova explosions, but are instead the result of accretion-induced collapse of white dwarfs.

1.2 Aims of this thesis

Many questions still remain concerning the origin and evolution of millisecond pulsars and LMXBs. This thesis represents several attacks on the general problem of the evolutionary link between LMXBs and pulsars, in the Galactic disk and the globular cluster system.

The first part investigates the question of the number of pulsars in globular clusters in several fashions. The strong association of LMXBs with clusters, and the large numbers of cluster pulsars being discovered, both indicate the efficiency of tidal capture in globular clusters. The number of pulsars in a cluster with central density ρ_c is expected to scale as ρ_c^2 . However, pulsar searches, particularly those from Arecibo, are finding pulsars in very sparse clusters, indicating that the number of pulsars is not scaling with central density as expected.

Strong selection effects hamper pulsar surveys, which affect all attempts to extrapolate these surveys to the whole cluster system. One of these is the fact that pulsars in tight binaries are difficult to find using standard pulse search techniques. The binaries formed by tidal capture are very tight, $P \lesssim 1$ d, so the speed of the pulsar varies considerably over a typical integration. This problem is attacked in this thesis in two ways: by analyzing the extent of the pulse smearing and suggesting ways to ameliorate the problem, and by searching for pulsars using radio imaging, which is immune to this effect.

I then present an analysis of all the current pulsar searches, and present an estimate for the total pulsar population. This is very dependent on the assumptions made about the pulsar luminosity function, so I attempt to measure both of these quantities from the data.

Part II contains three chapters on X-ray binaries in the disk. As presumed progenitors for the disk millisecond pulsars, these objects can provide us with important clues to the evolutionary history of recycled pulsars. I present spectroscopy of the black hole candidate A0620–00, and confirm that the central object must be a black hole. I present spectroscopy of the recurrent nova U Scorpii, which has been suggested to be a candidate for a white dwarf about to collapse to form a neutron star. Finally, I present an analysis of the kinematics of the disk LMXBs, in an attempt to discriminate between two possible models for their origin.

1.3 Structure of this thesis

This thesis is organized in two parts, the first dealing with pulsars in globular clusters, the second with low mass X-ray binaries and similar objects in the disk.

Chapter 2 is an analysis of one of the selection effects that hampers searches for pulsars in the tight binaries that are formed in globular clusters. I present the results of numerical calculations of the extent to which a pulsar signal in a binary is smeared out by the effect of orbital motion, and suggest strategies for maximizing the probability of finding pulsars in tight binaries. I present empirical relations between the observing time and the parameters of the binaries which can be found. I conclude that the current pulse searches are already finding a reasonable fraction of tidal capture binaries in clusters.

Chapters 3 and 4 present the results of observations made with the Very Large Array, New Mexico. These observations are not searching for pulsed emission from cluster pulsars, but instead are looking for the time-averaged, integrated emission, which is immune to the binary smearing discussed in Chapter 2. In Chapter 3, I present deep images of four clusters, which suggest that there is *not* a large undiscovered population of pulsars in tight binaries, as would be expected in the standard model for their formation. Further, the absence of emission from the dense cluster Liller 1 indicates that the number of pulsars is not scaling as expected with central density. I identify several new sources, and put an upper limit on the number of previously undetected tight binary pulsars.

In Chapter 4, I present a sensitive image of the low mass X-ray binary 4U 1820–30 in NGC 6624. Our improvement of the X-ray position has interesting implications for models for the system. I also discuss the use of radio observations such as these in identifying

LMXBs in the crowded cores of clusters. I suggest that radio observations may be a powerful tool for discriminating between neutron star binaries and white dwarf binaries.

Chapter 5 presents some more observations of the integrated radio emission from globular clusters, using data taken with the VLA and with the Westerbork Synthesis Radio Telescope, The Netherlands. I then present a statistical analysis of the distribution of pulsars within the globular cluster system. Such an analysis is intimately tied up with the luminosity function of the pulsars; the method presented here determines this luminosity function as well as the density scaling. I conclude that the luminosity function of the cluster recycled pulsars is similar to that of disk recycled pulsars, and that the simple model for the scaling of pulsars with clusters parameters is not sufficient.

Section II deals with low mass X-ray binaries in the disk. Chapter 6 presents spectroscopic observations of the black hole candidate A0620-00. This object, which appeared as a nova in 1917 and 1975, is one of the best black hole candidates known. Our spectroscopy confirms that the mass of the central object is at least $3.3 M_{\odot}$, and therefore it must be a black hole.

In Chapter 7, I present spectroscopy of the recurrent nova U Scorpii. This object has been suggested as a candidate for accretion-induced collapse, being a white dwarf just below the Chandrasekhar limit. I measure the velocities of both the emission and absorption lines, and conclude the white dwarf is in fact not very massive. This means that a good candidate for a white dwarf capable of undergoing accretion-induced collapse has yet to be found.

In Chapter 8, I present spectroscopic observations of disk LMXBs. We discuss their distribution and kinematics in terms of the direct formation model, where the neutron star is formed directly by a supernova explosion instead of via AIC. I conclude that the data, though poor, are consistent with this interpretation.

References

Backer, D.C., Kulkarni, S.R., Heiles, C., Davis, M.M. & Goss, W.M. 1982,
Nature, 300, 615

Giacconi, R., Gursky, H., Paolini, F. & Rossi, B. 1962, Phys. Rev. Lett., 9, 439

Gursky, H. & Ruffini, R. 1974, in Neutron Stars, Black Holes and Binary X-ray
Sources, ed. H. Gursky & R. Ruffini (Dordrecht: Reidel), p. 1

Hamilton, T.T., Helfand, D.J. & Becker, R.H. 1985, AJ, 90, 606

Hewish, A., Bell, S.J., Pilkington, J.D.H., Scott, P.F. & Collins, R.A. 1968,
Nature, 217, 709

Hulse, R.A. & Taylor, J.H. 1975, ApJ, 195, L51

Lyne, A.G., Biggs, J.D., Brinklow, A., Ashworth, M. & McKenna, J. 1987,
Nature, 328, 399

Sandage, A.R., Osmer, P., Giacconi, R., Gorenstein, P., Gursky, H., Waters,
J.R., Bradt, H., Garmire, G., Sreekantan, B.V., Oda, M., Osawa, K. &
Jukago, J. 1966, ApJ, 146, 316

Schreier, E., Levinson, R., Gursky, H., Kellogg, E., Tananbaum, H. & Giacconi,
R. 1972, ApJ, 172, L79

Part I

Pulsars in Globular Clusters

Chapter 2

On the detectability of pulsars in close binary systems[†]

Helen M. Johnston and Shrinivas R. Kulkarni

Abstract

Globular clusters appear to contain a large number of radio pulsars and low mass X-ray binaries (LMXBs). These are believed to have been formed by tidal interaction of degenerate stars with field stars. Some analyses of cluster pulsar surveys indicate there is a large population of pulsars in clusters, with the discovered pulsars forming only the tip of the iceberg. However, most of the current pulsar searches are severely biased against finding pulsars in tight binaries because of the changing velocity of the pulsar. Recently several groups have attempted to improve this situation by using pulsar analysis codes which assume that the pulsar frequency changes linearly with time. This corresponds to assuming the acceleration of the pulsar is constant over the observation interval. A related problem is the search for coherent pulsations from LMXBs. Detection of such pulsations would provide the definitive proof that the LMXBs are the progenitors of the cluster pulsars. In this paper, we address both these issues. We introduce an efficiency factor γ to describe the amount by which the Fourier amplitude of the pulsar signal is reduced by binary motion, and explore the extent to which this amplitude can be recovered by using acceleration codes. We present the results of numerical calculations of γ as a function of pulsar spin period, binary orbital period, companion mass and orbital inclination. We examine the advantage of using acceleration codes over standard pulse search techniques in this parameter space. We suggest strategies for maximizing the probability of finding pulsars in tight binaries. Finally, we show how current surveys are already placing interesting constraints on the tidal capture model of cluster pulsar formation.

[†] This paper originally appeared in ApJ, 368, 504 (1991)

2.1 Introduction

The high incidence of low-mass X-ray binaries (LMXBs) in clusters, and the suggestion of an evolutionary link between millisecond pulsars and LMXBs, led to the discovery of a point radio source in the core of M28 (Hamilton *et al.* 1985), and subsequently coherent pulsations were found from this object (Lyne *et al.* 1987). Since then, several searches have been or are being made of globular clusters, and to date there are twenty known pulsars in clusters (see Phinney & Kulkarni 1992, henceforth PK92, for a recent review). The standard model for the formation of these pulsars is that ‘primordial’[†] neutron stars tidally capture non-degenerate field stars (Fabian, Pringle & Rees 1975; also see below), and eventually become visible as binary millisecond pulsars. However, most of these tidal binaries have small orbital periods and are not detected in standard pulse surveys. This selection effect is so severe that further progress in understanding the formation of cluster pulsars requires a thorough understanding of the portion of parameter space covered by current pulsar searches, and what techniques can be used to improve this coverage.

The orbital period distribution of cluster pulsars and LMXBs provides a crucial key to our understanding of the formation of these objects. Consider first the standard model. Tidal capture of a single star by a neutron star can only occur if the distance of closest approach is less than about three stellar radii (*e.g.*, Verbunt 1988, 1990). The initial binary is highly eccentric, but circularizes with a final orbital radius up to twice the capture distance. Verbunt (1988) combines estimates of the number of giants in clusters, together with the fact that the larger radius of giants leads to enhanced capture rates, to predict that about 10% of neutron star captures will occur with giants, the rest with main sequence stars. This has important implications for the distribution of initial orbital periods, as even the widest tidal captures on main sequence stars have orbital periods $\lesssim 1$ d. For example, a $1.4 M_{\odot}$ neutron star which captures a $0.8 M_{\odot}$ main sequence star and eventually achieves a circular orbit at the maximum orbital radius of $6R_* \simeq 5 R_{\odot}$, will have an orbital period of 0^d9 (Table 2.1); for less massive secondaries the periods will be even shorter. Hence the ratio of the number of ‘tight’ binaries (those with orbital periods less than a few days) to the number of wide binaries (including single pulsars) is expected to be about the ratio of the number of captures of main sequence stars to captures of giants, *i.e.*, about 9. Following Kulkarni, Narayan & Romani (1990), we denote this ratio by β .

As we shall see, tight binaries are very difficult to find using pulse searches, and so

[†] ‘Primordial’ neutron stars, here and in previous literature on this topic, refer to neutron stars that were created in the early history of the cluster. These are distinguished from neutron stars that may have been created in recent times via accretion-induced collapse of massive white dwarfs, *etc.*

a prediction that $\beta \sim 9$ means there are an order of magnitude more pulsars in globular clusters than can be observed with standard pulse searches, which only search through dispersion measure and pulsar period. However, this in turn would imply that clusters contain an exceedingly large number of pulsars. Kulkarni, Narayan & Romani (1990) extrapolated the success of the major pulsar surveys of clusters to the entire cluster system, and concluded that there are $\sim 200(1 + \beta)$ to $1000(1 + \beta)$ pulsars in the globular cluster system, or about 20 to 100 per rich cluster if $\beta \sim 9$. In the standard theory, even in the cores of dense clusters only about 10% of the primordial neutron stars undergo tidal capture. Thus a prediction of as many as 100 pulsars per rich cluster means there should be as many as 10^3 neutron stars per rich cluster. While this number is not ruled out by current dynamical studies of clusters, it appears to directly contradict recent theoretical studies of the evolution of globular clusters (Chernoff & Weinberg 1990), which find that only clusters with very steep initial mass functions (IMFs) can survive the first epoch of star formation. Steep IMFs, however, produce very few neutron stars.

Bailyn & Grindlay (1990) present this as a strong objection to the standard model, and suggest that the cluster pulsars were formed by the accretion-induced collapse (AIC) of white dwarfs. In this model, a white dwarf captures a main sequence or giant companion, and subsequent accretion pushes the white dwarf over the Chandrasekhar mass and forms a neutron star. However, theoretically it is unclear whether the AIC mechanism works at all. Also, these accreting white dwarfs should be visible as cataclysmic variables, but searches for these objects in globular clusters have been singularly unsuccessful (Verbunt *et al.* 1989).

Currently, the only observational constraint we have on β comes from VLA imaging of the cores of clusters. Imaging searches are not affected by the acceleration of pulsars in binaries, and so should detect all pulsars, regardless of whether they are in binaries or not. Kulkarni *et al.* (1990) mapped four clusters, and concluded that $\beta \lesssim 1$.

The orbital period distribution of known cluster pulsars is not in agreement with either model — there are many more long period binaries and single pulsars than predicted (Romani 1990). Additionally, recent theoretical work suggests that the tidal energy deposited in the secondary star during tidal capture causes the star to expand, overflow its Roche lobe and form a common envelope with the neutron star. Whether the eventual outcome is complete destruction of the non-degenerate star or the formation of a tidal binary system depends on the relative values of various timescales (Ray, Kembhavi & Antia 1987). Thus the simple tidal capture theory of Fabian *et al.* (1975) may need substantial revision.

Furthermore, the standard model predicts that since these binaries are formed by tidal

capture, the number of pulsars in clusters should scale as the square of the cluster central density, which varies by a factor of 10^3 between relatively sparse clusters like M53 and M13, and dense, post-core collapse clusters like M15. However, there is no evidence for such a steep trend in the number of recycled pulsars with central density (PK92). It appears that primordial binaries in clusters may play a larger role than was previously thought (PK92; Phinney & Sigurdsson 1990).

From this discussion, it is clear that it is important to observationally determine the orbital period distribution of cluster pulsars. This can be done in two ways: by improving pulse search techniques, and by doing deep VLA imaging of clusters to find point sources. We are carrying out a program of VLA observations. In this paper we discuss ways to improve pulse searches to maximize the probability of detecting pulsars in tight binaries.

In standard pulsar searches, there are two unknown parameters which must be searched for — dispersion measure (DM) and pulsar period. Propagation of the pulsar signal through the interstellar medium results in a frequency-dependent dispersion of the signal. The first step in standard pulse searches is to de-disperse using a variety of trial dispersion measures, and then search each data stream for a pulsed signal by taking its Fourier power spectrum and looking for significant, harmonically related peaks representing coherent pulsations. Pulsars in compact binaries are missed in this scheme as the changing velocity of the pulsar leads to a changing pulse period, and hence blurring of the peak in the power spectrum. Recently, several groups have attempted to improve this situation by using codes which assume a constant acceleration over the portion of the orbit observed (Middleditch & Priedhorsky 1986; Hertz *et al.* 1990; Anderson *et al.* 1990). Correcting for such an acceleration consists of stretching (or compressing) the time bins in the data stream quadratically by an amount given by the assumed acceleration, rebinning the data into equal time steps, and searching again for peaks in the power spectrum. This adds another parameter to the search, as many different accelerations must be tried, and so this technique is expensive in computer time. However, when the dispersion measure of the pulsar is known, as is the case for a cluster when at least one pulsar in the cluster has already been found, the search is reduced to manageable proportions. This kind of search resulted in the discovery of the 8 h binary pulsar in M15, 2127+11C (Anderson *et al.* 1990). Since these searches have the limitation that the assumed acceleration must be constant (or else the number of orbits to be searched increases enormously), they are still severely limited in their sensitivity to the very short period binaries which are so interesting for theories of tidal capture.

All this discussion is fully applicable to the problem of searches for coherent pulsations from LMXBs. LMXBs are supposed to be the progenitors of millisecond and binary pulsars.

However, the most important proof of this hypothesis, *i.e.* the detection of coherent X-ray pulsations as the accreting neutron star is spun up, still eludes us. Many of the earlier searches for coherent pulsations were flawed because they did not recognize the limitations introduced by binary motion. Recently, several groups, notably Hertz *et al.* (1990), have started using acceleration searches to look for millisecond pulsations from LMXBs. Here we investigate the parameter space covered by such searches.

The goal of this paper is to quantitatively investigate the limitations of standard pulse searches. In § 2.2 we introduce an efficiency factor γ to describe the ease with which binary pulsars can be found, and present the results of calculations of γ as a function of pulsar spin period P_p and binary orbital period P_o , both for standard pulse searches and for searches using sophisticated acceleration codes. In §§ 2.3 and 2.4 we suggest two strategies which maximize the probability of finding pulsars in close binaries, and present empirical relations between the optimum observation time and the parameters of a binary orbit. We conclude in § 2.5 with a discussion of what current searches can already tell us about β .

2.2 The detectability of pulsars in binary systems

The signal from a pulsar is a broad-band signal pulsed at the rotation period of the pulsar, P_p . Because a pulsar signal is typically not sinusoidal, but has a small duty cycle, the power spectrum has several harmonics. Standard pulse searches take advantage of this small duty cycle by performing ‘harmonic summing’ of the power spectrum of the de-dispersed time series. Duty cycles range between 1% and 50%, with a mean value of 4% (Srinivasan 1989), and so the Fourier transform has between 1 and 50 harmonics. Harmonic summing consists of summing the power in the Fourier transform at frequency ν with those at frequencies $2\nu, 3\nu, 4\nu, \dots, n\nu$. The detection sensitivity is increased by up to \sqrt{n} , where n is the number of harmonics used in the harmonic summing.

Consider an isolated pulsar with a rotation period P_p . The pulsed signal, $S_P(t)$, can be represented as a sum of Fourier components:

$$S_P(t) = \sum_{k=1}^{\infty} a_k \exp(ik\omega_p t + i\psi_k), \quad (2.1)$$

where $\omega_p = 2\pi/P_p$ is the angular frequency of the pulsar, and $a_k \exp(i\psi_k)$ is the complex amplitude of the k^{th} harmonic. Let $P(\omega)$ be the Fourier power spectrum of this signal:

$$P(\omega) = |\mathcal{F}[S_P(t)]|^2 = \left| \int_0^T S_P(t) \exp(-i\omega t) dt \right|^2; \quad (2.2)$$

here T is the length of the observation. $P(\omega)$ then consists of n spikes of height a_k^2 at frequency $\omega_p, 2\omega_p, \dots, n\omega_p$.

Now consider a pulsar whose distance to the observer $d(t)$ is changing with time t . The pulsar signal emitted at time t is received at time $t + d(t)/c$ by the observer. Thus the received signal $S_R(t)$ can now be written as

$$S_R(t) = \sum_{k=1}^{\infty} a_k \exp[ik\omega_p(t + d(t)/c) + i\psi_k]. \quad (2.3)$$

Expanding $d(t)$ in a Taylor series, we can write

$$d(t) = d_0 + v_0 t + a_0 \frac{t^2}{2!} + j_0 \frac{t^3}{3!} + \dots \quad (2.4)$$

where $v(t) = dd/dt$, $a(t) = d^2d/dt^2$ and $j(t) = d^3d/dt^3$ are the instantaneous velocity, acceleration and rate of change of acceleration, respectively, and $d_0 = d(0)$. Then we can

rewrite equation (2.3) as

$$S_R(t) = \sum_{k=1}^{\infty} a_k e^{i\psi_k} \exp\left[\frac{ik\omega_p d_0}{c}\right] \exp\left[ik\omega_p t(1 + \frac{v_0}{c})\right] \exp\left[\frac{ik\omega_p a_0 t^2}{2!c}\right] \exp\left[\frac{ik\omega_p j_0 t^3}{3!c}\right] \dots \quad (2.5)$$

We see that d_0 merely results in a phase gradient $\omega_p d_0$, *i.e.*, only results in the shifting of the pulse pattern. The second factor, $k\omega_p(1 + v_0/c)$ is the familiar Doppler effect, and results in the displacement of harmonics from $k\omega_p$ to $k\omega_p(1 + v_0/c)$. This effect is not measurable, since the period of a pulsar, unlike for instance the frequencies of spectral lines, is not known *a priori*. The higher order factors in the Taylor expansion result in time dependent phase errors which degrade the amplitude of the harmonics in the power spectrum. In the next section we investigate the effects of these phase errors, and explore to what extent the Fourier amplitudes can be recovered by sophisticated algorithms.

2.2.1 Standard pulse searches

In order to keep the discussion simple, we consider only one representative harmonic (say the m^{th}) of the pulsar signal. Let $S_R^m(t)$ represent this component of the received signal. Since the pulsar signal is simply a linear sum of harmonics, the following discussion is valid for each harmonic separately, and we can combine the results for all harmonics at the end. Using the Taylor expansion for $d(t)$ (eq. [2.4]) and then Fourier transforming results in

$$\begin{aligned} \mathcal{F}[S_R^m(t)] &= a_m \exp\left(\frac{im\omega_p d_0}{c} + i\psi_m\right) \\ &\times \int_0^T \exp\left(\frac{im\omega_p}{c}[(1 + \frac{v_0}{c})ct + \frac{a_0 t^2}{2!} + \frac{j_0 t^3}{3!} + \dots]\right) \exp(-i\omega t) dt \end{aligned} \quad (2.6)$$

where m is the harmonic number. The velocity is essentially constant over the integration time T if the acceleration term is small, *i.e.*,

$$\frac{m\omega_p a_0 T^2}{2c} \ll 2\pi. \quad (2.7)$$

Equation (2.7) can be interpreted physically: here ‘small’ means that the distance the pulsar has travelled over the integration time due to acceleration, $a_0 T^2 / 2$, is much less than the distance between the emitted wavefronts, cP_p/m .

This condition means that when the pulse train is folded back on itself by the pulse period P_p , no wavefront has accumulated enough phase error to blur the folded profile. The

condition is clearly satisfied for a single pulsar moving at constant velocity, and for pulsars in wide binaries. Then under this condition, we can neglect the higher order terms. The harmonic is Doppler shifted to a new Fourier frequency $\omega_p(1 + v_0/c)$, but the amplitude is completely recovered. Thus standard searches can account for any linear motion of the pulsar, but not accelerations or higher order terms.

We now consider the astrophysically interesting case of a pulsar in a binary orbit, explicitly evaluating the factors in equation (2.6). Let the angular frequency be $\omega_o = 2\pi/P_o$, where P_o is the orbital period, and let M_1 be the mass of the pulsar and M_2 the mass of the companion. Then the line of sight velocity of the pulsar is given by

$$v(t) = A \sin(\omega_o t + \phi). \quad (2.8)$$

Here ϕ denotes the phase of the orbit at the start of the observation, and the amplitude A is derived from elementary mechanics:

$$A = \frac{2\pi}{P_o} \times \frac{M_2}{M_1 + M_2} \left(\frac{G(M_1 + M_2)P_o^2}{(2\pi)^2} \right)^{1/3} \sin i \quad (2.9)$$

where i is the inclination angle of the orbital plane. As before, we can expand $v(t)$ in a Taylor series, and explicitly evaluate d_0 , v_0 , etc.:

$$\begin{aligned} d_0 &= \frac{A}{\omega_o} (1 - \cos \phi) \\ v_0 &= A \sin \phi \\ a_0 &= A \omega_o \cos \phi \\ j_0 &= -A \omega_o^2 \sin \phi. \end{aligned} \quad (2.10)$$

Now define γ to be

$$\gamma(\alpha_2, T) = \frac{1}{T} \left| \int_0^T \exp \left(\frac{im\omega_p}{c} (v_0 t + \frac{a_0 t^2}{2!} + \frac{j_0 t^3}{3!} + \dots - \alpha_2 t) \right) dt \right|. \quad (2.11)$$

By comparing this with equation (2.6), it will be seen that γ^2 is the ratio of the height of the power of the peak in the Fourier power spectrum when the pulsar is accelerated, to the height when the pulsar has constant velocity. Thus γ measures the decrease in the amplitude of the peak caused by the phase errors from the pulsar's motion.

The free parameter α_2 is chosen so as to maximize γ . The pulsar will now be detected at the frequency

$$\omega' = m\omega_p \left(1 + \frac{\alpha_2}{c} \right). \quad (2.12)$$

Physically, α_2 represents some sort of mean of the velocity of the pulsar over the integration time T . If the pulsar had been single, moving at constant velocity v_0 , all the power would have been collected in one frequency bin in the power spectrum[†], at $\omega_p(1+v_0/c)$. When the pulsar is in a binary system, however, the continuously changing velocity means power is collected in frequency bins between $\omega_p(1+v_{\min}/c)$ and $\omega_p(1+v_{\max}/c)$, where v_{\min} and v_{\max} are the minimum and maximum line of sight velocities of the pulsar over the integration time. The heights of the peak in each bin between these two frequencies are given by equation (2.11), setting $\alpha_2 = v$ for $v_{\min} \leq v \leq v_{\max}$. The pulsar will be detected, then, at the frequency where $\gamma(\alpha_2, T)$ is maximum, *i.e.*, where the Fourier transform of the signal has the most power. We call this the velocity of detection of the pulsar, even though, as is clear from the above discussion, the pulsar is actually being detected at several velocities. In the current work, which is simulating the effect of pulsar search codes, we have to explicitly vary α_2 to find the maximum γ . In a real pulsar search code, of course, this is done automatically by the Fourier transform.

For $a_0 T^2/2$ small, it is clear that $\gamma(T)$ is maximized by setting $\alpha_2 = v_0$. Then $\omega' = m\omega_p(1+v_0/c)$ and we recover our previous result. When the higher order terms are not small, then α_2 is neither the mean velocity nor the starting velocity. The meaning of α_2 can best be illustrated by considering a particular case. Figure 2.1 shows the $v(t)$ curves for two pulsars, with $P_o = 0^d 03$, and $P_o = 0^d 1$, and $T = 1000$ s. For $T < P_o$, only a portion of the orbit is seen, and the mean velocity of the pulsar will not necessarily be zero. If we define

$$v'(t) = A \sin(\omega_o t + \phi) - \alpha_2 \quad (2.13)$$

to be the velocity residuals around the value α_2 , then

$$\begin{aligned} d'(t) &= \int_0^t v'(t) dt \\ &= \frac{A \cos \phi}{\omega_o} - \frac{A \cos(\omega_o t + \phi)}{\omega_o} - \alpha_2 t. \end{aligned} \quad (2.14)$$

Then we can write γ using equation (2.11), and in order to maximize this, we have to solve

$$\frac{\partial \gamma}{\partial \alpha_2} = \frac{\partial}{\partial \alpha_2} \left| \int_0^T \exp \left(\frac{im\omega_p d'(t)}{c} \right) dt \right|^2 = 0 \quad (2.15)$$

[†] In practice, the peak may be spread over two bins, since the FFT algorithm evaluates the power spectrum at discrete frequency intervals. However, this power can be fully recovered with additional computation. Thus for the purpose of this paper we will assume that the peaks are centered in single bins.

for α_2 . This integral is not analytic, and so we have to find the solution numerically. Figure 2.1 shows the result of two representative calculations. The solid line shows $v(t) = \alpha_2$ in each case, where α_2 has been calculated according to the above prescription. For comparison, the arrow at the left of the plot shows \bar{v} , the mean velocity over the integration time, and v_0 is given by the y -intercept.

We have calculated the quantity $\gamma(T)$ for a 80×80 grid of values in the (P_o, P_p) plane. We used an observation time $T = 1000$ s, a mass for the companion star of $0.3 M_\odot$, a pulsar mass of $1.4 M_\odot$, and an inclination angle $i = 30^\circ$. γ was calculated for initial orbital phases at 10° intervals from 0° to 180° (clearly there is symmetry from 180° to 360°) and averaged. We have taken $m = 4$ as a typical value for the detected harmonic. This is a reasonable choice, especially for fast pulsars and the sampling rates employed in current pulsar searches. The number of harmonics that are detected depends on the ratio of the sampling frequency to the pulsar rotation frequency. The sampling rates of current pulsar surveys vary between 2 kHz and 5 kHz, and thus only 2 to 5 harmonics of a 2 ms pulsar are detected with such surveys. Hence we have chosen $m = 4$. However, if a different harmonic is desired, the spin period P_p can be multiplied by the appropriate factor $m/4$: all other factors remain constant. The results of this calculation are plotted in Figure 2.2, along with the contour at $\gamma = 0.5$, which we take as the limit of detectability.

We have chosen $\gamma = 0.5$ as our ‘detection limit’ for detecting pulsars. This is an arbitrary choice, as γ^2 only represents the decrease in the height of the power spectrum peak. A very bright pulsar, such as PSR1937+21, which is a 200 mJy source, is detected at several hundred σ in Arecibo data, and so could conceivably be detected even when badly smeared by acceleration. However, typically pulsars are detected at only a few σ , frequently 2σ in each of several harmonics, and so a reduction of a factor of 2 in the peak height effectively means that the pulsar will be undetected.

Now in equation (2.3), we wrote the received pulsar signal $S_R(t)$ as a sum of harmonics $S_R^m(t)$. In detecting a real pulsar, ‘harmonic summing’ is performed, where the power in bins corresponding to each harmonic of the pulse frequency is added to increase the signal to noise ratio. In our scheme, γ can be computed separately for each harmonic n . Hence the efficiency for detecting the pulsar is the average of the γ^2 for all the harmonics.

2.2.2 Searches using an acceleration code

Now consider the case where a code is used which allows an acceleration search to be made. Only accelerations which are constant over the observation time can be searched for, which amounts to finding the best fitting straight line to the $v(t)$ curve. Here again, ‘best’ means that fit which maximizes $\gamma(T)$. When no acceleration code is used, the best fitting line is constrained to be horizontal; when an acceleration code is used, the restriction on the slope of the line is lifted. In other words, we are adding a second parameter to the search, which can account for some of the higher order terms in equation (2.11). We extend our definition of the efficiency factor γ to be

$$\gamma(\alpha_1, \alpha_2, T) = \frac{1}{T} \left| \int_0^T \exp \left(\frac{im\omega_p}{c} (v_0 t + \frac{a_0 t^2}{2!} + \frac{j_0 t^3}{3!} + \dots - \alpha_1 t^2 - \alpha_2 t) \right) dt \right|. \quad (2.16)$$

The velocity residual about our best-fit line is given by

$$v'(t) = A \sin(\omega_o t + \phi) - \alpha_1 t - \alpha_2 \quad (2.17)$$

and $d'(t)$ is defined analogously to equation (2.14) as the integral of $v'(t)$.

With this extra parameter, we can now completely recover the amplitude when $a_0 T^2/2$ is not small but $j_0 T^3/6$ is small, *i.e.*,

$$\frac{m\omega_p j_0 T^3}{6c} \ll 2\pi. \quad (2.18)$$

The physical reasoning behind this inequality is the same as that of equation (2.7). In this limit, clearly $\gamma(\alpha_1, \alpha_2, T)$ is maximized by setting $\alpha_2 = v_0$ and $\alpha_1 = a_0$.

In the general case when $j_0 T^3/6$ is not small, α_1 and α_2 will not necessarily be equal to a_0 and v_0 . There is no simple prescription for finding α_1 and α_2 , and indeed it is possible to arrive at different values, depending on the details of the algorithm. This corresponds to the freedom, in a real pulsar code, to choose to stretch the data quadratically from the first bin, or the last, or any other. But whatever values of α_1 and α_2 are used, these will correspond to (respectively) the effective acceleration and effective velocity of the pulsar recovered by the code. The real parameters of the orbit, of course, can be found by re-observing the system and tracing out the orbit.

So for any given set of orbital and observational parameters, we use equation (2.16) to calculate $\gamma(T)$, and vary α_1 and α_2 to maximize γ . Figure 2.1 also shows the best fit with two parameters to the two pulsars discussed before, as the dashed line. Clearly using two parameters greatly reduces the velocity residuals (the distance between the sine curve

and the solid straight line, in one case, or the dashed straight line, in the other) and thus increases $\gamma(T)$. It is important to note that in general α_2 , the velocity of detection of the pulsar, will not be the same when using an acceleration code as when using a standard code. This is also illustrated in Figure 2.1. When using a standard code, the pulsar is detected at the velocity of the intercept of the horizontal line with the y -axis; when an acceleration code is used, the intercept of the other straight line is the detection velocity.

Figure 2.3 shows the results of our calculation as a function of P_o and P_p , when using an acceleration code, averaging over orbital phase as before. The line is a contour at $\gamma = 0.5$. For comparison, the contour $\gamma = 0.5$ from Figure 2.2, with no acceleration code, is also shown; the area between the two lines is the additional portion of the (P_o, P_p) parameter space which we can explore by using an acceleration code. The two lines are not parallel, because using an acceleration code gives more advantage at long P_o than at short. This can be understood by reference to Figure 2.1. Clearly the approximation that the acceleration is constant is much better for long orbital periods than short ones. Conversely, the advantage of using an acceleration code is greater at *short* spin periods than long ones. For a fixed P_o , and hence fixed $d(t)$, the phase error is greater for short periods (eq. [2.6]), and so using an acceleration code gives a greater advantage than for long P_p .

2.3 Improving the odds: Repeated observations

The calculations so far have all been averages over orbital phase. We have assumed a fixed inclination angle for the system as this is not a variable which can be altered by the observer. A system which is exactly face on to the observer, $i = 0^\circ$, produces no blurring of the pulse peak, as there is no change in the radial velocity, and so a pulsar will be detected in a binary system of any period; conversely, an orbit whose normal is perpendicular to the line of sight, $i = 90^\circ$, produces maximum acceleration along the line of sight, and so the worst blurring. We have chosen $i = 30^\circ$ as an intermediate case. However, the orbital phase of the start of the observation, ϕ , can be altered, even when the orbit is not known. Specifically, there are some portions of the orbit where the projected velocity is more nearly linear with time than others, and pulsars which are observed at an optimal time in the orbit can be discovered even when on average they would not be. This means that it can be advantageous to observe a cluster several times, in order to maximize the probability that a pulsar in a binary orbit will be observed at a favorable portion of its orbit. Figure 2.4 shows a graphical representation of this; we have plotted here the probability that, in five observations of a binary orbit with parameters P_p and P_o , at least one of the observations will have $\gamma > 0.5$, again assuming an integration time of 1000 s.

In fact, the advantage of using repeated observations is not as great as might be expected, because γ falls quite steeply towards smaller pulsar and orbital periods. Thus there is a relatively small portion of the (P_p, P_o) plane where, for a fixed integration time, the pulsar is observable in one portion of its orbit and not in another. For pulsars in this part of the plane, observing several times can be vital, but in general a better technique is to vary the integration time to maximize the chance of finding a given pulsar, as discussed in the next section.

The advantage of repeated observations is amply illustrated by the discovery of the tight binary pulsar in Terzan 5 (Lyne *et al.* 1990), though for somewhat different reasons. In this case, the pulsar was discovered in a 2500 s data stream without an acceleration code. From the parameters listed in Table 2.2, it can be seen that the pulsar should not have been found in such a long integration time, as the pulsed signal should have been smeared out over many bins. In fact, because the system is eclipsing, the pulsar was only bright during part of that integration time, and so the peak showed up in the power spectrum, even though as soon as the data stream was folded, the drift of the peak due to the acceleration became obvious. Additionally, this pulsar is not seen at all during some orbits, and so repeated observations are even more necessary.

2.4 The optimum integration time

So far in all our discussion we have assumed a constant integration time, $T = 1000$ s. However, γ is a function of the length of the observation. There are two competing factors at work when trying to detect pulsars in compact binaries: reducing the observation time T allows pulsars in tighter binaries to be found, but since the detection limit of a survey goes as $T^{1/2}$, only bright pulsars will be found. This means there is no one optimum integration time for finding all pulsars, and so the best strategy is to observe for long integration times, to detect faint single pulsars and wide binary pulsars, but to analyze the data in smaller segments as well, in order to detect bright pulsars in compact binaries.

For any given binary period and spin period, however, there is an optimum integration time. $\gamma(T)$ decreases as T approaches P_o (γ is 1 at short integration times because a straight line can fit arbitrarily well to a portion of a sine curve of zero length, while as T approaches P_o , γ approaches zero), and so the detection efficiency goes down with increasing T . The signal in the pulsar peak, then, goes as $\gamma(T)T$, while the noise goes as $T^{1/2}$. Hence the maximum signal-to-noise ratio occurs at the maximum of $f(T) = \gamma(T)T^{1/2}$.

We plot a sample of these three functions in Figure 2.5 for $P_o = 1$ d and $P_p = 1$ ms, for code both with and without acceleration. The dashed line shows $\gamma(T)$, the dot-dashed line shows $T^{1/2}$, and the solid line shows $\gamma(T)T^{1/2}$. In this example, $T_{\text{best}} = 375$ s for the unaccelerated code, and $T_{\text{best}} = 2420$ s for the accelerated code, an increase of a factor of 6.5 in observation time and hence a factor of 2.5 in flux sensitivity.

We can calculate the optimum observation time T_{best} as a function of P_o and P_s ; this is plotted in Figure 2.6, as a ratio of T_{best}/P_o . Thus an ideal pulsar search code would search the parameter space of T in addition to dispersion measure, spin period and acceleration. Clearly this becomes prohibitively expensive of computer time, except in cases where one of these, presumably the dispersion measure, is known already. For example, a typical data stream for a globular cluster observation at Arecibo is 4000 s long. To detect a pulsar of period 1 ms in a 0.1 d orbit, $T_{\text{best}} = 460$ s. (From Arecibo, this allows a flux limit of about 4 mJy to be reached, which at a distance of 5 kpc corresponds to a luminosity $L_{400} = 100$ mJy kpc².) Thus if the data stream is halved three times, and the data analyzed in 4000 s, 2000 s, 1000 s and 500 s segments, this results in a factor of a few (~ 3) increase in computing time, on a job which already consumes about 33 NCUBE CPU hours for 1000 acceleration trials when the dispersion measure is known (S.B. Anderson, *pers. comm.*). Such an increase is acceptable in this case, but not if a dispersion measure search is needed as well. A 4000 s data stream is sensitive to a 1 ms pulsar in a 1.87 d orbit around a $0.3 M_\odot$ companion when using an acceleration code (see eq. [2.22] below); a 2000 s stream to 0.77

orbits, and a 500 s stream to 0^d13 orbits. In fact, figure 2.5(b) shows that $f(T) = \gamma T^{1/2}$ does not fall steeply past the maximum T_{best} , so it may not be necessary to search all 15 subsegments in this example.

T_{best}/P_o changes as a function of both spin period and orbital period. The change as a function of spin period is easy to understand. For a given binary period P_o , the pulsar moves a distance $d(T)$ over the integration time, and this extra distance gives rise to a greater phase error for smaller pulsar periods P_p (see equation [2.6]). So to reach the same $\gamma(T)$, we can integrate for a greater fraction of the orbital period as the spin period goes up. Perhaps less intuitively, the fraction of an orbit that one can integrate over also depends on the orbital period. We have also repeated our calculations of T_{best} for a variety of companion masses M_2 , and a variety of inclination angles i ; m is the harmonic number. Empirically we find this dependence to be

$$\frac{T_{\text{best}}}{P_o} = 6.894 \times 10^{-3} \left(\frac{P_o}{1 \text{ d}} \right)^{-1/3} \left(\frac{P_p}{1 \text{ ms}} \right)^{1/2} \left(\frac{4}{m} \right)^{1/2} \left(\frac{M_2}{0.3 M_\odot} \right)^{-2/5} \left(\frac{\sin i}{\sin 30^\circ} \right)^{-1/2} \quad (2.19)$$

when using no acceleration code, and

$$\frac{T_{\text{best}}}{P_o} = 4.482 \times 10^{-2} \left(\frac{P_o}{1 \text{ d}} \right)^{-2/9} \left(\frac{P_p}{1 \text{ ms}} \right)^{1/3} \left(\frac{4}{m} \right)^{1/3} \left(\frac{M_2}{0.3 M_\odot} \right)^{-4/15} \left(\frac{\sin i}{\sin 30^\circ} \right)^{-1/3} \quad (2.20)$$

when using an acceleration code; or in other words (taking P_o to the right hand side)

$$T_{\text{best}} = 298 \text{ s} \left(\frac{P_o}{1 \text{ d}} \right)^{2/3} \left(\frac{P_p}{1 \text{ ms}} \right)^{1/2} \left(\frac{4}{m} \right)^{1/2} \left(\frac{M_2}{0.3 M_\odot} \right)^{-2/5} (\sin i)^{-1/2} \quad (2.21)$$

when not using an acceleration code, and

$$T_{\text{best}} = 1948 \text{ s} \left(\frac{P_o}{1 \text{ d}} \right)^{7/9} \left(\frac{P_p}{1 \text{ ms}} \right)^{1/3} \left(\frac{4}{m} \right)^{1/3} \left(\frac{M_2}{0.3 M_\odot} \right)^{-4/15} (\sin i)^{-1/3} \quad (2.22)$$

when using one. These empirical relations are good to at least 2% for the unaccelerated case and 10% for the accelerated case (slightly worse for the power law in M_2). Thus for a given sample time T and a given pulsar search code, it is possible to define a surface that represents the portion of the (P_o, P_p, M_2, i) parameter space that has been searched for pulsars.

In Table 2.2 we have calculated T_{best} for the binary pulsars with known parameters. The first four columns show the pulsar name, orbital and spin periods, and measured mass function (from PK92 or the discovery telegrams). The next two columns show the mass we assumed for the companion, and the derived orbital inclination from this mass. Finally, we show the optimum integration time T_{best} for both standard and accelerated codes, in seconds. Note that this is assuming a circular orbit, whereas several of these systems have measured non-zero eccentricities.

2.5 Discussion

We have shown that, while standard pulse searches can probably not detect pulsars in the tightest binaries, significant improvements can be made to the searching algorithms in order to cover the widest range of pulsar parameters. The optimum strategy would be to observe for long integration times, and to analyze the data in segments in a range of sizes. This strategy allows detection of any pulsars in wide binaries, and bright pulsars in close binaries. Less productively, but still potentially important, is the technique of observing the same cluster several times at staggered intervals to maximize the chances of detecting a pulsar in a favorable portion of its orbit.

We now discuss how much of the parameter space (spin period and orbital period) can be explored with current pulse searches. According to the standard tidal model, 90% of the captures involve main sequence stars. In Table 2.1 we have used the mass-radius relation from Allen (1973) and calculated the orbital period of a neutron star-main sequence binary with separation $a = 6R_*$, corresponding to an initial impact parameter of $3R_*$ (the maximum). We then calculated T_{best} from equation (2.22), for a pulsar with $P_p = 1 \text{ ms}$ and $P_p = 5 \text{ ms}$, in both cases assuming $i = 60^\circ$. The next two columns show the acceleration α in cm s^{-2} for the system, and the minimum number of acceleration steps N_α that need to be made. The steps have to be spaced such that a signal at the Nyquist frequency that is detected in one bin in one acceleration trial is broadened into no more than two bins in the next trial: $\delta\alpha = c/2n^2\tau$, where τ is the sampling interval, here assumed to be $500 \mu\text{s}$, and n is the total number of samples in the data stream, $n = 2T_{\text{best}}/\tau$. The factor of 2 arises because accelerations from $-\alpha$ to $+\alpha$ must be searched. We used T_{best} for $P_p = 5 \text{ ms}$, the longer of the two.

In the last five columns, we have repeated the same calculations for a smaller orbital separation of $3R_*$, approximating the separation at which the main sequence star fills its Roche lobe. These two orbital periods, then, represent the range of initial periods we can expect for main sequence binaries. We assume (and reasonably so) that binaries with initial impact parameter less than $1.5R_*$ result in physical destruction of the non-degenerate star. It is gratifying to note that the resulting orbital periods are in the range of the orbital periods of known LMXBs (Parmar & White 1988).

From Table 2.1 we see that acceleration searches will result in the coverage of a significant portion of the parameter space occupied by the classical tidal binaries. The true picture is even more optimistic than this. Mass segregation heavily favors the capture of stars close to the turnoff mass ($0.8 M_\odot$) (Verbunt 1988, 1990) and PK92 argue that the spin periods of cluster pulsars cannot be below 3 ms. Thus the optimal integration times are

typically quite long: between 1000 s and 2000 s. *Indeed, the cluster pulsars that have been found so far have resulted from analysis of data of about this duration.* Thus a thorough analysis of the existing data should reveal the hypothesized population of main-sequence tidal binaries.

In fact, much of the above discussion is more applicable to LMXBs than to radio pulsars, since radio pulsars become detectable when all mass transfer has ended. The situation with cluster pulsars is probably even better. The orbital periods of such systems will evolve as mass is transferred from the non-degenerate star to the neutron star and as angular momentum is lost via gravitational radiation and magnetic braking (see Verbunt 1988, 1990). The mass transfer in these systems is stable, since the mass ratio, $q \lesssim 0.8/1.4$, is significantly less than the critical value of 0.66 above which mass transfer becomes unstable, leading to a spiral-in (see Bailyn *et al.* 1990 for a recent discussion of this important point). Hence the binary separation will increase with time. This is offset by angular momentum losses which are somewhat uncertain. In all likelihood these losses will not dominate the increase in orbital separation due to mass transfer, and probably the orbital period will only increase and at best remain constant. If so, the optimal integration times shown in Table 2.1 are pessimistic.

Consider this discussion in the context of the Arecibo cluster search. One tape of data is 1360 s long. This length of data is sufficient to detect the 110-ms single pulsar 2127+11A and the binary pulsar 2127+11C (Anderson *et al.* 1990). It can be seen that with this integration time and use of an acceleration code, pulsars with luminosity comparable to PSR 2127+11C and with spin periods as fast as 5 ms in the the narrowest binaries with stars of spectral type earlier than about K0 should have been detected. This is for the average orbital inclination angle, $\cos i = 0.5$, which means we can detect half of the binaries of this spectral type if orbits are oriented randomly, more than half of earlier type binaries, and less than half of later type. Hence we can detect a substantial fraction of main sequence-neutron star binaries with $P_p > 5$ ms.

Now we don't know what fraction of pulsars have spin periods of less than 5 ms, although PK92 argue that the minimum period is likely to be 3 ms unless accretion occurs at super-Eddington rates. But unless this fraction is very large, then *we should have already detected a reasonable fraction of tidal capture binaries in clusters*, if the simple tidal capture model is correct. That we have not seen a huge population of short period pulsars already indicates that the simple tidal capture theory is in need of revision.

As remarked above, the range of optimal integration times are comparable to the range of durations of data which have led to the discovery of the current crop of cluster pulsars.

Thus, by a thorough reanalysis of the existing data we should be in a position to obtain quantitative limits on β ; the rather modest values of N_α make it feasible to carry out such an analysis. Motivated by this, we are currently in the process of reanalyzing the Arecibo data. The discussion applies equally to the putative progenitors of cluster pulsars, the LMXBs. Considerable data collected by the *EXOSAT* satellite are now available. Our work shows that a comprehensive search for coherent pulsations is within our reach and given the importance of this problem we strongly suggest that such searches be carried out in the near future.

This work was supported by NASA grant NAG5-1350. HMJ would like to thank A. Picard for helpful discussions during this work.

Table 2.1 P_o and T_{best} for tidal capture theory

| Spectral type | Mass (M_\odot) | Radius (R_\odot) | $a = 6R_*$ | | | | | $a = 3R_*$ | | | | |
|---------------|--------------------|----------------------|------------|----------------------|-----------------------|---------------------|----------|------------|-------|----------------------|-----------------------|---------------------|
| | | | P_o^a | | T_{best} (s) | | α | N_α | P_o | | T_{best} (s) | |
| | | | (d) | $P_p = 1 \text{ ms}$ | $P_p = 5 \text{ ms}$ | (cms^{-2}) | | | (d) | $P_p = 1 \text{ ms}$ | $P_p = 5 \text{ ms}$ | (cms^{-2}) |
| G0 | 1.10 | 1.05 | 1.155 | 1620 | 2760 | 760 | 1550 | 0.408 | 720 | 1230 | 3050 | 1230 |
| G5 | 0.93 | 0.93 | 1.005 | 1520 | 2600 | 820 | 1470 | 0.355 | 680 | 1150 | 3270 | 1150 |
| K0 | 0.78 | 0.85 | 0.907 | 1470 | 2510 | 820 | 1370 | 0.320 | 650 | 1120 | 3270 | 1100 |
| K5 | 0.69 | 0.74 | 0.751 | 1310 | 2240 | 960 | 1280 | 0.266 | 580 | 1000 | 3830 | 1020 |
| M0 | 0.47 | 0.63 | 0.625 | 1260 | 2150 | 900 | 1100 | 0.221 | 560 | 960 | 3580 | 880 |
| M2 | 0.39 | 0.50 | 0.452 | 1030 | 1760 | 1180 | 970 | 0.160 | 460 | 780 | 4710 | 760 |
| M5 | 0.21 | 0.32 | 0.238 | 740 | 1260 | 4820 | 690 | 0.084 | 330 | 560 | 6550 | 550 |

^a Orbital period. Assumed orbital inclination is $i = 60^\circ$.

Table 2.2 Disk and cluster pulsars in binary systems

| Pulsar | P_p (ms) | P_o (d) | $f(M)^a$ (M_\odot) | M_2^b (M_\odot) | i^c ($^\circ$) | T_{best} (s) unacc. | T_{best} (s) acc. |
|---------|---------------|--------------|---------------------------|--------------------------|-----------------------|---------------------------------|-------------------------------|
| 1820-11 | 279.8 | 358 | 0.068 | 1.4 | 35 | 1.79×10^5 | 9.85×10^5 |
| 1913+16 | 59.0 | 0.32 | 0.13 | 1.4 | 46 | 680 | 2310 |
| 2303+46 | 1066.4 | 12.3 | 0.246 | 1.4 | 63 | 2.97×10^4 | 9.66×10^4 |
| 0655+64 | 195.7 | 1.03 | 0.017 | 0.7 | 37 | 3910 | 1.09×10^4 |
| 0820+02 | 864.8 | 1232 | 0.003 | 0.3 | 43 | 1.22×10^6 | 5.34×10^6 |
| 1831-11 | 520.9 | 1.8 | 1.2×10^{-4} | 0.3 | 14 | 2.05×10^4 | 3.97×10^4 |
| 1855+09 | 5.4 | 12.3 | 5.2×10^{-3} | 0.3 | 55 | 4080 | 2.57×10^4 |
| 1953+29 | 6.1 | 117 | 2.7×10^{-3} | 0.3 | 41 | 2.17×10^4 | 1.66×10^5 |
| 1957+20 | 1.6 | 0.38 | 5.0×10^{-6} | 0.08 | 16 | 640 | 2350 |
| M15C | 30.5 | 0.33 | 0.15 | 1.4 | 49 | 910 | 2820 |
| M4 | 11.1 | 191 | 0.008 | 0.3 | 72 | 2.28×10^4 | 2.63×10^5 |
| TRZ5A | 11.6 | 0.075 | 3.2×10^{-4} | 0.089 | 90 | 290 | 810 |

^a Mass function.^b Assumed companion mass^c Derived orbital inclination

References

Anderson, S.B., Gorham, P.M., Kulkarni, S.R., Prince, T.A. & Wolszczan, A. 1990, *Nature*, 346, 42

Allen, C.W. 1973, *Astrophysical Quantities* (University of London: Athlone Press)

Bailyn, C.D., Grindlay, J.E. & Garcia, M.R. 1990, *ApJ*, 357, L35

Bailyn, C.D. & Grindlay, J.E. 1990, *ApJ*, 353, 159

Chernoff, D.F. & Weinberg, M.D. 1990, *ApJ*, 351, 121

Fabian, A.C., Pringle, J.E. & Rees, M.J. 1975, *MNRAS*, 172, 15p

Hamilton, T.T., Helfand, D.J. & Becker, R.H. 1985, *AJ*, 90, 606

Hertz, P., Norris, J.P., Wood, K.S., Vaughan, B.A. & Michelson, P.F. 1990, *ApJ*, 354, 267

Kulkarni, S.R., Narayan, R. & Romani, R.W. 1990, *ApJ*, 356, 174

Kulkarni, S.R., Goss, W.M., Wolszczan, A., & Middleditch, J.M. 1990, *ApJ*, 363, L5

Lyne, A.G., Biggs, J.D., Brinklow, A., Ashworth, M. & McKenna, J. 1987, *Nature*, 328, 399

Lyne, A.G., Manchester, R.N., D'Amico, N., Staveley-Smith, L., Johnston, S., Lim, J., Fruchter, A.S., Goss, W.M. & Frail, D. 1990, *Nature*, 347, 650

Middleditch, J. & Priedhorsky, W.C. 1986, *ApJ*, 306, 230

Parmar, A.N. & White, N.E. 1988, in *X-ray Astronomy with EXOSAT*, Mem. S. A. It., 59, 147

Phinney, E.S. & Kulkarni, S.R. 1992, *Nature*, submitted (PK92)

Phinney, E.S. & Sigurdsson, S. 1991, *Nature*, 349, 220

Ray, A., Kembhavi, A.K. & Antia, H.M. 1987, *A&A*, 184, 164

Romani, R.W. 1990, *ApJ*, 357, 493

Srinivasan, G. 1989, *A&A Rev*, 1, 209

Verbunt, F. 1988, in *The Physics of Compact Objects: Theory vs. Observation*, COSPAR/IAU Symposium, Sofia July 1987, eds. N.E. White, L. Filipov, Pergamon Press, p. 529

Verbunt, F. 1990, in *Neutron stars and their birth events*, ed. W. Kundt, Kluwer Academic Publishers, Dordrecht, p. 179

Verbunt, F., Lewin, W.H.G. & van Paradijs, J. 1989, MNRAS, 241, 51

Wolszczan, A., Anderson, S.B., Kulkarni, S.R. & Prince, T.A. 1989, IAU Circ.

#4880

Figure captions

Figure 2.1 — $v(t)$ curve for two pulsars with a binary period (a) $P_o = 0.03$ d, and (b) $P_o = 0.1$ d, and an observation time $T = 1000$ s. The orbital phase is $\phi = 0.1$. The dashed line shows the mean velocity $v = \alpha_2$, which is the mean velocity when zero acceleration is used. $v'(t)$ (eq. [2.16]) is then the difference between the sine curve and the solid line. α_2 is indicated on the y -axis, as is v_0 : note that the two are not equal. The distance travelled by the pulsar is then the area between the two lines. The dotted line shows the best fitting line assuming constant acceleration, $v' = \alpha'_1 t + \alpha'_2$. The fit is much better for longer orbital periods. α'_2 in this case is indicated as the y -intercept; note that it is not the same as α_2 in the unaccelerated case.

Figure 2.2 — Greyscale plot of γ as a function of P_o and P_p , in the absence of an acceleration code. We used an observation time $T = 1000$ s, the fourth harmonic $m = 4$, a mass for the companion star of $0.3 M_\odot$, a pulsar mass of $1.4 M_\odot$, and an inclination angle $i = 30^\circ$. The plotted value is an average of γ over orbital phase ϕ , as described in the text. The contour is plotted for $\gamma = 0.5$.

Figure 2.3 — As for Fig. 2.2, but assuming an acceleration code. The dashed contour shows $\gamma = 0.5$ from Fig. 2.2, for comparison: the area between the two contours is the additional phase space that becomes available by using acceleration codes.

Figure 2.4 — Greyscale plot of the probability that, in five observations of a binary pulsar with parameters P_p and P_o , at least one of the observations will have $\gamma > 0.5$, using an acceleration code. By catching the pulsar in an optimum phase of its orbit, binary pulsars which would not “on average” be found, can be located. Re-observing the same cluster at random orbital phases can improve the chances of finding a marginal pulsar dramatically. The dashed contour shows the corresponding line when not using an acceleration code.

Figure 2.5 — Plot showing $f(T) = \gamma T^{1/2}$, for a pulsar with $P_o = 1$ d and $P_p = 1$ ms, for code both (a) without and (b) with acceleration. The dashed line shows $\gamma(T)$, the dot-dashed line shows $T^{1/2}$, and the solid line shows $\gamma T^{1/2}$. Note that the scales are different; the best observation time when using an acceleration code (the maximum in $f(T)$) is 2420 s, while it is 375 s in a standard pulsar code.

Figure 2.6 — Greyscale plot showing the quantity T_{best}/P_o as a function of spin and orbital period, both (a) without and (b) with an acceleration code. T_{best} was calculated by finding the maximum of $\gamma(T)T^{1/2}$, as illustrated in Fig. 2.5.

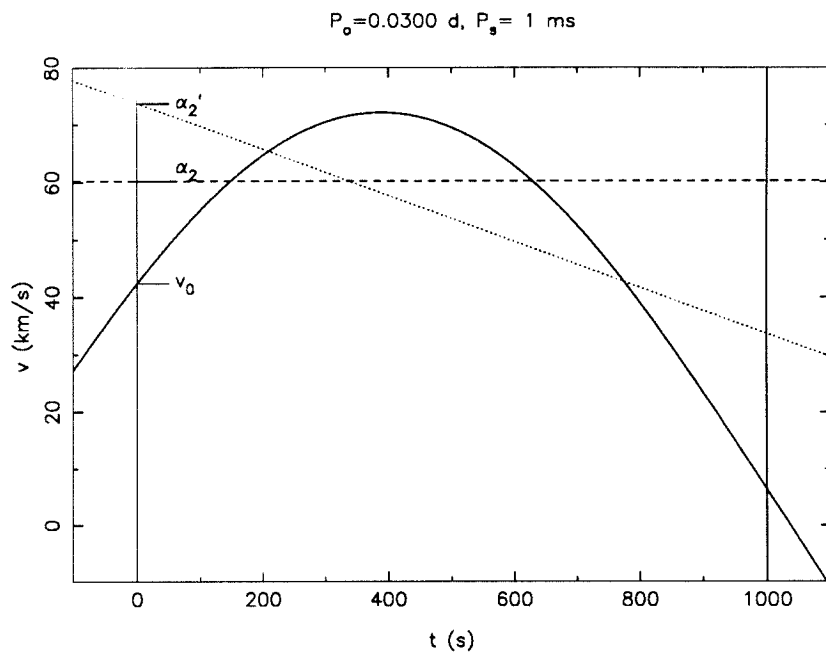
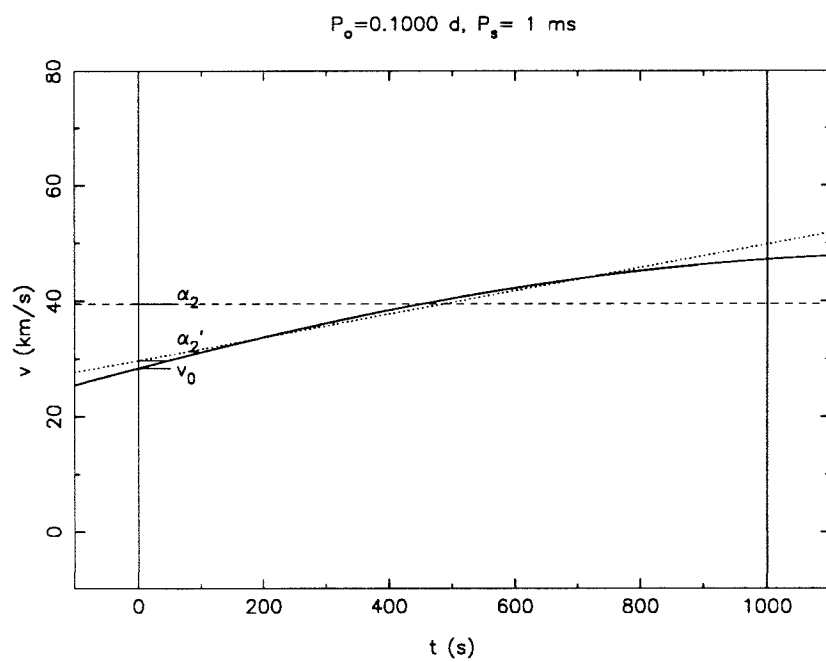
Figure 2.1a**Figure 2.1b**

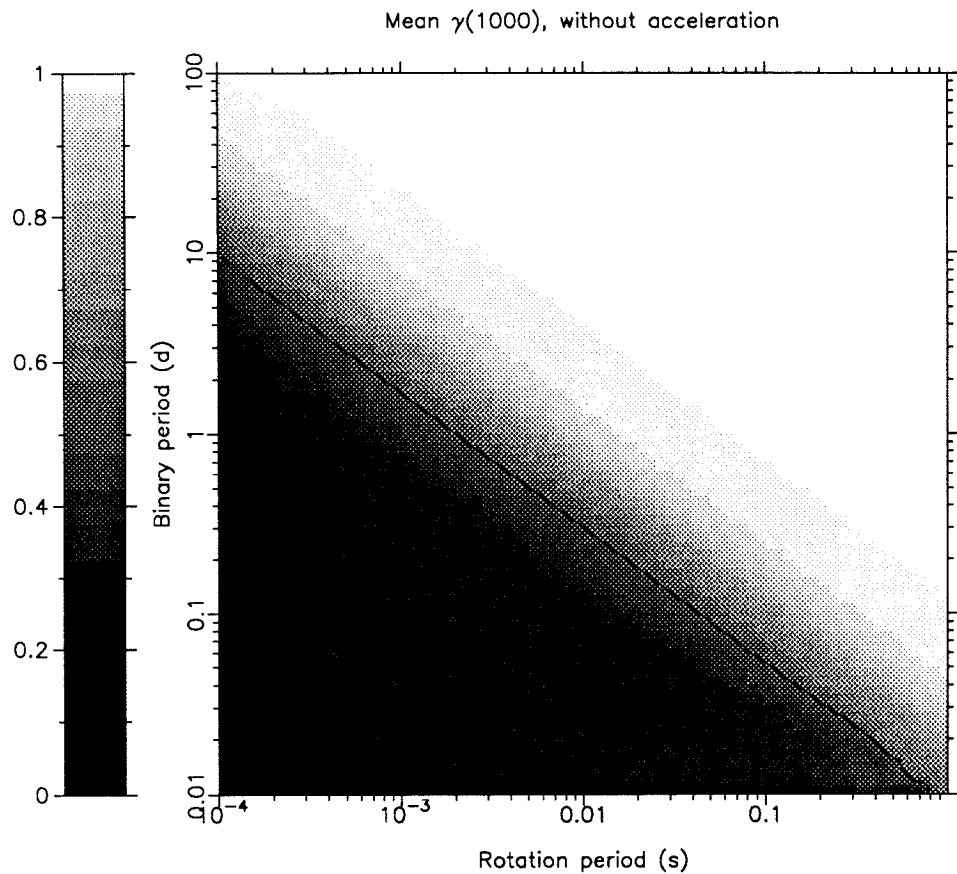
Figure 2.2

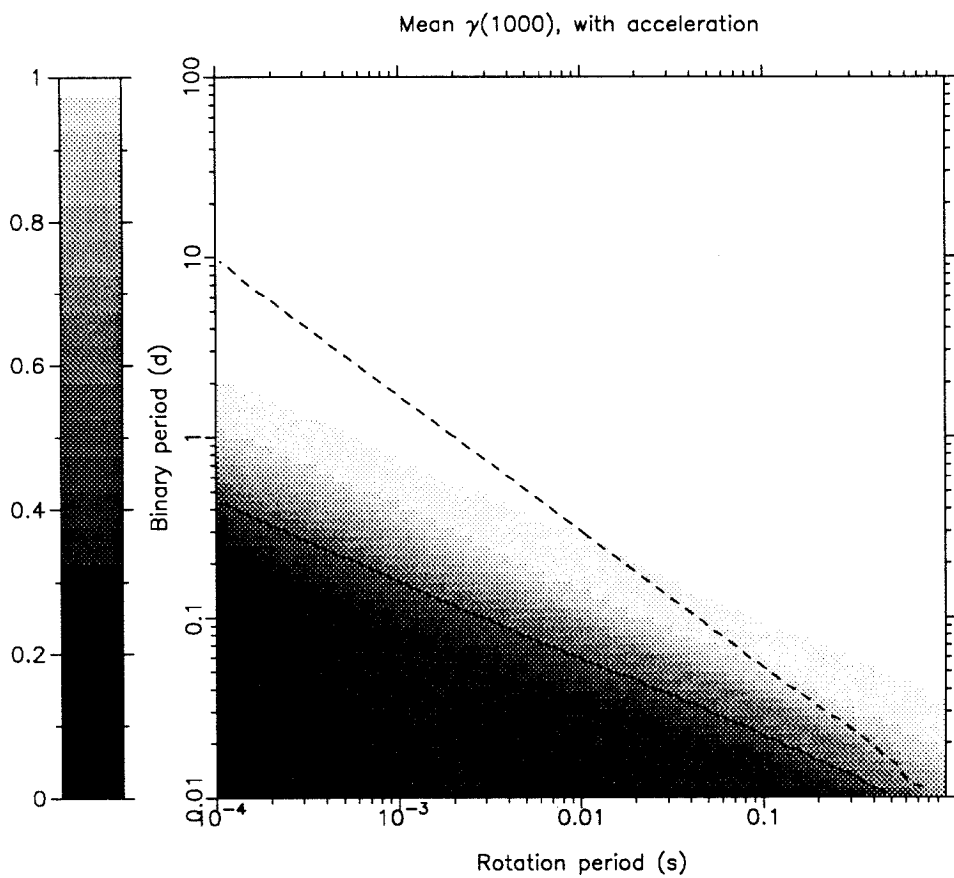
Figure 2.3

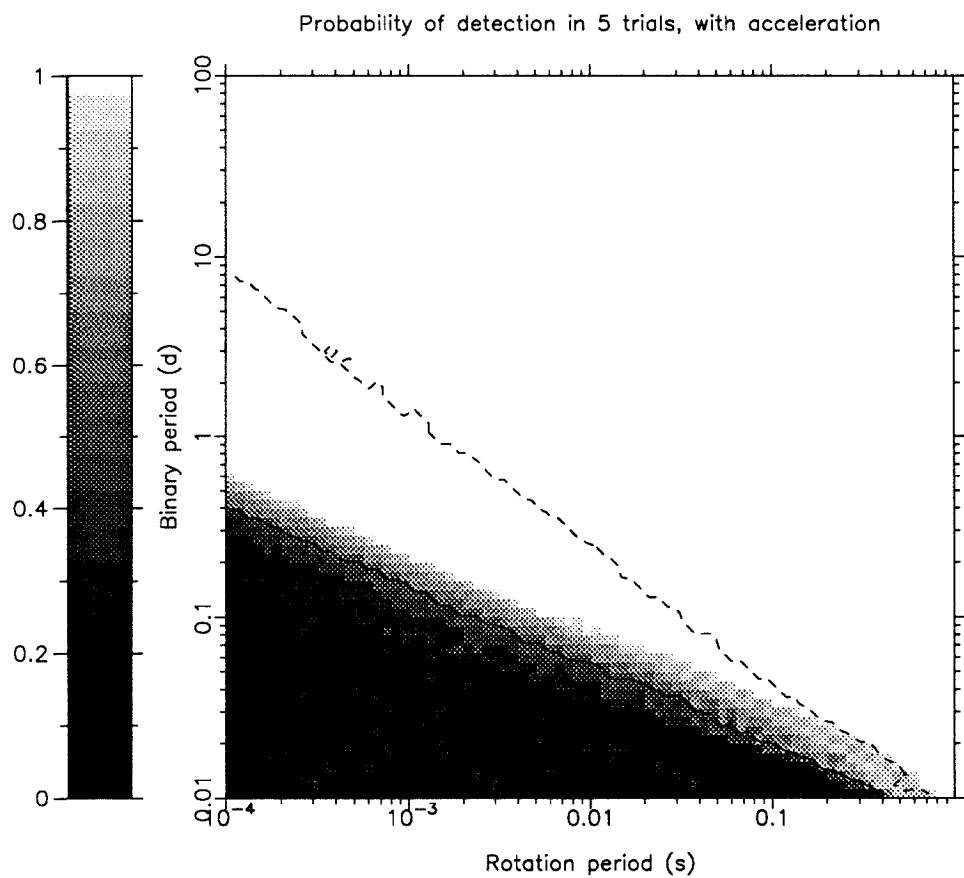
Figure 2.4

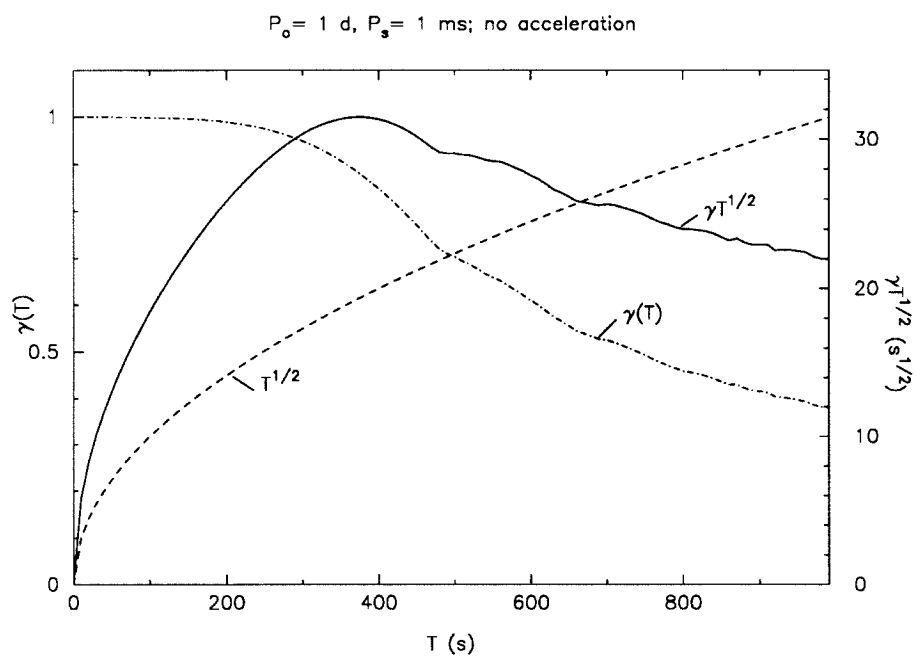
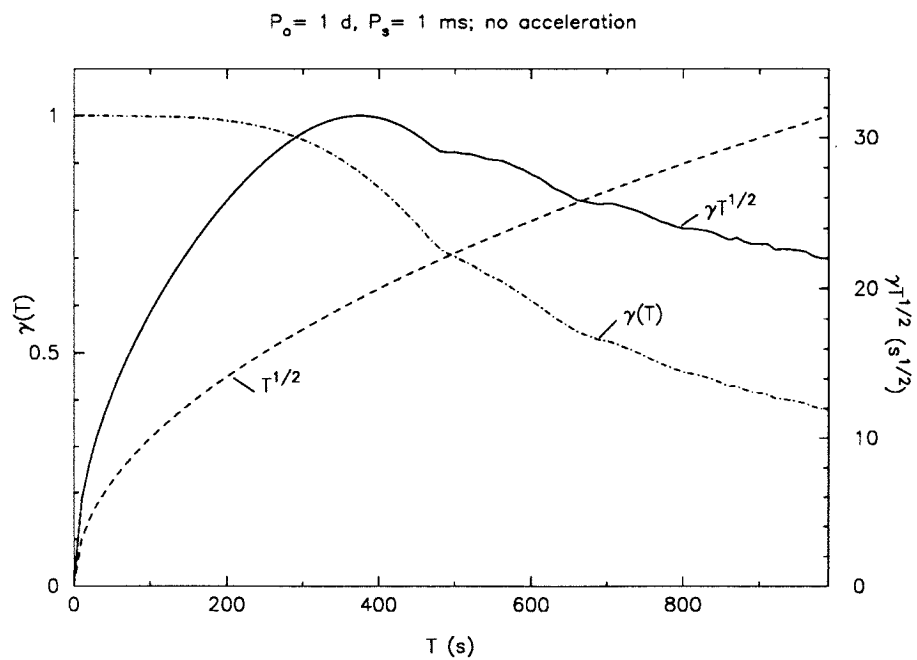
Figure 2.5a**Figure 2.5b**

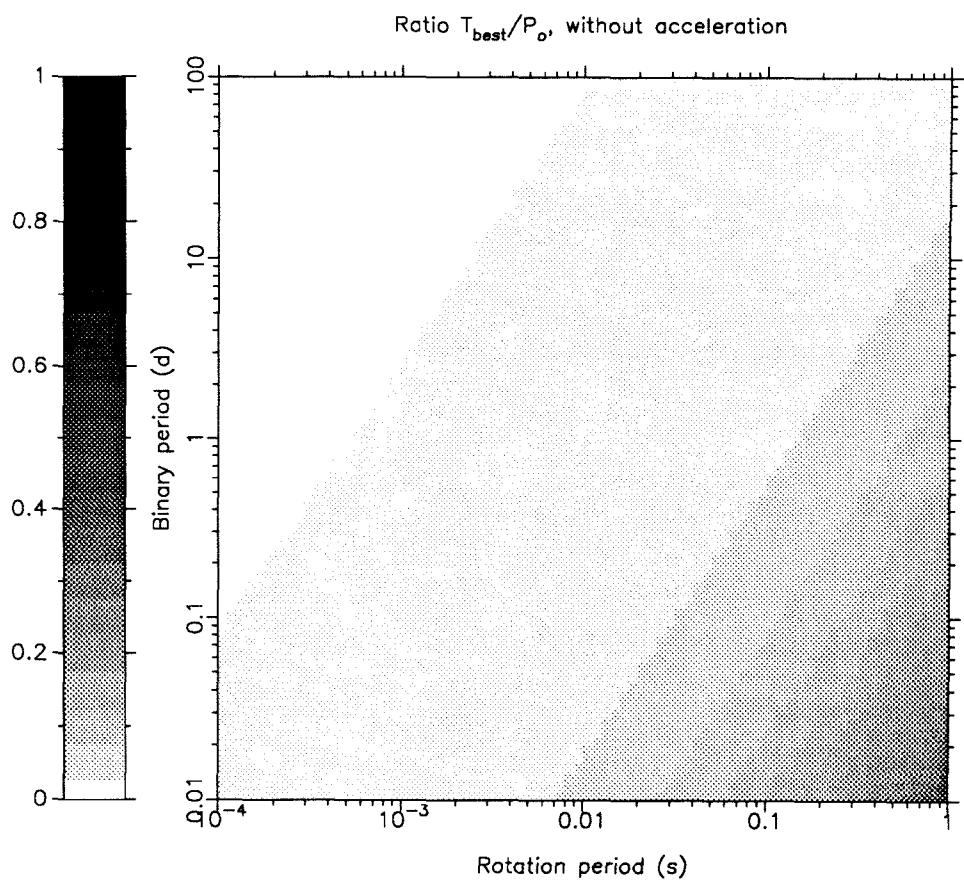
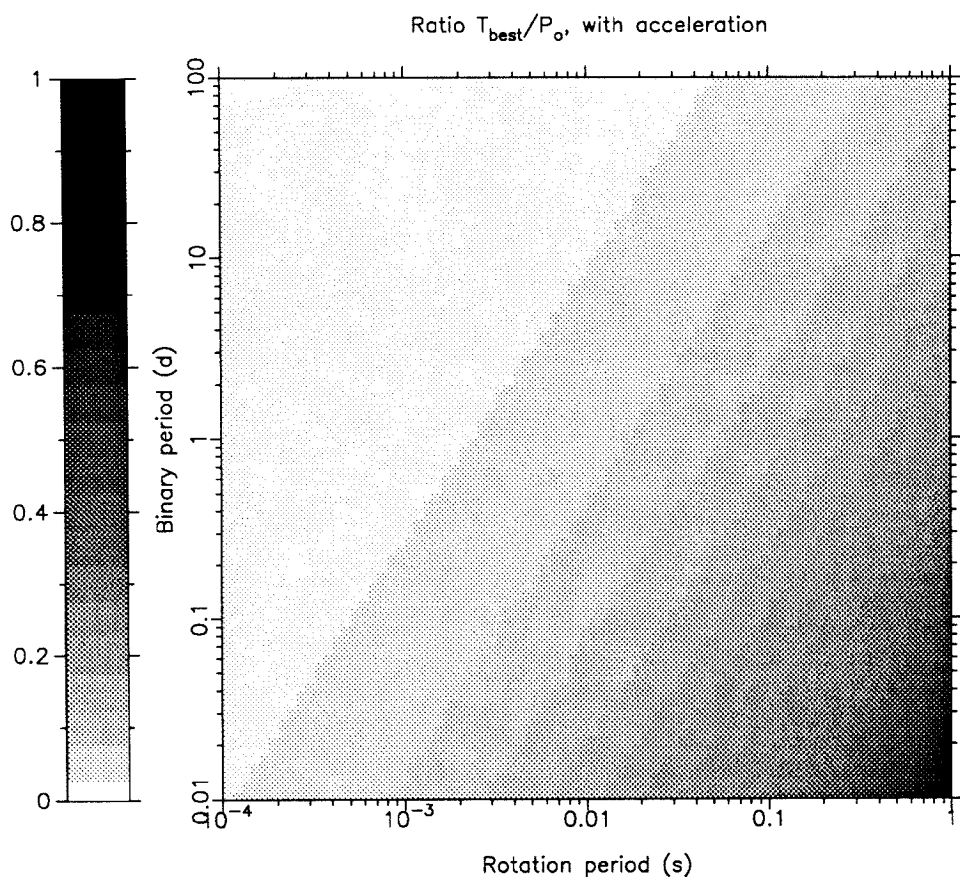
Figure 2.6a

Figure 2.6b

Chapter 3

Deep VLA images of globular clusters[†]

Helen M. Johnston and Shrinivas R. Kulkarni

and

W.M. Goss

Abstract

We present sensitive high resolution images of four globular clusters made with the VLA at 1.4 GHz. We detect a variety of objects: known pulsars, an X-ray binary, and two planetary nebulae. Surprisingly, we do not detect any emission from the rich cluster Liller 1. If Liller 1 is truly one of the densest clusters in the galaxy, then our results suggest that the pulsar population in a cluster is a function not merely of the structural parameters. We also report the detection of seven unidentified sources in or near the cores of three clusters. Some of these may well be unrelated background sources, but it is probable that some may be associated with the low-luminosity X-ray sources identified by the *Einstein* satellite.

[†] This paper originally appeared in ApJ, 382, L89 (1991)

3.1. Introduction

Despite the discovery of over 25 cluster pulsars to date, the origin and evolution of these objects is a matter of controversy. The principle observational issues are: the total number of cluster pulsars, the discrepancy between the birthrates of cluster pulsars and cluster LMXBs, and the binarity of cluster pulsars. In the simplest model, primeval neutron stars tidally capture cluster stars, and later mass transfer spins up the neutron star (Verbunt 1990). However, the large abundance of detected cluster pulsars has led some authors to suggest an alternate model, the accretion-induced collapse (AIC) of an accreting white dwarf into a neutron star.

Both models predict that most of the resulting millisecond pulsars will be in binary systems. However, standard pulse searches are insensitive to pulsars in tight binaries because of the Doppler smearing of the pulse (Johnston & Kulkarni 1990[†]). Kulkarni *et al.* (1989) parametrize the tight binary fraction by defining β to be the ratio of pulsars in tight binaries to those in wide orbits (including single pulsars). Radio imaging searches are the best way to constrain β , since they are sensitive to all pulsars.

We generalize the dependence of the number of pulsars in a cluster N_p as $N_p \propto M_c \rho_c^\alpha$; the standard model predicts $\alpha = 1$. However, the discovery of pulsars in sparse clusters like M53 and M13, where essentially no two-body captures should occur over a Hubble time, suggests a much smaller value of α .

In an analysis of all published surveys of globular clusters, Johnston *et al.* (1991)[‡] concluded that the observations are best fit by a model with $\alpha = 0.5$, a dependence significantly less steep than predicted by the standard model. Fruchter & Goss (1990), from analysis of VLA data, also arrive at a similar result. Tidal interactions with primordial binaries (with their attendant large cross-sections) appear to satisfactorily account for the inferred α (Phinney & Kulkarni 1992).

Motivated by these considerations, we undertook to image clusters with the following goals in mind: (i) to constrain the number of pulsars in tight binaries which are undetectable by standard pulse searches; (ii) to test how the number of pulsars in a cluster varies with cluster parameters such as density; and (iii) to attempt to detect pulsars which have been ejected by interactions with tight binaries to the outskirts of the cluster (as is indeed observed in M15; Anderson *et al.* 1990; Phinney & Sigurdsson 1991). Four clusters were imaged: two (M15 and M13) were known to contain pulsars, and two (Liller 1 and M22) are rich, nearby clusters without any prior detections.

[†] See Chapter 2.

[‡] See Chapter 5.

3.2. Observations

The data were taken in four sessions between 1990 April 9 and 1990 April 14 with the NRAO VLA[†] in A configuration. The data were taken in spectral line mode, using eight channels of width 6.25 MHz centered at the standard ‘L’-band frequencies of 1465 MHz and 1515 MHz. A total of 6.5 h was spent on each cluster, with phase calibrators observed every 20 m. The data were calibrated and imaged using NRAO’s AIPS package. One image was made for each field, summing the spectral channels, in order to achieve a large field of view.

The resulting maps are shown in Figure 3.1, and a list of detected sources is shown in Table 3.1 and are discussed below. The first four columns show the cluster name, the RMS noise, the distance and the core radius of the cluster. The last four columns show the detected sources, their offset from the cluster core, and the measured flux density. The predicted noise for each image is $24 \mu\text{Jy}$; the achieved noise, after CLEANing, was within a factor of 2 of this for all clusters. Here we discuss the sources located in each cluster.

M13. Three sources were detected at the 4σ level within the core. At the position of the pulsar, PSR1639+36A, (indicated by the cross) we marginally detect (at a level of 2.7σ) a source with a flux density of $90 \mu\text{Jy}$; this indicates a spectral index for the pulsar of -3.0 , given its 430 MHz flux density of 3 mJy (Kulkarni *et al.* 1991).

Liller 1. No point sources were detected within the central $100'' \times 100''$, to a flux density limit of 0.18 mJy (4σ). At the position of the X-ray source MXB 1730–335[‡], also known as the “Rapid Burster” (Lewin *et al.* 1976) no source is detected at a level of $135 \mu\text{Jy}$ (3σ).

M22. Two sources were found near the cluster core. Near the position of the planetary nebula/IR source 18333–2357, we detect a radio source with an integrated flux density of $248 \mu\text{Jy}$. The source, probably the radio counterpart of the planetary nebula, is marginally resolved, with a size of $2''.6 \times 1''.2$ and a position angle of 160° . The difference between our position and the $20 \mu\text{m}$ position (Gillett *et al.* 1989) is $\Delta\alpha = +3''.1$, $\Delta\delta = -1''.1$, consistent with the $\pm 2''$ (1σ , each axis) $20 \mu\text{m}$ positional error.

M15. Five sources are detected within the central $100''$. Three of these are known sources: the LMXB AC 211, the planetary nebula K648 (Gathier *et al.* 1983), and the pulsar PSR2127+11A. No source is detected at the position of M15C to a level of $129 \mu\text{Jy}$ (3σ).

[†] The VLA is operated by Associated Universities Inc., under cooperative agreement with the National Science Foundation.

[‡] It has been kindly pointed out to us by L. Lubin that we incorrectly referred to this object as MXB 1728-34 in the original paper.

There is an intriguing bright source $94''$ west of the core, ('S1'; Table 3.1). We made an image of this field at 5 GHz using archival data (taken on 1983 Mar 15 with the VLA in C configuration), and detected three sources at 5 GHz: K648, $(4.69 \pm 0.08 \text{ mJy})$; AC 211 $(0.45 \pm 0.04 \text{ mJy})$; and S1 $(5.65 \pm 0.2 \text{ mJy})$. This indicates a spectral index (ν^α) for S1 of $\alpha = +0.4$, quite unusual for an extragalactic source.

3.3. Cluster pulsars

3.3.1 Pulsars in binaries

The current observations allow us to constrain the number of as yet undetected pulsars in clusters. If we assume that all the unidentified sources in the cores of the clusters are undiscovered pulsars in tight binaries, then we have four unidentified sources in the cores of four clusters containing three pulsars of similar fluxes: M15A, M13A and M13B. The latter does not yet have an accurate timing position, but from our Arecibo observations of this source we know that M13B is about as bright as M13A at 1400 MHz. Hence we assume that one of the sources in our image is the B pulsar.

From the counts of Condon & Mitchell (1982), the expected number of background sources over the central $100'' \times 100''$ seconds of four clusters is 0.89. This indicates $\beta \lesssim 3$, allowing for Poisson statistics. This is consistent with results of other recent imaging surveys (Kulkarni *et al.* 1991; Wijers & van Paradijs 1991), and indicates that there is no large undiscovered population of pulsars in tight binaries in clusters.

3.3.2 The density scaling of cluster pulsars: A third parameter?

The lack of flux from Liller 1 is surprising in comparison with other dense clusters. Liller 1 is supposed to be one of the densest clusters in the galaxy (Webbink 1985), but it is heavily obscured, and so the derived structural parameters could be wrong. Assuming it is dense, we can compare our upper limit on any pulsar of $S_{1400} = 0.18$ mJy with other clusters. The flux density of the brightest pulsar in M15, Trz 5 and 47 Tuc, would correspond, at the distance of Liller 1, to $S_{1400} = 0.3$, 2.0 and 0.2 mJy respectively. Alternatively, we can look at the *integrated* emission from dense clusters. 47 Tuc is now known to contain at least eleven pulsars (Manchester *et al.* 1991), with an estimated 2.2 mJy of integrated flux at 1400 MHz (Johnston *et al.* 1991). At the distance of Liller 1 we would see 0.75 mJy of integrated flux from the detected pulsars alone. Fruchter & Goss (1990) measured the integrated emission from Trz 5 ($S_{1400} = 1.9$ mJy) and NGC 6440 ($S_{1400} = 1.45$ mJy), both dense clusters. We made a low resolution map of Liller 1 by using a Gaussian taper of 30 $k\lambda$; our limit on the integrated flux is $S_{1400} < 0.45$ mJy (3σ).

This must mean that either the cluster parameters for Liller 1 are grossly incorrect, and it is not as dense as assumed, or N_p is not a function of cluster density only. The characteristics of the 47 Tuc pulsars, particularly their short periods and binarity, suggest that N_p also depends on a third parameter. Sigurdsson & Phinney (1991) identify the third parameter (the first two being M_c , ρ_c) as the time since the cluster underwent core collapse. Clusters containing many pulsars, like 47 Tuc (and possibly M15), may be at the

peak of their pulsar forming activity, while in clusters like Liller 1 the neutron stars have long since formed tight binaries, and any pulsar activity is no longer visible. A prediction of this model is that clusters on the way to core collapse will be forming many tidal products, including mass-transfer X-ray sources. *ROSAT* should provide a useful test of this model in the near future.

3.3.3 The spectral index of cluster pulsars

We measure spectral indices of $\alpha = -1.8$ for M15A, and -3.0 for M13A. The lack of detection of the M15B and M15C pulsars puts limits on their spectral indices of $\alpha < -2.2$. This confirms that in general the recycled pulsars in clusters have very steep spectral indices. In fact, this is the main drawback of using 1.4 GHz imaging to constrain the cluster pulsar population. Our inability to detect M15C means that we cannot say anything about the presence of similar pulsars in the outskirts of other clusters. For this reason, lower frequency observations are to be preferred, although at lower frequencies confusion due to background radio sources is a severe problem.

3.4. Other sources

3.4.1 Planetary nebulae

The two known planetary nebulae in globular clusters — K648 in M15, and IRAS 18333–2357 in M22 (Gillett *et al.* 1989) — were detected, the M22 nebula for the first time in the radio. In our images, K648 is unresolved. The nebula in M22 is marginally resolved, with a much smaller size than the $10'' \times 7''$ measured by Gillett *et al.* (1989) in [OIII]; a discrepancy of this size is not unusual (Zijlstra 1989). The position angles of the radio and optical images are similar.

Assuming that K648 is optically thin with an electron temperature of 10^4 K, we derive an ionized mass $M_i = 1.6 \times 10^{-2} M_\odot$ and $n_e \sim 1.1 \times 10^4 \text{ cm}^{-3}$, in good agreement with Gathier *et al.* (1983). For the M22 nebula, we derive $M_i = 2 \times 10^{-4} M_\odot$ and $n_e \sim 9 \times 10^3 \text{ cm}^{-3}$. The ionized mass is in agreement with Gillett *et al.*'s estimate of $3 - 10 \times 10^{-4} M_\odot$, although our estimate of the density is higher because we assumed a smaller angular diameter.

The flux density we derive from the 5 GHz image is slightly higher than Gathier *et al.* (1983)'s measurement, and is in excellent agreement with a spectral index of -0.1 , as predicted for an optically thin nebula (Pottasch 1984). Our new observations and re-analysis of old 5 GHz data lay to rest speculations about the flux density of this nebula and its variability (*cf.* Johnson *et al.* 1979; Kwok *et al.* 1981; Mross *et al.* 1981; Birkinshaw *et al.* 1981; Isaacman 1984)

3.4.2 Low mass X-ray binaries: A new diagnostic?

Two clusters in our sample contain known LMXBs — M15 and Liller 1. We detect only the former in continuum radio emission. This detection of AC 211 in M15, confirming the detection by Kulkarni *et al.* 1991, brings the number of cluster LMXBs detected in the radio to three, the others being 4U 1850–08 in NGC 6712 (Lehto *et al.* 1990) and 4U 1820–30 in NGC 6624[†]. As deeper and deeper radio images of LMXBs (cluster and disk) are made, most seem to be detected at the sub-mJy level (Penninx 1989). [We do note that MXB 1730–335 in Liller 1 is one LMXB without detectable radio emission. It is worth pointing out that this object is the only X-ray source to exhibit Type II bursts. Perhaps the cause of the rapid succession of bursts also precludes the emission of radio continuum radiation.]

[†] Radio emission was marginally detected by Grindlay & Seaquist (1986); multi-frequency observations by Fruchter & Goss (1990) suggest that, while some of this flux may arise from the two pulsars (Biggs *et al.* 1990), the LMXB is probably contributing to the radio emission.

M22 (NGC 6656) also contains four low luminosity X-ray sources discovered by the *Einstein* satellite (Hertz & Grindlay 1983), whose nature is unclear. It is possible that a significant fraction of these may be chance superpositions of foreground or background objects on the cluster. However, those in the core region are almost certainly associated with the clusters. There are two appealing possibilities: these low-luminosity sources could be cataclysmic variables or quiescent LMXBs.

If they are LMXBs, they are very likely to be sources of radio continuum radiation. It is possible that some of the faint radio sources we detect could be associated with the dim X-ray sources. This suggestion is motivated by the observed radio emission of known accreting neutron star binaries (see above). We have proposed to use the *ROSAT* satellite to verify this by obtaining HRI images of these clusters: positional coincidence of the X-ray emission with the radio emission would be strongly suggestive that the dim sources are accreting neutron star systems.

Our estimate of the background source contamination comes from Condon & Mitchell's (1982) source counts. These only go down to $200 \mu\text{Jy}$, which is the level of interest here, and so their counts may not be reliable at this level. In a future paper we will calculate source counts in our images for regions well outside the cluster cores, and compare this with the density of sources near the cores; this will be an important confirmation that these sources are indeed associated with the clusters.

SRK is supported by an NSF Presidential Young Investigators award and a Packard fellowship. SRK's and HMJ's research at the VLA is in part supported by the Dudley Observatory.

Table 3.1. Globular cluster sources detected at 20 cm

| Cluster | RMS | d | r_c | ID | | $\Delta\alpha^a$ | $\Delta\delta^a$ | S_{1400} |
|----------------|-------------|-------|----------|-----------------|------------------|---------------------|------------------|------------|
| | (μ Jy) | (kpc) | ($''$) | | | ($''$) | ($''$) | (mJy) |
| M13 = NGC 6205 | 33 | 7.1 | 45 | Core | $16^h39^m54^s19$ | $36^\circ33'16''3$ | – | – |
| | | | | PSR1639+36A | –6.7 | –21.4 | 0.09 | |
| | | | | S1 | 0.6 | 13.0 | 0.16 | |
| | | | | S2 | –6.4 | –33.5 | 0.16 | |
| | | | | S3 | –30.4 | –4.9 | 0.14 | |
| Liller 1 | 45 | 7.9 | 1 | Core | $17^h30^m7^s0$ | $–33^\circ21'17''$ | – | – |
| M22 = NGC 6656 | 40 | 3.1 | 63 | Core | $18^h33^m21^s12$ | $–23^\circ56'44''2$ | – | – |
| | | | | IRAS 18333–2357 | –15.2 | –65.3 | 0.25 | |
| | | | | S1 | 2.9 | –10.7 | 0.52 | |
| M15 = NGC 7078 | 43 | 9.7 | 1 | Core | $21^h27^m33^s35$ | $11^\circ56'48''8$ | – | – |
| | | | | AC 211 | –1.2 | 2.2 | 0.91 | |
| | | | | PSR2127+12A | –1.5 | 0.7 | 0.20 | |
| | | | | K648 | 14.5 | 25.5 | 5.28 | |
| | | | | S1 | –93.8 | 16.7 | 3.28 | |
| | | | | S2 | 11.3 | –28.0 | 0.18 | |
| | | | | S3 | 4.2 | –25.5 | 0.18 | |

^a The first line for each cluster shows the core position from Shawl & White (1986). Subsequent entries are the offsets from this position $\Delta\alpha = \alpha_{\text{obj}} - \alpha_{\text{core}}$, $\Delta\delta = \delta_{\text{obj}} - \delta_{\text{core}}$.

References

Anderson, S., Gorham, P., Kulkarni, S.R., Prince, T. & Wolszczan, A. 1990
Nature 346 42

Aurière, M., Geffert, M. & Koch-Miramond, L. 1988, IAU Circ. #4559

Birkinshaw, M., Downes, A.J.B. & Pooley, G.G. 1981, *The Observatory*, 101, 120

Condon, J.J. & Mitchell, K.J. 1982, *AJ*, 87, 1429

Fruchter, A.S. & Goss, W.M. 1990, *ApJ*, 365, L63

Gathier, R., Pottasch, S.R. & Goss, W.M. 1983, *A&A*, 127, 320

Gillett, F.C., Jacoby, G.H., Joyce, R.R., Cohen, J.G., Neugebauer, G., Soifer, B.T., Nakajima, T. & Matthews, K. 1989, *ApJ*, 338, 862

Grindlay, J.E. & Seaquist, E.R. 1986, *ApJ*, 310, 172

Hertz, P. & Grindlay, J.E. 1983, *ApJ*, 275, 105

Isaacman, R. 1984, *MNRAS*, 208, 399

Johnson, H.M., Balick, B. & Thompson, A.R. 1979, *ApJ*, 233, 919

Johnston, H.M. & Kulkarni, S.R. 1990, *ApJ*, 368, 504

Johnston, H.M., Phinney, E.S. & Kulkarni, S.R. 1991, in *X-ray binaries and the formation of binary and millisecond pulsars*, ed. E.P.J. van den Heuvel & S.A. Rappaport, Kluwer, in press

Kulkarni, S.R., Anderson, S.B., Prince, T.A. & Wolszczan, A. 1991, *Nature*, 349, 47

Kulkarni, S.R., Goss, W.M., Wolszczan, A. & Middleditch, J. 1990, *ApJ*, 363, L5 (KGWM91)

Kulkarni, S.R., Narayan, R. & Romani, R.W. 1989, *ApJ*, 356, 174

Kwok, S., Purton, C.R. & Keenan, D.W. 1981, *ApJ*, 250, 232

Lehto, H.J., Machin, G., McHardy, I.M. & Callanan, P. 1990, *Nature*, 347, 49

Lewin, W.H.G. *et al.* 1976, *ApJ*, 207, L95

Lyne, A.G. 1991, talk presented at the NATO Workshop on "X-ray binaries and the formation of binary and millisecond pulsars," Santa Barbara, 21-25 Jan 1991

Manchester, R.N., Lyne, A.G., Robinson, C., D'Amico, N., Bailes, M. & Lim, J. 1991, *Nature*, 352, 219

Mross, R., Weinberger, R. & Hartl, H. 1981, A&AS, 43, 75

Penninx, W. 1989, in Proc. 23rd ESLAB Symp. on Two Topics in X-ray Astronomy, Bologna, Italy 13–20 September 1989, p. 215

Phinney, E.S. & Kulkarni, S.R. 1992, Nature, submitted

Phinney, E.S. & Sigurdsson, S. 1991, Nature, 349, 220

Pottasch, S.R. 1984, Planetary Nebulae (Reidel: Dordrecht)

Shawl, S.J. & White, R.E. 1986, AJ, 91, 312

Sigurdsson, S. & Phinney, E.S. 1991, in prep

Verbunt, F. 1990, in Neutron stars and their birth events, ed. W. Kundt, Kluwer, p. 179

Webbink, R.F. 1985, in IAU Symp. 113, Dynamics of Star Clusters, eds. J. Goodman, P. Hut, Reidel, p. 541

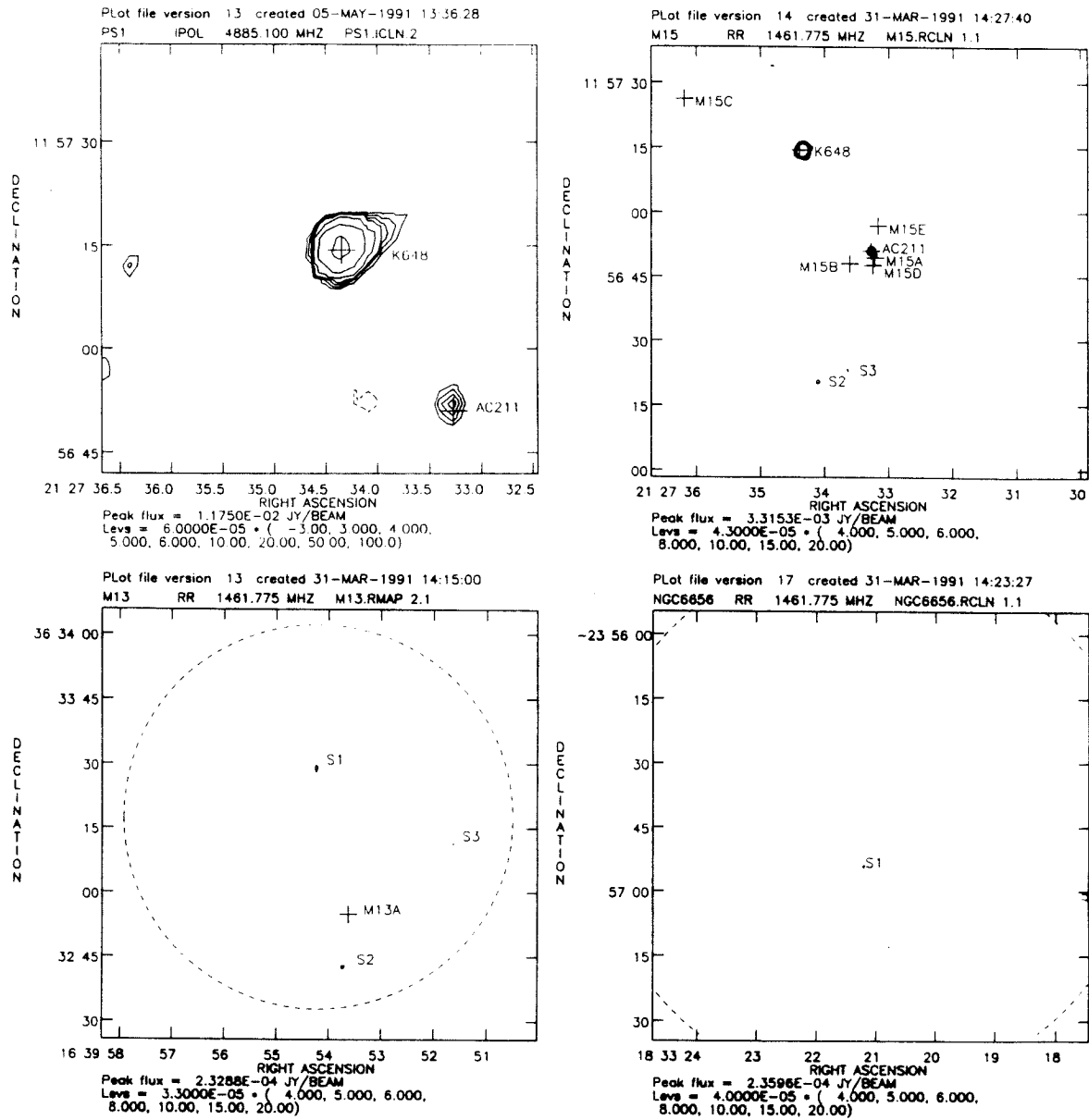
Wijers, R.A.M.J. & van Paradijs, J. 1991, A&A, 241, L37

Zijlstra, A.A. 1989, Ph. D. thesis, University of Groningen

Figure caption

Figure 3.1 — VLA radio maps of three globular cluster fields. M15 (*top two panels*), M13 (*bottom left*) and M22 (*bottom right*). The first M15 map is a $64'' \times 64''$ 5 GHz image, the others are $100'' \times 100''$ maps at 1400 MHz. The circle indicates the size of the core (see Table 3.1), except for M15, which is a core-collapsed cluster. Contours are drawn at levels of 4, 5, 6, 8, 10, 15, 20σ , where σ is the rms noise listed in Table 3.1; the first contour for the 5 GHz M15 map is 3σ instead of 4σ . In M15, the source S1 is $94''$ west of the core and is not shown on the maps. The 5 GHz map clearly shows the asymmetry of the planetary nebula; AC211 is also detected. The map for Liller 1 is not shown; no sources were detected to a flux density limit of 0.18 mJy (4σ). The beam size is typically $1''.5$, and the cell size is $0''.5$. The bandwidth smearing is less than 0.5 pixels for all images.

Figure 3.1



Chapter 4

Deep VLA images of globular clusters: NGC 6624[†]

Helen M. Johnston & Shrinivas R. Kulkarni

Abstract

We present a sensitive radio image of the bright X-ray source 4U 1820–30 in the globular cluster NGC 6624. We confirm that the source is several arc seconds away from the cluster core. This implies that the observed negative orbital period derivative cannot be due to gravitational acceleration by the cluster. This work brings to three the number of cluster X-ray sources detected in the radio. Identification of cluster X-ray sources via their radio emission can be profitably used for precision optical identification and to elucidate the nature of the enigmatic low luminosity cluster X-ray sources.

[†] To be published in ApJ (Letters).

4.1 Introduction

The bright X-ray binary 4U 1820–30 in the globular cluster NGC 6624 (Giacconi *et al.* 1974) was discovered to have an orbital period of 685 s (Stella *et al.* 1987), making it the shortest known binary period.

The short orbital period implies a very low mass companion, with the mass transfer driven by gravitational radiation; a helium degenerate dwarf filling its Roche lobe would have a mass of $0.055M_{\odot}$ (Stella *et al.* 1987). For such low mass secondaries, the thermal timescale is much longer than the mass transfer timescale. The star expands while losing mass, which drives the binary to longer periods. Using detailed models for the structure of the secondary star, Rappaport *et al.* (1987) showed that the period should be increasing at a rate of at least $\dot{P} \gtrsim 0.06 \text{ ms y}^{-1}$.

Surprisingly, Tan *et al.* (1991) found $\dot{P} = -0.074 \pm 0.013 \text{ ms y}^{-1}$, calling into question the basic model for the evolution of such systems. Alternatively, the negative period derivative is perhaps not intrinsic to the system, but is produced by gravitational acceleration by the cluster, as is seen with the negative rotation period derivatives of several cluster pulsars (see Phinney & Kulkarni 1992). The cluster's gravitational potential accelerates a binary, which results in a \dot{P}/P of $-a/c$. The acceleration, a can arise from attractions by passing stars and from the combined effect of all stars in the cluster. In general, the latter will dominate (Phinney 1992), and the acceleration is zero at $\pm\infty$ or when the star and the cluster core are both located on the tangent plane of the sky. It reaches a maximum value for a radial distance somewhere between the plane of the sky and the outer radius of the cluster; the exact location of this maximum depends on the structure of the cluster.

The position given by Hertz & Grindlay (1983) for 4U 1820–30 is $2.^{\circ}4 \pm 1.^{\circ}$ from the core of NGC 6624 as given by Shawl and White (1986). Hertz & Grindlay (1985) claimed that Shawl & White's core position was biased by several bright stars near the core, and give a core position which differs by $4.^{\circ}7$. Using their position for the optical core, the X-ray position is $3.^{\circ}4 \pm 1.^{\circ}$ from the core. Phinney (1992) gives a rule of thumb formula for the maximum acceleration, which is accurate to 10% for plausible cluster models:

$$\frac{|a_{\max}|}{c} \simeq 1.6 \times 10^{-10} \frac{M}{L_{\odot}V} \bar{I}_V (< R_{\perp}) \text{ y}^{-1} \quad (4.1)$$

where $\bar{I}_V (< R_{\perp})$ is the mean V-band surface brightness of the cluster interior to the pulsar's projected position, measured in units of $10^4 L_{\odot}V \text{ pc}^{-2}$. Using a surface brightness profile of the cluster (Djorgovski, *pers. comm.*) and $M/L \simeq 1$ (Pryor *et al.* 1989), we find the maximum acceleration observable at a distance of $2.^{\circ}4$ from the cluster core to be

$|a_{\max}|/c = 8.3 \times 10^{-10} \text{ y}^{-1}$, more than two orders of magnitude lower than the observed $|\dot{P}|/P$ of $1.1 \times 10^{-7} \text{ y}^{-1}$. Using the cluster core as defined by Hertz & Grindlay (1985) the discrepancy is even worse: $|a_{\max}|/c = 7.0 \times 10^{-10} \text{ y}^{-1}$. Van der Klis *et al.* (1992) have constructed a multi-component mass model of the cluster to calculate the maximum acceleration observable as a function of distance from the cluster core. They also conclude that the observed \dot{P} can only be explained by acceleration by the cluster if the X-ray binary is located very close ($< 1''$) to the cluster core.

Since Hertz & Grindlay's (1983) position for the X-ray source was only $2 - 3\sigma$ from the cluster core, and previous radio detections of the source have been contradictory (see §4.2), it is therefore of interest to confirm the position of 4U 1820–30. We present here high resolution VLA observations of NGC 6624.

4.2 Observations and Discussion

Observations were taken with the VLA[†] in A configuration on 1991 August 4. The data were taken in continuum mode, with two 50 MHz IFs centered at the standard L-band frequencies of 1465 and 1515 MHz, and a total of 4.8 h of on-source integration was achieved. The data were calibrated using NRAO's AIPS package. The field was mapped and cleaned using the AIPS task MX, using natural weighting of the *uv* points. The noise level in the final map was 25 μ Jy, close to the theoretical noise limit of 17 μ Jy.

A source was detected near the X-ray position of Hertz & Grindlay (1983; see Fig. 4.1). The measured position, assuming that the calibrator source 1748-253 is located at $\alpha = 17^{\text{h}}48^{\text{m}}45^{\text{s}}.789$, $\delta = -25^{\circ}23'17''.43$ (1950) is:

$$\alpha = 18^{\text{h}}20^{\text{m}}27^{\text{s}}.719 \pm 0^{\text{s}}.006, \quad \delta = -30^{\circ}23'15''.80 \pm 0''.08 \quad (1950),$$

consistent with the X-ray position (Table 4.1). The measured integrated flux density was $S_{1.4} = 0.558 \pm 0.06$ mJy.

This source has been detected in the radio several times before. Grindlay & Seaquist (1986) marginally detected a source with $S_{1.4} = 0.49 \pm 0.12$ mJy, at a position 0''.6 south of ours. Geldzahler (1983) detected a 2.44 mJy source 6''.3 from the cluster core. Machin *et al.* (1990) failed to detect any source near the cluster core, to a level of 87 μ Jy. Our position and flux are consistent with Grindlay & Seaquist's detection, given their large error bars. The disagreement with Geldzahler's results is very puzzling. Machin *et al.*'s lack of detection, taken at face value, implies that the source is highly variable.

Using Shawl & White's (1986) position, the distance of 4U 1820-30 from the core is $\delta\theta = 2''.7 \pm 0''.8$; using Hertz & Grindlay's (1985) position, $\delta\theta = 2''.1 \pm 0''.7$. At these distances from the core, $|a_{\text{max}}|/c = (8.0 \pm 1.3) \times 10^{-10} \text{ y}^{-1}$ and $|a_{\text{max}}|/c = (9.0 \pm 1.4) \times 10^{-10} \text{ y}^{-1}$ respectively (1σ errors). The error in both of these quantities is dominated by the error in the position of the optical core; thus only more accurate optical work can improve on this result. However, both values are still well below the observed $|\dot{P}|/P$ of $1.1 \times 10^{-7} \text{ y}^{-1}$, implying that the observed period derivative cannot be due to acceleration by the cluster.

[†] The VLA is operated by Associated Universities Inc., under cooperative agreement with the National Science Foundation.

4.3 Radio studies of cluster LMXBs: A powerful probe

This work brings the number of cluster LMXBs detected in the radio to three, the others being 4U 1850–08 in NGC 6712 (Lehto *et al.* 1990), and AC211 in M15 (Kulkarni *et al.* 1990). As deeper and deeper radio maps of LMXBs are made, most seem to be detected at the sub-mJy level (Penninx 1989). If this is generally true, then we have a new and powerful probe to study cluster LMXBs. Arc-second accuracy positions can be obtained immediately, enabling optical identification, a task that is difficult in the crowded cores of clusters. The energy emitted at radio wavelengths is a tiny fraction of the total energy being emitted by these objects.

The most interesting aspect of this radio-X-ray connection is in understanding the nature of the low luminosity X-ray sources. The cluster X-ray source population falls into two distinct categories: a high luminosity population, the LMXBs, with $L_x \gtrsim 10^{36} \text{ erg s}^{-1}$, and a low luminosity population, with $L_x \lesssim 10^{34.5} \text{ erg s}^{-1}$ (Hertz & Grindlay, 1983). The nature of the dim sources is quite unclear. It was early suggested that they are mass-exchange close binary systems (Hertz & Grindlay 1983). However, optical searches for the counterparts of these objects have been unsuccessful (Margon & Bolte 1987; Shara *et al.* 1988). It is possible that a significant fraction of these are chance superpositions of foreground or background objects on the cluster. However, those in the core region of the cluster are almost certainly associated with the clusters. There are two appealing possibilities: these dim sources could be cataclysmic variables or quiescent LMXBs. The latter alternative is supported by the fact that the X-ray luminosity of these cluster sources is an order of magnitude greater than CVs in the disk (Verbunt, van Paradijs & Elson 1984). In either case, the dim sources could well be the “missing” progenitors of the cluster pulsars. Unfortunately, their dimness and lack of good positional accuracy has precluded further detailed studies of this enigmatic class of radio sources.

It now appears that most LMXBs can be detected at the mJy level (Figure 4.2). In this figure we display a histogram of the radio luminosity of all detected LMXBs, $L_{1.4} = 4\pi S_{1.4}d^2$ where $S_{1.4}$ is the flux density at 1.4 GHz in mJy, and d is the distance to the source in kpc. If it is true that most or all accreting neutron stars are also radio emitters at the level of $\gtrsim 100 \text{ mJy kpc}^2$, then radio observations could discriminate between the two types of sources, since the radio luminosity of known CVs is several orders of magnitude smaller than that of the LMXBs (Chanmugam 1987; see Fig. 4.2).

Our deep radio imaging work on clusters favors the idea that the dim sources are accreting neutron star systems. Earlier we reported detection of two unidentified radio

sources in M22 and M3 (Johnston, Kulkarni & Goss 1991[†]), with luminosities of 50 and 270 mJy kpc² respectively. Both of these clusters contain low-luminosity X-ray sources discovered by the *Einstein* satellite (Hertz & Grindlay 1983), and as can be seen from Figure 4.2, the luminosities of these objects is not inconsistent with that of known sources. Preliminary analysis of *ROSAT* PSPC data (G. Hasinger & F. Verbunt, *pers. comm.*) on M22 find that the previously known *Einstein* IPC low luminosity source coincides with one of our radio sources (source 'S1' of Johnston *et al.*). It would be interesting to see if this correlation holds true for the dim sources in other clusters as well.

We thank Frank Verbunt and Günther Hasinger for providing data in advance of publication, and for bringing this object to our attention. We thank George Djorgovski for providing unpublished surface brightness profiles of NGC 6624. We also thank the Perkin Fund for support of our work at the VLA, and the NSF and the Packard foundation for general support of our research program.

[†] See Chapter 3.

Table 4.1 Previous detections of 4U 1820–30

| Band | Resolution (") | Offset from optical core ^a | | Flux (mJy) | Reference |
|-------------------|-------------------|---------------------------------------|-----------------|------------------|---------------------------|
| | | α (") | δ (") | | |
| Einstein HRI | 2×2 | -1.6 ± 1.0 | -1.8 ± 1.0 | — | Hertz & Grindlay 1983 |
| 20cm, VLA B array | 6×6 | -6.2 ± 0.4 | -0.9 ± 0.4 | 2.44 ± 0.04 | Geldzahler 1983 |
| 20cm, VLA A array | 2×2 | -2.6 ± 0.12 | 0 ± 0.12 | 0.49 ± 0.12 | Grindlay & Seaquist 1986 |
| 20cm, VLA C array | 18×10 | ^b | ^b | 0.95 ± 0.15 | Fruchter & Goss 1990 |
| 6cm, VLA D array | 18×10 | ^b | ^b | 0.38 ± 0.035 | Fruchter & Goss 1990 |
| 20cm, VLA A array | 2×2 | — | — | < 0.087 | Machin <i>et al.</i> 1990 |
| 20cm, VLA A array | 3.5×1.5 | -2.6 ± 0.08 | -0.6 ± 0.08 | 0.558 ± 0.06 | This work |

^a Offset from the optical core position (Shawl & White 1986): $\alpha = 18^{\text{h}}20^{\text{m}}27^{\text{s}}.92$, $\delta = -30^{\circ}23'15''.2$.

^b Integrated flux measurement only, thus flux also includes contribution from the two pulsars (Biggs *et al.* 1990).

References

Benz, A.O., Fürst, E. & Kiplinger, A.L. 1983, *Nature*, 302, 45

Biggs, J.D., Lyne, A.G., Manchester, R.N. & Ashworth, M. 1990, *IAU Circ.* #4988

Bookbinder, J. & Lamb, D.Q. 1987, *ApJ*, 323, L131

Bradt, H.V.D. & McClintock, J.E. 1983, *ARA&A*, 21, 13

Cassatella, A., Hassall, B.J.M., Harris, A. & Snijders, M.A.J. 1985, in *Recent Results on Cataclysmic Variables*, ed. W.R. Burke (Paris: ESA), p. 281

Chanmugam, G. 1987, *Ap. Space Sci.*, 130, 53

Dulk, G.A., Bastian, T.S. & Chanmugam, G. 1983, *ApJ*, 273, 249

Fruchter, A.S. & Goss, W.M. 1990, *ApJ*, 365, L63

Geldzahler, B.J. 1983, *ApJ*, 264, L49

Giacconi, R., Murray, S., Gursky, H., Kellogg, E., Scheir, E., Matilsky, T., Koch, D. & Tananbaum, H. 1974, *ApJS*, 27, 37

Grindlay, J.E. & Seaquist, E.R. 1986, *ApJ*, 310, 172

Hertz, P. & Grindlay, J.E. 1983, *ApJ*, 275, 105

Hertz, P. & Grindlay, J.E. 1985, *ApJ*, 298, 95

Hjellming, R.M. & Johnston, K.J. 1986, in *The physics of accretion onto compact objects*, ed. Mason, K.O., Watson, M.G., White, N.E. (Berlin: Springer) p. 287

Hjellming, R.M., van Gorkom, J.H., Taylor, A.R., Seaquist, E.R., Padin, S., Davis, R.J. & Bode, M.F. 1986, *ApJ*, 305, L71

Hjellming, R.M. & Wade, C.M. 1971, *ApJ*, 168, L21

Johnston, H.M., Kulkarni, S.R. & Goss, W.M. 1991, *ApJ*, 382, L89

Kulkarni, S.R., Goss, W.M., Wolszczan, A., & Middleditch, J.M. 1990, *ApJ*, 363, L5

Lehto, H.J., Machin, G., McHardy, I.M. & Callanan, P. 1990, *Nature*, 347, 49

Machin, G., Lehto, H.J., McHardy, I.M., Callanan, P.J. & Charles, P.A. 1990, *MNRAS*, 246, 237

Margon, B. & Bolte, M. 1987, *ApJ*, 321, L61

Penninx, W. 1989, in *Proc. 23rd ESLAB Symp. on Two Topics in X-ray Astronomy*, Bologna, Italy 13–20 September 1989, p. 215

Phinney, E.S. 1992, MNRAS, submitted

Phinney, E.S. & Kulkarni, S.R. 1992, Nature, submitted

Pryor, C., McClure, R.D., Fletcher, J.M. & Hesser, J.E. 1989, AJ, 98, 596

Rappaport, S., Nelson, L.A., Ma, C.P. & Joss, P.C. 1987, ApJ, 322, 842

Reynolds, S.P. & Chevalier, R.A. 1984, ApJ, 281, L33

Seaquist, E.R., Dubic, N., Israel, F.P., Spoelstra, T.A.T., Ulich, B.L. & Gregory, P.C. 1983, AJ, 85, 283

Shara, M.M., Kaluzny, J., Potter, M. & Moffat, A.F.J. 1988, ApJ, 328, 594

Shawl, S.J. & White, R.E. 1986, AJ, 91, 312

Stella, L., Friedhorsky, W. & White, N.E. 1987, ApJ, 312, L17

Tan, J., Morgan, E., Lewin, W.H.G., Penninx, W., van der Klis, M., van Paradijs, J., Makashima, K., Inoue, H., Dotani, T. & Mitsuda, K. 1991, ApJ, 374, 291

van der Klis, M., Hasinger, G., Dotani, T., Mitsuda, K., Verbunt, F., Murphy, B., van Paradijs, J., Belloni, T., Makashima, K., Morgan, E. & Lewin, W.H.G. 1992, in prep.

Verbunt, F., van Paradijs, J. & Elson, E. 1984, MNRAS, 210, 899

Figure captions

Figure 4.1 — VLA radio map of NGC 6624. The inner $20'' \times 20''$ is plotted, with contour levels at $-3, 3, 4, 5, 6, 8, 10$ and 15 times $25 \mu\text{Jy beam}^{-1}$ (the rms level of the map). The positions plotted are the position of the optical core position from Shawl & White (1986; marked “Core (SW)”); the optical core position from Hertz & Grindlay (1985; “Core (HG)”) the *Einstein* X-ray position from Hertz & Grindlay (1983; “HG”); the VLA detection by Grindlay & Seaquist (1986; “GS”) and the detection by Geldzahler (1983; “G”). The error bars represent the positional errors in the original measurements.

Figure 4.2 — Radio fluxes of known LMXBs and CVs: (a) Atoll sources. (b) Z sources. (c) Cataclysmic variables. The units of luminosity are mJy kpc^2 , and the bars show the range in luminosity observed, due mainly to variations in the radio flux rather than distance errors. References: LMXB fluxes and distances: Penninx 1989. CVs: *AM Her* – Dulk *et al.* 1983; *AE Aqr* – Bookbinder & Lamb 1987; *RS Oph* (in quiescence) – Hjellming *et al.* 1986, Cassatella *et al.* 1985; *GK Per* – Reynolds & Chevalier 1984; *HR Del* – Hjellming & Wade 1971; *V1500 Cyg* – Seaquist *et al.* 1980; *SU UMa* – Benz *et al.* 1983.

Figure 4.1

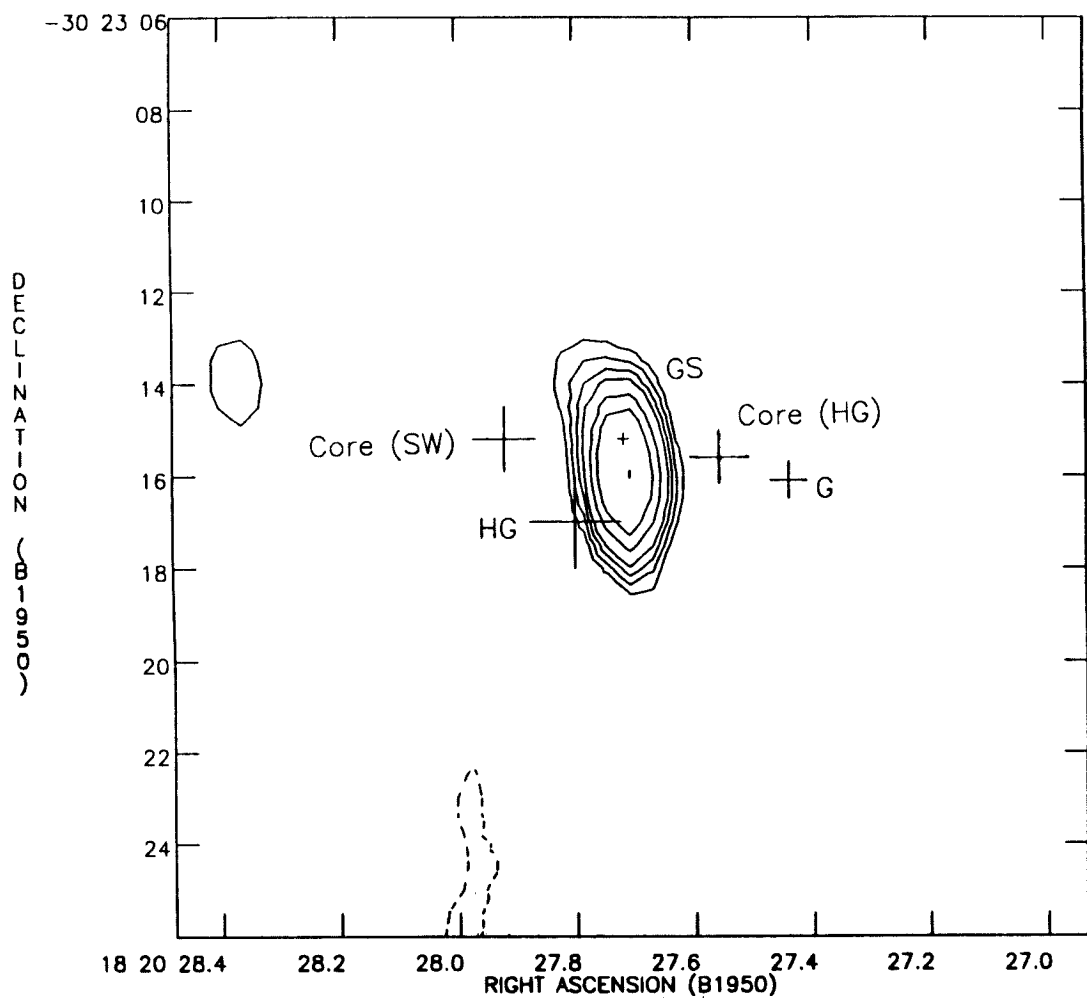
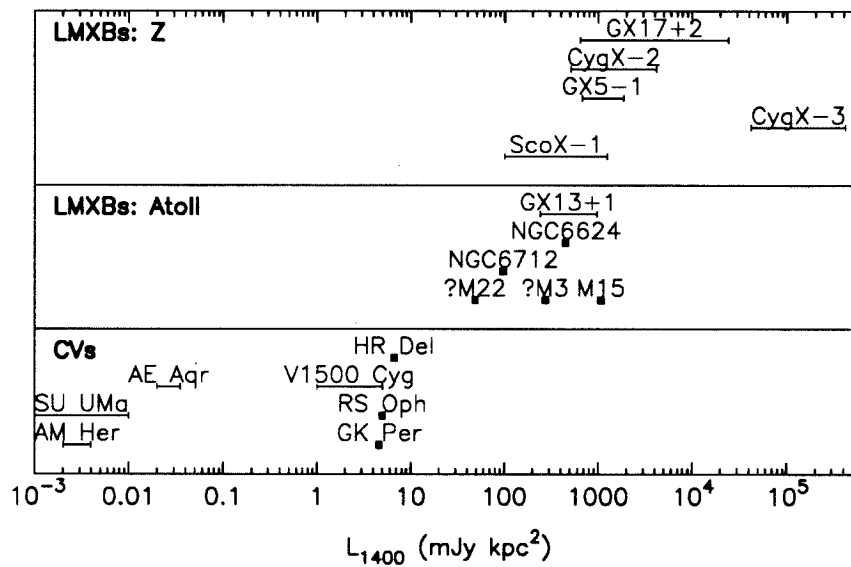


Figure 4.2



Chapter 5

The statistics of pulsars in globular clusters

Abstract

More than eighty globular clusters have now been surveyed for pulsars, either by single dish pulse searches, or using imaging techniques; nearly thirty cluster pulsars have so far been discovered. An interesting question for theories of pulsar formation is how the number of pulsars in a cluster scales with cluster parameters such as central density or cluster mass. However, any analysis of this scaling is inextricably tied up with the pulsar luminosity function, since the detected sample is heavily biased towards the brightest pulsars.

We have searched a total of nineteen clusters, eight at a wavelength of 20 cm using the VLA in C configuration, and twelve at 50 cm using the Westerbork synthesis array. Both surveys reached equivalent fluxes at 430 MHz of a few mJy, assuming a spectral index for recycled pulsars of -2.5 . One new source was detected in the cluster NGC 6517.

We present a statistical analysis of all the current cluster pulsar surveys. We determine the luminosity function of cluster pulsars to be $dN/dL \propto L^{-2}$, and conclude that the number of pulsars scales significantly less steeply than predicted by the tidal capture model. We suggest that this may be due to the importance of single star-binary interactions in globular clusters.

5.1 Introduction

The current count of globular cluster pulsars stands at 27, with more still being reported (Phinney & Kulkarni 1992; henceforth PK). The high luminosity of these objects and the great distances to globular clusters suggest that the discovered pulsars form only the “tip of the iceberg,” with many more faint pulsars being undiscovered. Estimates of the total number of cluster pulsars N_p have ranged from $2 \times 10^2/\bar{f}$ (Wijers & van Paradijs 1991) to $2 \times 10^3/\bar{f}$ (PK), and more if beaming is taken into account. Already these numbers are becoming uncomfortably large for the “standard model”. In this model, neutron stars, born in the first wave of star formation, tidally capture field stars. Subsequent mass transfer from the companion onto the neutron star results in X-ray emission, during which time the neutron star is visible as a Low Mass X-ray Binary (LMXB). This accretion also spins up the neutron star, which eventually appears as a millisecond pulsar.

This model has been successfully used to explain the distribution of LMXBs in clusters. Clusters, containing only 10^{-3} of the stars in the Galaxy, contain at least 10% of the LMXBs. This high abundance has been attributed to the efficiency of tidal capture in the cores of clusters (Fabian, Pringle & Rees 1975). Verbunt & Hut (1987) showed that the distribution of LMXBs in clusters was consistent with the standard model, with LMXBs being preferentially associated with the clusters having the highest rate of tidal captures. Clearly, if cluster pulsars are the descendants of the LMXBs, they too must follow a similar distribution.

Obtaining a census of the cluster pulsars is not simple. Unlike LMXBs, which are detectable anywhere in the Galaxy, pulsars are intrinsically faint. In addition, there are many selection effects. These include sampling time and interstellar scattering, which discriminate against finding fast pulsars; dispersion measure limitations, which select against distant pulsars or pulsars in regions of high electron density; the Galactic background radiation, which reduces sensitivity; and blurring of the pulse peak due to motion of the pulsar in tight binary systems. Most of these effects are most pronounced in the dense clusters near the Galactic centre, which are expected, in the standard model, to be producing pulsars at the highest rate. Thus establishing the size of the underlying population is fraught with difficulty, and is necessarily going to involve large extrapolations to the unseen population.

Several authors have attempted to estimate the size of the underlying population (Kulkarni, Narayan & Romani 1990; Fruchter & Goss 1990; Wijers & van Paradijs 1991; Phinney & Kulkarni 1992). These methods have depended on assumptions about the shape of the luminosity function and the density weighting function, or have depended on a small

number of observations. Our goal is to analyze all the current pulsar surveys and derive both the luminosity function and the density weighting from the observational data themselves.

We present here radio observations of nineteen globular clusters from the VLA and Westerbork. This brings the total number of clusters searched for pulsars to 84. We discuss the predictions of the way the number of pulsars should scale with cluster parameters in §5.2. We present new radio observations of globular clusters in §5.3 and discuss the details of previous surveys. We then discuss what is known about the luminosity function of the cluster pulsar population (§5.4) and the manner in which the propensity of a cluster to form pulsars depends on the cluster density (§5.5). We then present a self-consistent method to derive both of these dependencies from the observational data (§5.6), and discuss the reasons for the differences between various estimates of the pulsar population (§5.7).

5.2 Predictions of the standard model

The standard model involves the formation of LMXBs through the tidal capture of low mass stars by neutron stars, and subsequent spin-up of the neutron star by accretion and reappearance as a millisecond pulsar. In this model, the number of pulsars should be proportional to the number of tidal captures that are taking place. The number of two-body captures can be expressed as

$$N_p = n_{ns} n v \sigma V T \quad (5.1)$$

where n_{ns} and n are the number densities of neutron stars and non-degenerate stars, v is the relative velocity of the two stars, σ is the cross-section for tidal capture, and T and V are the time and volume over which the process is acting. Since the neutron stars are mostly confined to the core due to mass segregation, we can take $v = \sigma_c$, the core velocity dispersion of the cluster, $n \propto \rho_c$ the core density, and $n_{ns}V = N_{ns} = \nu M_t$, where ν is the specific incidence of neutron stars in the cluster, and M_t is the total cluster mass. The cross-section σ scales as $\sigma_c^{-2.14}$ (Lee & Ostriker 1986), so the total number of two-body tidal captures is

$$N_p \propto \nu M_t \rho_c \sigma_c^{-1.14} T. \quad (5.2)$$

T is usually assumed to be constant and set to the age of Galaxy. The assumption of constant T is certainly questionable since clusters evolve considerably over the age of the Galaxy.

Several lines of reasoning — the discovery of primordial binaries in optical spectroscopic surveys (Pryor *et al.* 1989), the discovery of pulsars (Kulkarni *et al.* 1991) or pulsar-like emission (Fruchter and Goss 1992) in low density clusters, *etc.* — have highlighted the dominant role of three-body (primordial binary and neutron star) collisions in all but the densest clusters. The cross-section for two-body encounters is

$$\sigma_2 = \pi d^2 \left(1 + \frac{2G(m_1 + m_2)}{v^2 d} \right) \simeq \pi d \frac{2G(m_1 + m_2)}{v^2} \quad (5.3)$$

where the second term in the parentheses is due to gravitational focussing, and will dominate for the small velocities found in globular clusters. Capture occurs when $d \lesssim 3R_*$, where R_* is the radius of the non-degenerate star (see, *e.g.*, Verbunt & Hut 1987). The cross-section for single star-binary interactions, on the other hand, is $\sigma_3 \sim \pi a a_c$, where a_c is the characteristic radius, $a_c \sim GM_{tot}/\sigma_c^2$ (Hills 1975). For a $1.4 M_\odot$ neutron star encountering a binary containing a binary containing two $0.8 M_\odot$ stars in a typical cluster with $\sigma_c = 10 \text{ km s}^{-1}$, $a_c \sim 25 \text{ A.U.}$ Since a , the orbital radius of a binary, is much greater than R_* , the radius of a typical star, we can see that, provided the binary fraction is reasonable,

three-body interactions will dominate over two-body captures. In dense clusters, stellar encounters destroy or harden (*i.e.*, reduce a) wide binaries, reducing the efficiency of single star-binary encounters. This can be effectively parametrized by making the dependence of N_p on ρ_c less than linear in equation (5.2). We generalize the dependence of N_p on ρ_c as ρ_c^α :

$$N_p \propto \nu M_t \rho_c^\alpha \sigma_c^{-1.14} T. \quad (5.4)$$

The specific incidence of neutron stars ν is related to the initial mass function (IMF) of the cluster stars. Assume a power-law differential IMF, $N(m) \propto m^{-(1+x)} dm$, valid for $m > m_l$, the minimum mass. The number of neutron stars per unit initial mass of the cluster at birth is then

$$\nu = \frac{x-1}{8x} \left(\frac{m_l}{8 M_\odot} \right)^{x-1} M_\odot^{-1} \quad (5.5)$$

where we assume that stars with $m > 8 M_\odot$ evolve to neutron stars. For a proto-cluster with Salpeter IMF, $x = 1.35$, total mass $10^6 M_\odot$ and $m_l = 0.08 M_\odot$, we obtain $\nu = 0.6\%$ and $N_{ns} = 6 \times 10^3$ primordial neutron stars. If cluster pulsars have similar velocities to those observed for field pulsars, $\bar{v} \sim 200 \text{ km s}^{-1}$ (Anderson & Lyne 1983), then a significant fraction of the neutron stars born in a cluster may escape at birth. Typical escape velocities for non-core collapsed clusters range from $20\text{--}70 \text{ km s}^{-1}$; this would imply that the fraction of neutron stars retained by the cluster is typically 0.1–0.3. Thus our typical cluster would be expected to retain $\sim 10^3$ neutron stars.

The shape of the cluster IMF is very poorly understood, and it is not even clear, on observational or theoretical grounds, whether the IMF can be characterized by a simple power law. Variations in the IMF between clusters have been reported, some of which are probably genuine, *e.g.*, in the LMC, clusters with x of ~ 0.3 to 2.5 have been found (Elson *et al.* 1989; Mateo 1988[†]). However, here one must be cautious of the many observational studies which suffer from improper accounting of the distortions to the observed MF introduced by mass segregation, *e.g.*, McClure *et al.* (1986) found a trend of x with metallicity, but their conclusions were based on luminosity functions obtained at distances of several core radii from the cluster centers.

Given the current observational situation, we will use the bare minimum number of parameters to derive the number of pulsars: ρ_c , M_t and α . For lack of detailed data and understanding, we assume ν and T are the same for all clusters. Note in particular that we are omitting the $\sigma_c^{-1.14}$ dependence (eq. [5.4]), in order to minimize the number of parameters. This could make a difference, as low density clusters tend to have low

[†] Richtler *et al.* (1991) recently attributed these earlier results to problems with crowding and incompleteness, and claim that all IMFs are consistent with a Salpeter slope.

core velocity dispersions as well, which would thus tend to reduce the dependence on ρ_c . However, the size of this effect is not large: typical velocity dispersions for core collapsed clusters are $10 - 15 \text{ km s}^{-1}$, while for low density clusters $\sigma_c \simeq 4 - 8 \text{ km s}^{-1}$, so $\sigma_c^{-1.14}$ varies by a factor of 3 between clusters, while ρ_c varies by a factor of 1000 or more.

5.3 New observations and description of previous surveys

5.3.1 VLA data

Observations were taken on 1990 November 25 and 1990 December 2 with the VLA[†] in the C configuration. The data were taken in continuum mode, with two 50 MHz IFs centered at the standard ‘L’-band frequencies of 1465 and 1515 MHz. Eight clusters were observed for 1.6 h each, with phase calibrators observed every 20 m. The data were calibrated and imaged using NRAO’s AIPS package.

Maps of each field were made and cleaned using MX. The noise levels in the final maps were between 80 and $110 \mu\text{Jy}/\text{beam}$. The only cluster showing detectable emission at the core was NGC 6517 (Figure 5.1). The flux density of this source and 3σ upper limits on the flux density from the other clusters are shown in Table 5.1.

5.3.2 Westerbork data

Twelve clusters were observed with the Westerbork Synthesis Radio Telescope (WSRT) at 610 MHz. Since many of these sources are southern sources, a full 12 h integration could not be achieved. Each source was observed at least twice, resulting in integration times of 14 to 24 h per cluster. The data were calibrated using the DWARF reduction package. Data from the redundant baselines were used to remove telescope dependent errors. The maps were then self-calibrated in an iterative fashion to reach the final noise levels of typically $0.5 \text{ mJy}/\text{beam}$.

Only one cluster shows detectable emission within the central $100'' \times 100''$: NGC 4147, which has a 25 mJy source $40''$ east, $68''$ south of the cluster core. However, since this represents a distance of 26 core radii from the core, the source is unlikely to be associated with the cluster. Flux limits on the emission from these clusters are shown in Table 5.1.

5.3.3 Previous pulsar surveys

Our new observations bring the total number of clusters searched for pulsars to 84. The last two columns of Table 5.2 show S_{430} , the faintest flux to which each cluster has

[†] The VLA is operated by Associated Universities Inc., under cooperative agreement with the National Science Foundation.

been searched at 430 MHz (assuming a spectral index (ν^α) of $\alpha = -2.5$ where the survey was not at 430 MHz) and the survey involved. This forms the observational data on which we are basing our statistical analysis. Here we briefly summarize the major cluster surveys that are included in our analysis.

Arecibo. All clusters observable with the Arecibo dish ($0^\circ \leq \delta \leq 37^\circ$) were searched at 1400 MHz with a sampling time of 507 μ s. This resulted in the discovery of PSR2127+11A, and PSR1908+00 in NGC 6760. A second search at 430 MHz resulted in the discovery of seven more pulsars. Partial details of the two surveys may be found in Wolszczan *et al.* (1989) and Anderson *et al.* (1990a).

Jodrell Bank. A total of 65 clusters were observed using the 76 m Lowell telescope, at two different frequencies: 610 MHz and 1420 MHz, using a sampling interval of 300 μ s (Lyne *et al.* 1988; Lyne & Biggs 1989). This resulted in the discovery of PSR1821–24 in M28, and PSR1620–26 in M4.

Parkes. Southern globular clusters are being searched by the Parkes telescope at 1400 MHz and 600 MHz, using 300 μ s sampling. Partial details of the survey may be found in Manchester *et al.* (1991) and Robinson *et al.* (1992). The survey has resulted in the discovery of many pulsars, including ten in 47 Tuc (Manchester *et al.* 1989; Biggs *et al.* 1990; D'Amico *et al.* 1990; Manchester *et al.* 1990; Lyne *et al.* 1990).

VLA surveys. There have been four surveys of clusters using the VLA. (i) Hamilton *et al.* (1985) imaged twelve clusters at 1400 MHz, to a flux limit of 0.7 mJy; they detected one point source in M28, which led to the discovery of the first cluster pulsar. (ii) Fruchter & Goss (1990) imaged seventeen clusters at 1400 MHz to a similar flux level, and found five point sources, four of which have since been shown to be pulsars. The fifth one is likely to be a pulsar as well. (iii) Kulkarni *et al.* (1990) imaged four clusters at 1400 MHz to levels between 0.1 mJy and 0.3 mJy. They identified already known pulsars in M15, M4 and M28, and located an intriguing point source in M3 which has yet to be identified. (iv) Johnston *et al.* (1991) imaged four clusters at 1400 MHz to levels between 0.1 mJy and 0.2 mJy. They found several sources in M13 and M22, not yet identified. The VLA surveys show that there cannot be a large number of tight binaries and limit $\beta < 2$ (Johnston *et al.* 1991).

5.4 The luminosity function of recycled pulsars

5.4.1 Ages and birthrates of cluster pulsars

The most model independent method of determining the number of cluster pulsars involves the birthrate, B . If every cluster pulsar is visible for a Hubble time and has a measured age, then on average we expect to see BT pulsars with ages less than T . The ages of cluster pulsars are relatively easy to determine: the characteristic age, $\tau_c = P/2\dot{P}$, forms a good estimate of the pulsar's true age. Such would not be the case if magnetic field decay was taking place in these pulsars, in which case τ_c would form an upper limit to the true age. However, the observational evidence seems to indicate that magnetic field decay is not taking place in these pulsars. In the disk, the white dwarf cooling age in binary pulsars in the disk is consistent with the characteristic age (Kulkarni 1986); τ_c for the binary pulsar in M4 is close to the timescale invoked to explain the observed eccentricity (Rappaport, Putney & Verbunt 1989); and the gravitational decay timescale of the binary in M15 (Anderson *et al.* 1990a) is comparable to τ_c . Thus we assume that the characteristic ages of cluster pulsars are good measures of their true ages.

For very young pulsars, however, τ_c can provide a misleading estimate of the pulsar's age. The initial spin period of recycled pulsars is expected to be given by equating the Alfvén radius of the neutron star to the Keplerian period of the inner edge of the accretion disk:

$$P_i = 1.9 \times 10^{-3} B_9^{6/7} \text{ s.} \quad (5.5)$$

The dipole magnetic field of a pulsar in units of 10^9 G is given by

$$B_9^2 = 10^{-21} P \dot{P} \quad (5.6)$$

where P is the pulsar period in seconds. Hence the characteristic age of a recycled pulsar at birth will be

$$\tau_c = P/2\dot{P} = 7.1 \times 10^6 P^{-1/3} \text{ y,} \quad (5.7)$$

i.e., if cluster pulsars are born on the rebirth line, then the ages of young pulsars ($\tau_c \lesssim 10^8$ y) will be overestimated: a 3 ms pulsar will have an apparent age at birth of 5×10^7 y. Thus if, for instance, the brightest pulsars have true ages of 10^6 y but apparent ages of 5×10^7 y, the birthrate will be underestimated by a factor of 50. However, since this only applies to the youngest pulsars, we expect this to be a rare problem.

5.4.2 The luminosities of cluster pulsars

The principal problem with the birthrate method is that there are severe luminosity selection effects present, as only the very brightest cluster pulsars are visible. This is

illustrated in Figure 5.2, where we show the histogram of the luminosities of all cluster pulsars, $L_{430} = S_{430}d^2$, where S_{430} is the flux density at 430 MHz and d is the distance to the source in kpc. The minimum luminosity of any cluster pulsar is 30 mJy kpc² (PSR1516+02B in M5). This is much brighter than the minimum luminosity of the observed sample of disk recycled pulsars, which itself is probably biased towards the brighter pulsars. Thus any estimate of the total number of cluster pulsars requires a large extrapolation to these undetected pulsars.

This selection effect could affect the birthrate calculations in one of several ways. If the luminosity of a pulsar is uncorrelated with its age, then we can use the observed pulsars to calculate the underlying luminosity function. The total number of pulsars N_t is then given by dividing the birthrate of the observed (bright) pulsars by the fraction of the total pulsar population this sample represents, as given by the luminosity function. On the other hand, if luminosity *is* correlated with age, so that pulsars beyond a certain age are no longer detectable, then only the number and birth rate of the bright, young pulsars is relevant, and the birthrate can be estimated with minimal correction for sample incompleteness.

In Figure 5.3 we plot the luminosities and ages of recycled pulsars both in the disk and in clusters. Ages for many of the cluster pulsars are not available since \dot{P} has not yet been measured; in other cases (*e.g.*, M15) the period derivatives are known to be corrupted by dynamical effects (Wolszczan *et al.* 1989, Phinney 1992). As can be seen from the figure, any trend of pulsar luminosity with age is at best modest. Thus we need to determine the luminosity function of the underlying population in order to determine the total number of cluster pulsars.

The shape of this luminosity function is not well understood. For lack of any better information, most authors adopt a power-law luminosity function

$$dN/dL \propto L^{-\gamma}. \quad (5.8)$$

Slow pulsars in the disk are well fitted by a luminosity function of this form with $\gamma = 2$ (Manchester and Taylor 1977). Note that a function of this form can be produced by a luminosity-age correlation: a luminosity decay law $L \propto t^{1/(1-\gamma)}$ would give such a power law luminosity function. Thus for $\gamma = 2$, the implied luminosity decay law is t^{-1} .

The number of recycled pulsars is too small for reliable determination of the exponent γ . Kulkarni, Narayan & Romani (1990, henceforth KNR) attempted to combine pulsar observations with a model for pulsar evolution to construct a luminosity function, which turns out to be almost a power law of the form (5.8), as follows.

For disk pulsars, an empirical relation has been found between the mean observed 400 MHz luminosity of a pulsar, L_m , and the quantity $Q \equiv \log(\dot{P}_{-15}/3P^3)$, where P is the pulsar period in seconds, and \dot{P}_{-15} is the period derivative in units of 10^{-15} ss $^{-1}$. Proszynski & Przybicien (1984), suggested a relation of the form $\log L_m = \frac{1}{3}Q + A$, and KNR found that for recycled pulsars (disk and cluster), $A = 1.1$, as opposed to 1.6 for slow pulsars.

KNR constructed a model luminosity function by assuming pulsars are born on the rebirth line uniformly spaced in $\log B_9$ in the range $-1 < \log B_9 < 1$, and evolved the population under assumption of constant B_9 . This defines an initial P and \dot{P} for each pulsar, and hence a mean luminosity L_m . The spread in luminosity about the mean was adapted from a relation given by Narayan & Ostriker (1990). The resulting population was found to have a luminosity distribution with $\gamma = 2$ and a turnover at $L_{400} \sim 3$ mJy kpc 2 . This is remarkably similar to the luminosity function of the single, slow pulsars. In §5.6 we will investigate this luminosity function as well as several power law exponents.

Notice that, in order for the pulsar population to be finite, a minimum luminosity L_{min} needs to be specified. The minimum luminosity observed for a disk recycled pulsar is 12 mJy kpc 2 at 430 MHz (PSR2303+46); the faintest field slow pulsar is 0.3 mJy kpc 2 (Dewey *et al.* 1985). The former is almost certainly biased towards bright pulsars, while the latter seems to represent a real cut-off in the luminosity function. The total number of pulsars derived from luminosity function extrapolations is extremely sensitive (factors of ten or more) to the choice of L_{min} . We have chosen $L_{min} = 1$ mJy kpc 2 for the rest of this work.

5.5 Density dependence of the cluster pulsar birthrate

That the rate of cluster pulsar formation is less dependent on cluster density than predicted by the two-body capture model is clear even from simple arguments. Consider the pulsars in M4 and M28, with characteristic ages $\tau_c = 3 \times 10^8$ y and 3×10^7 y respectively (McKenna and Lyne 1988; Foster *et al.* 1988). If a group of clusters has been producing pulsars at a constant rate for time T , then the expected number of pulsars of age less than t is $\sim N(t/T)$, where N is the total number of pulsars, and T is the time over which the cluster has been at its current density (PK). For M28 and M4, $T \sim 3 \times 10^9$ y, so PSR1620 – 26 in M4 implies 10 similar pulsars in similar clusters, and PSR1821 – 24 in M28 implies 100 similar pulsars *i.e.*, birthrates of 3×10^{-9} y $^{-1}$ and 3×10^{-8} y $^{-1}$ respectively.

M15 has a density at least 100 times as great as M4 or M28. If the number of cluster pulsars scaled linearly with density, then the birthrate of pulsars in dense clusters like M15 should also be 100 times larger. However, M15 has three pulsars with ages $\tau_c \sim 3 \times 10^8$ y (Anderson *et al.* 1990a) implying a birthrate of 3×10^{-8} y $^{-1}$ if the cluster central density has not changed dramatically over the last 10^8 y. The formation rate of pulsars in M15 is certainly not larger by a factor of 100 than the rate in M4 or M28, so the dependence on density must be less than linear.

◊ ◊ ◊ ◊ ◊

So what evidence we have points to cluster pulsars being less concentrated in dense clusters than would be predicted by the standard model, $\alpha < 1$, and having approximately a power-law luminosity function, with $\gamma \sim 2$. Because these two parameters are tied up together, we would like to estimate both at once from the observational data in a self-consistent fashion. For example, if we have detected five pulsars in a sparse cluster at a distance of 3 kpc, and five pulsars in a cluster with twice the central density at a distance of 6 kpc, then we need to know the shape of the underlying luminosity function to determine the scaling of N_p with cluster density. For a $\gamma = 2$ luminosity function, improving the survey luminosity limit by a factor of 2 doubles the number of pulsars that could be detected, implying that the density scaling must be linear. For $\gamma = 1.5$, improving the luminosity limit by a factor of 2 only increases the number of pulsars by $\sqrt{2}$, so the density dependence indicated is less than linear. We present a method for estimating both α and γ in a self-consistent fashion in the next section.

5.6 A self-consistent estimate of the cluster pulsar population

In order to quantify the dependence of N_p on cluster parameters, we present here a statistical analysis of cluster search data which we use to determine both the pulsar luminosity function and the density weighting function. It is a generalization of Verbunt and Hut's (1987) diagram for LMXBs, in which they assigned a weight to each cluster based on the 2-body tidal capture model, and showed that the distribution of LMXBs in clusters was (roughly) consistent with this model: $\alpha = 1$. Unlike the situation for LMXBs, which could have been detected anywhere in the galaxy, this method cannot be used as is for cluster pulsars, because of their intrinsic faintness. This means that the weight assigned to each cluster must depend not only on the birthrate of pulsars, but also on the fraction of all pulsars which could have been discovered by the surveys. This fraction will be large for nearby clusters, where even intrinsically faint pulsars could have been detected, or for clusters surveyed to low flux levels by *e.g.*, Arecibo or the VLA. Turning a survey flux limit into a fraction of the pulsar population requires knowledge of the underlying luminosity function.

Hence we need a two-dimensional diagram, to simultaneously explore both the weighting function assigned to the clusters, and the luminosity function of the pulsar population. In Verbunt & Hut's diagram, each cluster was assigned a weight w_i proportional to the number of two-body tidal captures, then each cluster was assigned a segment on a line between 0 and 1 with length proportional to w_i . With the correct choice of weighting function the LMXBs were uniformly distributed along this line. For the pulsars, we have two dimensions: a width, proportional to w_i , and a length, proportional to the fraction of the pulsar population surveyed (see §5.6.1). With the correct choice of weighting function w_i , parametrized by α (see eq. [5.3]), and luminosity function, parametrized by γ (eq. [5.8]) the pulsars should be uniformly distributed within the *area* defined by the pulsar surveys. In fact, since we do not have very many pulsars, we will not perform two-dimensional tests of uniformity, but will restrict ourselves to one-dimensional tests of the weighting function and luminosity function separately.

5.6.1 Choice of luminosity function

For each cluster, we have to determine the factor by which the observed number of pulsars needs to be corrected to account for the pulsars too faint to have been discovered. In order to do this, we need to know the shape of the underlying luminosity function. We first assume a luminosity function, then test whether our results have the right statistical properties.

For every cluster i , we assign a number x_i equal to the fraction of all pulsars that could have been discovered in that cluster with a survey of limiting luminosity $L_i = S_{430} d^2$ (see Table 5.2):

$$\begin{aligned} x_i &= \frac{N(> L_i)}{N(> L_{min})} \\ &= \frac{1}{N_t} \int_{L_i}^{\infty} \frac{dN}{dL} dL \end{aligned} \quad (5.9)$$

where $N_t = N(> L_{min})$ is the total number of pulsars. For a power law luminosity function, $x_i = L^{(1-\gamma)} / L_{min}^{(1-\gamma)}$. Then for each pulsar j in cluster i , we assign a number

$$x_i^j = \frac{N(> L_i^j)}{N(> L_{min})} \quad (5.10)$$

where L_i^j is the luminosity of the j 'th pulsar in cluster i (Table 5.3). By construction, $L_i^j \geq L_i$ for all j (since the pulsars have been discovered!). If we have chosen the luminosity function correctly, then the x_i^j 's will be uniformly distributed along the segment $[0, x_i]$.

This procedure is best illustrated by means of an example. Consider M15 (NGC7078), which has been surveyed to a flux limit of 0.5 mJy (Table 5.2), which corresponds at a distance of 9.7 kpc to a luminosity limit of 47 mJy kpc². M15 contains five pulsars, with luminosities of 188, 66, 94, 56 and 47 mJy kpc² (Table 5.3). These are plotted in Figure 5.4, with the pulsars as filled squares on the x -axis, and the luminosity limit as the thick vertical line. Only pulsars with luminosities to the right of this line could have been detected. The intersection of the dotted line then represents x_i ; for the cluster, the fraction of all pulsars

† But see below for caveats regarding this statement.

‡ This is the same technique used when we want to generate a distribution of y 's with a given probability distribution $p(y) = f(y)$. We take a uniform deviate x , with $p(x) dx = dx$ for $0 < x < 1$, 0 otherwise. Then the probability distribution of $y(x)$ is given by

$$p(y) = p(x) \left| \frac{dx}{dy} \right|$$

So if we want $p(y) = f(y)$, then we need to solve

$$\frac{dx}{dy} = f(y)$$

whose solution is $x = F(y)$, where $F(y)$ is the integral of $f(y)$. Thus

$$y(x) = F^{-1}(x)$$

transforms the uniform deviate x into one distributed as $f(y)$ (see Press *et al.* (1986), §7.2.) We are inverting this procedure: we test our assumption of the form of $f(y)$ by seeing if the x 's are uniformly distributed.

that could have been found. Note that this fraction depends strongly on which luminosity function is used, but in either case is small (just 8% of all pulsars could have been detected for the KNR function, 15% for the other). We also plot two integral luminosity functions, the solid line being the KNR luminosity function $\gamma \sim 2$) and the dot-dashed line a $\gamma = 1.5$ power-law. We then transform the observed luminosities into the x_i^j 's by means of the luminosity function, as shown by the dashed line for M15C. The resulting x_i^j 's are shown as the filled squares on the left axis (for KNR), or the crosses on the right axis (for $\gamma = 1.5$). If the luminosity function is correct, then these points should be uniformly distributed between 0 and x_i (the dotted line); note that this is certainly not the case for the observed *luminosities*. This condition is clearly better filled by the KNR function. A Kolmogorov-Smirnov (K-S) test yields probabilities that the distribution is uniform of 0.74 and 0.15 respectively, so both are acceptable fits for this one cluster alone.

Since few clusters contain many pulsars, however, we test all clusters together. The quantity

$$z^j = \frac{x_i^j}{x_i} \quad (5.11)$$

for all pulsars j should be distributed uniformly along the segment $[0, 1]$. This is illustrated by the strips at the bottom of Figure 5.5: the exponent of the luminosity function which has been used is indicated at the right. Clearly both the $\gamma = 1.5$ and $\gamma = 1$ luminosity functions have too many pulsars clustered towards the faint end of the surveys (K-S probabilities 10^{-5} and 10^{-14} respectively). Both the $\gamma = 2$ and the KNR luminosity function (essentially $\gamma = 2$ with a turnover at faint luminosities) are acceptable (K-S probabilities 0.09 and 0.22).

The principal problem with this method is that the fluxes of pulsars from pulse surveys are notoriously difficult to measure. This is compounded by the fact that the pulsars tend to be discovered only when they are scintillating up, and so are brighter than their average state:[†] PSR0021-72C in 47 Tuc, for instance, varies by more than a factor of ten in intensity from one observation to another (Manchester *et al.* 1991). This problem of measuring fluxes is particularly apparent in the case of the other 47 Tuc pulsars, where in 80 observations, some pulsars were detected as few as 2 or 3 times (Manchester *et al.* 1991). We have assumed that these observations are in the strong-scintillation, narrow bandwidth limit, with observation time much less than the scintillation time, so the distribution of intensities is an exponential distribution (Rickett 1977; see p. 494), so $\bar{S} = S_{lim}/[-\ln(P(> S_{lim}))]$, where S_{lim} is the detection threshold. Thus we have taken $S = S_{lim}/\ln(N_{\text{obs}}/N_{\text{det}})$, with $N_{\text{obs}} = 80$ and N_{det} from Table 1 of Manchester *et al.*

[†] Thus producing an effect similar to the Malmquist bias.

5.6.2 Choice of weighting function

We now consider the weights assigned to the other dimension of our test, w_i . These weights have the form

$$w_i = M_c \rho_c^\alpha. \quad (5.12)$$

This requires that we know the cluster parameters M_c and ρ_c . These are derived from the measured optical surface brightness profiles, by use of King (1966) models. We present these derived parameters in Table 5.2 (from Chernoff & Djorgovski 1989).

We have made several modifications to these derived parameters. These all relate to the core-collapsed clusters, both because of observational difficulties in measuring these properties, and because of evolutionary effects.

The core densities of clusters are estimated using King models (King 1966). Since King models are not applicable to core-collapsed clusters, the central density of these clusters is very poorly determined: naive application of the King formulae leads to nominal densities as high as $10^{11} M_\odot \text{ pc}^{-3}$. Thus we have set the central densities of all clusters classified by Chernoff & Djorgovski (1989) as core-collapsed to be $\rho_c = 10^6 M_\odot \text{ pc}^{-3}$. This is the maximum central density measured for any non-core-collapsed cluster, and represents the density at which the probability of a single neutron star tidally capturing a main sequence star in a Hubble time is unity (PK). Similarly, we have arbitrarily set the core mass M_c equal to $0.02 M_t$, assuming the fraction of the mass in the core is the same for all core collapsed clusters.

Since the number of neutron stars in the cluster depends on the initial conditions, not the present conditions, it is important to account for quantities which have been significantly altered over the cluster history. Chernoff & Djorgovski (1989) found that the core-collapsed clusters are much more concentrated towards the Galactic center than the King model clusters, suggesting that the dynamical history of the cluster is dependent on Galactic location. Theoretically, this has been explained as the result of interaction of the cluster with the Galactic tidal field, which strips stars from the cluster's tidal radius. This evaporation unbinds weakly bound clusters, and drives more concentrated clusters towards core collapse (Chernoff, Kochanek & Shapiro 1986; Chernoff & Weinberg 1990). We have simulated this effect by taking $M_t = 5M_t^{\text{obs}}$ for clusters with $R_{\text{gc}} \leq 2.2 \text{ kpc}$, assuming clusters near the Galactic center have lost 80% of their mass due to tidal stripping.

Hence for each cluster i , we can assign a density weight w_i as given by equation (5.12) with a choice of α , and a luminosity function weight x_i given by equation (5.9) with a

choice of γ . This defines for each cluster an area in the two-dimensional diagram:

$$\begin{aligned} a_i &= w_i x_i \\ &= w_i \frac{N(> L_i)}{N(> L_{min})}. \end{aligned} \quad (5.13)$$

Now assign each pulsar j the corresponding quantity a_i^j :

$$\begin{aligned} a_i^j &= w_i x_i^j \\ &= w_i \frac{N(> L_i^j)}{N(> L_{min})}. \end{aligned} \quad (5.14)$$

If segments of length a_i are laid end-to-end, they form a line of length

$$X = \sum_{i=1}^n x_i \quad (5.15)$$

the fraction of all pulsars, over the total number of clusters n , that have so far been detected (for the assumed density and luminosity function weighting). If we have chosen α and γ correctly, then the pulsars, at positions a_i^j along this segment, will be distributed uniformly.

The quantity a_i^j is not as sensitive as z^j (eq. [5.11]) to errors in the choice of luminosity function. Since these result only in clustering of the pulsars x_i^j within each x_i , an error in the choice of γ will lead to bunching of the pulsars along the segment X , but not to large gradients of pulsars along X . We showed in §5.6.1 that the distribution of the quantity z^j was a more sensitive way to test errors in the luminosity function exponent γ , and concluded that the KNR luminosity function gave the most acceptable fit.

The quantity a_i^j is much more sensitive to errors in the choice of weighting function w_i , but caution must be used. The test is very sensitive to the *ordering* of clusters in constructing X . While the correct choice of α and γ will always result in a uniform distribution of pulsars, the fact there are only a few or no pulsars in most clusters means that a random shuffling of the order of clusters can make almost any choice of weights appear uniform.

As an example, consider two hypotheses about the distribution of pulsars in clusters:

- (1) All clusters contain equal numbers of pulsars: $w_i = 1$ for all i ; and
- (2) Only clusters with central densities $\rho_c > 10^5 M_\odot \text{ pc}^{-3}$ contain pulsars: $w_i = 0$ for all clusters i with $\rho_{c,i} < 10^5 M_\odot \text{ pc}^{-3}$, 1 otherwise.

To discriminate between these two hypotheses, clearly the optimal choice is to order the clusters by density. Then if (2) is true, weighting by (1) will put all pulsars on one side of

the segment, a clearly non-uniform distribution. Ordering by anything *other* than density would scramble the clusters, which can only make the distribution more uniform. If (1) were true, then weighting by (2) would give an enormous concentration of clusters at the low-density end (since $a_i = 0$ if $w_i = 0$), again clearly non-uniform.

Thus we have assigned each cluster a value a_i as given by equation (5.13), and ordered the clusters by central density ρ_c in forming the segment X (eq. [5.15]). Two examples of X are shown on the right hand side of Figure 5.5, for $\alpha = 1$ and $\alpha = 0.5$. Clearly the $\alpha = 1$ weighting function has too many pulsars in clusters with low weight (K-S probability 3×10^{-6}). Our preferred choice is $\alpha = 0.5$ (K-S probability 0.12).

If LMXBs are the progenitors of the cluster pulsars, they should be distributed in the same fashion; recall that Verbunt & Hut (1987) found that for the LMXBs, $\alpha = 1$ gave a good fit, while for the pulsars we find α must be less than 1. In Figure 5.5, we plot down the right hand side of the figure the positions of cluster LMXBs. Their distribution is consistent with either $\alpha = 1$ or $\alpha = 0.5$ (K-S probability 0.52 and 0.90 respectively).

5.7 The total number of cluster pulsars

For our preferred density weighting scheme and luminosity function, we find the fraction of all cluster pulsars that has been observed to be $X = 1.3 \times 10^{-2}$, which, since there are 27 observed pulsars, means there are $N_p \sim 2000/\bar{f}$ pulsars in the entire globular cluster system.

Previous estimates of N_p have ranged from $2 \times 10^2/\bar{f}$ to $2 \times 10^3/\bar{f}$, where \bar{f} is the beaming fraction, assumed to lie between 0.2 and 1. Here we summarize the various methods that have been used and the estimates of N_p that were reached, and discuss the reasons for the large discrepancies.

The Birthrate Method. PK used the birthrate method, discussed in §5.4.1, where if a group of clusters has been producing pulsars at a constant rate for time T , then the expected number of pulsars of age less than t is $\sim N_p(t/T)$. The few measured \dot{P} s indicate high birthrates in M28 ($\tau_c = 3 \times 10^7$ y; Foster *et al.* 1991), M4 ($\tau_c = 3 \times 10^8$ y; McKenna & Lyne 1988) and M15 ($\tau_c \sim 3 \times 10^8$ y; Prince *et al.* 1991) and M13 ($\tau_c \sim 10^9$ y; Kulkarni *et al.* 1991). This has to be balanced by the non-detections and the choice of T . PK obtain a rough estimate $N_p \sim 2 \times 10^3/\bar{f}$ pulsars over the whole cluster system, over Hubble lifetime; here \bar{f} is the mean beaming factor and is expected to be between 0.2 and 1.

The Luminosity Function Method I. KNR used the semi-empirical luminosity law described in §5.4.2 to model the true underlying pulsar population in clusters. By comparing the estimates of the number of detectable pulsars with the actual detections, KNR estimated $N_p \sim 1000(1 + \beta)/\bar{f}$ (this value interpolated to $\alpha = 0.5$ to facilitate consistent comparison with other estimates.) Here β is the ratio of the number of pulsars in tight binaries to pulsars in wide binaries (including single pulsars), and is a correction factor to account for pulsars undetectable in standard pulse surveys. The VLA surveys show that there cannot be a large number of tight binaries and limit $\beta \lesssim 2$ (Johnston *et al.* 1991). It is interesting to note that KNR could *not* reproduce the young ages of the observed sample. This suggests that luminosity evolution may in fact be taking place, which implies an even higher birthrate and hence a substantial cluster pulsar population.

The Luminosity Function Method II. Fruchter & Goss (1990, henceforth FG) imaged 17 globular clusters with the VLA and detected pulsar-like emission (*i.e.*, steep spectrum emission close to the core) in five clusters. Assuming the standard luminosity function, $\gamma = 2$, $L_{min} = 3 \text{ mJy kpc}^2$ and $\alpha = 0.5$, they estimate $N_p \sim 500/\bar{f}(3/L_{min})$ to $2000/\bar{f}(3/L_{min})$.

The Luminosity Function Method III. Wijers & van Paradijs (1991; hereafter WvP) used the integrated flux from three globular clusters containing at least one detected pulsar to

constrain the underlying population. The basis of this powerful method is the statistic, $f_1 = L_1/L_t$, the ratio of the luminosity of the brightest (detected) pulsar to the integrated luminosity. The underlying pulsar population was assumed to be restricted to the same region of the $B-P$ diagram as in KNR; here B is the dipole field strength of pulsars. The use of the model luminosity law $L_m(P, \dot{P})$ (see §5.4.2) then specified L_{max} . The value of L_{min} was assumed to be 0.076 mJy kpc² at 1400 MHz, and 1 mJy kpc² (by a ν^{-2} extrapolation) at 400 MHz.

The method was applied to three clusters for which VLA data, at 1400 MHz were available (Terzan 5, NGC 6440 and NGC 6539). f_1 for two of these clusters is between 0.6 and 0.5 (after accounting for measurement errors). Recent observations (Fruchter & Goss 1992) reveal two pulsar-like source in Terzan 5, one in the core and the other outside the core (the famous eclipsing pulsar) and diffuse emission from the core region with steep spectrum and hence attributable to a sea of faint pulsars. f_1 for the whole cluster is $\lesssim 0.3$ and the f_1 for the core region alone is $\lesssim 0.4$.

For each cluster, the total luminosity of the cluster was fixed to the observed luminosity and pulsars drawn from a variety of luminosity functions, $dN/dL \propto L^{-\gamma}$. The luminosity function with $\gamma = 1.5$ gave the maximum number of pulsars satisfying the observed f_1 values. Assuming $\alpha = 0.5$, N_p (based on data excluding Terzan 5) was constrained to be less than $300/\bar{f}$ to $700/\bar{f}$, significantly less than the estimates of KNR and FG. Note that this estimate, as well as that of FG, is independent of β because it is based on imaging observations.

Thus estimates for N_p , the total number of pulsars in the cluster system vary widely: from the low estimate of $300/\bar{f}$ (WvP) to $2000/\bar{f}$ (PK and this work, §5.6) with KNR and FG (1990) in between at $\sim 1000/\bar{f}$. Some of this difference arises because not all methods are attempting to infer the same quantity. There are two questions one can ask:

- What is the number of active pulsars, N_p^a (pulsars above a minimum luminosity threshold)?
- What is the total number of pulsars produced in the cluster system so far, N_p^t ?

Some general comments are in order. WvP and FG are attempts to measure N_p^a , whereas the birthrate method yields N_p^t . To the extent that the statistical relations used to derive the KNR luminosity function ($L \propto f(P, \dot{P})$) are correct, then using the KNR luminosity function gives N_p^t ; this comment applies in particular to our two-dimensional scheme. Finally, $N_p^t > N_p^a$ which explains why the birthrate estimate and estimates using the KNR luminosity function are systematically larger than WvP.

The principal weakness of all luminosity methods is their sensitivity to the choice of L_{min} . Let us consider the case where the observed luminosity function arises due to luminosity decay in time. Then *a cutoff of L_{min} implies a cutoff in time*. For example, let the pulsar's luminosity decay as $L(t) = L_0 t_d (t + t_d)^{-\delta}$; t_d is the decay timescale, which we (arbitrarily) choose to be 10^7 y. This corresponds to a differential luminosity function $dN/dL \propto L^{-(1+\delta)/\delta} = L^{-\gamma}$. Then with $\delta = 1$ (or $\gamma = 2$), after 10^{10} y, the pulsar has decayed to 10^{-3} of its original luminosity. With $\delta = 1.5$ ($\gamma = 5/3$) the same pulsar would have decayed to a similar luminosity in only 10^9 y; with $\delta = 2$ ($\gamma = 3/2$), the pulsar is only 3×10^8 y old.

This means that if luminosity decay is taking place, then the figure of 300 pulsars that WvP estimate for the cluster population, using $\gamma = 3/2$ ($\delta = 2$), refers only to pulsars born in the last $\sim 3 \times 10^8$ y. This is illustrated in Table 5.4 where we show the results of a simulation in which pulsars were generated every τ_x y, subject to Poisson statistics between now ($t = 0$) and a Hubble time ($t = -10^{10}$ y). Each pulsar is born with a luminosity L_0 , and decays according to the decay law indicated in the first two columns. We have tabulated the values of f_1 and f_{12} , the ratio of the brightest pulsar to the total cluster flux, and of the brightest pulsar to the second brightest, for the 10th, 50th and 90th percentiles. The first section shows the result when we assume $L_{min} = 10^{-3} L_0$; the second is where we do not constrain L_{min} .

In order to satisfy the observed $f_1 \sim 0.4$ to 0.7, it can be seen that for $\gamma < 2$ luminosity functions, large values of N_p are indicated when the luminosity is allowed to decay with no lower threshold. Only for the $\gamma = 2$ luminosity law do we find the inferred N_p is the same in either case. If $\gamma < 2$ then the f_1 test shows that typically clusters cannot have more than 10–30 pulsars whereas for steeper luminosity laws the number of pulsars per cluster is large and somewhat unconstrained (30 to 300, depending on choice of L_{min}).

Because WvP wanted the probability that all three clusters simultaneously violate their quoted values of n_{psr} to be less than 0.023 (2σ), they chose a probability p for *each* cluster to be $p = 0.283$, corresponding to a level of 28% in Table 5.4. In order to satisfy the observed $f_1 \sim 0.5$ to 0.7, it can be seen that very small numbers of pulsars are required, if L_{min} is held fixed. However, if L_{min} is allowed to vary, then large numbers of pulsars are possible.

From Table 5.4, we can also conclude that the $\gamma = 2$ luminosity function is the only luminosity function for which $N_p^a \sim N_p^t$. For other choices ($\gamma < 2$), we find $N_p^a \ll N_p^t$. This explains the agreement between FG, KNR and our work.

It still remains to be understood why WvP and the other estimates do not agree on

N_p for the choice of $\gamma = 2$, our preferred luminosity function. This could be small number statistics or due to subtle selection effects. We believe that this arises because of a subtle selection effect that is present in the data used by WvP. The three clusters for which WvP had data were the three brightest pulsars in a sample which was already biased towards rich clusters (the FG survey). This introduces a major bias in the results. Our simulations show that the clusters with the highest total radio luminosity also tend to have the highest f_1 ratios, regardless of which luminosity function is being used. This means a more complete, unbiased sample is required in order for this potentially powerful technique to tell us about the underlying pulsar population. Clearly, these issues only highlight the importance of expanding the application of the powerful f_1 test from the current sample of 2 to a larger number.

In summary, the currently favored luminosity function, from a variety of evidence, is $dN/dL \propto L^{-2}$ and the choice of the weighting function is $\propto M_c \rho_c^{0.5}$. With this choice of luminosity function and weighting function, the inferred number of pulsars produced in the cluster system (active or otherwise) is $2000/\bar{f}$.

This dependence of N_p on ρ_c is purely phenomenological, containing no physics. What mechanism could cause this dependence to be less steep than the $\alpha = 1$ predicted by tidal capture theory? We suggest that the solution to this problem is three-body interactions (PK). Wide binaries can exist in low density clusters, and have large cross-sections for interaction there. However, in dense clusters such binaries are easily disrupted, and so the rates of interaction are lower. This weakens the dependence of pulsar formation on ρ_c . As shown above, our preferred solution is $N_p \propto \rho_c^{0.5}$. Note that we can also get a satisfactory fit by allowing $N_p \propto \rho_c M_c + C M_c$, where C is a free parameter. This function also reduces the steep dependence of N_p on ρ_c .

Note in Figure 5.5 that 47 Tuc is clearly anomalous, producing a large bunching of pulsars at one place. While the distribution is still consistent with being uniform, this may be a suggestion that our model is too simplistic. Since we know that globular clusters evolve considerably over their lifetime, it seems reasonable that the number of pulsars in a cluster is time dependent (corresponding to relaxing the assumption that T is constant in §5.2). Sigurdsson & Phinney (1991) suggest that during the onset of core-collapse, the pulsar formation rate is greatly accelerated. As the core starts to collapse, binaries are “burnt” in encounters, gradually hardening the binaries until the time-scale for interaction becomes very large or until an encounter ejects the binary from the core completely. At this stage core-collapse recommences, and further pulsar formation is unlikely. This model predicts that the number of pulsars in a cluster is strongly dependent on the past history

of the cluster, in particular the time since core collapse. Further evidence is suggested by clusters like Liller 1, a dense, core-collapsed cluster, whose integrated flux is very small (Johnston *et al.* 1991). In this model, Liller 1 would represent a cluster long past core collapse, whose pulsars have faded to lower luminosities.

Table 5.1. New observations**VLA observations**

| Cluster | $d(\text{kpc})$ | $r_c(\text{''})$ | $S_{1400}(\text{mJy}) (3\sigma)$ | $S_{430} (\text{mJy})^a$ |
|---------------|-----------------|------------------|----------------------------------|--------------------------|
| NGC 6325 | 6.2 | c | ≤ 0.28 | ≤ 6.3 |
| NGC 6333 = M9 | 7.5 | 16 | ≤ 0.25 | ≤ 5.6 |
| NGC 6355 | 7.1 | c | ≤ 0.33 | ≤ 7.4 |
| NGC 6517 | 6.1 | c? | 0.26 | 5.8 |
| NGC 6528 | 6.8 | 7 | ≤ 0.30 | ≤ 6.7 |
| NGC 6553 | 5.7 | 28 | ≤ 0.32 | ≤ 7.1 |
| NGC 6642 | 5.5 | c? | ≤ 0.28 | ≤ 6.3 |
| NGC 6712 | 6.2 | 40 | ≤ 0.26 | ≤ 5.8 |

Westerbork observations

| Cluster | $d(\text{kpc})$ | $r_c(\text{''})$ | $S_{610}(\text{mJy})(3\sigma)$ | $S_{430} (\text{mJy})^a$ |
|----------------|-----------------|------------------|--------------------------------|--------------------------|
| Pal 2 | 13.6 | 5 | ≤ 1.6 | ≤ 3.8 |
| NGC 4147 | 17.3 | 3 | ≤ 1.8 | ≤ 4.3 |
| NGC 5024 = M53 | 18.5 | 22 | ≤ 1.5 | ≤ 3.6 |
| NGC 5904 = M5 | 7.6 | 25 | ≤ 1.7 | ≤ 4.1 |
| NGC 6325 | 6.2 | c | ≤ 1.9 | ≤ 4.6 |
| NGC 6342 | 11.6 | c | ≤ 2.1 | ≤ 5.1 |
| NGC 6356 | 16.7 | 10 | ≤ 3.6 | ≤ 8.5 |
| NGC 6426 | 17.5 | 16 | ≤ 1.4 | ≤ 3.3 |
| NGC 6717 | 7.8 | c? | ≤ 1.6 | ≤ 3.8 |
| NGC 6779 | 9.8 | 32 | ≤ 1.3 | ≤ 3.0 |
| NGC 6934 | 14.9 | 16 | ≤ 1.5 | ≤ 3.5 |
| NGC 7089 = M2 | 11.9 | 18 | ≤ 3.3 | ≤ 8.0 |

^a Flux at 430 MHz, assuming a spectral index (ν^α) of $\alpha = -2.5$.

Table 5.2. Globular cluster parameters and search limits

| Cluster | IAU name | $\log(r_c/\text{pc})$ | $\log(\rho_c/\text{M}_\odot\text{pc}^{-3})$ | R_{gc}^a | d (kpc) | d (kpc) | $\log(M_t/\text{M}_\odot)$ | S_{430}^b (mJy) | Survey |
|----------|-------------|-----------------------|---|-------------------|--------------|--------------|----------------------------|----------------------|--------|
| NGC 104 | 0021-723 | -0.25 | 5.048 | 8.1 | 4.6 | 6.06 | 1.5 | P1 | |
| NGC 288 | 0050-268 | 0.45 | 2.049 | 12.1 | 8.2 | 4.45 | ... | ... | |
| NGC 362 | 0100-711 | -0.42 | 5.456 | 9.9 | 8.7 | 5.72 | ... | ... | |
| NGC 1261 | 0310-554 | 0.19 | 3.599 | 18.3 | 16.1 | 5.49 | ... | ... | |
| Pal 1 | 0325+794 | -0.23 | 2.739 | 20.3 | 13.7 | 3.43 | ... | ... | |
| AM 1 | 0354-498 | 1.05 | 0.325 | 117.9 | 116.4 | 4.23 | ... | ... | |
| Eridanus | 0422-213 | 0.81 | 0.493 | 90.2 | 84.7 | 4.06 | ... | ... | |
| Pal 2 | 0443+313 | -0.48 | 5.219 | 22.2 | 13.6 | 5.28 | 1.0 | A | |
| NGC 1851 | 0512-400 | -0.64 | 5.724 | 17.2 | 12.0 | 5.70 | 5.0 | P2 | |
| NGC 1904 | 0522-245 | -0.30 | 4.747 | 19.5 | 13.0 | 5.50 | 10.8 | J1 | |
| NGC 2298 | 0647-359 | 0.01 | 3.463 | 16.2 | 10.6 | 4.87 | ... | ... | |
| NGC 2419 | 0734+390 | 1.00 | 1.664 | 99.4 | 91.4 | 6.09 | ... | ... | |
| NGC 2808 | 0911-646 | -0.19 | 5.134 | 11.6 | 9.5 | 6.15 | ... | ... | |
| Pal 3 | 1003+003 | 1.08 | -0.303 | 91.5 | 87.9 | 4.25 | 2.4 | A | |
| NGC 3201 | 1015-461 | 0.18 | 3.422 | 9.5 | 5.0 | 5.26 | ... | ... | |
| Pal 4 | 1126+292 | 1.36 | -0.245 | 96.2 | 93.3 | 4.69 | ... | ... | |
| NGC 4147 | 1207+188 | -0.58 | 4.459 | 19.9 | 17.3 | 4.77 | 4.3 | W | |
| NGC 4372 | 1223-724 | 0.38 | 2.636 | 7.6 | 4.9 | 4.89 | ... | ... | |
| NGC 4590 | 1236-264 | 0.27 | 2.860 | 10.1 | 9.6 | 5.10 | 7.0 | J2 | |
| NGC 4833 | 1256-706 | 0.30 | 3.447 | 7.4 | 5.8 | 5.47 | ... | ... | |
| NGC 5024 | 1310+184 | 0.30 | 3.515 | 19.2 | 18.5 | 5.86 | 0.7 | A | |
| NGC 5053 | 1313+179 | 0.98 | 1.019 | 16.7 | 15.8 | 4.84 | ... | ... | |
| NGC 5139 | 1323-472 | 0.65 | 2.702 | 7.0 | 5.2 | 6.16 | ... | ... | |
| NGC 5272 | 1339+286 | 0.20 | 3.718 | 12.6 | 10.4 | 5.94 | 0.7 | A | |
| NGC 5286 | 1343-511 | -0.18 | 4.627 | 7.7 | 9.7 | 5.67 | ... | ... | |
| NGC 5466 | 1403+287 | 0.98 | 1.001 | 16.4 | 15.8 | 5.08 | 2.0 | A | |
| NGC 5634 | 1427-057 | 0.18 | 4.163 | 20.7 | 25.0 | 6.15 | 7.0 | J2 | |
| NGC 5694 | 1436-263 | -0.22 | 4.911 | 25.4 | 31.3 | 5.83 | 8.0 | J2 | |
| NGC 5824 | 1500-328 | -0.42 | 4.990 | 18.0 | 24.6 | 5.76 | 30.0 | J2 | |
| Pal 5 | 1513+000 | 1.22 | -0.431 | 16.5 | 21.4 | 4.41 | ... | ... | |
| NGC 5897 | 1514-208 | 0.66 | 2.015 | 6.7 | 11.8 | 5.18 | ... | ... | |
| NGC 5904 | 1516+022 | -0.03 | 4.697 | 6.6 | 7.6 | 5.91 | 0.5 | A | |
| NGC 5927 | 1524-505 | 0.03 | 4.083 | 5.1 | 8.8 | 5.61 | ... | ... | |
| NGC 5946 | 1531-504 | -2.35 | 9.493 | 5.1 | 9.2 | 5.32 | ... | ... | |
| NGC 5986 | 1542-376 | 0.21 | 3.795 | 4.7 | 10.5 | 5.67 | ... | ... | |
| Pal 14 | 1608+150 | 1.16 | 0.031 | 69.9 | 75.3 | 4.33 | 2.0 | A | |
| NGC 6093 | 1614-228 | -0.61 | 5.678 | 3.1 | 8.0 | 5.54 | 19.0 | J2 | |
| NGC 6101 | 1620-720 | 0.79 | 1.634 | 11.6 | 16.1 | 4.88 | ... | ... | |
| NGC 6121 | 1620-264 | -0.24 | 4.373 | 6.8 | 2.1 | 5.15 | 3.7 | V4 | |
| NGC 6139 | 1624-387 | -0.31 | 4.869 | 2.9 | 8.1 | 5.49 | ... | ... | |
| NGC 6144 | 1624-259 | 0.41 | 2.646 | 2.9 | 9.5 | 5.14 | ... | ... | |
| NGC 6171 | 1629-129 | 0.08 | 3.459 | 3.9 | 6.2 | 5.13 | 9.0 | J2 | |
| NGC 6205 | 1635+365 | 0.19 | 3.975 | 8.9 | 7.1 | 5.82 | 2.0 | A | |
| NGC 6218 | 1644-018 | -0.19 | 4.457 | 5.0 | 5.3 | 5.39 | 9.0 | J2 | |

Table 5.2. — *Continued*

| Cluster | IAU name | $\log(r_c/\text{pc})$ | $\log(\rho_c/\text{M}_\odot\text{pc}^{-3})$ | R_{gc} | d (kpc) | $\log(M_t/\text{M}_\odot)$ | S_{430} (mJy) | Survey |
|----------|-------------|-----------------------|---|-----------------|--------------|----------------------------|--------------------|--------|
| NGC 6229 | 1645+476 | 0.19 | 3.800 | 30.9 | 31.6 | 5.67 | 30.0 | J2 |
| NGC 6235 | 1650-220 | 0.06 | 3.711 | 2.3 | 9.5 | 4.77 | 30.0 | J2 |
| NGC 6254 | 1654-040 | 0.04 | 3.837 | 5.3 | 4.5 | 5.39 | 9.0 | J2 |
| NGC 6256 | 1656-370 | -2.36 | 8.548 | 2.0 | 9.1 | 4.36 | ... | ... |
| Pal 15 | 1657-004 | 1.38 | -0.166 | 62.3 | 69.7 | 4.58 | ... | ... |
| NGC 6266 | 1658-300 | -0.48 | 5.702 | 3.0 | 6.1 | 5.84 | 14.0 | P2 |
| NGC 6273 | 1659-262 | 0.11 | 4.418 | 2.5 | 10.6 | 6.22 | 14.0 | P2 |
| NGC 6284 | 1701-246 | -2.30 | 9.236 | 2.2 | 10.3 | 5.21 | 7.0 | J2 |
| NGC 6287 | 1702-226 | -0.26 | 4.364 | 2.2 | 7.2 | 5.03 | 7.0 | J2 |
| NGC 6293 | 1707-265 | -2.43 | 9.635 | 1.6 | 7.7 | 5.23 | 14.0 | P2 |
| NGC 6304 | 1711-294 | -0.39 | 4.813 | 2.9 | 6.0 | 5.23 | 32.0 | J2 |
| NGC 6316 | 1713-280 | -0.21 | 4.826 | 4.2 | 12.8 | 5.78 | 9.0 | J2 |
| NGC 6325 | 1714-237 | -2.52 | 9.518 | 2.8 | 6.2 | 4.83 | 4.6 | W |
| NGC 6333 | 1716-184 | -0.24 | 4.761 | 2.2 | 7.5 | 5.48 | 5.6 | V5 |
| NGC 6341 | 1715+432 | -0.53 | 5.700 | 9.8 | 7.7 | 5.62 | 1.7 | V4 |
| NGC 6342 | 1718-195 | -2.25 | 9.141 | 3.4 | 11.6 | 5.27 | 5.1 | W |
| NGC 6352 | 1721-484 | 0.21 | 3.278 | 3.4 | 6.6 | 5.02 | ... | ... |
| Ter 2 | 1724-307 | -2.31 | 8.435 | 1.4 | 10.0 | 4.37 | 40.0 | J2 |
| NGC 6355 | 1720-263 | -2.46 | 9.841 | 1.8 | 7.1 | 5.33 | 7.4 | V5 |
| NGC 6356 | 1720-177 | -0.09 | 4.679 | 8.3 | 16.7 | 5.98 | 8.5 | W |
| NGC 6362 | 1726-670 | 0.47 | 2.491 | 5.5 | 7.7 | 5.10 | ... | - |
| NGC 6366 | 1725-050 | 0.39 | 1.653 | 5.4 | 4.0 | 4.19 | 12.0 | J1 |
| HP 1 | 1727-299 | -2.34 | 9.292 | 0.9 | 9.5 | 5.16 | 14.0 | P2 |
| Liller 1 | 1730-333 | -2.42 | 11.045 | 1.2 | 7.9 | 5.58 | 4.0 | V3 |
| NGC 6380 | 1731-390 | -2.71 | 9.819 | 5.0 | 4.0 | 4.56 | 9.0 | V1 |
| Ter 1 | 1732-304 | -2.29 | 8.029 | 1.9 | 10.6 | 4.04 | ... | ... |
| NGC 6388 | 1732-447 | -0.38 | 5.938 | 5.6 | 13.5 | 6.40 | ... | ... |
| Ton 2 | 1733-390 | 0.13 | 2.930 | 1.5 | 8.7 | 4.56 | ... | ... |
| NGC 6397 | 1736-536 | -2.97 | 10.808 | 6.9 | 2.2 | 4.77 | ... | ... |
| NGC 6401 | 1735-238 | -0.31 | 4.475 | 1.8 | 7.1 | 5.19 | ... | ... |
| NGC 6402 | 1735-032 | 0.39 | 3.511 | 4.5 | 10.2 | 6.13 | 23.0 | V2 |
| NGC 6426 | 1742+031 | 0.13 | 3.271 | 11.1 | 17.5 | 5.16 | 1.0 | A |
| Ter 5 | 1745-247 | -0.37 | 5.875 | 1.8 | 7.1 | 5.00 | 12.0 | P2 |
| NGC 6440 | 1746-203 | -0.61 | 5.887 | 2.1 | 7.1 | 5.88 | 14.0 | P2 |
| NGC 6441 | 1746-370 | -0.40 | 5.833 | 3.3 | 11.7 | 6.22 | 14.0 | P2 |
| Ter 6 | 1747-312 | -2.21 | 8.703 | 4.0 | 12.8 | 4.96 | 25.0 | J1 |
| NGC 6453 | 1748-346 | -2.29 | 9.297 | 2.1 | 10.7 | 5.32 | ... | ... |
| NGC 6496 | 1755-442 | 0.28 | 2.725 | 3.2 | 6.3 | 4.33 | ... | ... |
| Ter 9 | 1758-268 | -2.47 | 8.430 | 1.9 | 7.0 | 3.90 | 40.0 | J2 |
| NGC 6517 | 1759-089 | -2.53 | 9.869 | 3.8 | 6.1 | 5.16 | 5.8 | V5 |
| NGC 6522 | 1800-300 | -2.49 | 9.886 | 2.3 | 6.6 | 5.28 | 14.0 | P2 |
| NGC 6528 | 1801-300 | -0.63 | 5.390 | 2.1 | 6.8 | 5.07 | 6.7 | V5 |
| NGC 6535 | 1801-003 | -0.08 | 2.883 | 4.3 | 6.9 | 4.27 | 7.0 | J2 |
| NGC 6539 | 1802-075 | -0.32 | 4.402 | 6.0 | 3.1 | 4.87 | 14.0 | P2 |
| NGC 6541 | 1804-437 | -0.22 | 4.498 | 2.8 | 7.0 | 5.58 | 13.4 | V1 |

Table 5.2. — *Continued*

| Cluster | IAU name | $\log(r_c/\text{pc})$ | $\log(\rho_c/\text{M}_\odot \text{pc}^{-3})$ | R_{gc} | d | S_{430} | Survey |
|----------|----------|-----------------------|--|-----------------|-------|----------------------------|--------|
| | | | | (kpc) | (kpc) | $\log(M_t/\text{M}_\odot)$ | |
| NGC 6544 | 1804-250 | -2.90 | 10.870 | 6.2 | 2.6 | 5.05 | 14.0 |
| NGC 6553 | 1806-259 | -0.11 | 4.609 | 3.2 | 5.7 | 5.72 | 7.1 |
| NGC 6558 | 1807-317 | -2.37 | 9.111 | 0.9 | 8.8 | 4.88 | ... |
| Ter 11 | 1809-227 | 0.76 | 1.568 | 15.1 | 23.7 | 4.60 | ... |
| NGC 6569 | 1810-318 | -0.07 | 4.361 | 1.0 | 8.9 | 5.48 | 30.0 |
| NGC 6584 | 1814-522 | 0.41 | 3.062 | 7.8 | 15.0 | 5.49 | ... |
| NGC 6624 | 1820-303 | -2.41 | 9.656 | 1.5 | 8.0 | 5.30 | 5.0 |
| NGC 6626 | 1821-249 | -0.50 | 5.547 | 3.2 | 5.8 | 5.62 | 3.4 |
| NGC 6637 | 1828-323 | -0.05 | 4.278 | 2.3 | 10.3 | 5.56 | 30.0 |
| NGC 6638 | 1827-255 | -0.39 | 4.901 | 2.5 | 6.7 | 5.08 | 15.0 |
| NGC 6642 | 1828-235 | -2.57 | 9.494 | 3.6 | 5.5 | 4.65 | 6.3 |
| NGC 6652 | 1832-330 | -0.46 | 5.077 | 6.0 | 14.3 | 5.44 | 15.0 |
| NGC 6656 | 1833-239 | -0.02 | 4.283 | 5.8 | 3.1 | 5.79 | 3.6 |
| Pal 8 | 1838-198 | 0.63 | 1.873 | 19.8 | 28.1 | 5.15 | 16.0 |
| NGC 6681 | 1840-323 | -2.35 | 9.389 | 2.1 | 9.3 | 5.23 | 16.0 |
| NGC 6712 | 1850-087 | 0.08 | 3.900 | 4.2 | 6.2 | 5.26 | 5.8 |
| NGC 6715 | 1851-305 | -0.18 | 5.122 | 13.2 | 21.5 | 6.19 | ... |
| NGC 6717 | 1852-227 | -2.42 | 9.229 | 2.6 | 7.8 | 4.84 | 3.8 |
| NGC 6723 | 1856-367 | 0.20 | 3.498 | 2.7 | 9.2 | 5.41 | ... |
| NGC 6749 | 1902+017 | 0.69 | 2.019 | 7.7 | 12.8 | 4.91 | 2.0 |
| NGC 6752 | 1906-600 | -2.70 | 10.556 | 5.9 | 4.1 | 5.33 | ... |
| NGC 6760 | 1908+009 | -0.20 | 4.248 | 6.0 | 4.1 | 5.08 | 2.5 |
| Ter 7 | 1914-347 | 0.85 | 1.519 | 28.4 | 36.4 | 4.81 | 40.0 |
| NGC 6779 | 1914+300 | 0.18 | 3.375 | 9.8 | 9.8 | 5.28 | 2.0 |
| Pal 10 | 1916+184 | 0.36 | 2.441 | 8.7 | 10.6 | 4.65 | 40.0 |
| Arp 2 | 1925-304 | 1.14 | 0.065 | 20.4 | 28.3 | 4.53 | ... |
| NGC 6809 | 1936-310 | 0.39 | 2.978 | 4.7 | 5.1 | 5.35 | 7.0 |
| Pal 11 | 1942-081 | 0.43 | 1.541 | 8.3 | 13.8 | 3.63 | 40.0 |
| NGC 6838 | 1951+186 | -0.02 | 3.669 | 7.4 | 4.4 | 4.98 | 19.0 |
| NGC 6864 | 2003-220 | -0.35 | 5.128 | 12.0 | 18.5 | 5.70 | 12.0 |
| NGC 6934 | 2031+072 | 0.06 | 3.997 | 12.1 | 14.9 | 5.61 | 1.0 |
| NGC 6981 | 2050-127 | 0.42 | 2.528 | 12.7 | 17.0 | 5.15 | 7.0 |
| NGC 7006 | 2059+160 | 0.58 | 2.343 | 36.3 | 39.1 | 5.39 | 40.0 |
| NGC 7078 | 2127+119 | -2.33 | 10.054 | 10.4 | 9.7 | 5.95 | 0.5 |
| NGC 7089 | 2130-010 | 0.01 | 4.530 | 10.9 | 11.9 | 6.00 | 3.0 |
| NGC 7099 | 2137-234 | -2.46 | 9.673 | 7.2 | 7.2 | 5.18 | 19.0 |
| Pal 12 | 2143-214 | 0.47 | 1.366 | 16.0 | 19.4 | 4.04 | ... |
| Pal 13 | 2304+124 | 0.42 | 0.768 | 25.7 | 24.4 | 3.09 | ... |
| NGC 7492 | 2305-159 | 0.67 | 1.257 | 18.7 | 19.1 | 4.31 | 40.0 |

Table 5.4 — Cluster parameters used in determining the statistics of the cluster pulsar population. The columns show the cluster name and IAU designation, the logarithm of the core radius (in pc), the logarithm of the core density (in $\text{M}_\odot \text{pc}^{-3}$), the distance from the Galactic centre (in kpc), the distance from the sun (in kpc), the total mass (in M_\odot)

(from Chernoff & Djorgovski (1989), Djorgovski, *pers. comm.*). The last two columns show the minimum flux density surveyed at 430 MHz, transformed assuming a spectral index (ν^α) of $\alpha = -2.5$ when the observing frequency was not 430 MHz, and the survey which attained this limit. The letter indicates the telescope used in the survey (A=Arecibo, G=Greenbank, J=Jodrell Bank, P=Parkes, V=VLA, W=Westerbork) and the number indicates the reference:

| | |
|---|--------------------------------------|
| A — Kulkarni <i>et al.</i> 1992, pers. comm. | V1 — Fruchter & Goss 1990 |
| G — Backer, D.C. & Dey, A. 1988 | V2 — Hamilton, Helfand & Becker 1985 |
| J1 — Biggs, Lyne & Brinklow 1989 | V3 — Johnston, Kulkarni & Goss 1991 |
| J2 — Lyne & Biggs 1989, pers. comm. | V4 — Kulkarni <i>et al.</i> 1990 |
| P1 — Manchester <i>et al.</i> 1991 | V5 — This work |
| P2 — Manchester <i>et al.</i> 1991, pers. comm. | W — This work |

Table 5.3. Pulsar fluxes

| Cluster | <i>d</i> (kpc) | Pulsar | <i>S</i> ₄₃₀ (mJy) | Reference |
|------------------|----------------|----------|-------------------------------|-------------------------------|
| NGC 104 = 47 Tuc | 4.6 | 0021-72C | 8.6 | Manchester <i>et al.</i> 1990 |
| | | 0021-72D | 3.4 | Manchester <i>et al.</i> 1991 |
| | | 0021-72E | 3.2 | ” ” |
| | | 0021-72F | 2.5 | ” ” |
| | | 0021-72G | 1.6 | ” ” |
| | | 0021-72H | 2.3 | ” ” |
| | | 0021-72I | 2.6 | ” ” |
| | | 0021-72J | 2.9 | ” ” |
| | | 0021-72L | 1.8 | ” ” |
| NGC 5024 = M53 | 18.5 | 1310+18 | 1.0 | Kulkarni <i>et al.</i> 1991 |
| NGC 5904 = M5 | 7.6 | 1516+02A | 1.0 | Wolszczan <i>et al.</i> 1989 |
| | | 1516+02B | 0.5 | ” ” |
| NGC 6121 = M4 | 2.1 | 1620-26 | 15.0 | Lyne <i>et al.</i> 1988 |
| NGC 6205 = M13 | 7.1 | 1639+36A | 3.0 | Kulkarni <i>et al.</i> 1991 |
| | | 1639+36B | 2.0 | Anderson <i>et al.</i> 1992 |
| Ter 5 | 7.1 | 1744-24A | 12.0 | Lyne <i>et al.</i> 1990 |
| NGC 6440 | 7.1 | 1745-20 | 25.0 | Manchester <i>et al.</i> 1989 |
| NGC 6539 | 6.0 | 1802-07 | 18.0 | D'Amico <i>et al.</i> 1990 |
| NGC 6624 | 8.0 | 1820-30A | 5.0 | Biggs <i>et al.</i> 1990 |
| | | 1820-30B | 6.0 | ” ” |
| NGC 6626 = M28 | 5.8 | 1821-24 | 27.0 | Foster <i>et al.</i> 1991 |
| NGC 6760 | 4.1 | 1908+00 | 10.0 | Anderson <i>et al.</i> 1990b |
| NGC 7078 = M15 | 9.7 | 2127+11A | 2.0 | Wolszczan <i>et al.</i> 1989 |
| | | 2127+11B | 0.7 | Anderson <i>et al.</i> 1990a |
| | | 2127+11C | 1.0 | Prince <i>et al.</i> 1991 |
| | | 2127+11D | 0.6 | ” ” |
| | | 2127+11E | 0.5 | ” ” |

Table 5.3 — Fluxes of the detected cluster pulsars. The columns show the cluster name and distance (in kpc), then the pulsar name, mean flux at 430 MHz (in mJy), and the reference. For the 47 Tuc pulsars, whose fluxes at detection are dominated by scintillation, we have taken $S = S_{lim} / \ln(N_{obs}/N_{det})$ (see §4.1), where S_{lim} is the detection limit of the 610 MHz system (Manchester *et al.* 1991), $S_{lim} = 2.5$ mJy (6 mJy at 430 MHz, for $\nu^{-2.5}$), $N_{obs} = 80$ and N_{det} from Table 1 of Manchester *et al.* PSR0021-72K has since been found to be a harmonic of PSR0021-72D and thus has not been included in this list.

Table 5.4. Luminosity function simulations

| Decay dN/dL law | | τ_x (10^7 y) | $L_{min} = 10^{-3}L_0$ | | | | | | L_{min} free | | | | | | | | |
|----------------------|----------|-------------------------|------------------------|-----|-----|----------|-----|------|----------------|-------|-----|-----|----------|-----|------|-----------|-----|
| | | | f_1 | | | f_{12} | | | n_{psr} | f_1 | | | f_{12} | | | n_{psr} | |
| t^{-1} | L^{-2} | 3.3 | 0.1 | 0.2 | 0.3 | 1.0 | 1.5 | 3.9 | 300 | 0.1 | 0.2 | 0.3 | 1.0 | 1.8 | 4.6 | 300 | |
| | | 10 | 0.1 | 0.2 | 0.5 | 1.1 | 2.0 | 5.8 | 100 | 0.1 | 0.2 | 0.5 | 1.1 | 1.9 | 6.4 | 100 | |
| | | 33 | 0.1 | 0.3 | 0.7 | 1.1 | 2.0 | 9.4 | 30 | 0.1 | 0.3 | 0.7 | 1.1 | 1.9 | 11.8 | 30 | |
| | | — | 0.2 | 0.4 | 0.7 | 1.1 | 2.0 | 10.1 | 10 | 0.2 | 0.4 | 0.7 | 1.1 | 2.1 | 8.0 | 10 | |
| $t^{-1.5}$ | | $L^{-5/3}$ | 3.3 | 0.2 | 0.5 | 0.7 | 1.0 | 1.0 | 1.0 | 30 | 0.2 | 0.4 | 0.7 | 1.0 | 2.3 | 10.7 | 300 |
| | | 10 | 0.3 | 0.5 | 0.9 | 1.0 | 1.0 | 1.0 | 10 | 0.2 | 0.5 | 0.8 | 1.2 | 2.7 | 17.7 | 100 | |
| | | 33 | 0.4 | 0.7 | 1.0 | 1.0 | 1.1 | 1.3 | 3 | 0.2 | 0.5 | 0.9 | 1.2 | 2.7 | 48.9 | 30 | |
| | | — | * | 0.7 | 1.0 | 1.1 | — | — | 1 | 0.3 | 0.5 | 0.9 | 1.1 | 3.0 | 24.0 | 10 | |
| t^{-2} | | $L^{-3/2}$ | 3.3 | 0.3 | 0.6 | 0.9 | 1.0 | 1.0 | 1.0 | 10 | 0.3 | 0.6 | 0.9 | 1.0 | 3.3 | 26.7 | 300 |
| | | 10 | 0.4 | 0.8 | 1.0 | 1.0 | 1.0 | — | 3 | 0.3 | 0.6 | 1.0 | 1.2 | 3.9 | 50.9 | 100 | |
| | | 33 | * | 0.7 | 1.0 | 1.0 | — | — | 1 | 0.3 | 0.6 | 1.0 | 1.2 | 3.8 | 190. | 30 | |
| | | — | * | * | 1.0 | — | — | — | 0.3 | 0.3 | 0.6 | 1.0 | 1.2 | 4.3 | 70.1 | 10 | |
| e^{-t/t_d} | | L^{-1} | 3.3 | * | 0.9 | 1.0 | — | — | — | 2 | 0.5 | 0.9 | 1.0 | 1.0 | 7.4 | — | 300 |
| | | 10 | * | 0.4 | 1.0 | — | — | — | 0.7 | * | 1.0 | 1.0 | 2.7 | — | — | 100 | |
| | | 33 | * | * | 1.0 | — | — | — | 0.2 | * | * | 1.0 | 403 | — | — | 30 | |

* Total integrated flux from cluster too small

— $f_{12} > 100$

Table 8.4 — Table showing the results of Monte Carlo simulations of a pulsar population with a luminosity decay law $L(t) = L_0 t_d (t + t_d)^{-\delta}$, which corresponds to a luminosity function $dN/dL \propto L^{-(1+\delta)/\delta} = L^{-\gamma}$. Columns 1 and 2 show the time decay/luminosity decay law; col. 3 the mean time between births (in units of 10^7 y). We tabulate f_1 , the ratio of the flux of the brightest pulsar to the total flux, f_{12} , the ratio of the flux of the brightest pulsar to the second brightest, and n_{psr} , the total number of pulsars generated. The first set of columns show the 10th, 50th and 90th percentiles of these values, fixing the minimum luminosity L_{min} to be 0.1% of L_0 ; the second set shows the results when we do not constrain L_{min} .

References

Anderson, B. & Lyne, A.G. 1983, *Nature*, 303, 597

Anderson, S., Gorham, P., Kulkarni, S.R., Prince, T. & Wolszczan, A. 1990a
Nature 346 42

Anderson, S., Kulkarni, S.R., Prince, T. & Wolszczan, A. 1990b, *IAU Circ.* #5013

Anderson, S., Kulkarni, S.R., Prince, T. & Wolszczan, A. 1991, *pers. comm*

Backer, D.C. & Dey, A. 1988, *Adv. Space Res.*, 8, 353

Biggs, J.D., Lyne, A.G. & Brinklow, A. 1989, in *Timing Neutron Stars*, eds. H. Ögelman, E.J.P. van den Heuvel, Kluwel, p. 157-162

Biggs, J.D., Lyne, A.G., Manchester, R.N. & Ashworth, M. 1990, *IAU Circ.* #4988

Chernoff, D.F. & Djorgovski, S.G. 1989, *ApJ*, 339, 904

Chernoff, D.F., Kochanek, C.S. & Shapiro, S.L. 1986, *ApJ*, 309, 183

Chernoff, D.F. & Weinberg, M.D. 1990, *ApJ*, 351, 121

D'Amico, N., Lyne, A.G., Bailes, M., Johnston, S., Manchester, R.N., Staveley-Smith, L., Lim, J., Fruchter, A.S. & Goss, W.M. 1990, *IAU Circ.* #5013

Dewey, R.J., Taylor, J.H., Weisberg, J.M. & Stokes, G.H. 1985, *ApJ*, 294, L25

Elson, R.A.W., Fall, S.M. & Freeman, K.C. 1989, *ApJ*, 336, 734

Fabian, A.C., Pringle, J.E. & Rees, M.J. 1975, *MNRAS*, 172, 15p

Foster, R.S., Backer, D.C., Taylor, J.H. & Goss, W.M. 1988, *ApJ*, 326, L13

Foster, R.S., Fairhead, L. & Backer, D.C. 1991, *ApJ*, 378, 687

Fruchter, A.S. & Goss, W.M. 1990, *ApJ*, 365, L63

Fruchter, A.S. & Goss, W.M. 1992, in *X-ray binaries and the formation of binary and millisecond pulsars*, ed. E.P.J. van den Heuvel & S.A. Rappaport, Kluwer, in press

Hamilton, T.T., Helfand, D.J. & Becker, R.H. 1985, *AJ*, 90, 606

Hills, 1975, *AJ*, 80, 809

Johnston, H.M., Kulkarni, S.R. & Goss, W.M. 1991, *ApJ*, 382, L89

King, I.R. 1966, *AJ*, 71, 64

Kulkarni, S.R. 1986, *ApJ*, 306, L85

Kulkarni, S.R., Anderson, S.B., Prince, T.A. & Wolszczan, A. 1991, *Nature*, 349, 47

Kulkarni, S.R., Goss, W.M., Wolszczan, A. & Middleditch, J. 1990, *ApJ*, 363, L5

Kulkarni, S.R., Narayan, R. & Romani, R.W. 1990, *ApJ*, 356, 174 (KNR)

Lee, H.M. & Ostriker, J.P. 1986, *ApJ*, 310, 176

Lyne, A.G. & Biggs, J.D. 1989, *pers. comm*

Lyne, A.G., Biggs, J.D., Brinklow, A., Ashworth, M. & McKenna, J. 1988, *Nature*, 332, 45

Lyne, A.G., Manchester, R.N., D'Amico, N., Stavely-Smith, L., Johnston, S., Lim, J., Fruchter, A.S., Goss, W.M. & Frail, D. 1990, *Nature*, 347, 650

Manchester, R.N., Lyne, A.G., Johnston, S., D'Amico, N., Lim, J. & Kniffen, D.A. 1990, *Nature*, 345, 598

Manchester, R.N., Lyne, A.G., Johnston, S., D'Amico, N., Lim, J., Kniffen, D.A., Fruchter, A.S. & Goss, W.M. 1989, *IAU Circ.* #4905

Manchester, R.N., Lyne, A.G., Robinson, C., D'Amico, N., Bailes, M. & Lim, J. 1991, *Nature*, 352, 219

Manchester, R.N. & Taylor, J.H. 1977, *Pulsars* (San Francisco: W.H. Freeman)

Mateo, M. 1988, *ApJ*, 331, 261

McClure, R.D., Vandenburg, D.A., Smith, G.H., Fahlman, G.G., Richer, H.B., Hesser, J.E., Harris, W.E., Stetson, P.B. & Bell, R.A. 1986, *ApJ*, 307, L49

McKenna, J. & Lyne, A.G. 1988, *Nature*, 336, 226

Narayan, R. & Ostriker, J.P. 1990, *ApJ*, 352, 222

Phinney, E.S. 1992, *MNRAS*, submitted

Phinney, E.S. & Kulkarni, S.R. 1992, *Nature*, submitted (PK)

Press, W. H., Flannery, B. P., Teukolsky, S. A., Vetterling, W. T., 1986, *Numerical Recipes* (Cambridge: Cambridge University Press)

Prince, T., Anderson, S.B., Kulkarni, S.R. & Wolszczan, A. 1991, *ApJ*, 374, L41

Proszynski, M. & Przybicien, D. 1984, in *Millisecond Pulsars*, ed. S.P. Reynolds & D.R. Stinebring (Green Bank: NRAO), p. 151

Pryor, C., McClure, R.D., Hesser, J.E. & Fletcher, J.M. 1989, in Dynamics of Dense Stellar Systems, ed. D. Merritt (Cambridge University Press: Cambridge), p. 175

Rappaport, S., Putney, A. & Verbunt, F. 1989, *ApJ*, 345, 210

Richtler, T., de Boer, K.S. & Sagar, R. 1991, *Messenger*, 64, 50

Rickett, B.J. 1977, *ARA&A*, 15, 479

Robinson, C., Lyne, A.G., Bailes, M., Biggs, J.D., Manchester, R. & D'Amico, N. 1992, in X-ray binaries and the formation of binary and millisecond pulsars, ed. E.P.J. van den Heuvel & S.A. Rappaport, Kluwer, in press

Sigurdsson, S. & Phinney, E.S. 1992, in prep

Verbunt, F. & Hut, P. 1987, in The Origin and Evolution of Neutron Stars, IAU Symp. No. 125, eds. D.J. Helfand, J.-H. Huang, Reidel, Dordrecht, p. 187

Wijers, R.A.M.J. & van Paradijs, J. 1991, *A&A*, 241, L37

Wolszczan, A., Kulkarni, S.R., Middleditch, J., Backer, D.C., Fruchter, A.S. & Dewey, R.J. 1989, *Nature*, 337, 531

Figure captions

Figure 5.1 — VLA radio map of NGC 6517. The inner $240'' \times 240''$ is plotted, with contour levels at $-3, 2.5, 3, 4, 5$ and 8 times $87.8 \mu\text{Jy, beam}^{-1}$ (the rms level of the map). The position plotted is the position of the optical core from Shawl & White (1986).

Figure 5.2 — Histogram of the luminosities of all cluster pulsars. The units of luminosity are mJy kpc^2 .

Figure 5.3 — Luminosity as a function of spin down age for disk and cluster recycled pulsars: cluster pulsars are shown as open boxes.

Figure 5.4 — Diagram illustrating the statistical testing of our choice of luminosity function. The solid line is the KNR luminosity function (in integral form), the dashed line a $\gamma = 1.5$ power-law, with $L_{\min} = 1 \text{ mJy kpc}^2$ for both. The filled squares on the x -axis represent the five M15 pulsars (Table 5.3), and the vertical line represents the luminosity limit of the Arecibo survey. If our choice of luminosity function is right, the points on the y -axis will be uniformly distributed. See §5.1.

Figure 5.5 — Two-dimensional version of the Verbunt and Hut (1987) diagram, for determining the luminosity function and density weighting of cluster pulsars, from PK. The assumed luminosity function (from KNR) is plotted at the top of each figure. The boxes represent the clusters, ordered by density (densest clusters at the top), where the width of each box is proportional to the predicted number of pulsars $N_p = M_c \rho_c^\alpha$, and the length is proportional to the fraction of all pulsars that would have been found, calculated from the flux limit of each survey using the luminosity function. The known cluster pulsars are shown as crosses. The strips at the bottom of each figure test the luminosity function, and to the right the density weighting function. The first strip in each group represents our preferred weighting scheme; the others are shown for comparison. The cluster with the longest box is M4, where the deep VLA images by Kulkarni *et al.* (1990) reached a flux limit of $24 \mu\text{Jy}$, which corresponds at the distance of M4 (2.1 kpc) to a luminosity of 0.41 mJy kpc^2 , only slightly above the assumed minimum luminosity of 0.1 mJy kpc^2 . The box extends past the plotted edge of the diagram to 0.45, *i.e.*, 45% of all pulsars in this luminosity function would have been seen in M4 by a survey this deep.

Figure 5.1

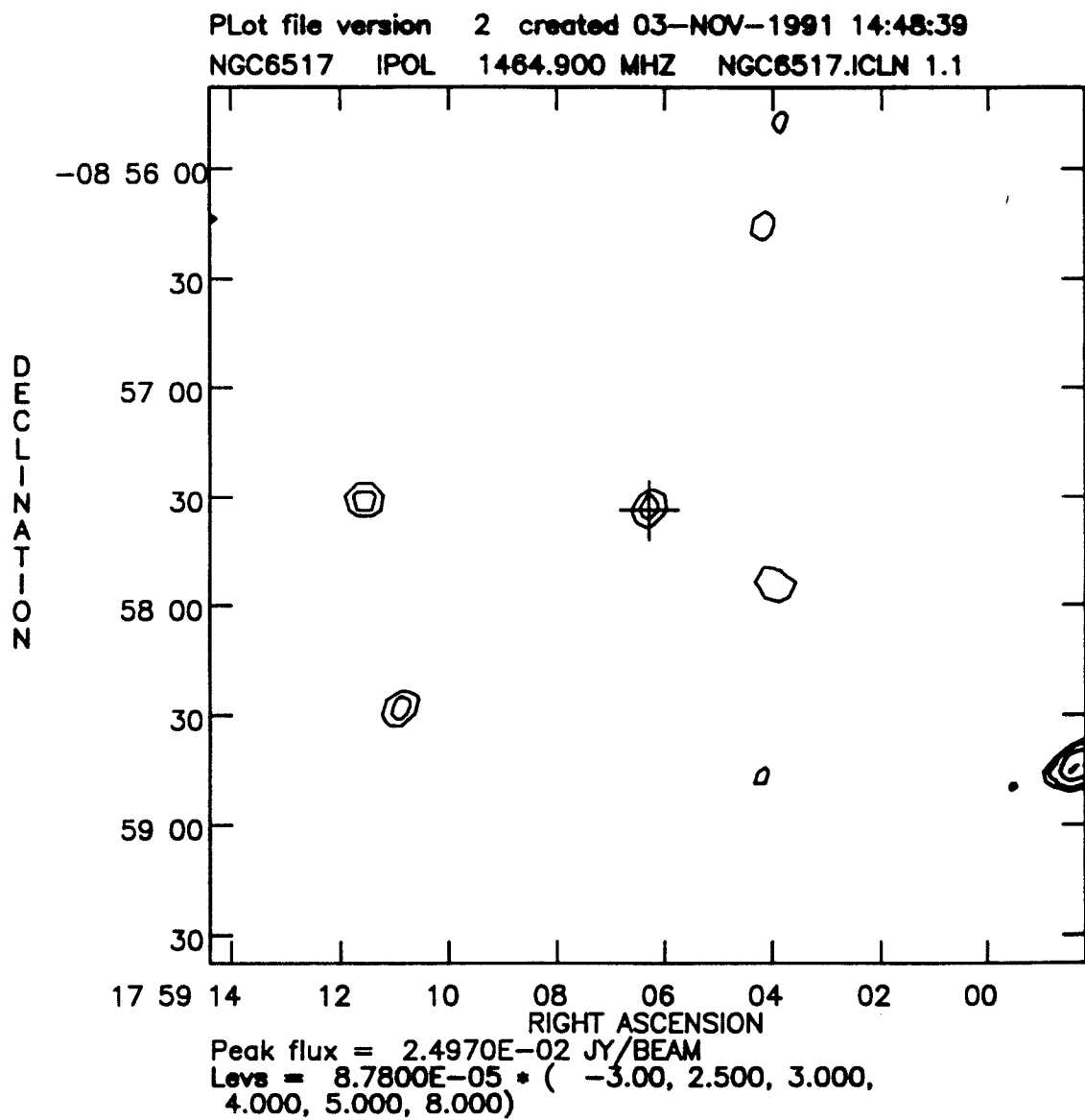


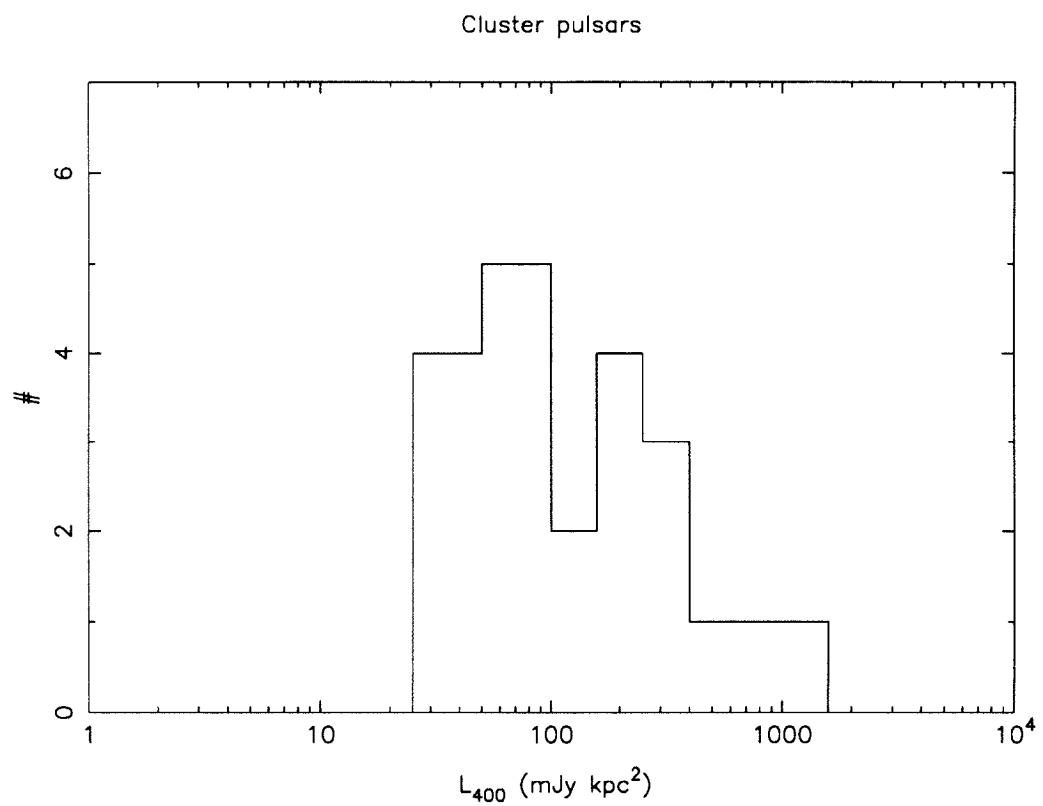
Figure 5.2

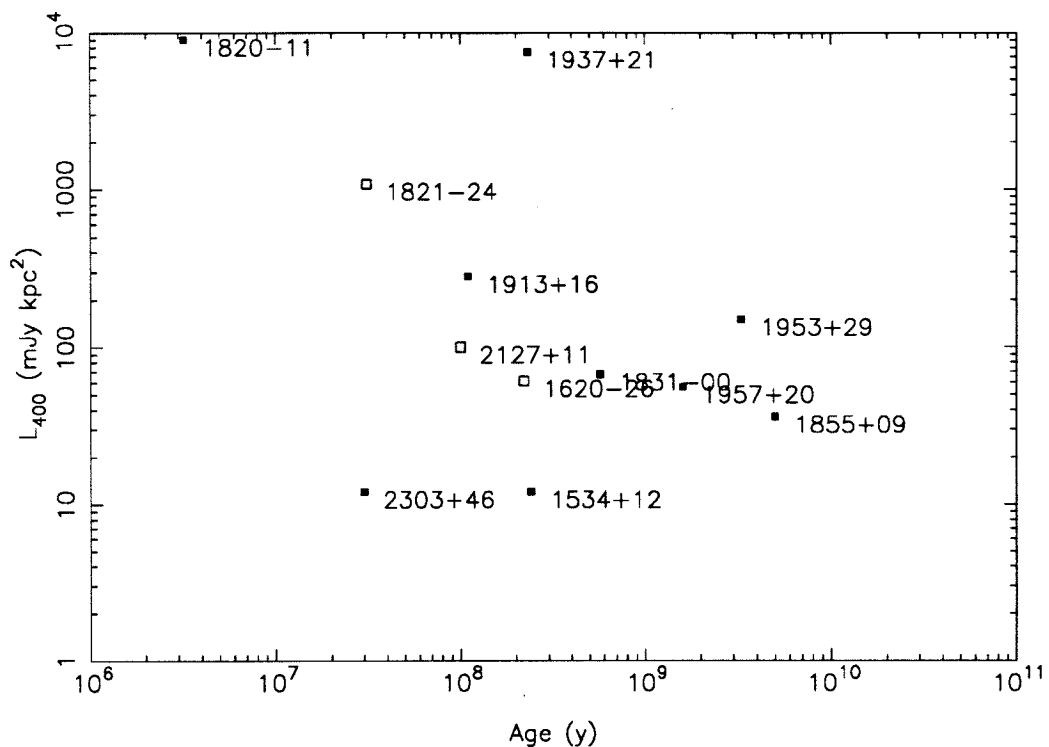
Figure 5.3

Figure 5.4

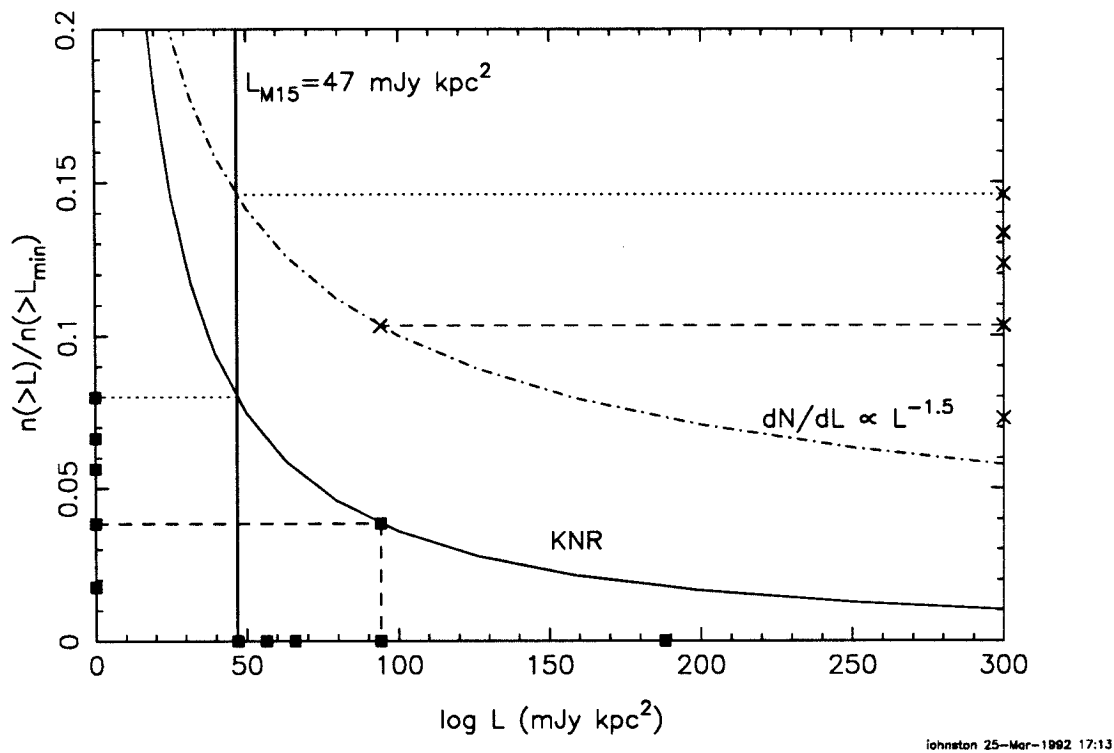
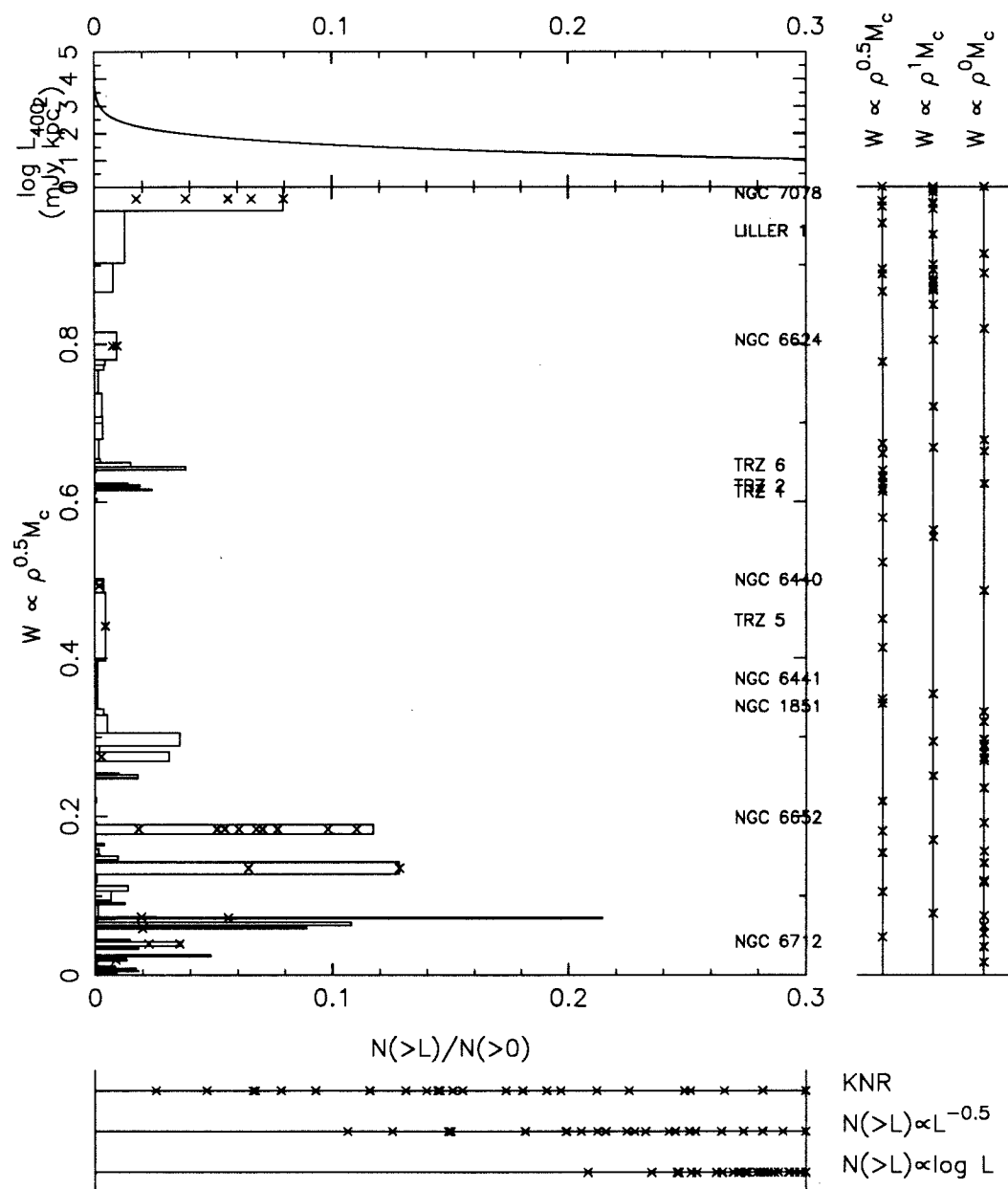


Figure 5.5



Part II

Low-Mass X-ray Binaries in the Disk

Chapter 6

The black hole A0620–00 and its accretion disk[†]

Helen M. Johnston, Shrinivas R. Kulkarni and J. B. Oke

Abstract

We present optical spectroscopic observations of the X-ray nova A0620–00 taken in 1986 March. Our radial velocity data confirm the results of McClintock & Remillard (1986) that the minimum mass of the central object, $3.2 M_{\odot}$, is above the maximum allowed mass for a neutron star, and hence the compact object must be a black hole. We also present new observations of emission lines arising from the accretion disk. These show the characteristic double-peaked profile associated with disk emission, although the peaks are asymmetrical and vary systematically over the orbit. Analysis of these profiles enables us to obtain the velocity at the outer edge of the optical emission region of the disk. This velocity, combined with the orbital velocity of the companion, puts a new *lower* limit on the mass of the central object: $\mu \leq 0.07$, $M_1 \geq 9.3 M_{\odot}$ if $M_2 = 0.7 M_{\odot}$, $\geq 4 M_{\odot}$ if $M_2 = 0.25 M_{\odot}$, where M_2 is the mass of the companion, μ is the mass ratio $M_2/(M_1 + M_2)$ and the limits are 3σ limits. These limits can be improved with higher resolution data and a better knowledge of the mass of the companion.

[†] This paper originally appeared in ApJ, 345, 492 (1989)

6.1 Introduction

A0620-00 is the best black hole candidate so far discovered (McClintock 1986). Spectroscopic studies by Oke (1977), Murdin *et al.* (1980) and others found that the optical spectrum consisted of a K4 V-K7 V stellar spectrum plus an emission line component from an accretion disk. The K4-K7 spectrum is thought to arise from the less massive secondary star and the accretion disk is assumed to be centered on the more massive primary star. McClintock & Remillard (1986; hereafter MR) analysed spectral and photometric data from the system, from which they found the orbital period to be 7.75 hours, and from dynamical arguments determined a lower limit on the mass of the primary of $3.20 M_{\odot}$. This limit exceeds the maximum mass of a neutron star under any present model, and thus they concluded that the compact primary in A0620-00 is in fact a black hole.

There are only three good candidates for stellar mass black holes known at this time, of which A0620-00 is the best. The system warrants further study, particularly because of peculiarities which have led to some doubts about present models for the system. Since the 1975 outburst, A0620-00 has been unobservably faint in X-rays, and yet there is still optical emission from the accretion disk. Thus while the secondary is supposed to be losing mass, the primary *i.e.*, the black hole, appears not to be accreting. De Kool (1988) has produced a model where a low \dot{M} can account for this lack of X-ray emission. However, verification of this model is not possible without an independent measure of \dot{M} . Additionally, the pairing of a K star with a black hole is not an expected one, requiring the mass ratio of the precursor to be as high as 40:1. Hence we decided to do spectroscopic monitoring of the system to verify the claims of MR. We present two conclusions in this article. We confirm MR's determination of the velocity curve and hence the mass function of the compact object. Then, from new observations of emission lines from the accretion disk, we present an improved *lower* limit on the mass of the central object. This limit only strengthens the now commonly accepted view that A0620-00 contains a black hole, subject to the caveats at the end of the paper.

6.2 Observations

Spectra were obtained using the Double Spectrograph (Oke & Gunn, 1982) at the Cassegrain focus of the Hale 5 m telescope on the nights of 1986 March 1, March 7 and March 8 UT. For the night of March 1, eleven 1200 s exposures were obtained under excellent seeing conditions ($\lesssim 1''$), using only the red camera of the Double Spectrograph. The resolution of the data was 15 Å and the dispersion 6.1 Å/pixel. For the nights of March 7 and 8, both cameras were used; eight 1200 s spectra were obtained under moderate ($1''$ – $2''$) seeing conditions. For the blue camera, the wavelength coverage was 3750 Å to 5450 Å with a dispersion of 2.1 Å/pixel and a resolution of 7.5 Å. The resolution of the red camera was 9.3 Å, and the dispersion 3.1 Å/pixel. Spectra of two K stars were also obtained as velocity standards. All the object exposures were accompanied by short arc lamp exposures. A complete journal of observations is given in Table 6.1.

The data were reduced using the FIGARO data reduction package, devised by Keith Shortridge at Caltech and the Anglo-Australian Observatory. Wavelength calibration was done by fitting a fourth order polynomial to the comparison arc lines immediately preceding the object exposure. The RMS residual was found to be better than 0.1 Å.

6.3 Radial velocity measurements

We assumed the photometric period of $0^d323014$ found by MR in order to calculate the relative phase for each spectrum. Following the technique of Tonry & Davis (1979), we cross-correlated the 19 red spectra against the comparison K stars, using only those portions uncontaminated by either emission lines or sky lines. This restricted the range to 4900–6510 Å for the night of 1 Mar, and 5300–6510 Å for the nights of 7 and 8 Mar (see spectra in Fig. 6.1). The data were binned onto a logarithmic scale, a low order polynomial fit to the continuum was subtracted, and the spectra were apodized with a cosine bell covering 10% of the spectrum, prior to the correlation. The position of the correlation peak was measured by fitting a parabola to the central five pixels of the highest peak. The heights of the peaks ranged from 0.35 to 0.8, with a typical value being 0.6, and a typical noise level of 0.15. We then fit the velocity data to a sine curve with a period of $0^d323014$ using the method of least-squares (Fig. 6.2). The calculated velocity minimum falls within 3.5 minutes of that determined by MR’s ephemeris. The semi-amplitude of the velocity variation, K , is $468 \pm 44 \text{ km s}^{-1}$ (1σ).

MR claimed substantial improvement in the velocity measurements by correlating the individual spectra against a rest-frame stack of all spectra instead of against a K star. We tried this approach (in fact the fit shown in Fig. 6.2 used the rest frame stack as the template) but did not achieve the big improvement that MR claim. Indeed, we do not expect to see any improvement in the scatter, as the errors in velocity in the initial determination are almost entirely due to the noise of the object spectrum rather than that of the K dwarf template. We found $K = 462 \pm 44 \text{ km s}^{-1}$, consistent with that obtained by using the K star velocity standards. It is this value of K that we use in the rest of the discussion. The systemic velocity is 22 km s^{-1} . We then calculated the orbital phase of each observation, defined by the photometric variations measured by MR; the origin of the orbital phase ($\phi = 0.0$) is defined to be secondary photometric minimum, which is inferred to be when the K star is directly behind the compact object. This agrees with our velocity curve: $\phi = 0.75$ corresponds to the maximum velocity. These are the phases tabulated in Table 6.1 and used in the rest of the discussion; this definition is the same as the photometric phase of MR.

6.4 Emission line analysis

Oke (1977) found that the spectrum of A0620-00 could be separated into two components, a cool K star plus a power law component $F_\lambda \propto \lambda^{-\alpha}$, with $\alpha \approx 2.0$. This power law component together with the Balmer series emission lines were attributed to an accretion disk. To date no systematic study has been made. Murdin *et al.* (1980), observing the system during 1976 and 1978, noted that the Balmer emission peaks were double, with a separation of 1080 km s^{-1} , and variable. MR reported gross variations in the shape of the $\text{H}\beta$ emission lines over the orbit, but they saw no systematic orbital variation.

We have 19 observations of the $\text{H}\alpha$ line, covering the entire orbit, 8 observations of $\text{H}\beta$ from the nights of 7 and 8 Mar 1986, and 11 observations of the Ca II $\lambda\lambda 8498, 8542, 8662$ triplet from the night of 1 Mar 1986. Figure 6.3 shows our observations of the disk emission lines, arranged in order of phase of the K star orbit as calculated in §6.3. Clearly the variation of the shape of the emission lines is not random over the orbit. All lines show the double-peaked profiles associated with emission from extended rotating accretion disks (Smak 1981). However, the two peaks are not symmetric, as is the case when the disk emission is assumed to be cylindrically symmetric. Note that, as the nights were not photometric, there could be variations in the *total* flux in the emission line, but this should not influence the shape of the line profiles.

We therefore added the 19 spectra together, after normalising each to the local continuum, to produce an average $\text{H}\alpha$ profile over the orbit (Fig. 6.4). This profile is symmetric (due to our having achieved a complete orbit coverage), and so we fit this to a profile of the form described by Smak (1981). We assume that the disk is cylindrically symmetric and optically thin, and that the volume emission from the disk varies as a function of radius r as $f(r)$. Assuming that the disk is flat and Keplerian enables us to calculate u , the radial velocity. Then the observed emission line profile $F(u)$ can be shown to be

$$F(u) \propto \int_{r_1}^{r_z} \frac{r^{3/2} f(r) dr}{(1 - u^2 r)^{1/2}} \quad (6.1)$$

where u and r are dimensionless and normalized to their values at the outer edge of the disk, r_1 is the ratio of the inner and outer radii of the disk, and $r_z = \min(1, u^{-2})$. Observations of CVs show that $f(r) \sim r^{-\alpha}$ with $1 \leq \alpha \leq 2$ is a good approximation for $f(r)$. Incidentally, if the emission is optically thick, equation (6.1) still applies with $f(r)$ denoting the surface brightness. We calculated this profile for half-integral values of α between 0.5 and 2.5, and then broadened each profile by a Gaussian of FWHM Δu to allow for the effects of finite spectral resolution, and compared each to our stacked profile. Here Δu is an *effective*

instrumental resolution since we are adding together two data sets of different resolution. The best fit was found to have $\alpha = 1.5$, $v_{\text{disk}} = 550 \text{ km s}^{-1}$, $\Delta u = 470 \text{ km s}^{-1}$, $r_1 = 0.10$. This value for α was then assumed for the following analysis. Incidentally, this was also the value found by Filippenko *et al.* (1988) in their study of disk emission from the bizarre object SS 433.

To try to reproduce the observed asymmetry in the spectra, we considered models where the presence of the K star disturbed the disk. The simplest model to imagine is a “hot spot” on the disk which orbits with the K star but at some fixed angle from it. We relaxed the assumption of cylindrical symmetry in the disk emission, by assuming

$$f(r, \phi) \sim r^{-\alpha} (1 + \beta \cos(\phi - \psi_0 - \psi_{\text{hs}})) \quad (6.2)$$

where ψ_0 is the orbital phase of the observation, and ψ_{hs} the (assumed constant) phase of the hot spot with respect to the K star, so $\psi = \psi_0 + \psi_{\text{hs}}$ is the orbital phase of the hot spot. The observed line profile is then

$$\begin{aligned} F(u) \propto u^{-2} \left[-(1 - x^2)^{1/2} \right]_{x_1}^{x_z} - \beta \sin \psi u^{-2} \left[-\frac{x}{2}(1 - x^2)^{1/2} + \frac{1}{2} \arcsin x \right]_{x_1}^{x_z} \\ + \beta \cos \psi u^{-2} \left[\frac{x^2}{2} \right]_{x_1}^{x_z} \end{aligned} \quad (6.3)$$

where $x_z = \min(u, 1)$, $x_1 = u r_1^{1/2}$.

The free parameters of this model are thus v_{disk} , the projected velocity of the outer edge of the disk, r_1 , the ratio of the radii of the inner and outer edges of the disk, β , the amplitude of the hotspot, and ψ_{hs} , the phase of the hot spot with respect to the K star. We wrote a computer program which allowed all these parameters to be varied and the computed profiles compared to all 19 H α spectra. The parameters were manually tweaked to minimise the total sum of the squares of the deviation of the model from the observed profile. The resulting best fit is shown plotted with the spectra in Figure 6.3. The best fit values were $v_{\text{disk}} = 540 \pm 15 \text{ km s}^{-1}$, $r_1 = 0.09$, $\beta = 0.21$, $\psi_{\text{hs}} = 0.02$. Δu was 590 km s^{-1} (phase 0.5 to 1.0) and 360 km s^{-1} (phase 0.1 to 0.5), or 2.3 pixels. The 1σ error on v_{disk} was estimated from single spectrum near phase 0.5.

As an alternative, we also tried a model where $f(r, \phi)$ consisted of a single delta function hot spot on the disk in addition to the $r^{-\alpha}$ contribution from the rest of the disk; however, the fit was not satisfactory, as this model predicts a third peak moving across the centre of the profile as the hot spot moves across the line of sight.

We had approximately half-orbit coverage in each of H β and the Ca II $\lambda\lambda$ 8498, 8542, 8662 triplet, so we performed the same analysis with them. The resulting best fits are also plotted in Figure 6.3. The fits were consistent with those obtained from H α . However, the signal-to-noise ratio on both of these was much worse than for H α . The line ratios for the calcium triplet were found to be 1.05:1.05:1 for $\lambda\lambda$ 8498:8542:8662, which implies the lines are optically thick. For comparison, the line strengths for optically thin emission are 1:9:5 (McGregor, Persson & Cohen, 1984). The line ratio for H α /H β could not be measured as no flux standard was observed. However, if the Balmer lines are also optically thick, this could explain why our model (*i.e.*, eq. [6.3]) fits the H α profile rather better than the H β profile; with optically thick lines, the emission is coming from a completely different region of the disk and so an independent fit should be made.

6.5 The mass of the black hole

We find for the mass function $f(M) = 3.30 \pm 0.95 M_{\odot}$, in agreement with MR's value. However, we can now put a better lower limit on the mass of the black hole, M_1 , by using our measurement of the projected velocity at the outer edge of the disk, v_{disk} . The ratio of this to the projected velocity of the K star, K , is independent of $\sin i$, provided the accretion disk is in the orbital plane of the binary. We therefore investigate possible configurations of the system which could reproduce our observed value, $v_{\text{disk}}/K = 1.17 \pm 0.12$.

As a first estimate, we assume that the material in the disk is moving in circular orbits around the black hole, with velocities given by Kepler's law. We then impose the constraint that the radius of the outer edge of the disk must be less than the distance from the black hole to the L_1 point of the system, calculated from the expression for the gravitational potential

$$\Phi = -\frac{GM_1}{(x^2 + y^2)^{1/2}} - \frac{GM_2}{[(x - a)^2 + y^2]^{1/2}} - \frac{\Omega^2}{2} [(x - \mu a)^2 - y^2] \quad (6.4)$$

where a is the separation between M_1 and M_2 , $\mu = M_2/(M_1 + M_2)$, Ω is the angular frequency of the orbit, and M_1 is at the origin. We need to choose a mass for the K star for the following discussion: a liberal estimate for its spectral type is K2–K7 V, which for a star on the main sequence corresponds to a mass of 0.5 to 0.8 M_{\odot} . The preferred value (Oke 1977) is a K5 V star, with mass of 0.7 M_{\odot} , so we assume this value for M_2 . For varying values of M_1 , we can calculate the velocity of the companion and the distance to the L_1 point, and hence the velocity at that radius from Kepler's law. Comparison of the ratio of these two with our observed value puts a *lower* limit on the mass of the black hole and an *upper* limit on i : $\mu \leq 0.048$, $M_1 \geq 14.0 \pm 4.2 M_{\odot}$, $i \leq 40^\circ \pm 5^\circ$ for $M_2 = 0.7 M_{\odot}$, where the higher value of M_1 and the lower value of i arise from the lower limit on v_{disk} .

Note that this is a very conservative lower limit, as a circular orbit of this radius will not fit within the Roche lobe of the compact object. It is also clear that the assumption of circularity is not valid for such large orbits. In order to improve our estimate, we considered the largest stable orbit that can exist in a system with mass ratio μ . Following Paczyński's (1977) method, we performed restricted three-body simulations to find the largest stable streamlines in a binary system, by finding the largest non-overlapping, stable, simple periodic orbits of test particles. Table 6.2 shows the results of these calculations. The columns give μ , the distance to the L_1 point, the intercept of the largest stable orbit with the positive x -axis ρ_1 , the mean velocity v_{disk} , the maximum and minimum velocities v_{max} and v_{min} , and the ratio of the disk velocity to the K star velocity v_{disk}/K . The unit of length is a and the unit of velocity is $a\Omega$. In these units, the velocity of the K star is

$K = 1 - \mu$. From our observed value for v_{disk}/K , $\mu \lesssim 0.01$. For the smallest possible mass for the K star, $M_2 = 0.25 M_{\odot}$ (see MR), this means $M_1 \gtrsim 25 M_{\odot}$ (1σ), with correspondingly higher limits for greater values of M_2 . An *absolute* lower limit can be found by using a value for v_{disk}/K which is 3σ higher than our measured value; this yields $\mu \leq 0.07$, $M_1 \geq 9.3 M_{\odot}$ if $M_2 = 0.7 M_{\odot}$, and $M_1 \geq 4 M_{\odot}$ if $M_2 = 0.25 M_{\odot}$. For such large masses for the black hole, we actually need a small K star mass in order to fit the K star within its Roche lobe. We also note that for a disk of this size, we expect to see variations in the disk velocity on the order of 40 km s^{-1} over the orbit; our observations do not rule out this value, but higher resolution observations might see this.

6.6 Discussion

We repeated MR's analysis of the radial velocity data for A0620–00 and confirm their conclusion: that the velocity semi-amplitude of the dwarf companion leads to a value for the mass function which is above the maximum mass allowed for a neutron star. From analysis of the emission lines, presumed to arise from the accretion disk, we have derived an upper limit on the mass ratio and a *minimum* mass for the compact object which depends only on M_2 : $\mu \leq 0.07$, $M_1 \geq 4 M_\odot$ if $M_2 = 0.25 M_\odot$, $\geq 9.3 M_\odot$ if $M_2 = 0.7 M_\odot$.

This limit arises from simple dynamical and geometrical constraints on the shape of the system. Indeed, these arguments would not give rise to interesting limits in most binary systems because the accretion disk is usually deep inside the Roche lobe of the compact object. It is only because the observed velocity at the outer edge of the disk is so close to the observed velocity of the companion star that we can use these two measurements to constrain the mass of the compact object. This interpretation is supported by the fact that in our model for the system, the point on the disk brightest in $H\alpha$ leads the K star by 0.02 of an orbit, or about 7° . In contrast, studies of CVs have usually found that hot spots caused by an accretion stream impacting on the disk have much larger ψ_{hs} , usually $\psi_{hs} \gtrsim 45^\circ$ (Warner 1976; Flannery 1975).

We therefore conclude that the central object of A0620–00 is indeed a black hole, and perhaps even a rather massive black hole. Further high-resolution observations of the system are warranted, as there are several predicted effects which it should be possible to observe, none of which were seen at the resolution of our data. We should be able to observe the variation of the disk velocity between v_{\min} and v_{\max} that our model predicts, and perhaps even the orbital motion of the black hole itself, reflected in variations of the central velocity[†]. The errors on both velocity measurements are limited by the data, so higher resolution observations could also improve the velocity measurement and hence the mass determination.

The assumptions made in arriving at these limits are reasonable. However, a better understanding of a disk so close to the Roche lobe is needed before we accept the mass limits quoted here as being absolutely *firm*. For example, we have assumed that the disk and the K star are coplanar. If the disk was tilted at a smaller angle to our line of sight than the plane of the orbit, then the ratio of the disk velocity to the K star velocity would be artificially reduced. However, the angle of tilt would need to be large, on the order of

[†] Since this paper was published, Haswell & Shafter (1990, ApJ 359 L47) detected the motion of the black hole in the motion of the emission lines, and measured the mass of the black hole to be $> 3.8 M_\odot$, with a most likely value $\sim 7 M_\odot$.

30°. Also, it is highly unlikely that a thin disk would develop out of the plane of the binary orbit, unless perhaps the K star was spinning very rapidly on an axis not aligned with the axis of the system. However there is no evidence for such high velocities in the Na D lines of the K star spectrum. Other scenarios can be imagined which might make our inference of the mass wrong, such as winds, outflows, non-Keplerian disks, and so on. Such possibilities need to be investigated.

We would like to thank R. Romani and E.S. Phinney for their constructive criticism, and A. Picard for his help with the programming. SRK's research is partly supported by a grant from the Sloan Foundation and a Presidential Young Investigator award. JBO's research is partly supported by a grant from NSF (AST-84-15404).

Table 6.1 Journal of observations

| UT date | Object | UT start exposure | Mean phase | Red camera | |
|------------|---------------------------|--|------------|----------------------|----------------|
| | | | | Wavelength range (Å) | Resolution (Å) |
| 1 Mar 1986 | A0620-00 | 2 ^h 59 ^m 36 ^s | 0.501 | 4640 - 9490 | 15 |
| " | " | 3 24 27 | 0.554 | " | " |
| " | " | 3 47 04 | 0.596 | " | " |
| " | " | 4 10 27 | 0.653 | " | " |
| " | " | 4 33 54 | 0.704 | " | " |
| " | " | 4 56 32 | 0.752 | " | " |
| " | " | 5 19 13 | 0.801 | " | " |
| " | " | 5 42 04 | 0.850 | " | " |
| " | " | 6 04 48 | 0.899 | " | " |
| " | " | 6 27 29 | 0.948 | " | " |
| " | " | 6 47 16 | 0.990 | " | " |
| " | Hy 117 - K3-K5 comparison | 2 53 11 | ... | " | " |
| 7 Mar 1986 | A0620-00 | 3 30 17 | 0.142 | 5280 - 7740 | 9.3 |
| " | " | 4 00 05 | 0.206 | " | " |
| " | " | 4 25 56 | 0.261 | " | " |
| 8 Mar 1986 | " | 3 04 30 | 0.182 | 5210 - 7670 | 9.3 |
| " | " | 3 21 00 | 0.239 | " | " |
| " | " | 3 56 53 | 0.295 | " | " |
| " | " | 4 22 47 | 0.350 | " | " |
| " | " | 4 48 31 | 0.406 | " | " |
| " | HD36003 - K0 comparison | 2 50 29 | ... | " | " |

Table 6.2 Parameters for the largest stable orbit for a range of μ

| μ | L_1 | ρ_1 | v_{disk} | v_{max} | v_{min} | v_{disk}/K |
|-------|--------|----------|-------------------|------------------|------------------|---------------------|
| 0.10 | 0.7090 | 0.4346 | 1.4054 | 1.6070 | 1.2882 | 1.5616 |
| 0.07 | 0.7395 | 0.4458 | 1.4207 | 1.5655 | 1.3351 | 1.5277 |
| 0.05 | 0.7652 | 0.4920 | 1.3248 | 1.4967 | 1.2046 | 1.3945 |
| 0.04 | 0.7809 | 0.5035 | 1.3209 | 1.4743 | 1.2107 | 1.3760 |
| 0.03 | 0.7996 | 0.5171 | 1.3151 | 1.4487 | 1.2157 | 1.3558 |
| 0.02 | 0.8235 | 0.5340 | 1.3088 | 1.4171 | 1.2248 | 1.3355 |
| 0.01 | 0.8581 | 0.5579 | 1.2971 | 1.3750 | 1.2329 | 1.3102 |

References

de Kool, M. 1988, *ApJ*, 334, 336

Filippenko, A. V., Romani, R. W., Sargent, W. L. W. & Blandford, R. D. 1988, *AJ*, 96, 242

Flannery, B. P. 1975, *MNRAS*, 170, 325

Hénon, M. 1965, *Ann. d'Ap.*, 28, 992

McClintock, J. E. 1986, in *The physics of accretion onto compact objects*, ed. Mason, K. O., Watson, M. G. & White, N. E. (Berlin; Springer-Verlag) p. 211

McClintock, J. E. & Remillard, R. A. 1986, *ApJ*, 308, 110

McGregor, P. J., Persson, S. E. & Cohen, J. G. 1984, *ApJ*, 286, 609

Murdin, P., Allen, D. A., Morton, D. C., Whelan, J. A. J. & Thomas, R. M. 1980, *MNRAS*, 192, 709

Oke, J. B. 1977, *ApJ*, 217, 181

Oke, J. B. & Gunn, J. E. 1982, *PASP*, 94, 586

Paczyński, B. 1977, *ApJ*, 216, 822

Smak, J. 1981, *Acta Astr.*, 31, 395

Tonry, J. & Davis, M. 1979, *AJ*, 84, 1511

Warner, B. 1976, in *IAU Symposium 73, The Structure and Evolution of Close Binary Systems*, ed. Eggleton, P., Mitton, S. & Whelan, J. (Dordrecht; Reidel), p. 85

Figure captions

Figure 6.1 — Spectra of the K comparison star Hy 117, summed spectra of A0620-00 in the rest frame of the K companion at low and high resolution, and HD 36003, over the wavelength range used for the cross-correlation. H β and H α in emission are seen at the left and right of the plot. The vertical scale is arbitrary.

Figure 6.2 — Radial velocities of the K dwarf derived from correlation with the stacked spectrum, as described in the text. The scatter from the fit has not been reduced from the fit obtained from correlating against K standards by changing the template.

Figure 6.3 — Variation of the disk emission lines over the orbit. The two sets of three columns show H α , H β and the Ca II $\lambda\lambda$ 8498, 8542, 8662 triplet. The fit calculated as described in §6.4 is shown as the solid line. The data were normalised by a low order polynomial fit to the local continuum and then a constant 1.0 was subtracted from all spectra. The horizontal scale is $\pm 2500 \text{ km s}^{-1}$ for H α and H β , and for the Ca lines -5000 to 7000 km s^{-1} in the frame of $\lambda 8542$, or about 8399.7 \AA to 8741.4 \AA on a logarithmic scale. The first Ca spectrum shows the three individual lines as well as their summed profile. The vertical scale is 0 to 2.0 for H α , and 0 to 1.0 for the other two lines.

Figure 6.4 — The summed profile of all H α spectra. Each spectrum was normalised by a low order polynomial fit to the local continuum before summing, and the low resolution data was rebinned to the same scale as the high resolution data. The Smak profiles with $\alpha = 1, 1.5$ and 2 are shown as dashed, solid and dot-dashed lines respectively. The value $\alpha = 1.5$ was adopted throughout the subsequent analysis.

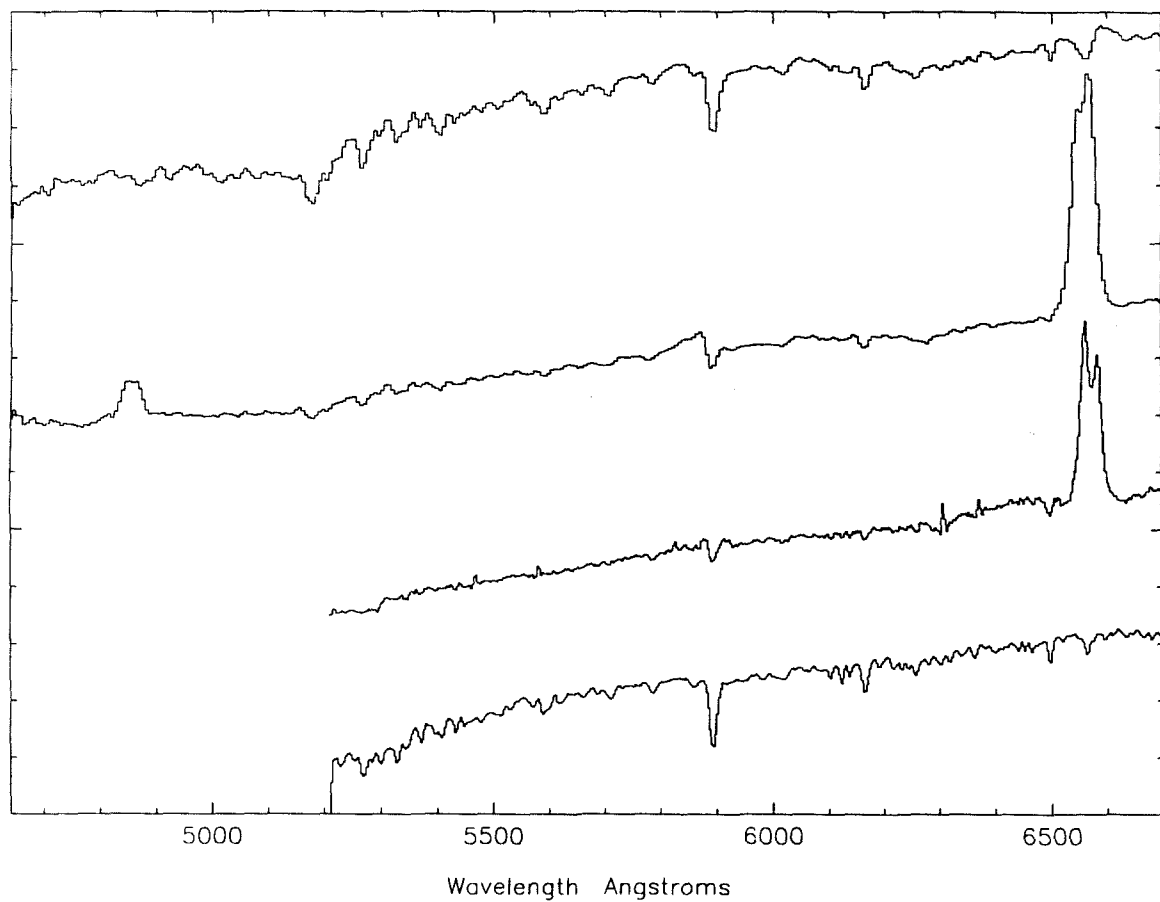
Figure 6.1

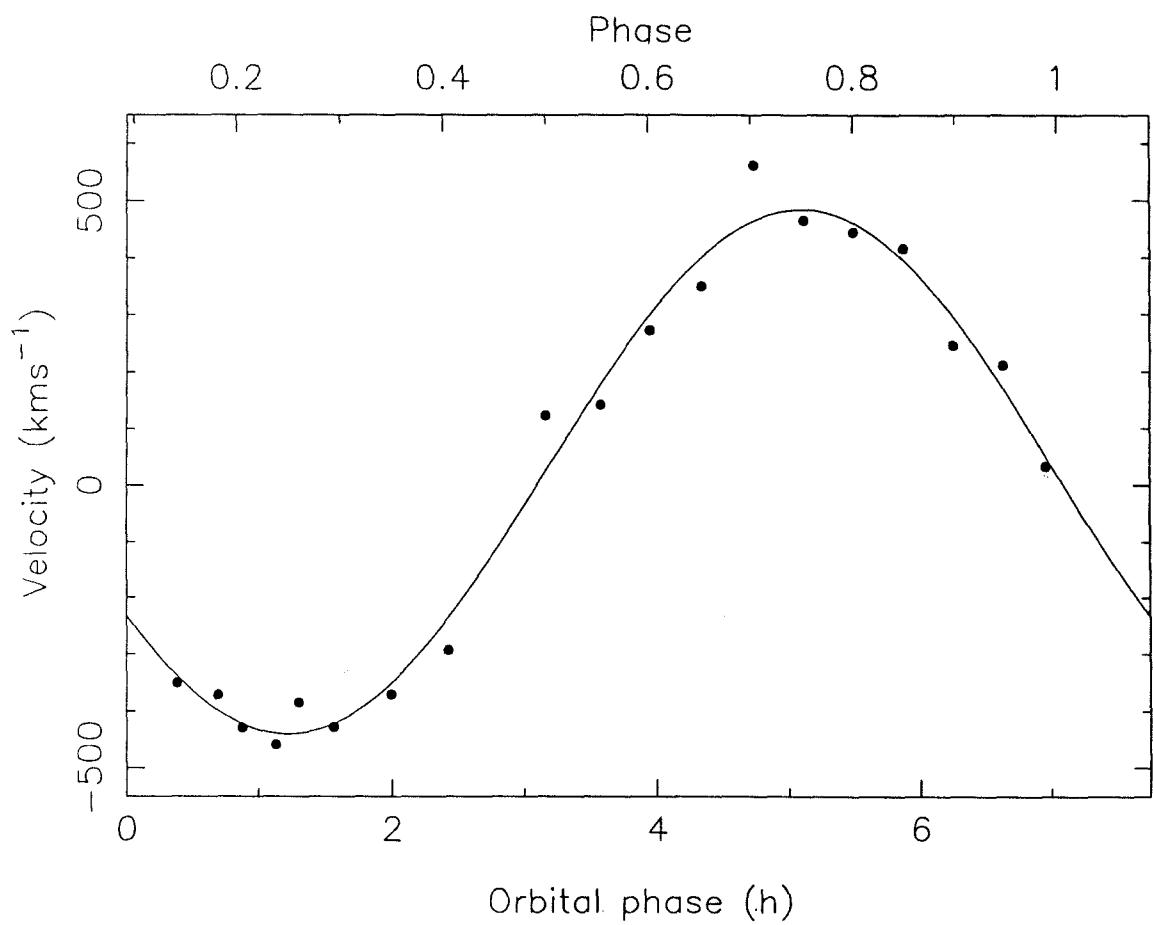
Figure 6.2

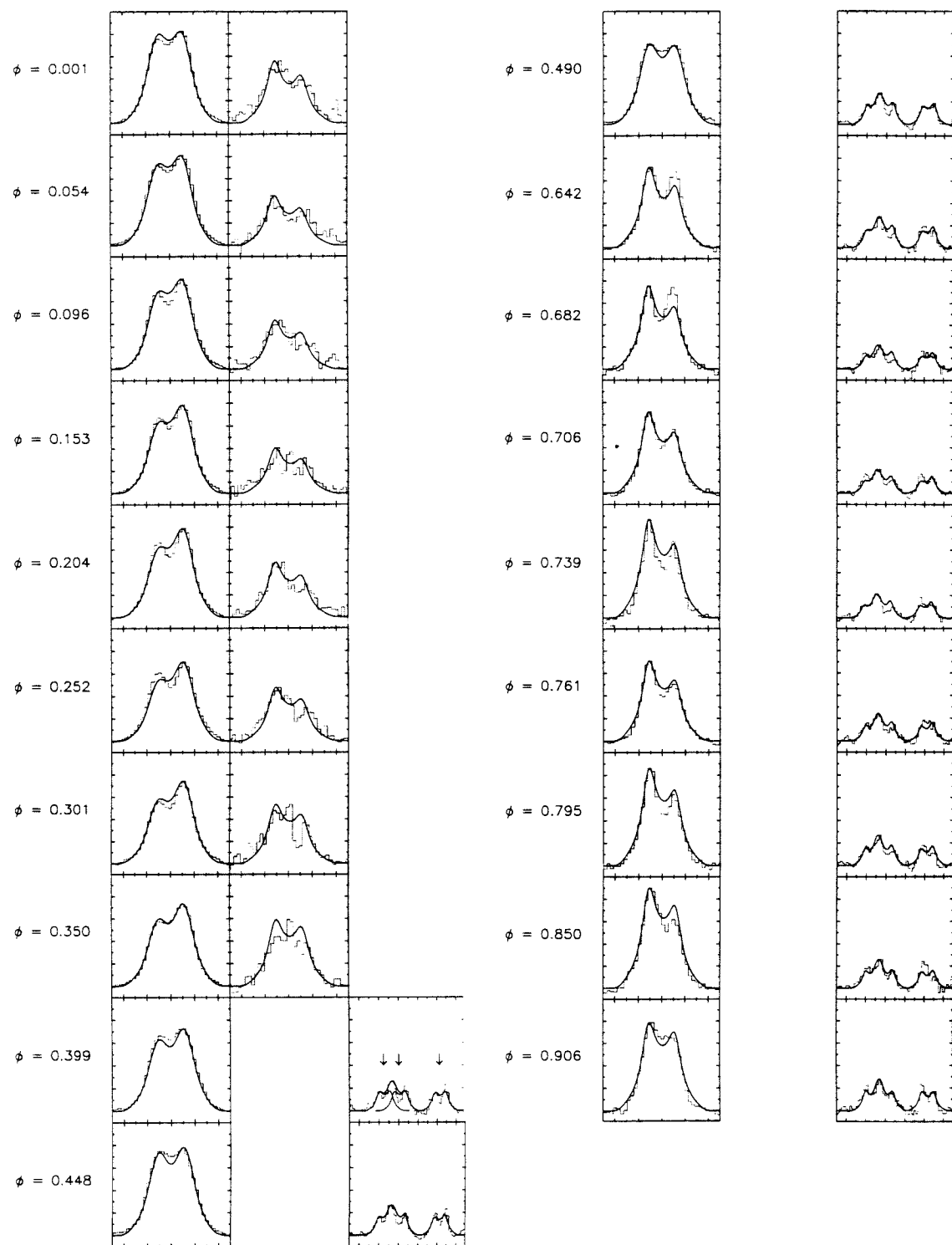
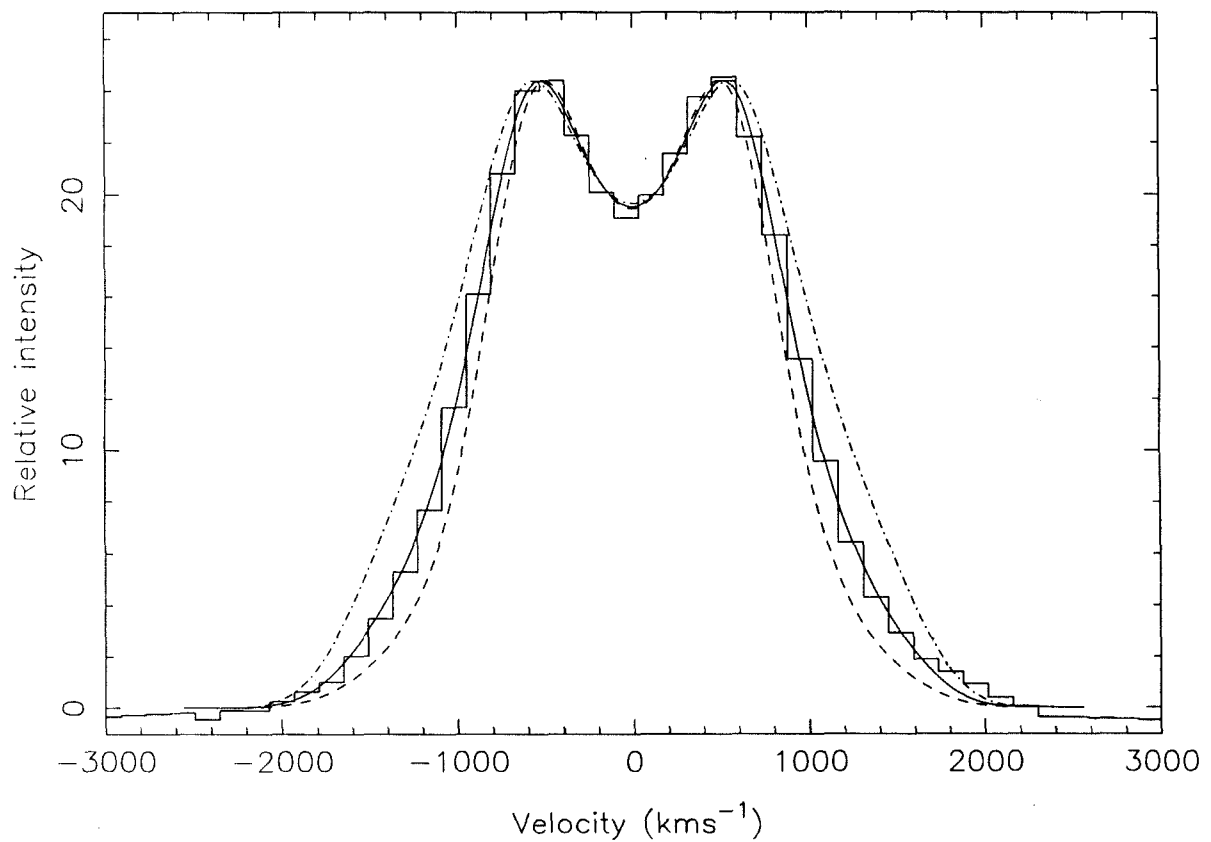
Figure 6.3

Figure 6.4

Appendix: Further observations of A0620–00

We present new, higher velocity resolution data of the system A0620–00, the motivation being both to improve the errors on the velocity of the companion and hence improve our measurement of the mass ratio, and possibly to measure the variations in the disk velocity and even the orbital motion of the black hole itself, thus unambiguously determining its mass.

We observed A0620–00 on the night of 13 February 1989 UT, using the Double Spectrograph on the Hale 5-m telescope. We used a 1200 lines mm^{-1} grating in the red camera, yielding a resolution of 1.8 Å. Conditions were less than ideal, with $\sim 3''$ seeing, so it should prove possible to obtain better data. The data from the blue camera will not be discussed as the signal-to-noise ratio was too poor; the wavelength coverage of the red data was 5985–6640 Å. Nine 1800 s exposures were taken, together with spectra of four K dwarf radial velocity standards. Data reduction followed exactly the procedure described in Chapter 6.

Figure A1 shows a substantially improved radial velocity curve for the secondary. The sine curve was fit assuming the photometric period from MR of 7^h75234. The velocity semi-amplitude is $K = 453 \pm 11 \text{ km s}^{-1}$, giving a value for the mass function of $f(M) = 3.1 \pm 0.2 \text{ M}_\odot (1\sigma)$, the best determination of the mass function so far. Figure A2 shows the H α lines as a function of orbital phase. As before, we found we needed to include an azimuthal term in the standard Smak profile in order to fit our data. However, the amplitude of this term was substantially reduced, from 21% to 9%, and was consistent with zero at the 1σ level. This would seem to indicate the disk is still varying on several year timescales. The full details of the fit are presented in Table A1, with the values obtained from the 1986 low-resolution data for comparison. The velocity at the outer edge of the disk was measured to be $v_{\text{disk}} = 580 \pm 20 \text{ km s}^{-1} (1\sigma)$, giving $v_{\text{disk}}/K = 1.28 \pm 0.08$. This puts a 1σ upper limit on μ of $\mu \leq 0.01$, or a 3σ upper limit of $\mu \leq 0.07$, as before. The quality of the present data prevented us from measuring the disk orbital motion.

Thus, our original analysis would appear to be borne out. Our observations yield the best determination of the mass function, showing that the central object of the A0620–00 system is almost certainly a black hole, possibly even a very massive black hole. It must be noted, of course, that scenarios can be imagined where the above analysis, assuming a Keplerian disk in the orbital plane of the system, might break down.

Table A1 Parameters derived from fit

| | Low resolution | High resolution |
|--------------------------|---------------------------------|--------------------------------|
| K | $460 \pm 40 \text{ km s}^{-1}$ | $453 \pm 11 \text{ km s}^{-1}$ |
| $f(M)$ | $3.30 \pm 0.95 \text{ M}_\odot$ | $3.1 \pm 0.2 \text{ M}_\odot$ |
| v_{disk} | $540 \pm 40 \text{ km s}^{-1}$ | $580 \pm 20 \text{ km s}^{-1}$ |
| β | 0.21 ± 0.05 | 0.09 ± 0.08 |
| ψ_{hs} | 0.02 ± 0.18 | 0.02 ± 0.15 |

Figure captions

Figure A1 — Radial velocity of the K dwarf of A0620–00 derived from a correlation with a comparison K5 V star. The error bars are measurement errors derived from the width of the cross-correlation peak.

Figure A2 — Variation in the H α emission of A0620–00 over the orbit. The histogram shows the data, the solid line the model fit. The data were normalized by a low-order polynomial fit to the local continuum and then a constant 1.0 was subtracted. The horizontal scale is ± 2500 km s $^{-1}$.

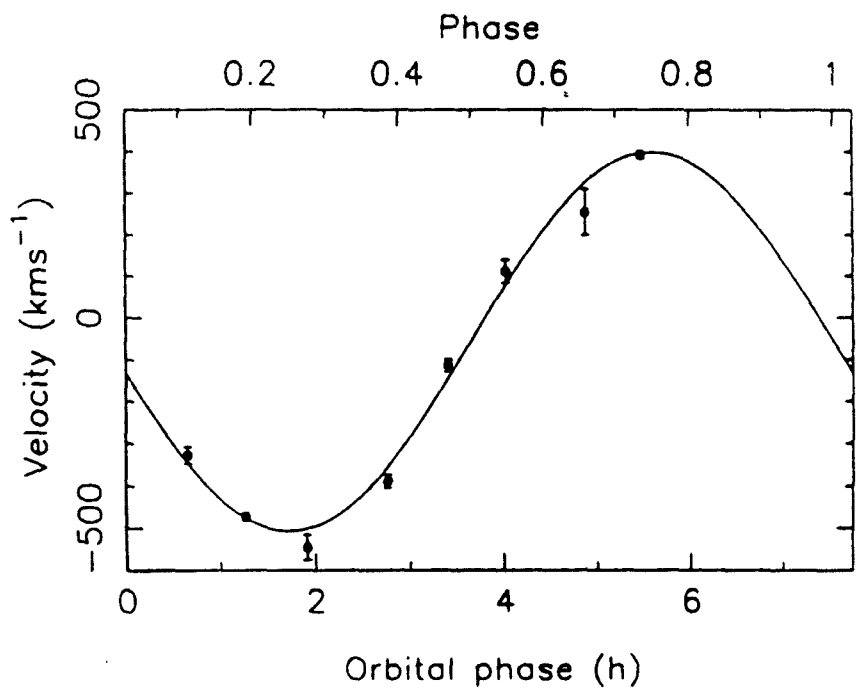


Figure A1

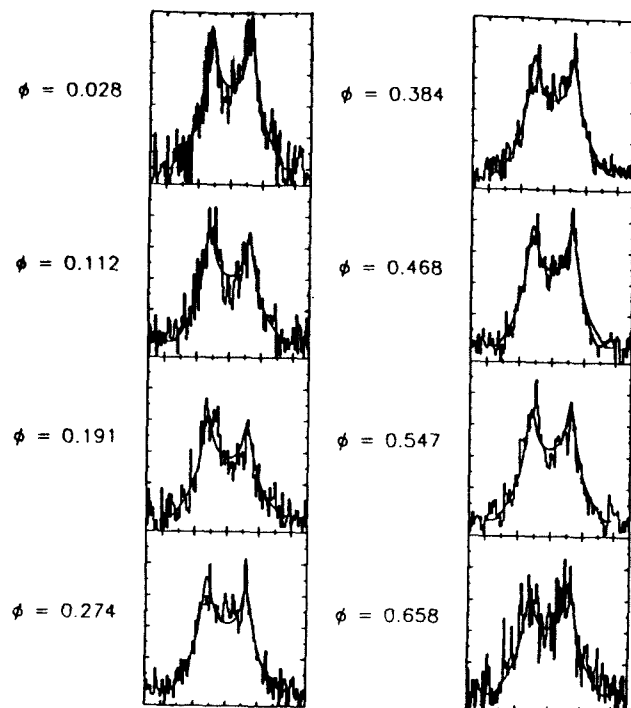


Figure A2

Chapter 7

Spectroscopy of the recurrent nova U Scorpii[†]

Helen M. Johnston and Shrinivas R. Kulkarni

Abstract

U Sco, the recurrent nova with the shortest known recurrence time, has been argued to be a strong case for a very massive accreting white dwarf undergoing thermonuclear explosions. Such massive white dwarfs have also been proposed as the progenitors of millisecond pulsars in the disk and in globular clusters. We present optical spectroscopic observations of the system and measure both emission- and absorption-line velocities. We derive an upper limit to the mass for the white dwarf of $\lesssim 0.9 M_{\odot}$ (3σ) in direct contradiction to the thermonuclear instability models. Hydrogen is seen in absorption for the first time, strongly suggesting that the donor is reasonably normal. This, and the observed high helium abundance in the emission spectrum, pose additional difficulties to the accretion instability models. Thus it appears there is no viable model for this interesting source.

[†] To be published in ApJ, 1 September 1992 issue.

7.1 Introduction

Recurrent novae form a class of objects intermediate between the dwarf novae and the classical novae, both in terms of the amplitude of the eruption, and the time between successive outbursts. It is now believed that classical novae, which by definition erupt only once, represent thermonuclear explosions on the surface of a white dwarf. Dwarf novae, which undergo eruptions on timescales of days to months, are believed to be powered by accretion instabilities, either as a result of an instability of the disk, or because of an increase in the amount of material being transferred from the secondary. For recurrent novae, both kinds of models have been suggested to explain the 10–80 y outburst recurrence timescale (see Webbink *et al.* 1987 and Webbink 1990 for reviews).

U Scorpii is a recurrent nova, with the shortest known recurrence interval as well as the fastest known development time. Five outbursts have been observed since 1863, with the interval between the last two outbursts being only 8 y, raising the possibility that some outbursts may have been missed. The observed high helium abundance of the ejecta poses difficulties for the accretion instability models.

In the framework of the thermonuclear explosion model, the frequency of outburst requires that the white dwarf be massive. When the pressure at the base of the envelope of the accreted matter, $P \sim GM_{wd} \Delta M / 4\pi R_{wd}^4$ reaches a critical value, nuclear ignition takes place; here M_{wd} , R_{wd} are the mass and radius of the white dwarf, and ΔM is the mass of the accreted matter. Since the material is degenerate, thermonuclear burning is unstable. The extraordinarily short recurrence timescale observed for U Sco requires the white dwarf to be very close to the Chandrasekhar limit, $M_{wd} \sim 1.38 M_{\odot}$ for acceptable accretion rates (Starrfield, Sparks & Shaviv 1988; Duschl, Livio & Truran 1990).

Such massive white dwarfs have also been invoked as the progenitors of millisecond pulsars (*e.g.*, Bhattacharya & van den Heuvel 1991). In this model, it has been hypothesized that accreting massive white dwarfs collapse to neutron stars when their mass exceeds the Chandrasekhar limit. This mechanism has been invoked to account for the large observed abundance of millisecond pulsars in the disk and in globular clusters. However, the model is controversial, especially with regard to the paucity of observed massive white dwarfs and the physics of collapse. U Sco, as a possible extremely massive white dwarf, is therefore a prime candidate for testing such a model.

Schaefer (1990) recently determined the photometric periods of three of the recurrent novae. U Sco was found to be an *eclipsing* system, with a period $P = 1^d2344 \pm 0^d0025$, providing a perfect opportunity to measure the mass of the white dwarf, and test the above

theoretical predictions. In this paper we present observations which directly contradict these predictions.

7.2 Observations

Spectra were obtained using the Double Spectrograph (Oke & Gunn 1982) at the Cassegrain focus of the Hale 5 m telescope during two observing seasons (Table 7.1). The data were reduced using the FIGARO data reduction package. Wavelength calibration was performed by fitting a third order polynomial to the comparison arcs taken immediately after each exposure. The stability of the spectrograph was checked by comparing the shift between arc exposures; in no case was the shift greater than 0.2 Å. The RMS residuals of the wavelength fits were in all cases better than 0.5 Å, except for the nights of 1991 July 11–12, for which the RMS residuals were 0.77 Å.

7.3 Results

Most of the results discussed below are based on the blue spectra (Figure 7.1). In the red spectra (Fig. 7.2), we only detected He II $\lambda 6562$ in emission, and a blend of Na D and He I $\lambda 5875$ in absorption. Because of the lower spectral resolution and the blending, we could not use these spectra to obtain velocities, so they will not be discussed further.

7.3.1 Emission features.

In the best spectra, we detect in emission He II $\lambda 4686$. We also detect lines at $\lambda\lambda 4200$, 4339, 4542, 4860 and 5413 (Fig. 7.3; Table 7.2). There is some question as to whether the second and fourth of these are $H\gamma$ and $H\beta$, since the resolution of our spectra are not sufficient to enable us to distinguish the contribution of the relevant H and He II contributions to the features with approximately the same wavelength. The other three lines are from the Pickering series of ionized helium: $\lambda 5411$ ($n_2 = 7$), $\lambda 4542$ ($n_2 = 9$) and $\lambda 4200$ ($n_2 = 11$). This makes it virtually certain that at least some He II $\lambda 4860$ ($n_2 = 8$) and $\lambda 4339$ ($n_2 = 10$) is present. Thus we agree with Hanes (1985) in assigning these lines to ionized helium and not to hydrogen (Duerbeck & Seitter 1990).

7.3.2 Absorption features.

We detect in absorption the Ca H and K lines and several lines of the Balmer series of hydrogen ($H\gamma$, $H\delta$). $H\beta$ and $H\alpha$ are not seen, being overwhelmed by the He II emission lines. Given the peculiar emission spectrum, it is of some interest that we are detecting hydrogen in absorption, not helium. It is unlikely that these lines are actually the Pickering series of ionized helium, as we do not detect the intermediate lines, *e.g.*, at 4025 Å. Based on the observed line ratio of the calcium lines to $H\delta$ (which should not be very much affected by the presence of a hot continuum) of ~ 0.5 , as well as the absence of the G band ($\lambda \sim 4200$) we estimate the spectral type of the companion to be somewhat earlier than the $G0 \pm 5$ estimated by Hanes (1985); our preferred value is $F8 \pm 2$ (see *e.g.*, Jacoby, Hunter & Christian 1984). This implies a secondary mass of $\sim 1.1 - 1.3 M_{\odot}$. Schaefer (1990), from the colors at minimum light, preferred a spectral type G3–6 ($M_2 \sim 0.9 - 1.0 M_{\odot}$).

We also detect several lines of neutral helium in absorption, at $\lambda 4471$, $\lambda 5875$ (blended with Na D), and $\lambda 3888$ (blended with $H\zeta$). The detection of He I $\lambda 3888$ is reasonably secure, because of the strength of this feature relative to $H\delta$ and $H\gamma$. These lines are transitions in the triplet series of neutral helium from the metastable 2^3S level or the 2^3P level. Collisions rapidly convert helium atoms from the triplet branch to the singlet branch, which then rapidly decay by radiation to the ground state. Thus the He I lines must arise

in regions of low density, $N_e \lesssim 4 \times 10^3 \text{ cm}^{-3}$ (Osterbrock 1989). The lines are not resolved in our spectra and are therefore unlikely to arise in the disk. On the other hand, since the velocity of the lines is not high, $v \sim 120 \text{ km s}^{-1}$, these lines are unlikely to arise in the shell of previous nova eruptions. Such lines have been seen in LMXBs: AC211 (Naylor *et al.* 1988), X0921-630 (Branduardi-Raymont *et al.* 1983) and X1822-371 (Mason *et al.* 1982). In AC211 these lines are assumed to arise in the disk; in U Sco, on the other hand, these lines appear to follow the calcium absorption lines, presumed to arise in the atmosphere of the companion. Taken together, this suggests that the helium lines are arising in some sort of corona around the secondary star. Higher resolution observations should be able to measure a difference in width between the stellar and the nonstellar lines.

It is quite possible that *none* of the absorption lines are coming from the secondary star. However, the fact that the calcium lines are resolved (Table 7.2) would suggest that they are stellar; we also detect the Mg b band, which is a certain indication of stellar origin. Therefore we are confident that we are indeed seeing lines from the stellar companion.

7.3.3 Emission line velocities.

The spectra were first normalized by a seventh order polynomial fit to the continuum. The velocity was determined by fitting Gaussian profiles to all emission lines present, keeping the wavelength ratios fixed to the known values. The errors quoted are formal errors of the fit assuming Poisson errors on the object spectrum, added in quadrature to the error on the wavelength calibration.

Because the error in Schaefer's period ($P = 1^d2344 \pm \sigma_p$, where $\sigma_p = 0^d0025$) was large enough to preclude unambiguous phase connection of the 1990 with the 1991 data, we needed a better determination of the orbital period of the system. R. Wade (*personal communication*) observed an eclipse on 1990 June 1.20. Using this time, Schaefer's eclipse ephemeris and our absorption line velocities, it is possible to refine the period. We searched periods within $\pm 10\sigma$ of Schaefer's period, and two solutions with acceptable χ^2 values were found: $P_1 = 1^d225806 \pm 0^d000129$, and $P_2 = 1^d221163 \pm 0^d000055$. The former has 263 periods between the two eclipses, and the latter 264. P_1 is $3.4\sigma_p$ smaller than the photometric period, and P_2 is $5\sigma_p$ smaller. Thus *a priori* P_1 is the preferred period. However, χ^2_ν for the fit to the absorption line radial velocities is 0.9 for P_2 as opposed to 2.1 for P_1 , favoring P_2 . Given the radial velocity uncertainties and the continuous phase coverage of Schaefer's photometry, we prefer the longer period P_1 . In Table 7.3 we show the solutions for both the emission and absorption line systems for both periods, with and without the constraint that the γ -velocities of the two systems should be the same.

The emission-line velocities were fitted to a sine curve with these two orbital periods. The best fit with $P = 1^d221163$ is shown in Figure 7.4 ($\chi^2_\nu = 3.7$), and the results are shown in Table 7.1.

The full width at zero intensity of the He II 4686 emission line ranges from 33 to 49 Å, with a mean value of 44 Å. The shape of the line varies systematically with the orbit, indicating the presence of an S-wave component. The blue wavelength side is enhanced when the emission lines are moving toward us, so our derived amplitude is probably an upper estimate for the velocity of the white dwarf. The variation of the equivalent width of the line does not appear to be correlated with orbital phase (Figure 7.5).

7.3.4 Absorption line velocities

For each spectrum, we measured the absorption line velocity (Table 7.1) using the cross-correlation technique of Tonry & Davis (1979). The emission lines were excised and replaced by a polynomial fit to the continuum. The cross-correlation was performed over the range 3800-5450 Å, except where the wavelength coverage fell slightly short of this (1990 June 22 and 1991 July), in which case the region was 200 Å shorter. We used the spectrum from 1990 June 23.2551 as the template, being the spectrum with the highest signal-to-noise ratio; the velocity of this spectrum was determined using profile fitting to the absorption lines. The position of the correlation peak was measured by fitting a parabola to the central 5 pixels of the highest peak. The heights of the peaks varied from 0.32 to 0.80. The error on each measurement was obtained using Monte Carlo simulations, by measuring the RMS of the shift in the peak when spurious peaks, derived from the noise in the cross-correlation spectrum, were added to it.

The data and the best fit solution are plotted in Figure 7.4, and the results shown in Table 7.1. The best fit had $\chi^2_\nu = 0.9$, using the period P_2 . The preferred period P_1 had $\chi^2_\nu = 2.1$, higher but still acceptable. With the preferred period, the phase lag of the emission lines with respect to the absorption lines is 0.4, close to the expected value of 0.5. With the shorter period the lag is 0.24. This is not unusual, especially with LMXBs, *e.g.*, in Cen X-4 (McClintock & Remillard 1990), and presumably indicates the emission is coming from a “hot spot” on the disk.

In case our cross-correlation was being biased by the neutral helium absorption lines, which may not be associated with the companion, we also measured the velocities when these lines were excised and replaced by the continuum fit. In all cases, these velocities are consistent with the original cross-correlation velocities, so the small K we measure is not

due to contamination by nonstellar lines. Similar results are obtained when we measure only the velocity of the calcium lines.

The discrepancy between γ_a and γ_e was worrying. We repeated the fit to both sets of velocities, subject to the constraint that $\gamma_a = \gamma_e$. The resulting fits are shown in Table 7.3. The χ^2_ν of the constrained fit was only marginally worse than without the constraint, and the velocity amplitudes were consistent within the errors.

7.4 Discussion

We have established U Sco to be a double-lined spectroscopic binary. Since emission lines are not necessarily reliable indicators of the motion of the primary (Horne & Marsh 1986; see also our remarks about the S-wave component above), we begin by considering only the motion of the secondary, as represented by the absorption line system. Using our preferred value $P_1 = 1^d225806$, we measure the mass function to be $f_a(M_{wd}) = 0.0054 M_\odot$. Taking the companion mass to be $M_2 = 1.3 M_\odot$ (appropriate for an F5V, the most massive of the suggested spectral types for the companion), and $\sin i = 1$, since the system is eclipsing, we infer $M_{wd} = 0.23 \pm 0.12 M_\odot$. Using the shorter period $P_2 = 1^d221163$, we find $f_a(M_{wd}) = 0.032 M_\odot$, and $M_{wd} = 0.46 \pm 0.15 M_\odot$. If M_2 is really as low as $0.23 M_\odot$, then the white dwarf progenitor evolution must have been aborted soon after it left the main sequence; a $3 M_\odot$ star, for instance, has a core mass of $0.3 M_\odot$ when it leaves the main sequence. The unusually long period of U Sco is also consistent with this inference.

Thus an upper limit to the mass of the white dwarf is given by the lower value of the period, although this is not the value favored by the photometry (Schaefer 1990). Using the shorter period, we find a 3σ upper limit to the mass of the white dwarf of $0.9 M_\odot$.

If we assume the velocity of the emission lines represents the velocity of the white dwarf, then the ratio of the velocity amplitudes gives us the mass ratio: $K_a/K_e = M_{wd}/M_2$. Taking the preferred value for the period P_1 , and again assuming $M_2 = 1.3 M_\odot$, we find $M_{wd} = 0.29 \pm 0.14 M_\odot$, in excellent agreement with our first determination. For the shorter of the period P_2 , we derive $M_{wd} = 0.60 \pm 0.14 M_\odot$. In the latter case, the white dwarf appears to be very ordinary; in the former case, which is preferred by the photometry, the white dwarf appears to be undermassive.

It has been pointed out (R.F. Webbink, *personal communication*) that the six high emission line velocities all fall within phase 0.1 of eclipse, as defined by the absorption line ephemeris, and thus may be contaminated. If these velocities are removed, a sine fit to the remaining twelve velocities with $P = 1^d221163$ gives an amplitude of $48 \pm 23 \text{ km s}^{-1}$, *in phase* with the absorption line system. However, the systemic velocity is $-66 \pm 20 \text{ km s}^{-1}$, very different from $\gamma_a = 71 \pm 8 \text{ km s}^{-1}$ measured for the absorption lines. Thus we do not believe this solution is physical. In any case, provided the absorption lines are associated with the companion, the mass function from the absorption lines provides an upper limit on M_{wd} .

We note that we have also finally detected hydrogen in the spectrum of the companion. This in turn suggests that the anomalous emission spectrum is not due to anomalous com-

position of companion. This finding exacerbates the objections to the proposed accretion instability models.

Our observations suggest that neither of the two proposed models for the outburst of U Sco is viable. The white dwarf is not massive, as demanded by the thermonuclear models. The composition of the secondary does not appear to be anomalous, as required for the accretion models. In passing, we also note that this means that the high mass white dwarfs demanded by the AIC model have yet to be discovered.

We thank Ron Webbink for helpful comments on an early draft of this paper. We also thank Jim Houck, Michael Strauss, Alain Picard, and George Djorgovski for obtaining some of the spectra, and Wal Sargent, Jesse Greenstein, and T. Prabhu for helpful discussions. We acknowledge the Packard foundation and the NSF for the support of this research.

Table 7.1 Journal of observations

| Number | UT date | Emission line velocity (km s ⁻¹) | Absorption line velocity (km s ⁻¹) |
|--------|------------------|--|--|
| 1 | 1990 Jun 21.2490 | -39 ± 35 | 46 ± 36 |
| 2 | 1990 Jun 21.2730 | -89 ± 35 | 143 ± 54 |
| 3 | 1990 Jun 22.2085 | -54 ± 35 | 154 ± 37 |
| 4 | 1990 Jun 22.2289 | -18 ± 35 | 95 ± 42 |
| 5 | 1990 Jun 22.2491 | -10 ± 35 | 219 ± 68 |
| 6 | 1990 Jun 23.2144 | 128 ± 34 | 82 ± 20 |
| 7 | 1990 Jun 23.2346 | 168 ± 34 | 93 ± 21 |
| 8 | 1990 Jun 23.2551 | 222 ± 34 | 93 ± 14 |
| 9 | 1990 Jun 24.2410 | 167 ± 34 | 9 ± 27 |
| 10 | 1990 Jun 24.2617 | 169 ± 34 | 53 ± 19 |
| 11 | 1990 Jun 24.2824 | 177 ± 34 | 29 ± 33 |
| 12 | 1991 Jun 10.2161 | 6 ± 34 | 230 ± 47 |
| 13 | 1991 Jun 10.3608 | -190 ± 34 | 112 ± 31 |
| 14 | 1991 Jul 11.2351 | -91 ± 34 | 30 ± 30 |
| 15 | 1991 Jul 12.1874 | -19 ± 35 | 54 ± 38 |
| 16 | 1991 Jul 12.2065 | -36 ± 35 | 29 ± 56 |
| 17 | 1991 Aug 8.2033 | -177 ± 35 | ... |
| 18 | 1991 Aug 8.2252 | -111 ± 36 | -11 ± 61 |

Notes — All exposures except the first two were 1500 s in duration; the exposures from 1990 June 21 were 1800 s long. The wavelength coverage for the blue camera was 3800 – 5500 Å with a dispersion of 2.1 Å pixel⁻¹, and a 1" slit. A variety of setups was used for the red camera: for 1990 June the wavelength coverage was 5400 – 10260 Å with a dispersion of 6.1 Å pixel⁻¹; for 1991 June/July 5460 – 8000 Å, dispersion 3.2 Å pixel⁻¹; for 1991 August 5570 – 6880 Å, dispersion 1.6 Å pixel⁻¹.

Table 7.2 Line widths and intensities

| Line | FWHM ^a (Å) | Eq. width (Å) |
|------------------------|--------------------------|------------------|
| Absorption lines | | |
| He I λ 3888 | 5.9 | 2.2 |
| Ca K λ 3933 | 6.7 | 2.8 |
| Ca H λ 3968 | 9.4 | 0.7 |
| H δ | 4.5 | 1.7 |
| H γ | 8.0 | 1.1 |
| He I λ 4471 | 4.5 | 0.6 |
| He I λ 5015 | 6.0 | 0.3 |
| Emission lines | | |
| He II λ 4200 | 7.6 | 0.6 |
| He II λ 4338 | 6.9 | 0.6 |
| He II λ 4542 | 8.1 | 1.5 |
| He II λ 4686 | 10.7 | 13.4 |
| He II λ 4860 | 9.2 | 2.5 |
| [O III] λ 5007 | 5.9 | 1.0 |
| He II λ 5412 | 12.2 | 2.9 |

^a The instrumental resolution was 4.5 Å.

Table 7.3 Orbital parameters for U Sco

| Parameter | $P_2 = 1^d221163$ | | $P_1 = 1^d225806$ | |
|--------------------------------|----------------------|----------------------|----------------------|----------------------|
| | free | constrained | free | constrained |
| $K_a(\text{ km s}^{-1})$ | 64 ± 14 | 72 ± 16 | 35 ± 17 | 42 ± 19 |
| $\gamma_a(\text{ km s}^{-1})$ | 71 ± 8 | 52 ± 10 | 76 ± 11 | 64 ± 13 |
| $T_{0,a}^a(\text{JD-2448000})$ | 63.2296 ± 0.0041 | 63.2085 ± 0.0050 | 63.2839 ± 0.0060 | 63.2635 ± 0.0085 |
| χ^2_ν | 0.96 | 2.7 | 2.1 | 2.5 |
| $K_e(\text{ km s}^{-1})$ | 145 ± 13 | 145 ± 14 | 156 ± 19 | 158 ± 21 |
| $\gamma_e(\text{ km s}^{-1})$ | 24 ± 16 | 52 ± 10 | 38 ± 11 | 64 ± 13 |
| $T_{0,e}^a(\text{JD-2448000})$ | 63.555 ± 0.034 | 63.534 ± 0.045 | 63.759 ± 0.032 | 63.748 ± 0.042 |
| χ^2_ν | 3.7 | 2.7 | 2.4 | 2.5 |

^a T_0 is the time of spectroscopic conjunction.

References

Bhattacharya, D. & van den Heuvel, E.P.J. 1991, *Phys Rep*, 203, 1

Branduardi-Raymont, G., Corbet, R.H.D., Mason, K.O., Parmar, A.N., Murdin, P.G. & White, N.E. 1983, *MNRAS*, 205, 403

Duerbeck, H.W. & Seitter, W.C. 1990, in IAU Colloq. 122, *Physics of Classical Novae*, ed. A. Cassatella & R. Viotti, (Berlin: Springer), p. 425

Duschl, W.J., Livio, M. & Truran, J.W. 1990, *ApJ*, 360, 232

Hanes, D.A. 1985, *MNRAS*, 213, 443

Horne, K. & Marsh, T.R. 1986, *MNRAS*, 218, 761

Jacoby, G.H., Hunter, D.A. & Christian, C.A. 1984, *ApJS*, 56, 257

Mason, K.O., Murdin, P.G., Tuohy, I.R., Seitzer, P. & Branduardi-Raymont, G. 1982, *MNRAS*, 200, 793

McClintock, J.E. & Remillard, R.A. 1990, *ApJ*, 350, 386

Naylor, T., Charles, P.A., Drew, J.E. & Hassall, B.J.M. 1988, *MNRAS*, 233, 285

Oke, J. B. & Gunn, J. E. 1982, *PASP*, 94, 586

Osterbrock, D.E. 1989, *Astrophysics of gaseous nebulae and active galactic nuclei* (Mill Valley: University Science Books)

Schaefer, B.E. 1990, *ApJ*, 355, L39

Starrfield, S., Sparks, W.M. & Shaviv, G. 1988, *ApJ*, 325, L35

Tonry, J. & Davis, M. 1979, *AJ*, 84, 1511

Webbink, R.F. 1990, in IAU Colloq. 122, *Physics of Classical Novae*, ed. A. Cassatella & R. Viotti, (Berlin: Springer), p. 405

Webbink, R.F., Livio, M., Truran, J.W. & Orio, M. 1987, *ApJ*, 314, 653

Figure captions

Figure 7.1 — All eighteen blue spectra, plotted in order of phase; the phase of the observation is shown at left, and the figure at right identifies the observation (col. 1 of Table 7.1). The spectra have been normalized by a polynomial fit to the continuum. The spectra of 1991 July 11–12 have a slightly different wavelength coverage. Note that the spectra vary in quality considerably because of different seeing conditions.

Figure 7.2 — A red spectrum from the night of 1991 June 10. The only stellar features are He II λ 6562 and a blend of Na D and He I λ 5875.

Figure 7.3 — Two of our best blue spectra, taken on the night of 1990 June 23 and 1991 June 10, with the emission and absorption lines identified. The lines at λ 4046 and λ 4358 are due to poor night sky subtraction. Gaussian profile fits to the lines with fixed wavelength ratios are also shown.

Figure 7.4 — Sine fits to the emission lines (*filled circles, solid line*) and absorption lines (*open squares, dashed line*), using $P = 1^d221163$. The x -axis shows phase as defined by the absorption line ephemeris.

Figure 7.5 — Equivalent width of He II λ 4686 as a function of orbital phase. No significant variation is seen.

Figure 7.1

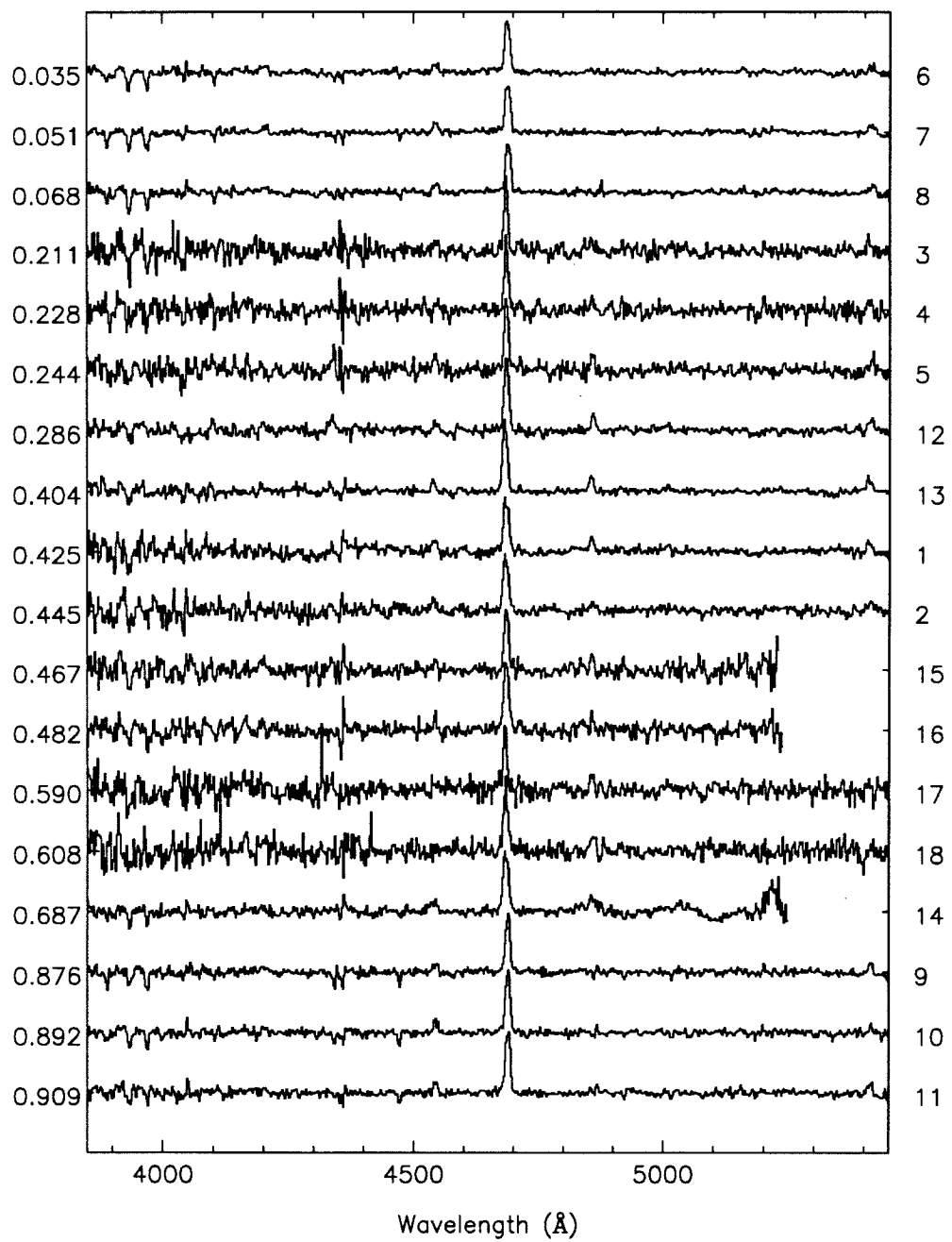


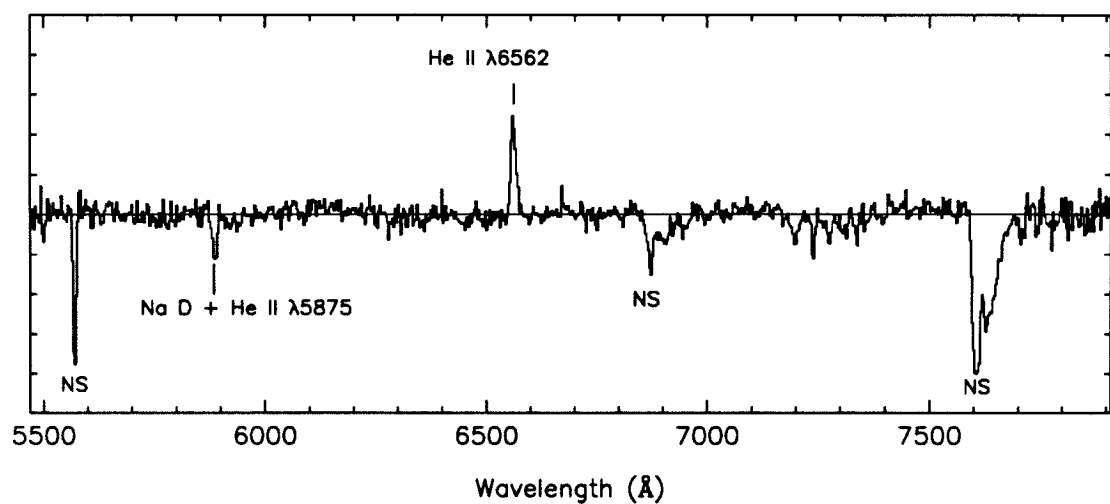
Figure 7.2

Figure 7.3

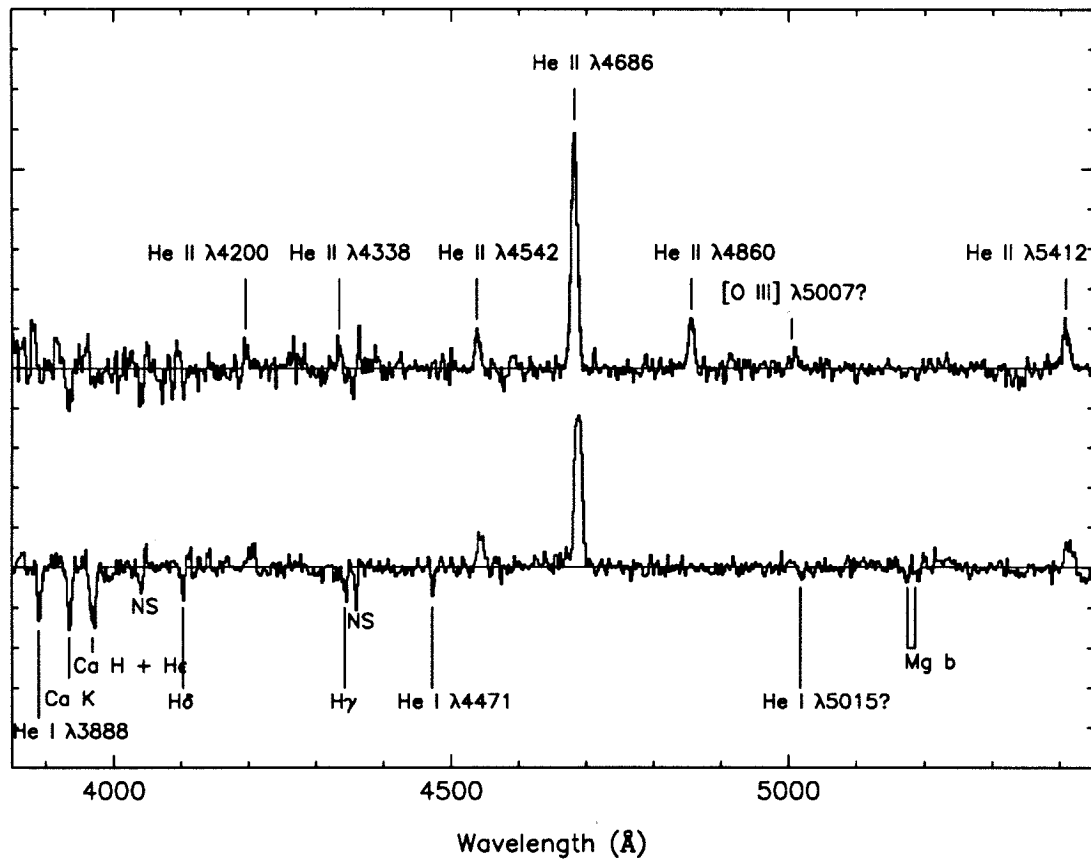


Figure 7.4

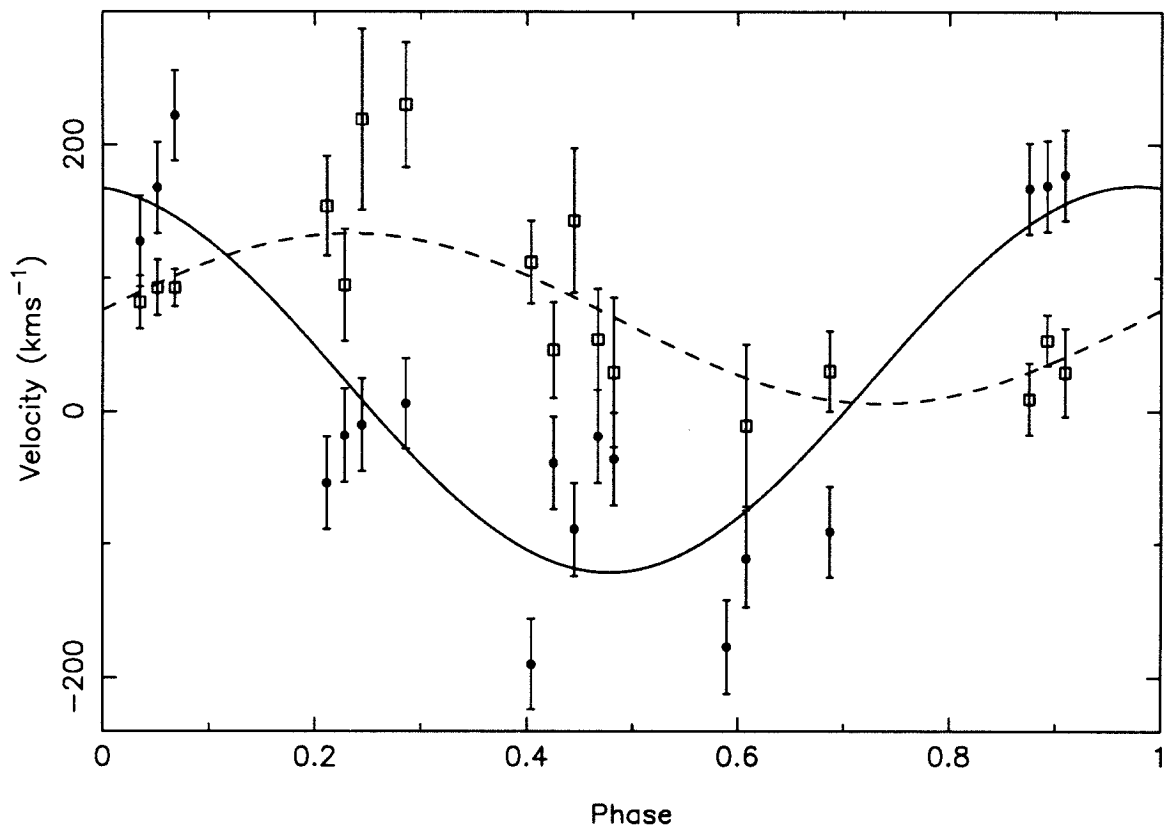
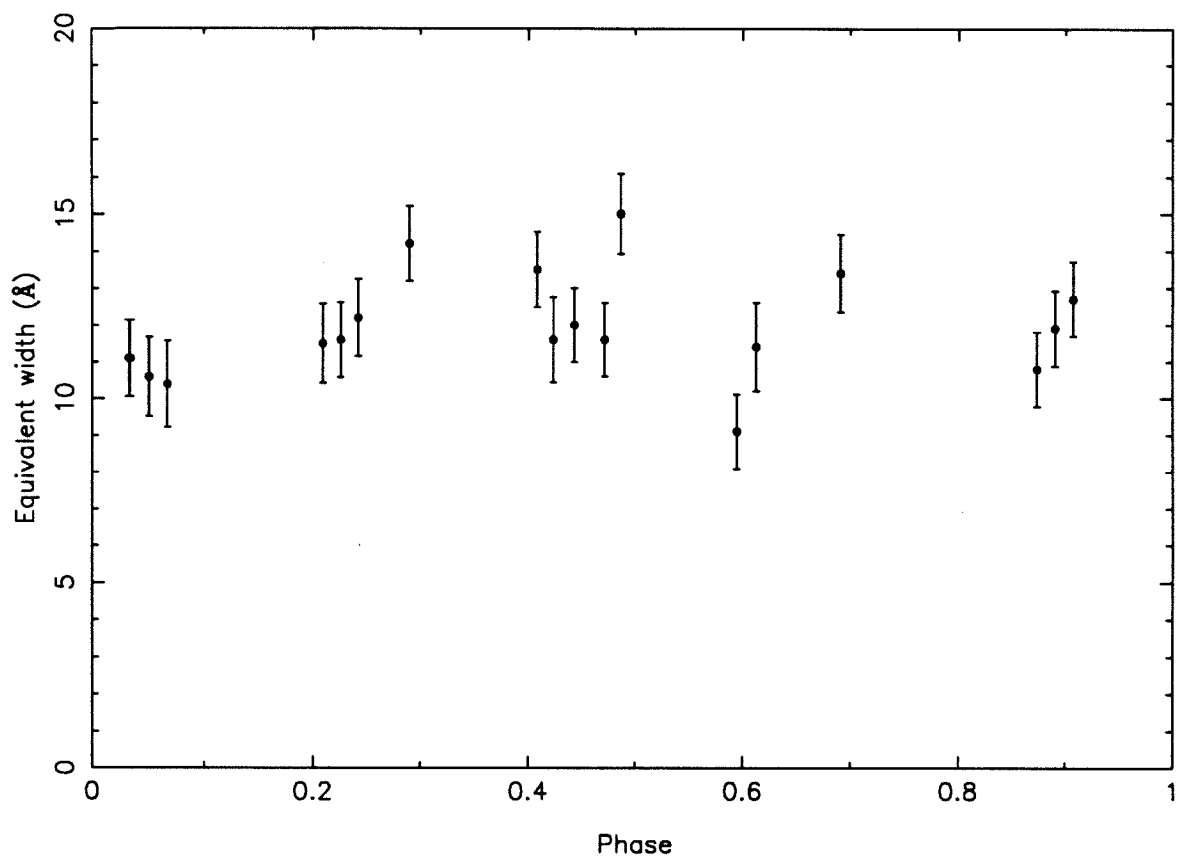


Figure 7.5

Chapter 8

The kinematics of low mass X-ray binaries

Abstract

There are two competing models for the formation of low mass X-ray binaries (LMXBs) in the disk: the direct formation model, where the neutron star is formed by the supernova explosion of a massive star in a binary system, and the accretion-induced collapse model (AIC), where accretion pushes a white dwarf over the Chandrasekhar mass, whereupon it collapses to form a neutron star. Cowley and coworkers have argued that the kinematics and distribution of LMXBs in the Galaxy favor the latter model.

We explore the possibility that the direct formation model could also be consistent with the observations. We present new spectroscopic observations of disk LMXBs which we use to measure their radial velocities. We collect together from the literature a reliable list of LMXB velocities. We present numerical simulations of a supernova explosion in a tight binary system, with and without an extra velocity “kick”, of the kind thought to be associated with the birth of pulsars. We conclude that the observed velocities, scale height, and period distribution of disk LMXBs are also consistent with such an origin.

8.1 Introduction

Low mass X-ray binaries (LMXBs) are systems consisting of a neutron star accreting matter from a low mass ($\lesssim 1 M_{\odot}$) companion, in an orbit with period between 0.2 h and 10 d or longer. The presence of a low mass star so close to a neutron star is surprising. Neutron stars are usually thought to be the remnants of a Type II supernova explosion of a massive star, with $M_1 \gtrsim 8 M_{\odot}$. At the current orbital separation, the secondary star in LMXBs is within the main sequence radius of the neutron star progenitor, let alone the stellar radius immediately before the supernova explosion. In addition, in the formation of a $1.4 M_{\odot}$ neutron star from a $8 M_{\odot}$ primary, more than half the mass of the binary is lost, and so the system should have become unbound.

Two solutions to this problem have been proposed. The first proposes that the binary began as a very wide system. When the primary fills its Roche lobe, its envelope engulfs the secondary. During this common-envelope phase, the two stars spiral together. The final system consists of the highly evolved core of the massive star, and the essentially unevolved secondary. The evolved core then undergoes a Type II supernova explosion, leaving a neutron star as a remnant. If the binary survives, it can eventually become visible as an LMXB when the secondary fills its Roche lobe and begins transferring matter onto the neutron star. We will refer to this as the direct formation model.

The alternate hypothesis, known as the Accretion Induced Collapse (AIC) model, is that the neutron star is not born explosively. In this scenario, if a white dwarf, with mass close to the Chandrasekhar limit, accretes enough matter to drive it over this limit, it can implode and form a neutron star. The only mass lost from the system in this case is the difference in binding energy between a white dwarf and a neutron star,

$$\Delta M = \frac{3GM^2}{5R_{\text{ns}}c^2} \sim 0.18 M_{\odot} \quad (8.1)$$

(Verbunt, Wijers & Burm 1990). This then obviates the problem of the supernova explosion disrupting the binary.

Helfand, Ruderman & Shaham (1983) invoked AIC to explain the presence of low-mass white dwarf in a wide binary around a neutron star in PSR1953+29. They argued that AIC is necessary to explain not only the survival and circularity of the binary, but also the small distance of the system from the Galactic plane ($l = 0^{\circ}4$); the mass loss associated with the birth of the neutron star in the direct formation model would have left the system with a velocity $v \sim 100 \text{ km s}^{-1}$.

This scenario received support with the discovery of apparently young, high field pulsars in binaries with old companions. Since the magnetic fields of neutron stars were thought

to decay on timescales of order 10^7 y, the discovery of high field pulsars in binaries such as PSR0820+02 and Her X-1 suggested that these neutron stars must have formed recently via AIC.

Observational support for the AIC model is found in the distribution of LMXBs in the Galaxy (Fig. 8.1). While the massive X-ray binaries are clearly a disk population, being concentrated close to the galactic plane ($\langle |b| \rangle = 3^\circ.2$) and spread along the galactic equator, the LMXBs are concentrated towards the bulge and have a wider latitude distribution ($\langle |b| \rangle = 7^\circ.0$). These characteristics suggest they belong to an old population, which is allowed (but not demanded) by the AIC model. Support for this was found by a study of the kinematics of disk[†] LMXBs by Cowley *et al.* (1987). They found that the LMXBs have a large velocity dispersion and a small galactic rotation, again suggesting that they represent an old population.

However, there are serious problems with the AIC hypothesis. First, the conditions required for collapse are very stringent. Most accreting white dwarfs, in cataclysmic variables, appear to be being eroded in mass with each outburst rather than gaining mass. Theoretical calculations indicate that only very massive white dwarfs just below the Chandrasekhar limit and accreting at very high rates ($\dot{M} \gtrsim 10^{-7} M_\odot \text{ yr}^{-1}$) will grow in mass, and therefore be candidates for AIC. However, the existence of such white dwarfs has yet to be demonstrated. The recurrent novae were considered to be the best candidates for such objects, but spectroscopy of the recurrent nova U Sco (Johnston & Kulkarni 1992[‡]) put an upper limit of $0.9 M_\odot$ on the mass of the white dwarf in this system. Thus no good candidates for the massive white dwarfs needed for AIC have yet been found.

Furthermore, there are philosophical objections to the AIC formation mechanism for the neutron stars in LMXBs. The low mass black hole binaries, such as A0620-00, cannot have formed via this route. The lower limit for the mass of the black hole in this system is $3.3 M_\odot$, and so it clearly cannot have been formed by accretion onto a $1.4 M_\odot$ white dwarf from a companion with mass $\lesssim 1 M_\odot$. Under the AIC model, such a system requires a completely different mechanism, either the direct formation of the black hole, or possibly triple star evolution, where the current low mass secondary was originally the distant third star orbiting around a massive, close binary (Eggleton & Verbunt 1986). The direct formation model, on the other hand, can encompass systems like A0620-00 by a straightforward extension to higher mass progenitors.

[†] A confusing turn of phrase, but one we will use to distinguish the LMXBs under discussion from globular cluster LMXBs, whose formation mechanism is probably entirely different, due to the efficacy of tidal capture in clusters.

[‡] See Chapter 7.

Secondly, one of the motivations for the AIC model was the need to explain apparently young neutron stars in old binaries, in the light of the belief that pulsar magnetic fields decay with age. This belief arose from population studies of galactic pulsars, where the spindown age, dependent on the magnetic field, was much older than the “kinematic age” as measured by the height above the disk (see Bhattacharya 1989 for a review). However, as the velocities of more pulsars have been measured, the discrepancy between these ages has essentially disappeared. New statistical studies favor models without field decay (Bailes 1989; Bhattacharya *et al.* 1991). In addition, Her X-1, one of the prototypical examples for a neutron star formed by AIC, is at such a large distance from the galactic plane that Verbunt *et al.* (1990) concluded that the neutron star must have formed from a massive progenitor, acquiring a large velocity from the mass loss associated with the supernova explosion.

Thus the evidence in favor of an AIC origin for the neutron stars in LMXBs appears to rest on their sky distribution and their kinematics. However, the kinematics analysis (Cowley *et al.* 1987, 1988) was based on a modest number of velocity determinations, quite a few of which are unreliable (see § 8.3). Here we explore the possibility that both the kinematics and sky distribution could be consistent with the direct formation model. In § 8.2, we present the results of a program to increase the number of disk LMXBs with measured radial velocities. We have observed a total of nine objects, and present new velocities for seven of them. In § 8.3, we present a list of *reliable* velocities compiled from the literature. In § 8.4, we discuss the direct formation model in more detail. We present the results of simulations of supernovae in close binary systems. The results are discussed in § 8.5.

8.2 Observations

Spectra were obtained using the Double Spectrograph (Oke & Gunn, 1982) at the Cassegrain focus of the Hale 5 m telescope, during five observing runs from August 1989 to August 1991. A complete log of observations is shown in Table 8.1. A variety of instrumental setups was used, resulting in dispersion ranging from $\sim 12 \text{ \AA}$ to $\sim 1.1 \text{ \AA}$; our preferred setup resulted in a resolution of 4 \AA in the blue camera, and 3 \AA in the red camera. A total of nine objects was observed at least twice, in order to remove the effects of the orbital motion. Exposure times were 1800 s or (in some cases) 2400 s. As we were only interested in velocities, a narrow slit ($1''$) was used, and the data were not flux-calibrated.

The data were reduced using the FIGARO data reduction package (Shortridge 1986). Wavelength calibration was done by fitting a 3rd order polynomial to the comparison arc lines obtained immediately after the object exposure. Comparison of arcs taken for different objects show that the instrument is extremely stable, with shifts typically less than 0.2 pixels, so instrument flexure is not a problem.

Velocities were obtained by either using cross-correlation with a radial velocity standard, or by profile fits to the emission lines. In the former case, the data were binned onto a logarithmic scale, a low order polynomial fit to the continuum was subtracted, and the spectra were apodized with a cosine bell covering 10% of the spectrum. The position of the correlation peak was measured by fitting a parabola to the central 5 pixels of the highest peak, and the error determined using the technique of Tonry & Davis (1979). For the emission lines, the spectrum was normalized by a 7th order polynomial fit to the continuum. The center of the emission line was then determined using Gaussian fits to all emission lines present. The errors quoted are formal errors of the fit assuming Poisson errors on the object spectrum.

8.3.1 Reliability of the velocities

There are many observational problems associated with measuring the radial velocities of these objects. All the objects are faint, typically $mv \gtrsim 18$. In some cases the only observable features were in emission, and velocities measured from emission lines are susceptible to many effects which distort the velocity, such as outflows, asymmetries of the line due to disk structure, *etc.* In addition, we know *a priori* that all these objects are binary, and we therefore expect the velocities to be contaminated by the binary motion. Where we have enough data, we performed a sinusoidal fit to our measured velocities using the known orbital period; our only other recourse is to average a sufficient number of spectra that the orbital motion is taken out.

In particular, at least one object (AC211 in M15) shows large velocity differences between the He II $\lambda 4686$ emission line, which has a base approximately at rest with respect to the cluster and a peak redshifted by $\sim +100 \text{ km s}^{-1}$, and the He I $\lambda 4471$ absorption line, which has a velocity of $\sim -150 \text{ km s}^{-1}$ with respect to the cluster (Naylor *et al.* 1988). Naylor & Charles (1989) argue that the latter represents the true velocity of the object; Bailyn, Garcia & Grindlay (1989) argue that the absorption lines arise in an outflow from the outer Lagrangian point. If other LMXBs show similar discrepancies, then using emission lines to derive the space velocity of the system could give completely erroneous results. However, as no other LMXBs with measured absorption and emission line velocities show such a discrepancy (the apparent discrepancy in Cen X-4 found by Cowley *et al.* 1988 having disappeared on further analysis by McClintock & Remillard 1990), and since Naylor *et al.* did not present a full orbital solution for the emission lines, we will reserve judgement on this issue[†].

Variations in γ , the systemic velocity, have also been seen in some cataclysmic variables, notably the SU UMa class of dwarf novae. Z Cha shows narrow Balmer absorption whose γ -velocity varies by $\pm 200 \text{ km s}^{-1}$ from the systemic velocity during supermaximum; WZ Sge showed a similar effect during outburst (Vogt 1981). In these cases, the dynamics of the system are better understood, and the absorption can be modelled as arising in material moving in non-circular orbits around the primary.

8.3.2 Individual objects

Representative spectra of the objects are shown in Figure 8.2. Here we discuss features of individual objects.

- *X0042+327*. — The optical identification of this object is uncertain (Charles *et al.* 1978). No emission lines were seen in the spectrum; absorption lines consistent with the spectrum of a G0–G8 star (Ca H and K, H γ , H δ) are seen. The velocities are based on cross-correlation with a dG8 radial velocity standard. The two determined velocities (from 1989 and 1991) were very different, and so no average velocity is given.
- *X0142+614*. — No lines were seen in these spectra, therefore no velocity could be determined.
- *X0614+091 = V1055 Ori* — The C III/N III blend ($\sim \lambda 4640$) is clearly visible. No other identifiable features are present, so since the shape of this blend is highly variable (*e.g.*, Canizares, McClintock & Grindlay 1979), no velocity can be measured.

[†] It is conceivable that U Sco represents another case (see Chapter 7, § 7.4). Higher quality data are needed to resolve this.

- *X1728-169 = GX9+9* — The optical counterpart of this object is the southern component of a close triple (Schaefer 1990); the triple is labelled as star DMB in the finding chart of Doxsey *et al.* (1977). Our spectra show He II and H α in emission.
- *X1813-140 = GX17+2* — The identification of this object with the X-ray binary is made on the grounds of coincidence with a VLA radio position (Hjellming & Wade 1971; Braes & Miley 1973). No emission lines are seen in our spectra, which show strong Ca H and K lines, the Na D line, and other features typical of dwarf G stars. Thus the association of this object with the X-ray source is doubtful.
- *X1837+049 = Ser X-1* — Variable, weak He II emission is seen in this object, as well as the $\lambda 4640$ blend.
- *X1908+005 = Aql X-1* — Variable He II, H α , H β and the $\lambda 4640$ blend are seen.
- *X1916-053* — The optical counterpart of this object is a 22nd magnitude star right next to a much brighter object (Walter *et al.* 1982). A single spectrum of this object showed no identifiable features.
- *X1957+115* — We see He II and $\lambda 4640$ emission, as well as H β in a single spectrum.
- *X2129+47 = V1727 Cyg* — This object showed $\lambda 4640$ and He II emission during outburst (Thorstensen *et al.* 1979), but has shown no emission since (Thorstensen *et al.* 1988). The quiescent spectrum also resembles a late F star, instead of the expected low-mass dwarf. Chevalier (1989) suggests the optical counterpart is either an interloper along the line of sight, or is possibly the third star in a triple system. Our spectra show strong Ca H & K and hydrogen absorption features of the F star.

Table 8.1 shows our observed velocities, together with the features which were used to determine them.

8.3 A definitive list of LMXB velocities

In Table 8.2 we collect together a list of radial velocities for LMXBs that we consider reliable. The measurements for individual objects are discussed below. Our criteria were strict, demanding a full orbital solution so that the systemic velocity is well determined. Thus, in the light of the sparse data available, we will not use the velocities determined in this work for X0042+327, GX9+9, GX17+2 or Ser X-1. Nor will we include the velocities determined by Cowley *et al.* (1987) and Cowley *et al.* (1988) for the following objects: X1254-690, X1627-673, X1636-536, X1755-338. Several of their velocities were based on sparse data, and turned out to be inconsistent with later, more detailed studies.

- *X0748-676* — X0748-676 was discovered as a bright X-ray nova by EXOSAT in February 1985. Crampton *et al.* (1986) measured a velocity of $v = +20 \pm 64 \text{ km s}^{-1}$ using the He II $\lambda 4686$ line, from spectra taken one month after outburst. The distance was derived from the X-ray luminosity.
- *X0921-630* — The optical counterpart of this object shows emission lines of He II $\lambda 4686$, $\text{H}\beta$, the C III/N III blend at $\lambda 4640$, and some of the higher Balmer lines. Cowley *et al.* (1982b) measured $v = 52 \pm 8 \text{ km s}^{-1}$ using the base of the He II emission line, and determined a distance of 7 kpc from the absolute magnitude of the companion.
- *X1455-314 = Cen X-4* — Cen X-4 has been observed twice as an X-ray nova, in 1969 and 1979. McClintock & Remillard (1990) observed late-type absorption lines in the quiescent spectrum, as well as emission lines of $\text{H}\alpha$, $\text{H}\beta$ and He II. They measured a systemic velocity of $v = 137 \pm 17 \text{ km s}^{-1}$ from the absorption lines, and deduced a distance of 1.2 kpc from the X-ray luminosity.
- *X1516-569 = Cir X-1* — Cir X-1 has been argued to be associated with the nearby ($\sim 25'$ distant) supernova remnant G321.9-0.3 (Clark, Parkinson & Caswell 1975). Nicolson, Feast & Glass (1980) measured a high velocity for the $\text{H}\alpha$ emission, $v = 240 \pm 15 \text{ km s}^{-1}$, supporting this theory; from the X-ray luminosity as well as HI absorption, Goss & Mebold (1977) determined a distance to the source of 9 kpc.
- *X1556-605* — Emission lines of He II $\lambda 4686$ and $\text{H}\alpha$ are seen in this source; Motch *et al.* measured $v = 295 \pm 25 \text{ km s}^{-1}$, very different from the $v = -24 \text{ km s}^{-1}$ measured earlier by Cowley *et al.* (1987). The distance is estimated to be ~ 10 kpc from the total X-ray luminosity.
- *X1617-155 = Sco X-1* — The first non-solar X-ray source discovered, Sco X-1 is associated with a 12th magnitude blue emission-line star. Lines of He II, the hydrogen

Balmer series, and some metallic lines are seen: from the motion of the He II line, Cowley & Crampton (1975) measured $v = -139 \pm 3 \text{ km s}^{-1}$. The distance is poorly known: while many workers assume $d \sim 500 \text{ pc}$, Penninx (1989) argues it is more likely to be $d = 2 \text{ kpc}$.

- $X1656+354 = \text{Her X-1}$ — Hutchings *et al.* (1985) measured $v = -57 \pm 6 \text{ km s}^{-1}$ using the Balmer lines, Ca II and He I in absorption. Thomas, Schmidt & Schoermbs (1986) estimated the distance to be 5 kpc from the optical luminosity.
- $X1659-487 = \text{GX339-4}$ — Cowley, Crampton & Hutchings (1987) measured the velocity from emission lines of He II, He I and the Balmer lines to be $v = 20 \pm 10 \text{ km s}^{-1}$, and estimated a distance of 4 kpc from the X-ray luminosity and reddening. This object is a black hole candidate, but pending confirmation of the mass of the primary we have included it in our list.
- $X1702-429 = \text{GX349+02}$ — Penninx & Augusteijn (1991) identified the optical counterpart of this source as an 18th magnitude star, and measured $v = -310 \pm 30 \text{ km s}^{-1}$ from the velocity of the $\text{H}\alpha$ line. The distance, estimated from the X-ray and UV brightness, is 9.2 kpc (Penninx 1989).
- $X1728-247 = \text{GX1+4}$ — Davidsen, Malina & Bowyer (1977) found the optical counterpart of GX1+4 to be a symbiotic star, and measured $v = -100 \pm 50 \text{ km s}^{-1}$. The spectral type of the companion and the extinction imply a distance of 8.5 kpc, which would put the object at the Galactic center.
- $X1735-444$ — Smale & Corbet (1991), from a detailed study of the $\text{H}\alpha$ emission line, measured $v = -152 \pm 20 \text{ km s}^{-1}$, very different from the -254 km s^{-1} derived by Cowley *et al.* (1988). The distance, from X-ray properties, is taken to be 1 kpc.
- $X1822-371$ — Measurements of the broad He II $\lambda 4686$ line by Cowley, Crampton & Hutchings (1982a) give $v = -91 \pm 8 \text{ km s}^{-1}$; spectrophotometry indicates $d = 9 \text{ kpc}$ (Mason *et al.* 1982).
- $X1908+005 = \text{Aql X-1}$ — Chevalier & Illovaisky (1991) recently discovered a 19 h orbital period for this system; we fit a sine curve of this period to our six data points, and found $v = 148 \pm 16 \text{ km s}^{-1}$, with a velocity semi-amplitude $K = 53 \pm 25 \text{ km s}^{-1}$ (very uncertain because of the small number of points). Thorstensen, Charles & Bowyer (1978) give a distance of 2.5 kpc from the spectral type of the companion.

- *X1957+115* — We derive a velocity $v = -285 \pm 23 \text{ km s}^{-1}$ for this system, by fitting a sine wave to the eight velocities listed in Table 8.1; the velocity semi-amplitude is $K = 106 \pm 29 \text{ km s}^{-1}$. Margon, Thorstensen & Bowyer (1978) estimate a distance of 7 kpc from the properties of the companion.
- *X2142+380 = Cyg X-2* — This object shows hydrogen Ca II and metals in absorption, as well as He II, H β and some other Balmer lines in emission. Cowley, Crampton & Hutchings (1979) derived $v = -222 \pm 2 \text{ km s}^{-1}$ using both emission and absorption features; the spectral type of the companion indicates a distance of 7.9 kpc.

The list of velocities and periods given in Table 8.2 forms the input for our study of the kinematics of these objects. In Figure 8.3, we plot the observed radial velocities projected onto the galactic plane. Clearly their motion is not simple galactic rotation. In the next section, we describe in detail the direct formation model for the formation of LMXBs. Our goal is to see if the observed kinematics and distribution of these objects, even though un-disklike, could be consistent with a Population I origin.

8.4 The direct formation model for LMXB formation

8.4.1 Common envelope evolution

It is now widely accepted that cataclysmic variables (CVs), close binary systems consisting of a white dwarf and a mass-transferring companion in orbits with periods $P \sim 0.1 - 1$ d, are the outcome of common envelope evolution. The initial binary is wide, with orbital periods of order $10^2 - 10^4$ d. The primary evolves to fill its Roche lobe, and begins transferring matter onto the companion. Since mass transfer is from the heavier star to the lighter star, this quickly becomes a runaway process. The giant's envelope engulfs the companion, and a common envelope is formed. Each embedded star feels a frictional drag from the envelope, which extracts energy from the binary and imparts it to the envelope, so the two stars spiral together. The energy lost in the spiral-in is

$$\Delta E_{\text{orb}} = -\frac{GM_c M_2}{2a_f} + \frac{GM_1 M_2}{2a_i} \quad (8.2)$$

where M_1 and M_2 are the initial masses of the primary and secondary, M_c is the mass of the final core of the primary, and a_i and a_f are the initial and final orbital separations. We can write the initial binding energy of the envelope as (Webbink 1992)

$$E_e = -\frac{GM_c M_e}{\lambda r_L} \quad (8.3)$$

where $M_e = M_1 - M_c$ is the mass of the envelope, r_L is the Roche lobe radius of the initial giant, and λ is a measure of the degree of central concentration of the envelope. Then if the orbital energy is transferred to the envelope with some efficiency α , we can use equations (8.3) and (8.2) to estimate the final orbital parameters. For example, consider a $10 M_\odot$ primary in a $500 R_\odot$ orbit with a $0.5 M_\odot$ companion evolving to a $1.4 M_\odot$ neutron star. If we take $\lambda \sim 1$ and $\alpha \sim 0.5$, then the final binary will have orbital separation $5 R_\odot$, corresponding to an orbital period of 0^d9.

The duration of the common envelope phase is short, typically $\sim 10^3$ y (Hjellming & Taam 1991), and neither star accretes a significant amount of mass during this phase. The resulting system consists of the degenerate core of the primary plus the secondary in a tight orbit. When the secondary overflows its Roche lobe, either due to evolution or loss of angular momentum, the binary becomes visible as a CV.

The scenario for forming the neutron star in LMXBs is similar, except that the neutron star is formed after the ejection of the envelope. The core of a massive ($\sim 8 - 12 M_\odot$) star is exposed by common envelope evolution. The helium core has mass $\gtrsim 3 M_\odot$, and the carbon-oxygen core produced by helium burning has a mass above the Chandrasekhar

limit (van den Heuvel 1981). This core collapses violently to a neutron star, which we assume to have a mass $M_c = 1.4 M_\odot$, expelling the remainder of the mass in a shell.

Note that the conditions for forming a visible LMXB after the spiral-in phase are very stringent. The initial orbital separation a_i must be large enough that the primary does not fill its Roche lobe until the core has had time to grow to $\sim 3 M_\odot$, or it will not form a neutron star. This means the orbit must be wide enough to accommodate the primary while it is on the giant branch, $a_i \gtrsim 300 R_\odot$. Conversely, a_i must not be so large that the primary never fills its Roche lobe and initiates the common envelope phase: $a_i \lesssim 1000 R_\odot$. The initial orbit must have enough energy to expel the envelope, a condition which depends on the initial masses and separation, but also on the envelope concentration λ and the efficiency of the ejection α (eqns. [8.2] and [8.3]). Additionally, if the final system is to be stable while the secondary is transferring mass to the newly-formed neutron star, the mass of the secondary must not be higher than the mass of the compact remnant: $M_2 < 1.4 M_\odot$, which constrains the initial mass ratio $q = M_2/M_1 \lesssim 0.14$ (Webbink 1992). Thus there is a very narrow range of initial binaries that can lead to LMXBs in this model. On the other hand, the birthrate of disk LMXBs is very low ($\sim 10^{-7} \text{ y}^{-1}$) so a very rare scenario will suffice.

Because typically less than half of the mass of the system is lost ($3 M_\odot + 0.5 M_\odot \rightarrow 1.4 M_\odot + 0.5 M_\odot$), the system will remain bound. The binary as a whole will receive a large velocity as a result of the mass loss:

$$v_s = -\frac{M_1 - M_c}{M_2 + M_c} v_1 \quad (8.4)$$

where M_1 and M_2 are the initial (post-common envelope phase) masses of the primary and secondary, $M_c = M_1 - \Delta M$ is the mass of the compact remnant, and v_1 and v_s are the initial orbital velocity of the primary and final system velocity (in the rest frame of the initial binary). Thus for the system above, if $M_c = 1.4 M_\odot$, the binary after the supernova explosion has a velocity 84% of the original velocity of the primary; for a 0.5 d initial orbit, $v_1 = 60 \text{ km s}^{-1}$ so $v_s = 50 \text{ km s}^{-1}$.

Thus mass loss alone will produce substantial system velocities for tight binaries. However, there is growing evidence that neutron stars may at birth receive an additional “kick” in a random direction, presumably arising from a small ($\sim 1\%$) asymmetry in the core collapse. Field pulsars have velocities of up to several hundred kilometers per second (Anderson & Lyne 1983; Cordes 1986). Several authors have suggested that these velocities are due to the orbital motion of the neutron star progenitor in a binary which is disrupted by the supernova explosion. However, Dewey & Cordes (1987), in a detailed Monte Carlo

simulation of the observed pulsar population, concluded that the observed velocities cannot be explained only by the breakup of binaries, and require an additional kick at the birth of the neutron star of order 100 km s^{-1} . Bailes (1989) found that this model also reproduces the observed velocity-magnetic moment correlation. Such a kick had also been postulated earlier from a study of pulsar scale heights (Gunn & Ostriker 1970).

8.4.2 The numerical experiment

Such a kick, imparted to the collapsing core in the proto-LMXB, could account for the high velocities observed. We performed the following numerical experiment to test the effect of the mass loss from the binary, with and without an additional kick given to the neutron star. Our object was to compare the outcome with the observed period and velocity distribution observed in the disk LMXBs.

We begin with two stars, masses M_1 and M_2 , with $M_1 > M_2$, in a circular orbit with period P_i . The initial orbital separation can then be trivially calculated from Kepler's law:

$$\left(\frac{P}{2\pi}\right)^2 = \frac{a_i^3}{G(M_1 + M_2)}. \quad (8.5)$$

The primary then ejects an amount of mass $\Delta M = M_1 - M_c$, and receives a kick velocity of magnitude v_k in a random direction. We assume the explosion and ejection of mass is instantaneous, and neglect the effect of the expelled shell on the secondary. Immediately after the explosion, the primary (now greatly reduced in mass) is moving at velocity

$$\mathbf{v}'_1 = \mathbf{v}_1 + \mathbf{v}_k, \quad (8.6)$$

and the secondary is moving at velocity

$$\mathbf{v}'_2 = \mathbf{v}_2 = -\frac{M_1}{M_2}\mathbf{v}_1, \quad (8.7)$$

where \mathbf{v}_1 , \mathbf{v}_2 are the center-of-mass velocities of the two stars immediately prior to the explosion, and the primes denote the values immediately after the explosion. We can then calculate the velocity of the center of mass of the new system

$$M_c\mathbf{v}'_1 + M_2\mathbf{v}'_2 = (M_c + M_2)\mathbf{v}_s \quad (8.8)$$

and the total energy of the system

$$E = \frac{M_c(\mathbf{v}'_1 - \mathbf{v}_s)^2}{2} + \frac{M_2(\mathbf{v}'_2 - \mathbf{v}_s)^2}{2} - \frac{GM_cM_2}{a_i}. \quad (8.9)$$

If $E > 0$, the system is unbound. For $E < 0$, we can calculate the new orbital parameters. We can also calculate the new angular momentum of the binary. The final orbit is usually

highly eccentric; we assume it circularizes (conserving angular momentum) before the object becomes visible as an LMXB. We checked our algorithm by reproducing the results of Sutantyo (1978) and Bailes (1989).

Since a steep mass function ensures that most progenitors will be at the lowest end of the mass range, we assume that just prior to the explosion $M_1 = 3 M_\odot$, corresponding to an initial mass (before spiral-in) $M_{1,i} \sim 10 M_\odot$. We assume the remnant always has mass $M_c = 1.4 M_\odot$, and consider three values for the kick velocity: 0 km s^{-1} (no kick: only the effect of the mass loss is relevant), 100 km s^{-1} and 200 km s^{-1} . For each combination of initial orbital period P_i and kick speed v_k , we varied θ , the angle between \mathbf{v}_k and \mathbf{v}_1 in the orbital plane, between 0° and 180° in steps $\Delta(\cos \theta) = 0.1$, and ϕ , the angle out of the orbital plane, between 0° and 360° in steps of 20° . The final parameters of all systems which remained bound were then recorded.

Figure 8.4 shows the results of these calculations. We have assumed $M_2 = 0.5 M_\odot$, and initial binary periods between 0.03 d and 30 d . The filled circles represent the observed radial velocities and periods of disk LMXBs (Table 8.2), for those systems where both quantities are known; note that the observed velocities are 1-dimensional velocities, whereas the calculated velocities are 3-dimensional. Typical values for the systemic velocity after the supernova explosion are 60 km s^{-1} when no kick is given to the neutron star, 110 km s^{-1} for a 100 km s^{-1} kick, and 170 km s^{-1} for a 200 km s^{-1} kick.

The observed velocities and periods will be altered from their “birth” values in two ways. The periods of the systems will have evolved after the initial circularization. Since mass transfer is from the lighter star to the heavier, conservation of angular momentum drives the system to longer periods; for short period systems, however, the effects of gravitational radiation and magnetic braking dominate, causing the period to decrease. The critical period separating the two cases is on the order of $P_i \sim 1 \text{ d}$, and depends somewhat on the masses of the two stars (Pylyser & Savonije 1988). This means that the spread in periods in Figure 8.4 is wider than it was when the systems were born.

Secondly, under the direct formation scenario, the observed velocities also include a component of galactic rotation. However, the size of this contribution depends on where they were born, which may be quite far from their current position. At a speed of 100 km s^{-1} , the system will travel 1 kpc in 10^7 y . So assuming an average lifetime for these systems of a few times 10^7 y , we have calculated the minimum and maximum galactic rotation (using the rotation curve of Clemens 1985) in a circle of radius 3 kpc around the current position of the X-ray binary (see Fig. 8.3), and subtracted these extreme values from the observed velocities: this gives the range in birth velocity plotted in Figure 8.4.

Thus our simulations of the direct formation model predict:

- large systemic velocities, $v \sim 100 - 200 \text{ km s}^{-1}$;
- a thick z -distribution, of a few kpc. If the LMXBs have relaxed, then the z scale height at the solar circle will be about 1 kpc, and about a quarter that at the Galactic center (see, *e.g.* Paczyński 1990). If the LMXBs as a system have not relaxed, then their scale height will be correspondingly larger; and
- orbital periods in the range 0.01 – 100 d.

Figure 8.5 shows the histogram of observed velocities, corrected for galactic rotation. The mean one-dimensional velocity has magnitude around 100 km s^{-1} , with a long tail. This can be compared to the observed velocities of pulsars, which have a mean velocity of 200 km s^{-1} . In this model, these pulsars represent neutron stars which have escaped from binary systems at birth with a kick on the order of $100 - 200 \text{ km s}^{-1}$ (Dewey & Cordes 1987); thus we expect them to have a higher mean velocity.

The z -distribution of the LMXBs has a mean thickness of 0.8 kpc (Fig. 8.6). Thus the observational data, though extremely sparse, are in qualitative agreement with the predictions of the direct formation model.

8.4.3 Solar motion solutions

Cowley *et al.* (1987) found a solar motion relative to the LMXBs of $U = -66 \pm 43 \text{ km s}^{-1}$, compared with $U = -180 \pm 40 \text{ km s}^{-1}$ for metal-poor globular clusters (using velocities from Harris & Racine 1979; Cowley *et al.* find $U = -225 \pm 45$), and $U \simeq 15 \text{ km s}^{-1}$ for local disk stars (Mihalas & Binney 1981, Table 6-3). Here U is the linear velocity of the sun in the direction of galactic rotation with respect to these objects, and is the quantity denoted v'_\odot by Mihalas & Binney. Cowley *et al.* concluded that the LMXBs represent an intermediate population (“Pop. 1.5”) between the classical halo population, as represented by the metal-poor clusters, and the disk population.

We repeated this analysis for our revised list of velocities. Following Kinman (1959), the motion with respect to the sun of an object at galactic coordinates (l, b) with radial velocity v_r is

$$U \cos A = v_r \quad (8.10)$$

where A is the angle between the direction to the cluster and the direction of solar motion (assumed to be at right angles to the galactic center and in the galactic plane): $\cos A = \sin l \cos b$. For the fifteen objects listed in Table 8.2, we find $U = -148 \pm 64 \text{ km s}^{-1}$. Thus the disk LMXBs do appear to be rotating less than classical disk populations. However,

this difference is probably not significant, as the number of objects is so small (15). For comparison, we selected the fifteen globular clusters nearest to the LMXBs in l and b , and repeated the velocity analysis; the measured value of U dropped from -180 km s^{-1} to $-51 \pm 22 \text{ km s}^{-1}$. As another test, we drew samples of 15 objects from model populations of objects with disk rotation plus a random velocity of 200 km s^{-1} ; while the whole sample had $U = -22 \pm 13 \text{ km s}^{-1}$, 8% of the samples had $|U| \gtrsim 120 \text{ km s}^{-1}$.

8.5 Discussion

It appears, then, that the direct formation scenario can reproduce many of the properties of the observed LMXB population, with the inclusion of velocity kicks on the order of $100 - 200 \text{ km s}^{-1}$, values which are independently indicated by pulsar statistics. The observations are not consistent with AIC formation of the neutron stars in these binaries if they are born in the disk and receive no velocity kick at birth. However, if AIC involves a kick, or if the LMXBs are not disk objects but are part of an old population, then the observations cannot distinguish between these scenarios and the direct formation model. The kinematics and distribution of the LMXBs have been taken to mean that they belong to an old population. While the data are *consistent* with this interpretation, we consider this far from proven. Thus (in the absence of kicks during AIC — see below) the high velocities of LMXBs could either represent velocities given to the neutron stars at birth in the disk, or could represent primordial velocities of halo objects.

Due to the paucity of observational data, as well as unknown evolutionary effects that operate after the supernova explosion, it is virtually impossible to make more precise statements about the degree of correspondence between the direct formation model and the data. Unfortunately, these data will not improve substantially over what is presented here: there are far too few LMXBs with optical counterparts; the ones that exist are faint; and we can only measure one component of the velocity.

If the direct formation scenario is true, then the formation of LMXBs is part of a continuum, lying between CVs and the low-mass black hole binaries such as A0620-00. The white dwarf in a CV is formed by the spiral-in process, being just the stripped core of the giant star, and does not require a further explosion. Thus the CVs should not have acquired a large velocity at birth, and CVs should be found close to the plane. In Figure 8.6, we plot the height above the plane z for CVs with known distances (from Berriman 1987), as well as the same quantity for LMXBs.

The black hole binaries should also be found closer to the plane than the LMXBs, as they do not receive an asymmetric kick at birth: thus the only velocity they acquire is due to mass loss. Figure 8.1c shows the galactic distribution of the five good black hole candidates.

Because AIC does not impart a large velocity to the system (eq. [8.1]), the formation of an LMXB by common-envelope evolution followed by collapse of the white dwarf would leave the system close to its starting place. Of course, if the kicks being posited in the explosive formation of neutron stars also occur in their AIC formation, then we can say nothing about the origins of the systems we see based only on their kinematics. However,

one of the motivations for the introduction of the AIC model was that it did not produce high velocities. Bailyn & Grindlay (1990) argue that the fraction of newly-born neutron stars retained by a typical globular cluster is so low ($\lesssim 15\%$) that the cluster is almost certainly disrupted by the mass loss associated with the supernova explosions. They thus suggest AIC as an alternative hypothesis, as the fraction of (slow-moving) neutron stars retained by the cluster will be much higher. Helfand *et al.* (1983) also suggested the lack of a velocity kick as an attractive feature of the AIC model for explaining the wide low-mass binary pulsars. If AIC is also associated with a kick, this argument is no longer valid.

The spread of LMXBs away from the plane is thus adequately explained in this model. The concentration towards the bulge, on the other hand, is not predicted by this model. Figure 8.7 shows the cumulative distribution of $|l|$, for LMXBs (solid line) and for three Gaussian disk models with different scale radii. Clearly even the best fitting disk model (with $R_0 = 6$ kpc) has an excess of sources towards the bulge. Future work should perhaps consider the kinematics of a population given large random velocities in this manner while in the galactic gravitational potential, to see if the concentration towards the bulge can be reproduced.

We would like to thank Frank Verbunt and Ed van den Heuvel for helpful discussions during this work. This research has made use of the Simbad database, operated at CDS, Strasbourg, France.

Table 8.1. New velocity measurements

| Object | UT Date | Resolution (Å) | | Heliocentric velocity (km/s) | Lines measured |
|-----------|-----------------|----------------|------|------------------------------|----------------------------------|
| | | Blue | Red | | |
| X0042+327 | 1989 Aug 28.378 | 4.2 | 12.2 | 2 ± 39 | dG abs. in blue |
| | 1991 Aug 7.454 | 4.2 | 3.1 | -146 ± 44 | |
| X0614+091 | 1989 Nov 19.353 | 4.2 | 12.2 | - | C III/N III $\lambda 4640$ blend |
| GX9+9 | 1991 Aug 8.210 | 4.2 | 3.1 | 42 ± 53 | He II, H α |
| | 1991 Aug 9.212 | 4.2 | 3.1 | 45 ± 36 | |
| | 1991 Aug 9.235 | 4.2 | 3.1 | -30 ± 39 | |
| GX17+2 | 1990 Jul 17.317 | 4.2 | 12.2 | 58 ± 33 | dG abs. |
| | 1990 Jul 19.302 | 2.2 | 1.6 | -10 ± 34 | |
| | 1991 Aug 7.251 | 4.2 | 3.1 | -2 ± 33 | |
| | 1991 Aug 9.263 | 4.2 | 3.1 | -19 ± 33 | |
| Ser X-1 | 1991 Aug 7.288 | 4.2 | 3.1 | 46 ± 41 | He II |
| | 1991 Aug 8.245 | 4.2 | 3.1 | -86 ± 55 | |
| | 1991 Aug 9.296 | 4.2 | 3.1 | 1 ± 60 | |
| Aql X-1 | 1989 Aug 29.278 | 4.2 | 12.2 | 195 ± 37 | He II, H α , H β |
| | 1990 Jun 22.425 | 4.2 | 12.2 | 91 ± 60 | |
| | 1990 Jul 17.357 | 4.2 | 12.2 | 196 ± 47 | |
| | 1991 Aug 8.274 | 4.2 | 3.1 | 135 ± 22 | |
| | 1991 Aug 8.301 | 4.2 | 3.1 | 132 ± 32 | |
| | 1991 Aug 9.333 | 4.2 | 3.1 | 115 ± 31 | |
| X1957+115 | 1989 Aug 29.306 | 4.2 | 12.2 | -268 ± 58 | He II |
| | 1990 Jun 22.459 | 4.2 | 12.2 | -365 ± 50 | |
| | 1990 Jul 17.391 | 4.2 | 12.2 | -260 ± 39 | |
| | 1990 Jul 19.438 | 2.2 | 1.6 | -205 ± 36 | |
| | 1991 Aug 8.345 | 4.2 | 3.1 | -281 ± 42 | |
| | 1991 Aug 8.407 | 4.2 | 3.1 | -58 ± 48 | |
| | 1991 Aug 9.360 | 4.2 | 3.1 | -470 ± 55 | |
| | 1991 Aug 9.421 | 4.2 | 3.1 | -408 ± 70 | |
| V1727 Cyg | 1990 Jul 17.419 | 4.2 | 12.2 | 86 ± 35 | F abs. |
| | 1990 Jul 18.463 | 1.1 | 1.6 | 9 ± 10 | |
| | 1990 Jul 19.403 | 2.2 | 1.6 | -8 ± 21 | |
| | 1990 Jul 19.472 | 2.2 | 1.6 | 17 ± 19 | |
| | 1991 Aug 7.415 | 4.2 | 3.1 | -3 ± 28 | |
| | 1991 Aug 7.485 | 4.2 | 3.1 | -60 ± 27 | |
| | 1991 Aug 8.375 | 4.2 | 3.1 | -63 ± 33 | |
| | 1991 Aug 8.438 | 4.2 | 3.1 | -85 ± 31 | |
| | 1991 Aug 9.391 | 4.2 | 3.1 | -107 ± 29 | |
| | 1991 Aug 9.435 | 4.2 | 3.1 | -78 ± 29 | |

Table 8.2. Radial velocities of disk LMXBs

| Object | <i>l</i> (°) | <i>b</i> (°) | Orbital period (d) | Heliocentric velocity (km/s) | Distance (kpc) | Reference |
|---------------------|-----------------|-----------------|-----------------------|---------------------------------|-------------------|-----------|
| 0748-676 | 280.0 | -19.8 | 0.159 | +20 ± 64 | 6 | 7 |
| 0921-630 | 281.8 | -9.3 | 8.99 | +52 ± 8 | 8.5 | 5 |
| 1455-314 = Cen X-4 | 332.2 | +23.9 | 0.629 | +137 ± 17 | 1.2 | 13 |
| 1516-569 = Cir X-1 | 322.1 | 0.0 | 16.6 | +230 ± 15 | 8 | 9,15 |
| 1556-605 | 324.1 | -5.9 | ... | +295 ± 25 | 10 | 14 |
| 1617-155 = Sco X-1 | 359.1 | +23.8 | 0.788 | -145 ± 3 | 2 | 2,16 |
| 1656+354 = Her X-1 | 58.2 | +37.5 | 1.7 | -57 ± 6 | 5 | 10,19 |
| 1659-487 = GX339-4 | 338.9 | -4.3 | 0.618 | 20 ± 10 | 4 | 6 |
| 1702-429 = GX349+02 | 349.1 | +2.7 | ... | -310 ± 30 | 9 | 16,17 |
| 1728-247 = GX1+4 | 1.9 | +4.8 | 304. | -100 ± 50 | 10 | 8 |
| 1735-444 | 346.1 | -7.0 | 0.194 | -152 ± 20 | 1 | 18 |
| 1822-371 | 356.9 | -11.3 | 0.232 | -91 | 9 | 4,12 |
| 1908+005 = Aql X-1 | 35.7 | -4.1 | 0.791 | +148 ± 16 | 2.5 | 1,20,21 |
| 1957+115 | 51.3 | -9.3 | 0.389 | -277 ± 48 | 7 | 11,21 |
| 2142+380 = Cyg X-2 | 87.3 | -11.3 | 9.842 | -222 ± 2 | 8 | 3 |

Table 8.2 — Periods, distances and radial velocities of disk LMXBs. Periods are from Lewin & van Paradijs (1992), except for Aql X-1 (ref. [1]); the references in column 5 are to the following list.

1. Chevalier & Illovaisky 1991
2. Cowley & Crampton 1975
3. Cowley, Crampton & Hutchings 1979
4. Cowley, Crampton & Hutchings 1982a
5. Cowley, Crampton & Hutchings 1982b
6. Cowley, Crampton & Hutchings 1987
7. Crampton *et al.* 1986
8. Davidsen, Malina & Bowyer 1977
9. Goss & Mebold 1977
10. Hutchings *et al.* 1985
11. Margon, Thorstensen & Bowyer 1978
12. Mason *et al.* 1982
13. McClintock & Remillard 1990
14. Motch *et al.* 1989
15. Nicolson *et al.* 1980
16. Penninx 1989
17. Penninx & Augusteijn 1991
18. Smale & Corbet 1991
19. Thomas, Schmidt & Schoermbs 1986
20. Thorstensen, Charles & Bowyer 1978
21. This work

References

Anderson, B. & Lyne, A.G. 1983, *Nature*, 303, 597

Bailes, M. 1989, *ApJ*, 342, 917

Bailyn, C.D., Garcia, M.R. & Grindlay, J.E. 1989, *ApJ*, 344, 786

Bailyn, C.D. & Grindlay, J.E. 1990, *ApJ*, 353, 159

Berriman, G. 1987, *A&AS*, 68, 41

Bhattacharya, D. 1989, in *Proc. 23rd ESLAB Symp. on Two Topics in X-ray Astronomy*, Bologna, Italy 13–20 September 1989, p. 179

Bhattacharya, D., Wijers, R.A.M.J., Hartman, J.W. & Verbunt, F. 1991, *A&A*, 254, 198

Braes, L.L.E. & Miley, G.K. 1973, in *IAU Symposium 55, X- and Gamma-Ray Astronomy*, ed. H. Bradt & R. Giacconi (Dordrecht: Reidel), p. 86

Canizares, C.R., McClintock, J.E. & Grindlay, J.E. 1979, *ApJ*, 234, 556

Charles, P., Thorstensen, J. & Bowyer, S. 1978, *MNRAS*, 183, 29p

Chevalier, C. 1989, in *Proc. 23rd ESLAB Symp. on Two Topics in X-ray Astronomy*, Bologna, Italy 13–20 September 1989, p. 341

Chevalier, C. & Illovaisky, S.A. 1991, *A&A*, 251, L11

Clark, D.H., Parkinson, J.H. & Caswell, J.L. 1975, *Nature*, 254, 674

Clemens, D.P. 1985, *ApJ*, 295, 422

Cordes, J.M. 1986, *ApJ*, 311, 183

Cowley, A.P. & Crampton, D. 1975, *ApJ*, 201, L65

Cowley, A.P., Crampton, D. & Hutchings, J.B. 1979, *ApJ*, 231, 539

Cowley, A.P., Crampton, D. & Hutchings, J.B. 1982a, *ApJ*, 255, 596

Cowley, A.P., Crampton, D. & Hutchings, J.B. 1982b, *ApJ*, 256, 605

Cowley, A.P., Crampton, D. & Hutchings, J.B. 1987, *AJ*, 92, 195

Cowley, A.P., Hutchings, J.B. & Crampton, D. 1988, *ApJ*, 333, 906

Cowley, A.P., Hutchings, J.B., Crampton, D. & Hartwick, F.D.A. 1987, *ApJ*, 320, 296

Crampton, D., Cowley, A.P., Stauffer, J., Ianna, P. & Hutchings, J.B. 1986, *ApJ*, 306, 599

Davidsen, A., Malina, R. & Bowyer, S. 1977, *ApJ*, 211, 866

Dewey, R.J. & Cordes, J.M. 1987, *ApJ*, 321, 780

Doxsey, R.E., Apparao, K.M.V., Bradt, H.V., Dower, R.G. & Jernigan, J.G. 1977, *Nature*, 270, 586

Eggleton, P.P. & Verbunt, F. 1986, *MNRAS*, 220, 13p

Goss, W.M. & Mebold, U. 1977, *MNRAS*, 181, 255

Gunn, J.E. & Ostriker, J.P. 1970, *ApJ*, 160, 979

Harris, W.E. & Racine, R. 1979, *ARAA*, 17, 241

Heifand, D.J., Ruderman, M.A. & Shaham, J. 1983, *Nature*, 304, 423

Hjellming, M.S. & Taam, R.E. 1991, *ApJ*, 370, 709

Hjellming, R.M. & Wade, C.M. 1971, *ApJ*, 168, L21

Hutchings, J.B., Gibson, E.M., Crampton, D. & Fisher, W.A. 1985, *ApJ*, 292, 670

Johnston, H.M. & Kulkarni, S.R. 1992, *ApJ*, 1992 Sep 1, in press

Kinman, T.D. 1959, *MNRAS*, 119, 559

Lewin, W.H.G. & van Paradijs, J. 1992, in prep

Margon, B., Thorstensen, J.R. & Bowyer, S. 1978, *ApJ*, 221, 907

Mason, K.O., Murdin, P.G., Tuohy, I.R., Seitzer, P. & Branduardi-Raymont, G. 1982, *MNRAS*, 200, 793

McClintock, J.E. & Remillard, R.A. 1990, *ApJ*, 350, 386

Mihalas, D. & Binney, J. 1981, *Galactic Astronomy: Structure and Kinematics* (Freeman: New York)

Motch, C., Pakull, M.W., Mouchet, M. & Beuermann, K. 1989, *A&A*, 219, 158

Naylor, T. & Charles, P.A. 1989, *MNRAS*, 236, 1p

Naylor, T., Charles, P.A., Drew, J.E. & Hassall, B.J.M. 1988, *MNRAS*, 233, 285

Nicolson, G.D., Feast, M.W. & Glass, I.S. 1980, *MNRAS*, 191, 293

Oke, J. B. & Gunn, J. E. 1982, *Pub. A. S. P.*, 94, 586

Penninx, W. 1989, in *Proc. 23rd ESLAB Symp. on Two Topics in X-ray Astronomy*, Bologna, Italy 13–20 September 1989, ed. J. Hunt & B. Battrick (ESA: Paris), p. 215

Penninx, W. & Augusteijn, T. 1991, *A&A*, 246, L81

Pylyser, E. & Savonije, G.J. 1988, *A&A*, 191, 57

Schaefer, B.E. 1990, *ApJ*, 354, 720

Shortridge, K.I. 1986, FIGARO data reduction package, Version 2.1

Smale, A.P. & Corbet, R.H.D. 1991, *ApJ*, 383, 853

Sutantyo, W. 1978
Astrophys. Space Sci. 54 479

Thomas, H., Schmidt, H.U. & Schoermbs, R. 1986, in *The Evolution of Galactic X-ray Binaries*, ed. J. Trümper, W.H.G. Lewin & W. Brinkmann, NATO Advanced Sience Institutes (Reidel: Dordrecht), p. 221

Thorstensen, J.R., Charles, P.A. & Bowyer, S. 1980, *ApJ*, 238, 964

Thorstensen, J., Charles, P., Bowyer, S., Briel, U.G., Doxsey, R.E., Griffiths, R.E. & Schwartz, D.A. 1979, *ApJ*, 233, L57

Thorstensen, J.R., Brownsberger, K.R., Mook, D.E., Remillard, R.A., McClintock, J.E., Koo, D.C. & Charles, P.A. 1988, *ApJ*, 334, 430

Tonry, J. & Davis, M. 1979, *AJ*, 84, 1511

van den Heuvel, E.P.J. 1981, in *IAU Symposium No. 95, Pulsars*, ed. W. Sieber & R. Wielebinski (Dordrecht: Reidel), p. 379

Verbunt, F., Wijers, R.A.M.J. & Burm, H.M.G. 1990, *A&A*, 234, 195

Vogt, N. 1981, *ApJ*, 252, 653

Walter, F.M., Bowyer, S., Mason, K.O., Clarke, J.T., Henry, J.P., Halpern, J. & Grindlay, J.E. 1982, *ApJ*, 253, L67

Webbink, R.F. 1992, in *X-ray binaries and the formation of binary and millisecond pulsars*, ed. E.P.J. van den Heuvel & S.A. Rappaport, Kluwer, in press

Figure captions

Figure 8.1 — Galactic distribution of X-ray binaries: (a) Massive X-ray binaries. (b) Low mass X-ray binaries. (c) Black hole candidates (A0620-00, GS2000+25, GS2023+338, Cyg X-1, GX339-4). Data from Lewin & van Paradijs 1992. Note that the Magellanic Clouds are very clear in the distribution of HMXBs.

Figure 8.2 — Spectra of the sources observed in this program. (a) X0042+327. (b) X0614+091. (c) X1728-169 = GX9+9. (d) GX9+9, red spectrum. (e) X1813-140 = GX17+2. (f) X1837+049 = Ser X-1. (g) X1908+005 = Aql X-1. (h) Aql X-1, red spectrum. (i) X1957+115. (j) X1957+115, red spectrum. (k) X2129+47 = V1727 Cyg. (l) V1727 Cyg, red spectrum.

Figure 8.3 — Measured radial velocities (from this work and the literature) of “disk” LMXBs, projected onto the Galactic plane. The dashed circle represents the solar circle; for each LMXB, the symbol is plotted at its galactic position, and the vector represents the heliocentric velocity of the object, pointing away from the Sun (symbol \odot) for a redshift. For a single source (X0748-676), we have indicated the 3 kpc circle which represents the distance the binary could have moved at a speed of 100 km s^{-1} in 10^7 y (see text). The arrow at the right represents the solar galactic rotation.

Figure 8.4 — Median speed of the binary after the supernova explosion as a function of final orbital period, compared with the observed LMXBs (filled circles; Table 8.2). Three different values for the kick velocity were used: 0 km s^{-1} (*dot-dashed line*), 100 km s^{-1} (*dashed line*) and 200 km s^{-1} (*solid line*). The thin error bar at the left edge represents the range of velocities for $v_k = 200 \text{ km s}^{-1}$. The vertical bars on the filled circles represent a range of galactic rotation corrections, assuming the binary was born within 3 kpc of its current location.

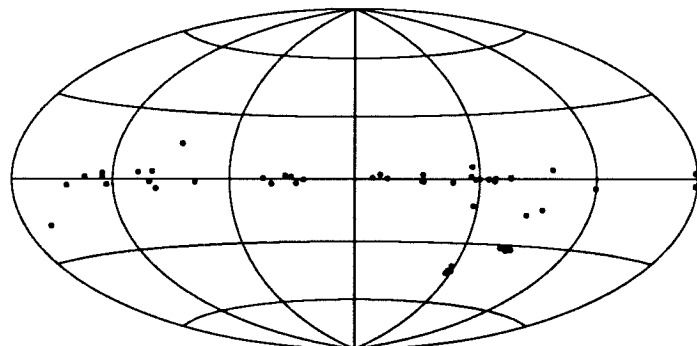
Figure 8.5 — Histogram of the observed velocities of LMXBs, corrected for Galactic rotation. A range of corrections has been used, corresponding to a range of initial birthplaces, as in Fig. 8.4; each object velocity was distributed over several bins corresponding to this range in velocities.

Figure 8.6 — Height above the plane for (a) Cataclysmic variables; (b) LMXBs. CV data is from Berriman (1987); most of his distances are uncertain by a factor of 2, but that is not enough to explain the discrepancy between the two classes of objects. Note also that the CVs do not form a complete sample.

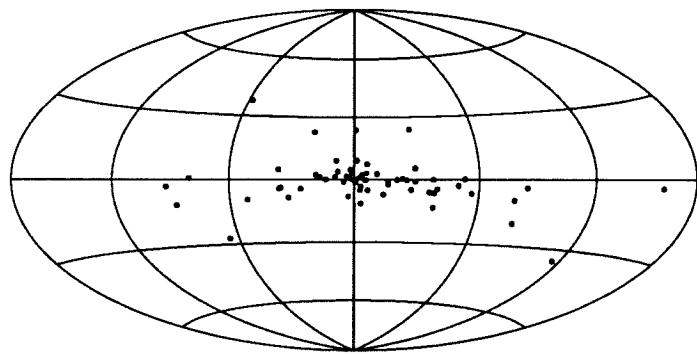
Figure 8.7 — Cumulative histogram of the longitudinal distribution of LMXBs (*solid line*), compared to Gaussian distributions. Three values of the scale length R_0 are shown: $R_0 = 8 \text{ kpc}$ (*dashed line*), $R_0 = 6 \text{ kpc}$ (*dot-dashed line*), and $R_0 = 4 \text{ kpc}$ (*dotted line*). Note the excess of LMXBs over the number expected in a disk model at small $|l|$, towards the Galactic bulge.

Figure 8.1

Galactic distribution of HMXBs



Galactic distribution of LMXBs



Galactic distribution of black hole candidates

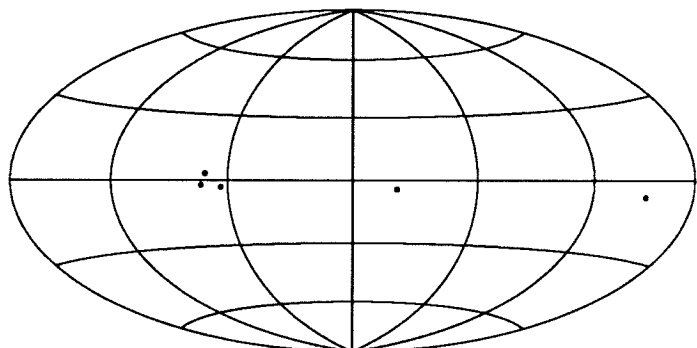
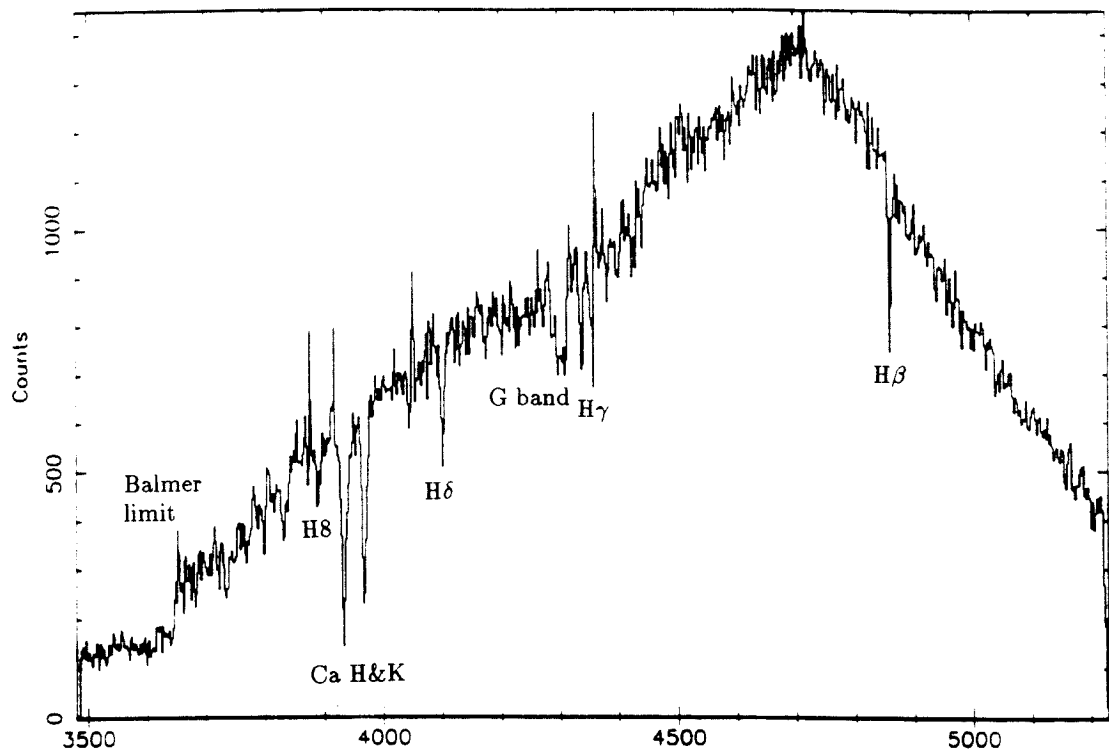


Figure 8.2 a & b
X0042+327 28 Aug 89



X0614+091 19 Nov 89

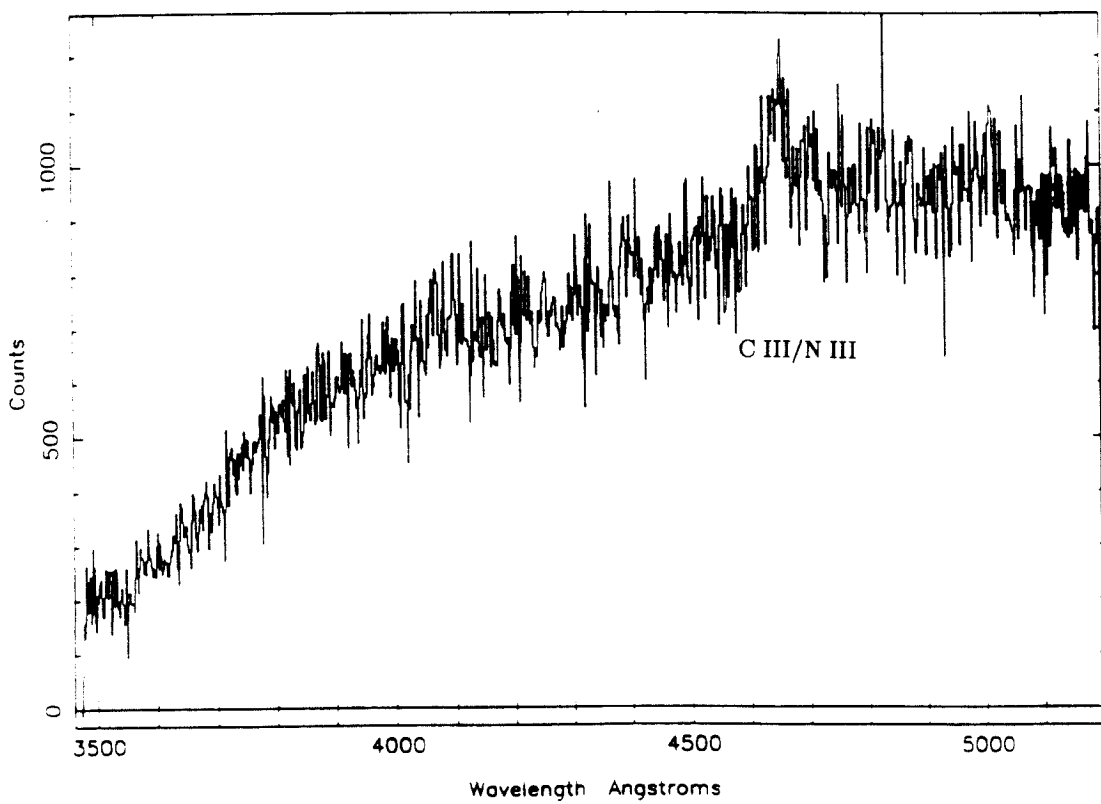


Figure 8.2 c & d
GX9+9 9 Aug 91

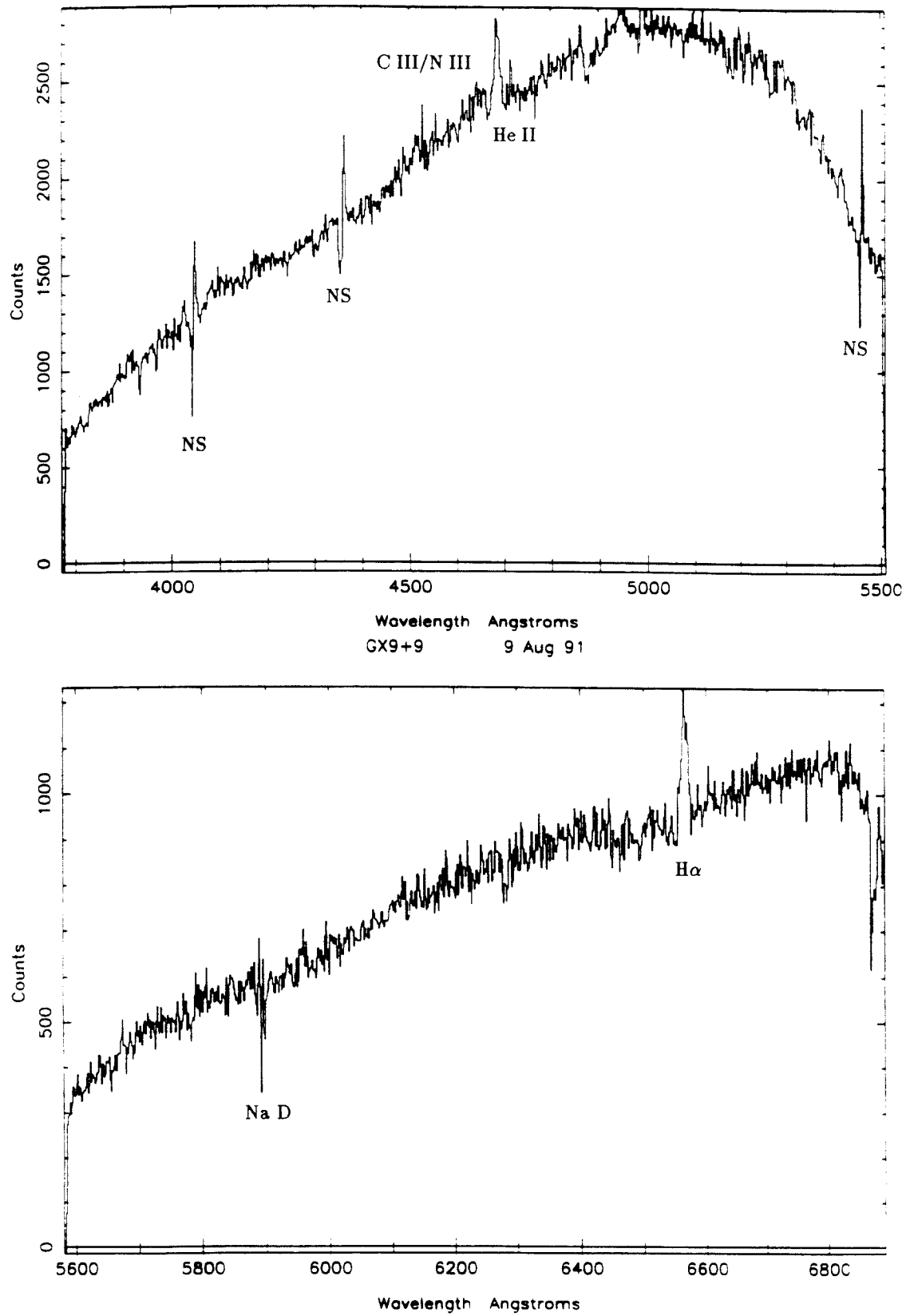


Figure 8.2 e & f

GX17+2 17 Jul 90

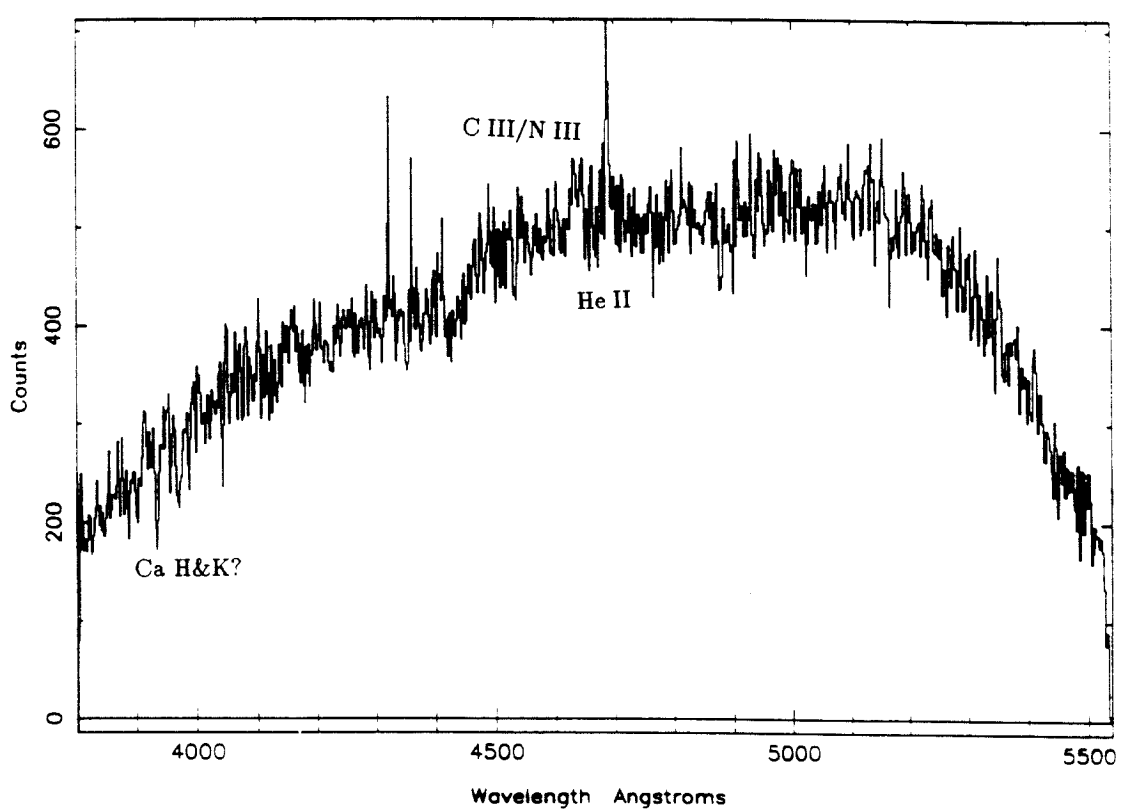
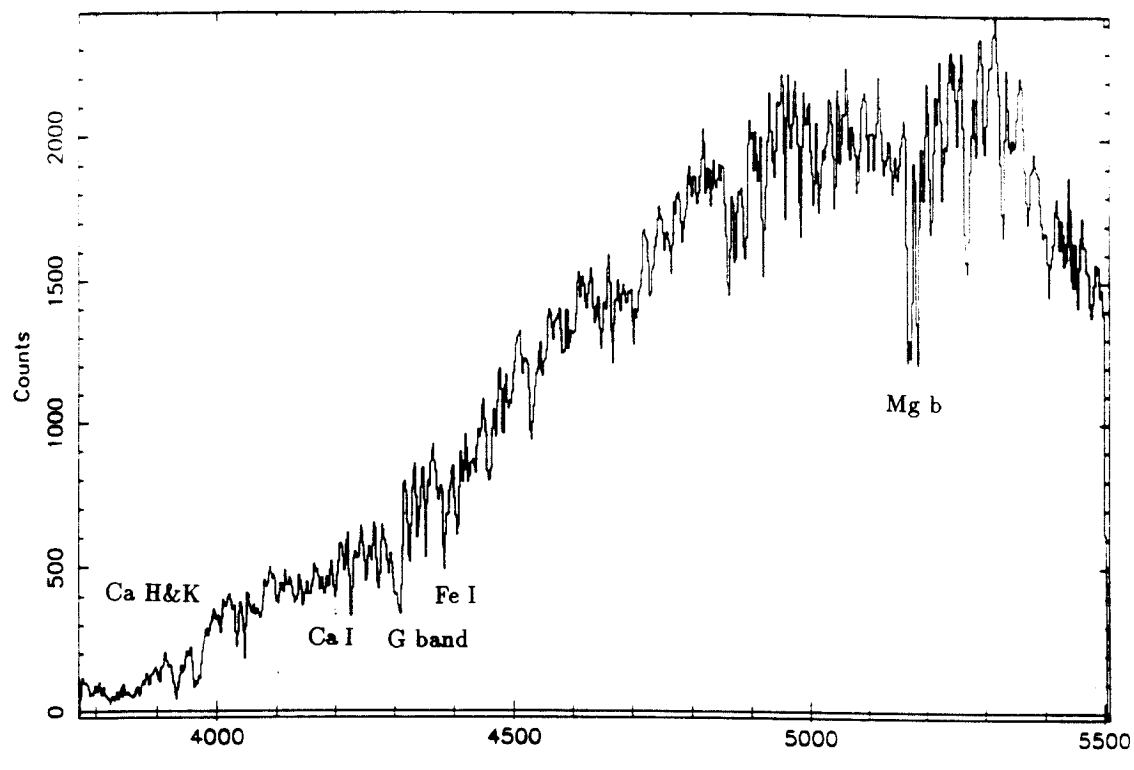


Figure 8.2 g & h

Aql X-1 17 Jul 90

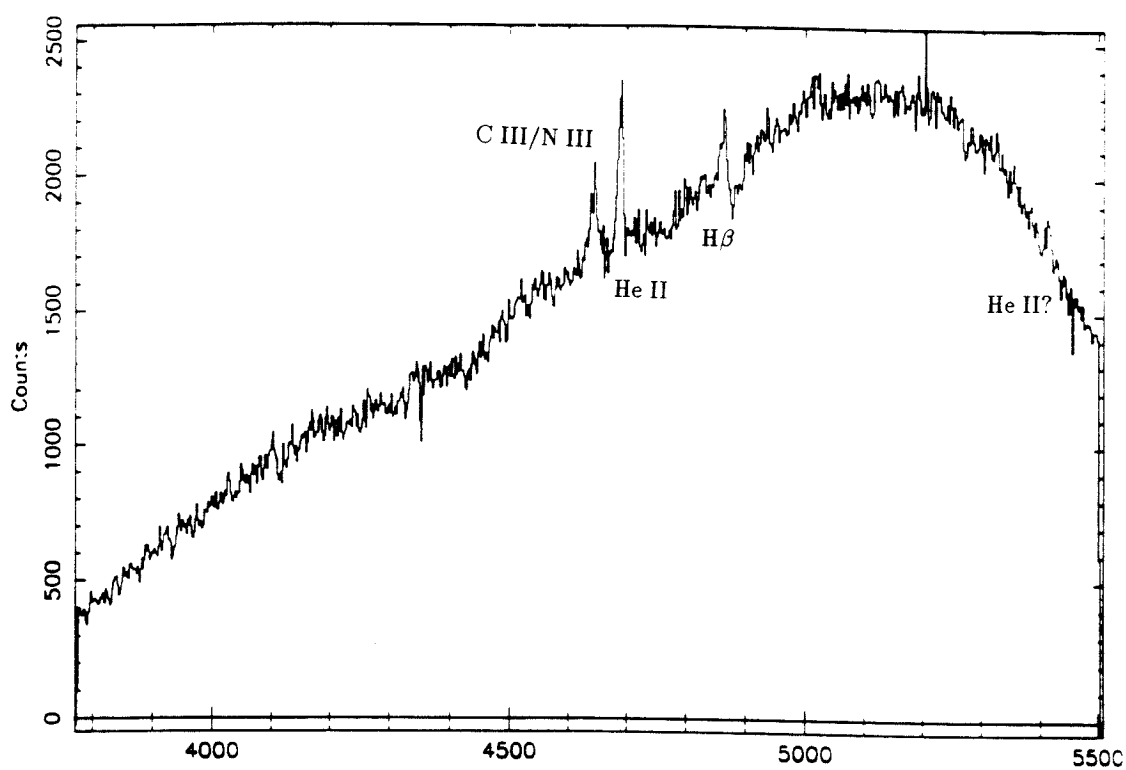
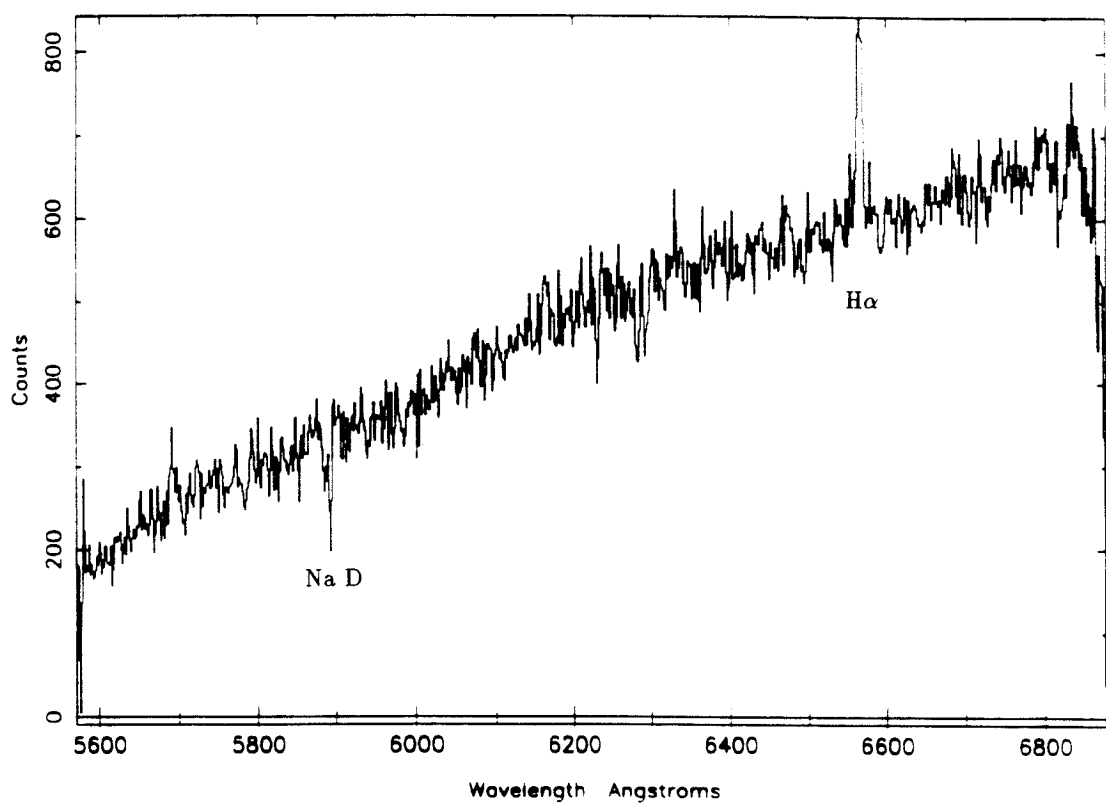
Wavelength Angstroms
Aql X-1 8 Aug 91

Figure 8.2 i & j

X1957+115 17 Jul 90

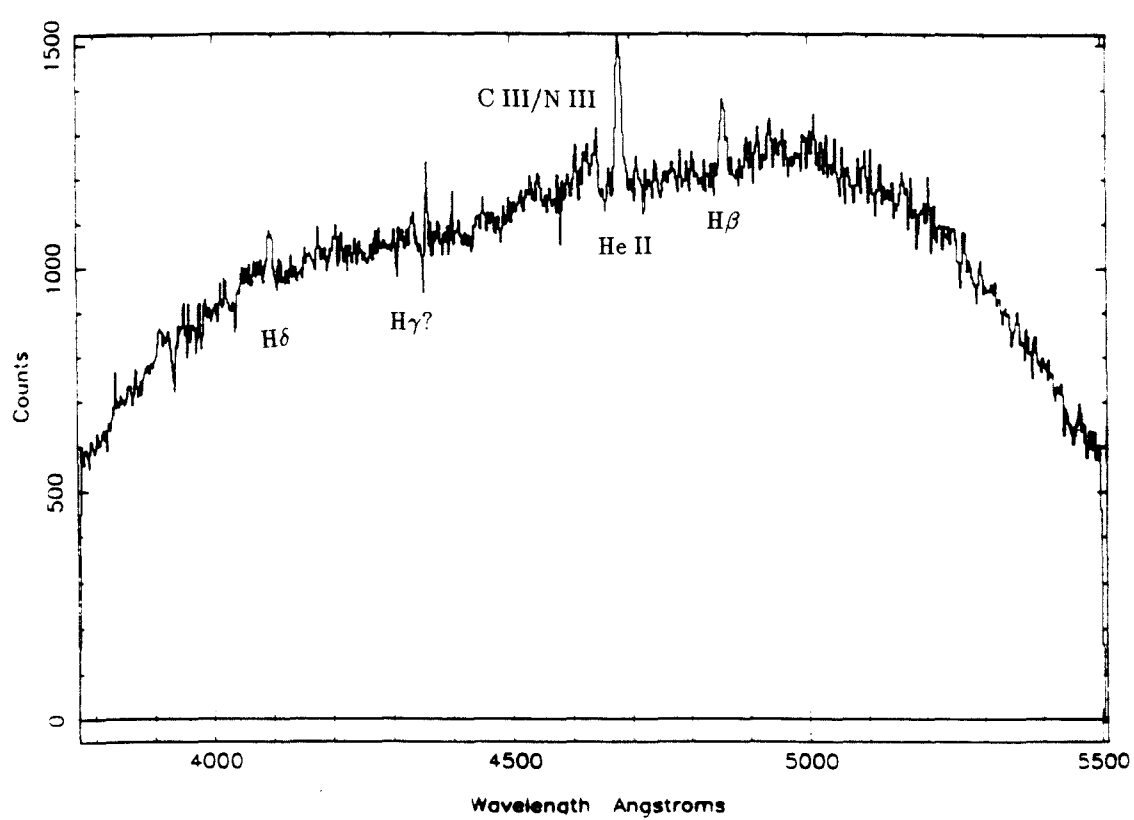
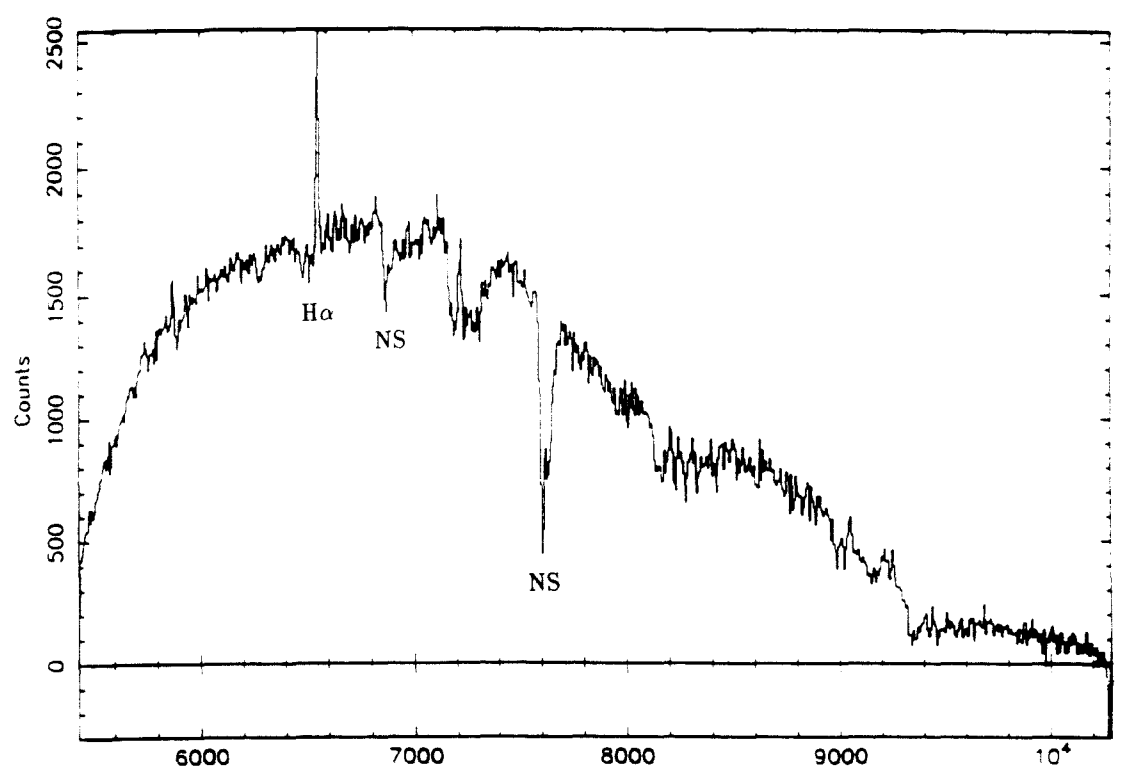


Figure 8.2 k & l
V1727 Cyg 7 Aug 91

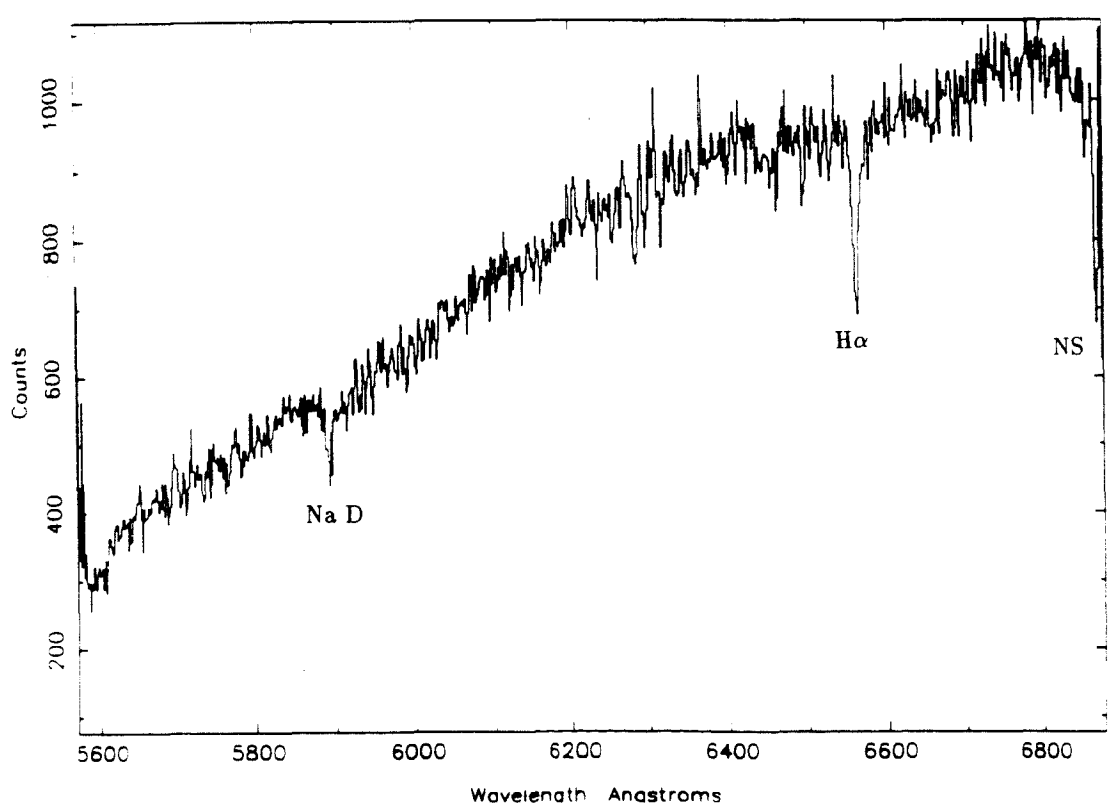
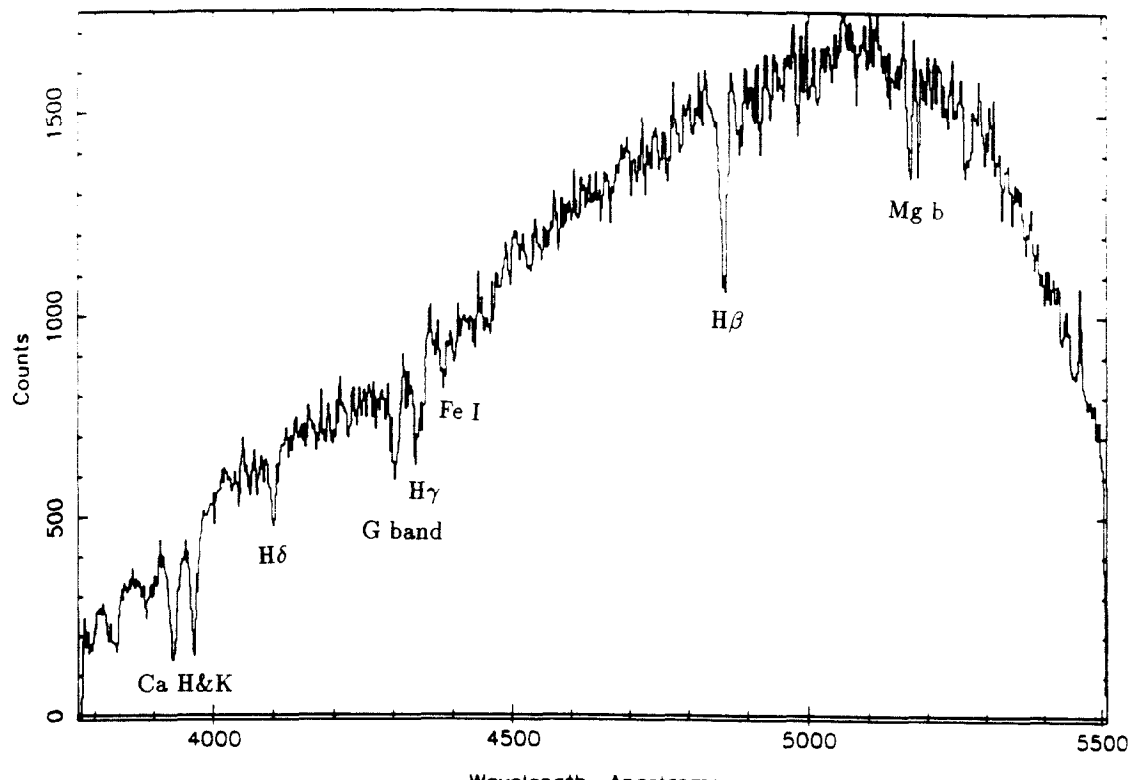


Figure 8.3

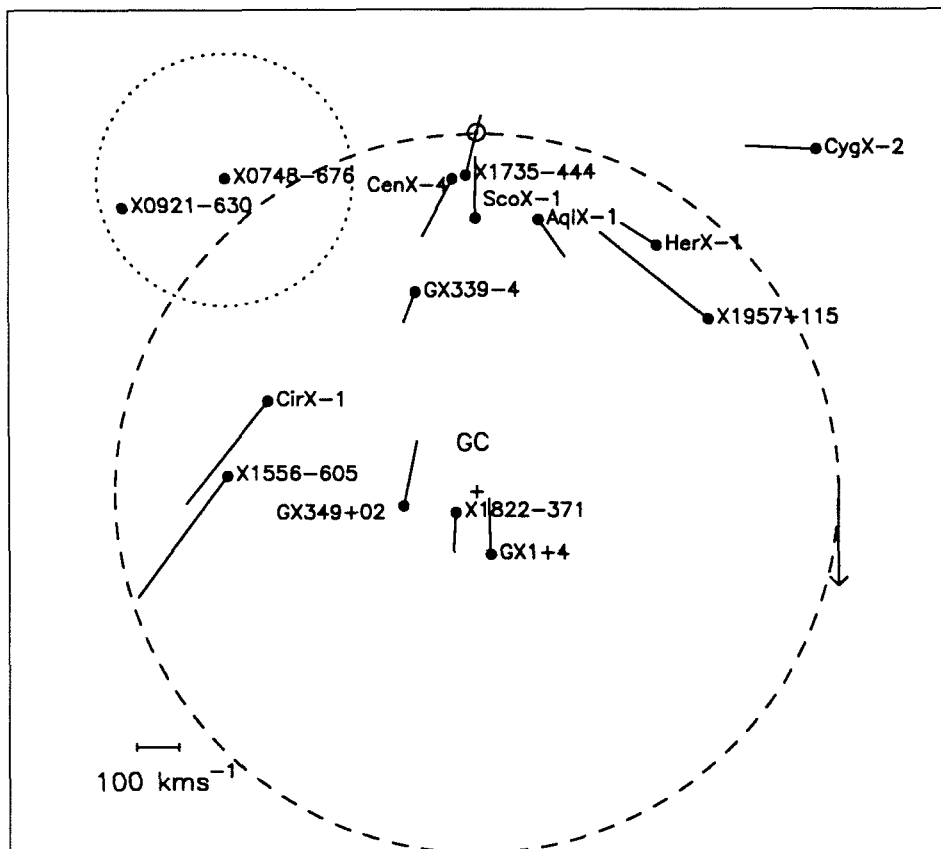


Figure 8.4

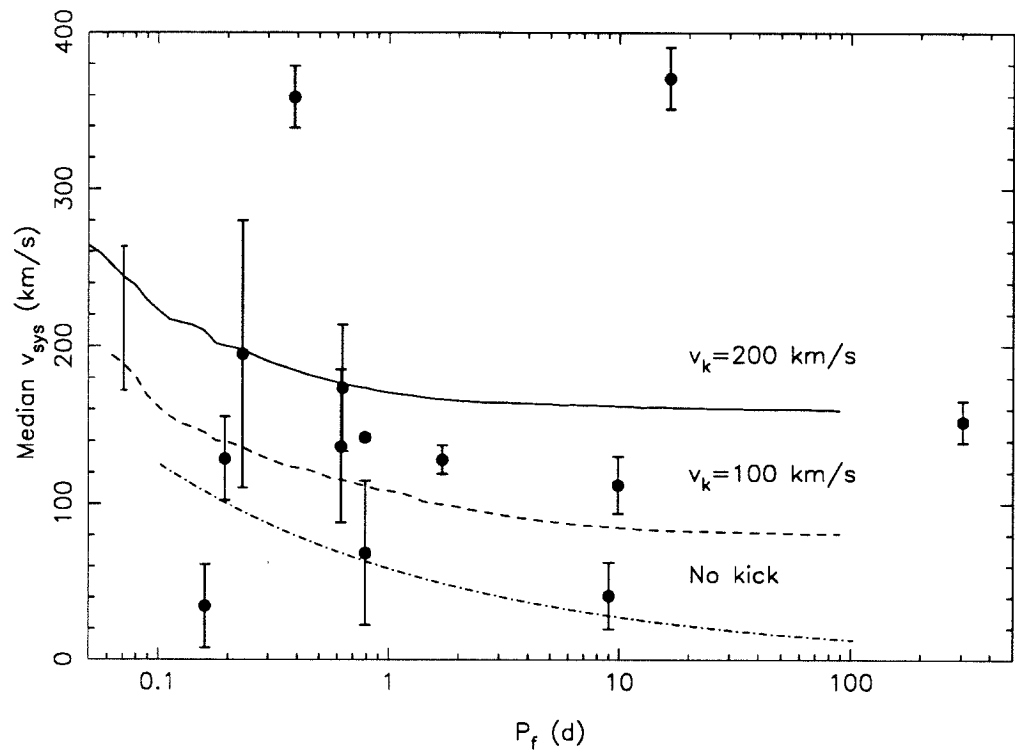


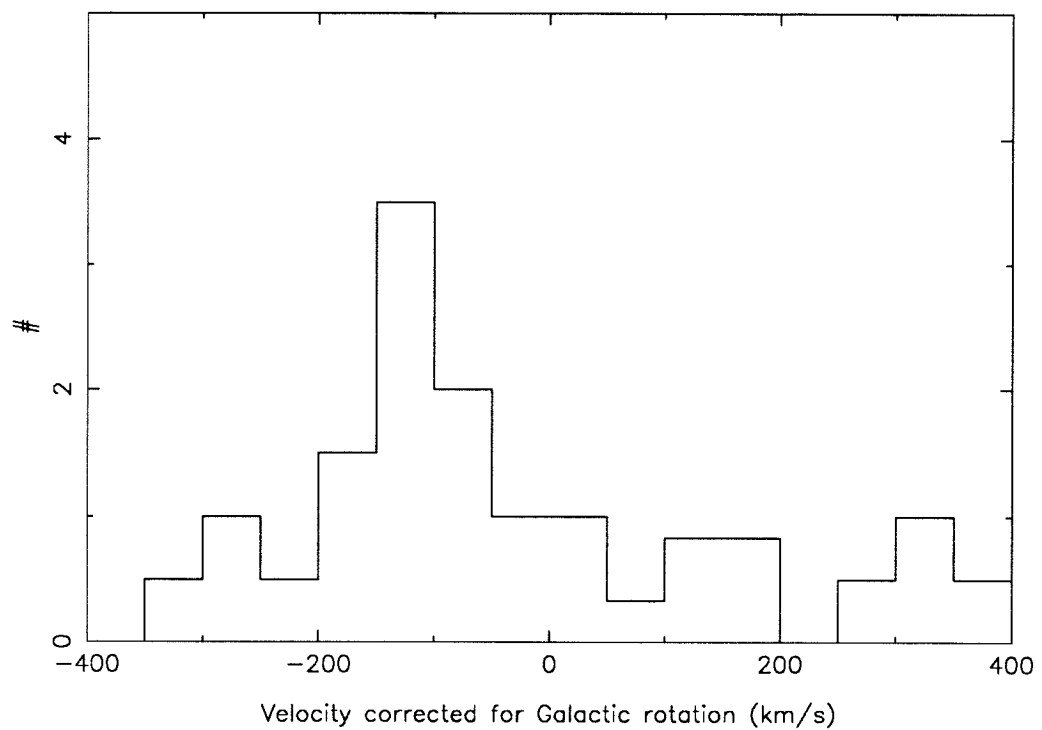
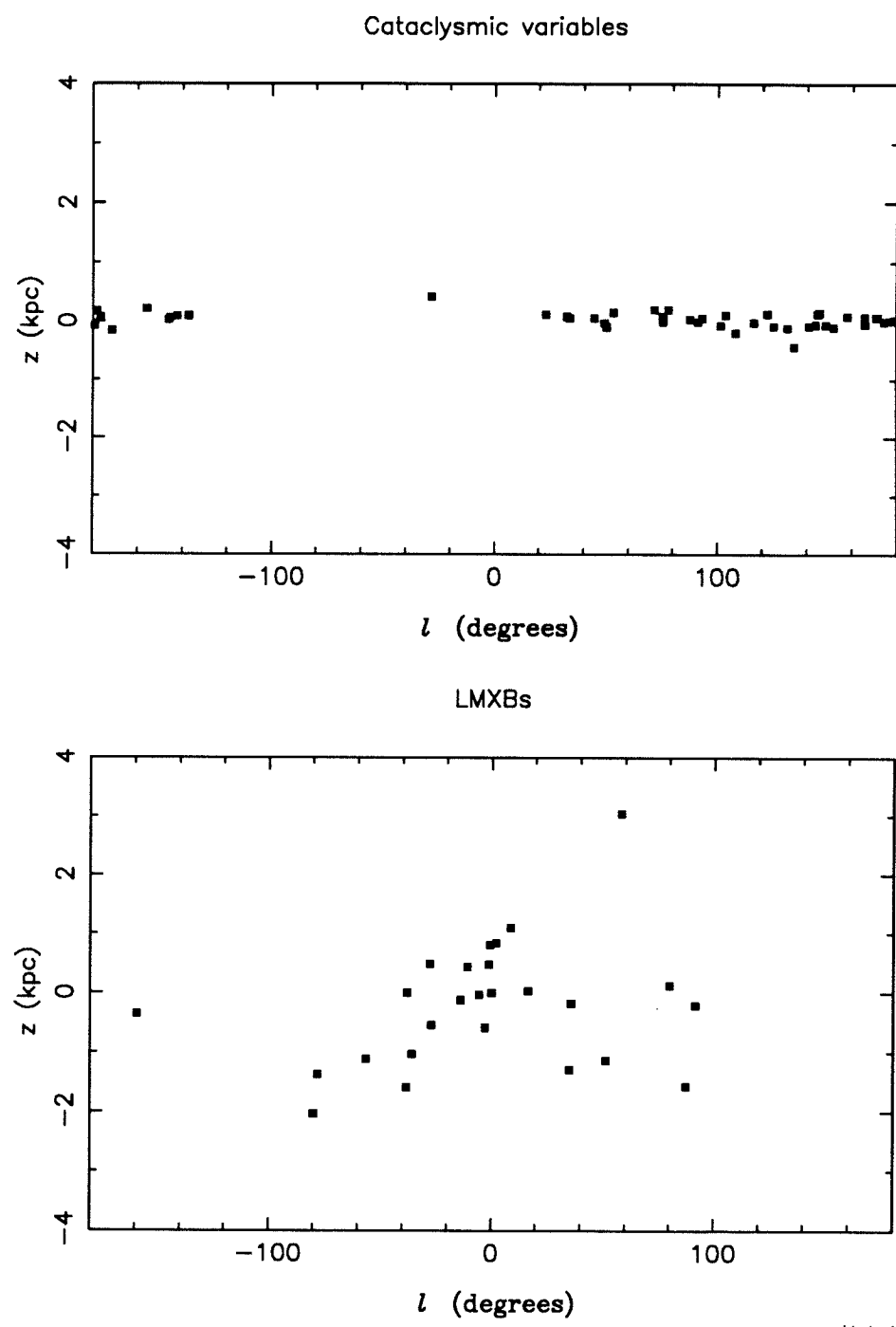
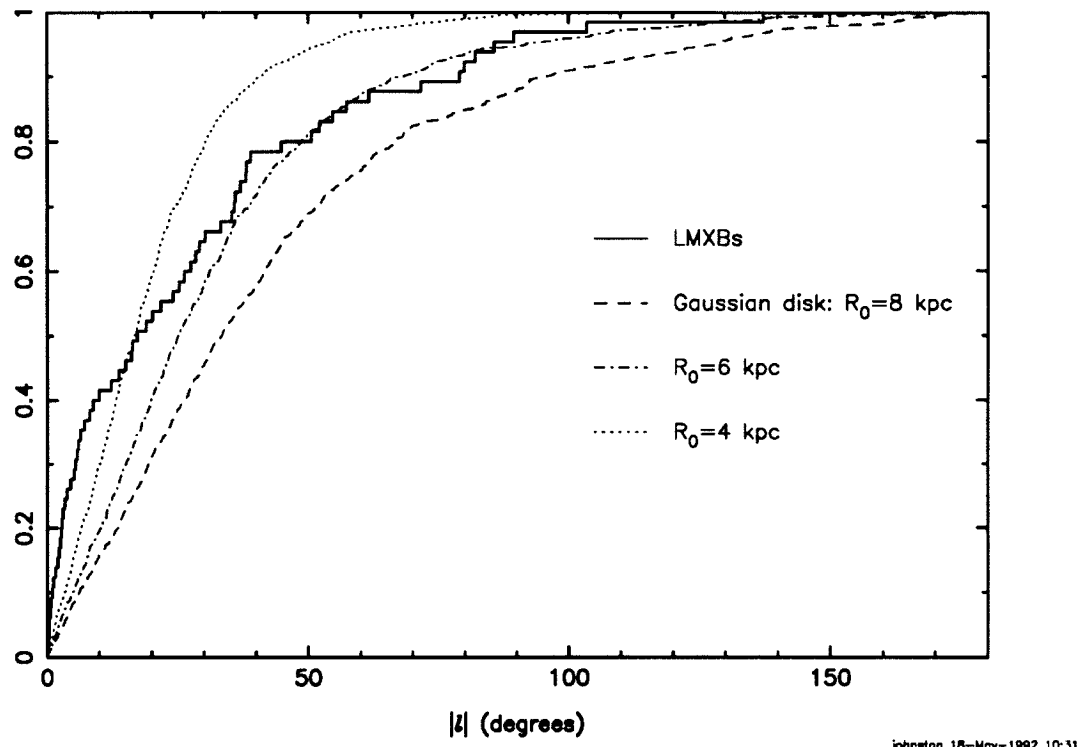
Figure 8.5

Figure 8.6



Iahnelan 10-Apr-1992 17:43

Figure 8.7



I am a poure dyvel, and my name ys Tytyvyllus...

*I muste eche day . . . brynge my master a thousand pokes
full of faylynges, and of neglygences in syllables and wordes.*

— *The Myrroure of our Ladye* (c. 1475 – 1530)